

Coherent Flux Qubits for Quantum Annealing

David López-Núñez

Coherent Flux Qubits for Quantum Annealing

Autor: David López-Núñez

Director: Pol Forn-Díaz

Tutor: Joan Soto Riera

Programa de Doctorat en Física



UNIVERSITAT DE
BARCELONA

Thesis Summary

Quantum annealing is a heuristic analog quantum algorithm that promises potential quantum speedup over classical algorithms for a huge variety of optimization problems. Current existing annealers, despite their technical complexity and large qubit number, in the several thousands, display very short coherence times, making the annealing process incoherent.

The main goal of this thesis is to initiate an alternative path towards building coherent quantum annealers based on superconducting flux qubits. In this thesis, many techniques and methods have been established, and the results obtained represent the first coherent control of superconducting qubits in the QCT group, and, in general, in Southern Europe.

An uncoupled flux qubit device is designed to benchmark qubit coherence that will be used as the building block for future iterations of coherent quantum annealers. The Hamiltonian design of the flux qubits is focused on reducing the persistent current to reduce flux noise susceptibility. The processor is designed so that common coherence benchmarking experiments, such as T1 and T2 measurements, are performed. The physical design has been iterated to understand the role the qubit loop configurations and the qubit frequency have on the coherence times.

The flux qubits are measured inside a dilution refrigerator, where special focus is put on magnetic shielding. Spectroscopy measurements provide initial information on the qubit parameters and quality. Coherent control of flux qubits is achieved in the form of coherent Rabi oscillations, which constitutes one of the most important results of this thesis. Rabi oscillations are repeated for many flux operation points to understand the noise mechanisms. Decay times of 40ns are shown, which are among the best results for flux qubits. However, the qubit coherence is low, leading to coherence times shorter than 20ns, probably because of flux noise. Moreover, due to device imperfections, the qubits could not be characterized at their optimal coherence conditions, which otherwise corresponds to the initial configuration for quantum annealing. In summary, the coherence results of the flux qubits measured represent an important benchmark in the development of a coherent quantum annealer and provide very valuable information on how to improve the flux qubits for future iterations of quantum annealing processors.

As an initial ramp-up phase of this thesis work, experiments with transmons qubits, which are a very well established technology, were performed to develop

the time-domain measurement techniques in the newly established QCT lab, and to set a superconducting quantum computing setup ready to perform quantum algorithms. Indeed, a Universal Approximant algorithm was executed on a single transmon qubit to experimentally prove the approximation capabilities of a single-qubit quantum algorithm.

In parallel to the development of qubit experiments, intrinsic properties of thin-film aluminum has been studied, being the most common material for building superconducting qubit circuits. The magnetic penetration depth of thin film superconducting aluminum has been studied as a function of the film thickness. This calibration, not previously performed in the literature, is especially relevant for the design of flux-sensitive devices, such as flux qubits. The penetration depth is closely related to the so-called kinetic inductance, which is a significant portion of the total inductance in superconductors. This study allows for a better design determination of the inductance in superconducting circuits. Moreover, it points to the possibility of a change in superconductivity type in aluminum in the typical range of thicknesses used in superconducting circuit experiments.

Finally, and in relation to improving the qubit readout fidelity, through a brief stay in NTT (Japan) a quantum-limited amplifier has been redesigned to improve its usability. The quantum-limited amplifier is theoretically identical as one already developed by Arpit Ranadive from the Grenoble team led by Dr. Nicolas Roch, a collaborator of the QCT group, which consists on an array of Superconducting Nonlinear Asymmetric Inductive eLement (SNAIL). The SNAIL circuit is identical to that of the flux qubit, but operated in a different regime. The work developed here will be continued with the fabrication of the actual devices.

Resumen

El "quantum annealing" es un algoritmo cuántico analógico heurístico que ofrece una posible ventaja cuántica sobre los algoritmos clásicos para una amplia gama de problemas de optimización. A pesar de la complejidad técnica y el considerable número de qubits en los procesadores de "quantum annealing" existentes, estos muestran tiempos de coherencia muy breves, lo que resulta en un proceso de annealing incoherente.

La tesis tiene como objetivo principal abrir un camino alternativo hacia la construcción de "quantum annealers" coherentes basados en "flux qubits" superconductores. Se han establecido diversas técnicas y métodos, y los resultados obtenidos representan el primer control coherente de qubits superconductores en el grupo QCT y, en general, en el sur de Europa.

Se ha diseñado un dispositivo de "flux qubits" desacoplados para medir la coherencia de los qubits, que se utilizarán como componente básico para futuras iteraciones de "quantum annealers" coherentes. Los flux qubits se miden dentro de un refrigerador de dilución, prestando especial atención al aislamiento magnético. El control coherente de los qubits de flujo se logra mediante oscilaciones de Rabi coherentes, repetidas en varios puntos de operación del flujo magnético para comprender los mecanismos del ruido. Se han observado tiempos de decaimiento de 40 us, que se encuentran entre los mejores resultados para "flux qubits". Sin embargo, la coherencia del qubit es baja, lo que resulta en tiempos de coherencia inferiores a 20 ns, probablemente debido al ruido magnético. Debido a imperfecciones en el dispositivo, los qubits no pudieron caracterizarse en condiciones óptimas de coherencia, que corresponderían a la configuración inicial para "quantum annealing". En resumen, los resultados de coherencia medidos en los qubits de flujo representan un hito importante en el desarrollo de un "quantum annealer" coherente y ofrecen información valiosa sobre cómo mejorar los qubits de flujo para futuras iteraciones de procesadores.

Paralelamente al desarrollo de experimentos con qubits, se han estudiado las propiedades intrínsecas de capas delgadas de aluminio, el material más común para construir circuitos de qubits superconductores. Se ha investigado la profundidad de penetración magnética del aluminio superconductor de capa fina en función del espesor de la capa. Esta calibración, que no se había realizado previamente en la literatura, es especialmente relevante para el diseño de dispositivos sensibles al flujo, como los "flux qubits".

Resum

El "quantum annealing" és un algorisme quàntic analògic heurístic que ofereix una possible avantatge quàntica sobre els algorismes clàssics per a una àmplia gamma de problemes d'optimització. Malgrat la complexitat tècnica i el considerable nombre de qubits en els processadors de "quantum annealing" existents, aquests mostren temps de coherència molt curts, resultant en un procés d'annealing incoherent.

La tesi té com a objectiu principal obrir un camí alternatiu cap a la construcció de "quantum annealers" coherents basats en "flux qubits" superconductors. S'han establert diverses tècniques i mètodes, i els resultats obtinguts representen el primer control coherent de qubits superconductors al grup QCT i, en general, al sud d'Europa.

S'ha dissenyat un dispositiu de "flux qubits" desacoblat per mesurar la coherència dels qubits, que s'utilitzaran com a component bàsic per a futures iteracions de "quantum annealers" coherents. Els flux qubits es mesuren dins d'un refrigerador de dilució, prestant especial atenció a l'aïllament magnètic. El control coherent dels qubits de flux s'aconsegueix mitjançant oscil·lacions de Rabi coherents, repetides en diversos punts d'operació del flux magnètic per comprendre els mecanismes del soroll. S'han observat temps de decaïment de 40 us, que es troben entre els millors resultats per a "flux qubits". No obstant això, la coherència del qubit és baixa, la qual cosa resulta en temps de coherència inferiors a 20 ns, probablement a causa del soroll magnètic. A causa d'imperficcions en el dispositiu, els qubits no van poder ser caracteritzats en condicions òptimes de coherència, que correspondrien a la configuració inicial per a "quantum annealing". En resum, els resultats de coherència mesurats en els qubits de flux representen un avenç important en el desenvolupament d'un "quantum annealer" coherent i ofereixen informació valuosa sobre com millorar els qubits de flux per a futures iteracions de processadors.

Paral·lelament al desenvolupament d'experiments amb qubits, s'han estudiat les propietats intrínseques de capes primes d'alumini, el material més comú per construir circuits de qubits superconductors. S'ha investigat la profunditat de penetració magnètica de l'alumini superconductor de capa prima en funció del gruix de la capa. Aquesta calibració, que no s'havia realitzat prèviament a la literatura, és especialment rellevant per al disseny de dispositius sensibles al flux, com els "flux qubits".

Publications derived from this thesis

- One qubit as a universal approximant. *Adrián Pérez-Salinas, **David López-Núñez**, Artur García-Sáez, P. Forn-Díaz, and José I. Latorre.* Phys. Rev. A 104, 012405 – Published 2 July 2021
- Superconducting nitridized-aluminum thin films. *Alba Torras-Coloma, Leyre Martínez de Olcoz, Eva Céspedes, Elia Bertoldo, **David López-Núñez**, Sagar Paul, Wolfgang Wernsdorfer, Gemma Rius, Pol Forn-Díaz.* (preprint) arXiv:2308.06240
- Magnetic penetration depth of Aluminum thin films. ***David López-Núñez**, Queralt Portell Montserrat, Gemma Rius, Elia Bertoldo, Alba Torras-Coloma, M. Martínez, P. Forn-Díaz* (preprint) arXiv:2311.14119
- Coherent Flux Qubits for Quantum Annealing. ***David López-Núñez**, Fabian Zwiehoff, Elia Bertoldo, Luca Cozzolino, Barkay Guttel, P. Forn-Díaz* (in progress)

Contents

1	Introduction to Analog Quantum Computers	23
1.1	Basics of quantum computing: qubits and algorithms	24
1.2	Analog Quantum Computing	25
1.2.1	Adiabatic Quantum Computing	26
1.2.2	Quantum Annealing	26
1.2.3	Beyond Standard Quantum Annealing	27
1.2.4	Comparison between Analog and Digital Quantum Computing	29
1.3	Implementations of Quantum Annealers	29
1.4	Thesis overview	30
2	Superconducting Qubits	33
2.1	Superconducting Circuits	33
2.1.1	The transmon qubit as an example of a superconducting quantum circuit	34
2.1.2	LC Circuit	35
2.1.3	Basics of Superconducting Circuits	37
2.1.4	Superconducting circuits as qubits	38
2.2	Transmon Qubits	39
2.3	Flux Qubits	40
2.3.1	Flux Qubits for Quantum Annealing	42
2.3.2	C-Shunted Flux Qubit	43
2.3.3	rf-SQUID	44
2.3.4	Fluxonium	45
2.4	Coupling Qubits	45
2.4.1	Coupling in AQC	45
2.5	Qubit Control	46
2.5.1	Driving Qubits with Microwave Pulses	47
2.5.2	Single-qubit rotations/gates	48
2.5.3	Flux Control	51
2.6	Qubit Readout	53
2.6.1	Dispersive Readout	53
2.6.2	Current-based Readout	55
2.6.3	Quantum-limited Amplifiers	55

2.7	Noise in Superconducting Qubits	56
2.7.1	Qubit Decay and T_1	57
2.7.2	Dephasing and T_2	58
2.7.3	Sources of noise	60
3	Superconducting Circuit Measurements	63
3.1	Setup	63
3.1.1	Refrigerator	63
3.1.2	Magnetic shielding	65
3.1.3	Cabling & Wiring	66
3.1.4	Grounding & Earthing	69
3.1.5	Software	71
3.2	Measurements	71
3.2.1	Spectroscopy Measurements	72
3.2.2	Time-domain Measurements	72
3.2.3	Flux Control	75
3.2.4	DC measurement and Control	76
4	Transmon Qubit Experiments	77
4.1	Introduction	77
4.2	Controlling and Characterizing a Transmon Qubit	77
4.2.1	System & Setup	78
4.2.2	Spectroscopy Measurements	79
4.2.3	Qubit Coherent Control and Characterization	82
4.2.4	Control and readout optimization	85
4.3	One Qubit as a Universal Approximant	91
4.3.1	Universality of a single-qubit approximant	92
4.3.2	Proofs of universality	92
4.3.3	Classical Numerical optimization	93
4.4	Universal Approximant Experiment	95
4.5	Results & Discussion	96
4.5.1	Single variable functions	96
4.5.2	Number of layers	99
4.5.3	Two-variable functions	100
4.5.4	Complex functions	101
4.6	Conclusions	103
5	Engineering Flux Qubit Hamiltonians	105
5.1	Analog Quantum Processor Prototype	106
5.2	Coherent Flux Qubits Design	107
5.2.1	Four-Josephson Junction C-Shunted Flux Qubit	107
5.2.2	Design Parameters	108
5.2.3	Annealing Constraints	109
5.2.4	Simulation Methods	110
5.2.5	Qubit Simulations	111
5.2.6	Final Design Parameters	113

5.3	Comparison between flux qubit types	115
5.3.1	Flux Qubit in the Symmetric Basis	115
5.3.2	3-Junction C-Shunted Flux Qubit	116
5.3.3	N-Junction C-Shunted Flux Qubit	117
5.3.4	C-Shunted Superinductance Flux Qubit	118
5.3.5	Comparison Between Flux Qubits	118
5.3.6	Comparing potential energies	119
5.4	Qubit-Resonator System	121
5.4.1	Readout Circuit	122
5.4.2	Dispersive shift derivation	123
5.4.3	Qubit-Resonator Simulations	124
5.4.4	Results	125
5.5	Coupling qubits	127
5.6	Annealing Schedules	129
5.6.1	Single qubit Annealing	130
5.6.2	Two-qubit Annealing	132
6	Flux Qubit Experiments	135
6.1	Chip Design	136
6.1.1	Device overview	136
6.1.2	Feedline and Resonators	138
6.1.3	Capacitance Network Analysis	139
6.1.4	Flux bias lines	143
6.1.5	Qubit loops	144
6.1.6	Josephson Junction and Fabrication	146
6.1.7	Modifications on designs	146
6.2	Device Inspection & Setup	147
6.2.1	Chip Packaging	148
6.3	Spectroscopy	149
6.3.1	First and Second Generation Devices	149
6.3.2	Third Generation Devices	152
6.4	Flux Qubit Coherent Control	153
6.4.1	Rabi oscillations	153
6.4.2	Readout calibration	154
6.4.3	Resonator Dispersive Shift	158
6.4.4	Rabi oscillations decay time	159
6.4.5	Rabi oscillations for different frequencies.	161
6.4.6	T_1 measurements	162
6.4.7	T_2 measurements	165
6.5	Conclusions & Outlook	167
7	Magnetic Penetration Depth of Aluminum	169
7.1	Theoretical Background	170
7.2	Methodology	172
7.2.1	Resonance Method	173
7.2.2	Resistivity Method	173

7.3	Resonator simulations	174
7.3.1	FastHenry Simulations	174
7.3.2	Sonnet Simulations	175
7.4	Device Design and Fabrication	180
7.4.1	Resonator designs	180
7.4.2	Resistance structure designs	183
7.4.3	Chip designs	183
7.4.4	Studied thicknesses	183
7.4.5	Fabrication	184
7.5	Experiment	185
7.5.1	Resistance measurements	186
7.5.2	Resonator measurements	186
7.6	Results	189
7.6.1	Kinetic inductance results	190
7.6.2	Design variations	191
7.6.3	Critical thickness	191
7.6.4	Temperature dependence	193
7.6.5	Measurements with external magnetic field	194
7.7	Discussion	194
7.8	Conclusions and outlook	196
8	Kerr-reversed TWPA	199
8.1	Quantum Amplification	199
8.1.1	Benchmarking a quantum-limited amplifier	200
8.2	Kerr-reversed TWPA	201
8.2.1	Mathematical Development of Amplification in TWPAs	202
8.2.2	Kerr-reversed TWPA Basics	204
8.3	Theoretical Design	206
8.3.1	Gain and Phase matching in Kerr-reversed amplifier	206
8.3.2	Design Parameters	207
8.4	Physical Design	210
8.4.1	Sonnet Simulations	210
8.4.2	Planar Designs	211
8.4.3	Multilayer designs	212
8.5	Conclusions & Future Work	215
9	Conclusions and Perspectives	217
9.1	Conclusions	217
9.2	Perspectives	218
9.2.1	Universal Approximant	218
9.2.2	Flux Qubits	218
9.2.3	Magnetic Penetration Depth of Thin Film Superconducting Aluminum	219
9.2.4	Kerr-reversed TWPA	219

A	Circuit Quantization	235
A.1	Introduction	235
A.2	Rules	235
A.2.1	Basic components	236
A.2.2	Spanning tree	237
A.3	Procedure	239
A.3.1	Movement equations	239
A.3.2	Lagrangian	241
A.3.3	Conjugate Momentum and Hamiltonian	242
B	4-Josephson Junction Flux Qubit Hamiltonian	243
C	Qubit-Resonator Coupling	245
C.1	Introduction	245
C.2	Circuit Quantization	245
C.2.1	Nodes, spanning tree and direction	246
C.2.2	Movement equations	246
C.2.3	Lagrangian	247
C.2.4	Hamiltonian	248
C.3	Numerical simulation	250
C.3.1	Qubit Hamiltonian	251
C.3.2	Resonator Hamiltonian	255
C.3.3	Coupling Hamiltonian	255
C.4	Dispersive shift	258
C.4.1	Schrieffer-Wolff perturbation theory	258
D	Grounded Loop Capacitance Extraction	265

Preface

I have had a great PhD thesis: I've met incredible people, studied amazing science, travelled to many places, and, in general, I learned a lot. I'm perfectly aware that this global satisfaction is not always the case, so I must be very happy and grateful for that.

It all started when I finished my Master's thesis, and I decided to take a break to think what I wanted to do next. That 9-month break took more than three years in the end, where I had enough time to mature. Work as a developer in a consultant company was much more valuable for my PhD than I thought at that time. This break allowed me to have a general picture of what a PhD meant.

During these three years I decided that I wanted to do experimental physics, unlike my previous studies. I needed to *feel the physics*. As much as I like theory, I felt I had to do experiments to comprehend what was the theory talking about. At that time, Bruno told me that there was one person, Pol, who was coming to build a quantum computer in Barcelona, and he was looking for PhD students. I got in contact with José Ignacio, and then with Pol. Afterwards, I knew that I finally found the PhD I wanted to pursue.

However, this nice story is not strictly true, as until the very last moment I was also searching for a climate science PhD. I remember visiting a climate physics researcher that advised me to go to quantum computing and *jump into the dollar*. After some years, I think I took the right decision, although studying how climate affects virus transmission was a good PhD topic to start at 2019. Quantum hype has been enormous, but even the word "quantum" has weaknesses fighting against a global pandemic.

My PhD started at the BSC Quantic group, a primarily theoretical group with Pol and I as the experimental counterparts. Soon, however, the experimental group moved to IFAE where we were going to have our own lab. Meanwhile, we were at Sergio Valenzuela's lab at ICN2 as visitors, which were my first two years of PhD. All this deeply complicated explaining my official workplace to my friends, although I managed to meet several different people along the way.

At the very beginning of my PhD, I could share a month with Chris Warren, a visiting researcher that managed to measure the qubit frequency just a week before leaving. However, soon after he left I found myself learning how to use a ton of time-domain new equipment to try quantum computing. Best learning experience you can get.

2019 started with me struggling with AWG drivers, and continued with a sub-optimal loss of Helium 3 of the dilution refrigerator. During this time, a new master's student joined the group, Rafael Luque, which deeply helped me develop my ping-pong skills. In May 2019 I had a brief stay at MIT, which was tremendously valuable to learn how to run time-domain experiments, and to get an experience on how a many-body scientific group work. Importantly, it was during this spring that Pol joined IFAE, which involved the addition of Manel to the team, and Qilimanjaro was founded.

Finally, one year after I started my PhD, I managed to run the first-ever coherent control of a superconducting qubit in Southern Europe*. I remember doing them remotely from my sofa, on a rather quiet weekend, and repeating them in many different shapes until feeling confident to say it out loud.

In november 2019, another PhD student joined, Fabian, which made me really happy. Also, I had a couple of months to replicate all the measurements I was reading in the literature to calibrate and characterize our setup. The experiments shown in Chapter 4 reflect some of the most fun part of my PhD. Finally, we deployed an algorithm on my beloved transmon qubit together with the Quantic BSC group. Working together with Adrian, a quantum algorithm researcher, was also a learning experience. Then, March 2020 had something to say.

After mid-2020, I have a hard time setting timestamps to events, as many things happened. In no order in particular, three new PhDs entered in the group, also a postdoc, Qilimanjaro started hiring people and we started sharing the lab with them, more master's and bachelor's students joined the group, we had a visitor researcher for a year, I went to Grenoble to do another short stay, I started attending to conferences and schools, etc. However, the most relevant part for the group was that the lab was finally built, and the first fridge installed in fall of 2020. Although building a lab don't directly lead to publications, it is an invaluable experience.

During these years (2020-2022), we started our pursue to experiment with flux qubits. Fabian and Yifei, together with Gemma, started trying to fabricate our own qubits, while Fabian and me performed the design of the flux qubits, with the help of the master's student Barkay. We sent the design to Glasgow University in what we called the *Glasgow qubits*. Pandemic heavily delayed these qubits, which were first measured in 2021. Unluckily, we couldn't see the qubits.

Meanwhile, I started working on the magnetic penetration depth of aluminum, which introduced me to hard superconductivity theory. It took me a while to fully understand which were and what meant all the superconducting length scales. Together with Queralt and Gemma, we started fabricating chips, and measuring them was a very important part of my PhD. This experiment led to my first presentation at a conference, in the APS March Meeting 2022 at Chicago, with the important help of David Eslava and Yifei during the

*This is the largest mass of land over which we feel entitled to claim the first Rabi oscillations.

measurements.

In general, 2022 occurred in between coffee breaks with Alba, Luca, and Elia. Another batch of flux qubits arrived, which showed that flux qubits were indeed there, but they were still not ready to be coherently controlled. Penetration depth studies showed promising results, but we still had to find out that the simulations couldn't be 2D. 2022 ended with a two-month life-changing stay at Japan. Japan showed me that onsens, izakayas, and TWPA's made a really nice combination. It was a long coffee break.

Then, we arrive at 2023, which has been probably the greatest year of all of them. It started with an otaku version of myself heading into another March Meeting at Las Vegas, in one of the most fun conferences I have been. Also, it was at that conference that I finally found myself understanding all the talks and getting the feeling that I knew the field.

In April 2023 Fabian and I organized a quantum school on superconducting qubits at Benasque, with the help of Pol. This was such an incredible school, and truly remarkable learning experience. Not many people get to organize a school during their PhD, and definitely not such an amazing one.

The PhD was heading to a happy end. After Benasque, I realized I had only one goal: finish my PhD thesis. In May we finally understood the penetration depth results after long hours with Sonnet simulations and Tinkham reading. The paper, which I started to write in August, was ready to go. The preprint was finally out few days before the thesis submission and the journal submission will be done right after I finish writing this preface.

Then, also in August, I put my life on hold to write the PhD dissertation. Honestly, except for 3-4 days of heavy stress a week before the submission, it has been a very interesting and enjoyable part of my PhD. Even more when, in the middle of the writing, a new batch of flux qubits arrived. Against all the odds, we managed to coherently control them. Arguably the most important results of my PhD came less than two months before submission, which was such a nice way to end a very enjoyable thesis.

Acknowledgements

I am honestly grateful to so many people, that I hope I don't miss anybody. First, obviously, to my supervisor, Pol. Someone said once that life is much easier if you have great parents and a great PhD supervisor[†]. I have had the luck to have both. Much of my great PhD experience is thanks to Pol's supervision. From all the learnings I get from him, I value the most the fact that he has led by example. I am also lucky that, being the first PhD, I managed to get a lot of time with him, which I am aware it is not a common experience in a PhD.

Then, I would like to thank all my colleagues. I must confess when I started the PhD alone, I thought I was not going to enjoy that much having colleagues. I would like to thank Alba, Luca and Elia for being such great colleagues and building a strong group core. Also to Fabian, as he has always been an example on how professional can one be, and still partying a lot. Then, to my Qilimanjaro friends, specially to David Eslava and Yifei, as we shared the beginnings of this tough journey, which is starting quantum computing measurements in a lab.

Then, I would like to thank a whole lot of people: Manel and Gemma, that I have felt always such a good connection and have shared with me their expertise; Queralt, for being such a great person and motivated student; Andy, for his sharing passion for shelters; Boris, for his much loved (by me) Bulgarian roots; all the other Qilimanjaro people: Chris, Ana, Matthias, Marta, Albert, David Quinn, Fabio, Paul etc., during my part-time work experience at Qilimanjaro, by the daily task sharing the lab and, to sharing some very nice moments during conferences; all the students that have passed through the group: Rafa, Barkay, Raquel, S.S., Adrian, etc.; and to all BSC group, with whom I shared most of my beginning times of the PHD: Diego, Artur, Adrian, Alba, Carlos and José Ignacio; to all ICN2 people that shared with me the starting days of my PhD.

I also would like to thank external people that have helped me in very diverse ways. First, to Imran, for being such a great work supervisor during my Japanese stay, while making my stay incredibly better. Also to Shiro Saito, for accepting me to go to NTT group at Japan, and to all the NTT group, especially Victor, for making my stay there much better. Thanks again to Marta also for making this experience possible. Then, to Sergio Valenzuela, for allowing us to use his lab during the two first years of my PhD. I would like to thank all the people I shared time with during my stays at MIT and at Grenoble, especially

[†]Maybe no one said that.

to Amir, Antti, Arpit and Nico. Going back to the start, I'm also thankful to Chris, for helping me during my first steps in my PhD. Finally, I would like to thank all IFAE and ICN2 engineers, all the administration stuff and the cafeteria people, which are also of utmost importance.

On a personal note, I would like to thank my family, especially my parents. In a silent way, but they had a strong influence on my academic career, for allowing me to pursue my goals, while knowing that they were always going to be there. Then, to my partner, Laura, for all the help and patience she had during these last PhD months, for the thesis cover we are still designing, and hopefully for celebrating it during the next month in Colombia. Then, it would be difficult to name all of the friends that have somehow made my life better. I would like to thank especially to the *Tordera* people, as their experience during their PhD years before I started mine helped to know what a PhD was going to be. Of course to Núria, for being there during the search of my PhD, my first doubts, and my first stresses. Finally, on a side note, to all my comedy peers that without knowing, have helped me deviate my mind from the burdens of science.

All in all, I have been surrounded by incredible people.

Chapter 1

Introduction to Analog Quantum Computers

Classical computers have progressed enormously over the past decades, and humankind has significantly benefited from many of the developments enabled by the computing technology. However, certain problems are still too complex for classical computers to tackle. These problems are sometimes solvable, but the resources needed make them unattainable, sometimes leading to millions of years of computing time even using the best supercomputers.

Quantum computing is a conceptually different approach to computation, since the fundamental basis is changed to follow quantum laws, which generates a *quantum logic*[Nie11]. This quantum logic is not *better* than the classical one, but it can lead to dramatic speedups in several problems of great interest[Sho04; Chi08; Lad10]. Although quantum computers are not expected to overcome classical computer performance in all aspects, there are many areas where it can lead to a substantial *quantum advantage*: ground state simulation in complex molecules[Bau20], portfolio optimization[Her22], decrypting RSA cryptography codes[Sho94], advanced combustion modeling[Jak22], designing metamaterials[Kit20], transportation route optimization[Neu17], many-body quantum physics simulations[Smi19], etc.

Building a quantum computer, however, is not as trivial a task, as one could imagine. In the last couple of decades, dramatic progress has been made, and now there exist several prototypes of quantum computers where quantum algorithms can be tested [McE21; Jur20; Zhu21; Kin21; Zha17; Pog21]. Much more development is needed in order to provide practical quantum advantages. On the software side, new algorithms have to be developed to leverage the current quantum processors. The promises are so high, deserving the effort of pursuing quantum computation.

The goal of this chapter is to give an introduction into the broad topic of quantum computing from the theoretical point of view, focusing on Analog Quantum Computing. Section 1.1 introduces the basics of quantum computa-

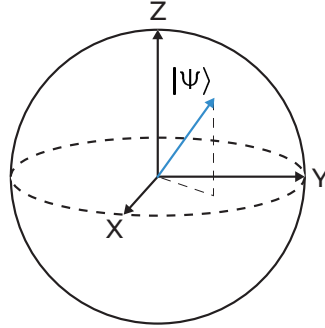


Figure 1.1: Bloch Sphere. The qubit state $|\Psi\rangle$ is represented as a vector pointing at the surface of the Bloch sphere.

tion: namely the qubits, and the quantum algorithms. The paradigm of Analog Quantum Computing is explained in Section 1.2, where its main founding base are detailed. There, the current state of the field and its main variations are exposed, while comparing it with the most dominant quantum computation paradigm: Digital Quantum Computing. Finally, in Section 1.4 this thesis is outlined and put into context.

1.1 Basics of quantum computing: qubits and algorithms

Bits are the unit of information in classical information and, thus, of classical computation. From the theoretical description, bits are binary variables with two possible values usually labeled as 0 and 1. Quantum computation has evolved analogously to classical computation and its unit of information is called a quantum bit, or *qubit*. Similar to classical bits, qubits also exist in binary states, labeled as 0 and 1. These binary values refer to the two possible qubit states, $|0\rangle$ and $|1\rangle$. However, the qubit can represent any arbitrary superposition of $|0\rangle$ and $|1\rangle$. The state of a qubit is often illustrated using a vector within a sphere, known as the Bloch sphere (see Fig. 1.1). Nevertheless, when measured, a qubit can yield only one of two values, 0 or 1, thus limiting its information capabilities.

In principle, *any* quantum system could be used as a qubit if it meets specific criteria[DiV00]. Summarizing, there should be a way in this quantum system to isolate its dynamics to just two states. Moreover, it should be possible to initialize, control and measure this qubit efficiently. If all this can be implemented before decoherence affects quantum evolution, and many qubits can be coupled together, that system is suitable for quantum computing. Various technologies are potential candidates for constructing quantum computers, with superconducting qubits proving to be one of the most successful thus far[Kra19].

A quantum computer made out of working qubits needs algorithms to perform actual tasks. These algorithms are, ultimately, a global unitary operation on the qubits, which brings them from an initial known state to the solution of a specific problem. The qubits are initialized in a state, $|\Psi_0\rangle$, which typically is the ground state of the system. $|\Psi_0\rangle$ is typically a product state, which can be expressed by their individual qubit states, $|\Psi_0\rangle = \prod_i |\varphi_0\rangle$. An algorithm evolves the qubit states over time until a final state $|\Psi_f\rangle$, which is then measured and a series of $|0\rangle$'s and $|1\rangle$'s are obtained, which are the answer to a problem. In Digital Quantum Computing, this evolution consists of discrete gates [Mon15], while in Analog Quantum Computing it involves a continuous evolution of the qubit control parameters [Alb16]. Ideally, $|\Psi_f\rangle$ should also be a product state with the individual qubits in one of the two computational eigenstates, ensuring a probability of measuring the solution equal to 1. If the solution is a superposition, one needs statistics.

However, real algorithms do not lead to the exact solution due to qubit decoherence [Pre18; Bha21]. This limitation is acceptable as long as a problem solution is achieved in a reasonable number of trials or if a satisfactory solution, even if not exact, is obtained, particularly in optimization problems. Eventually, one needs quantum error correction [qec] to be immune to individual errors. However, the current combination of high error rates and limited number of qubits in existing processors requires further advancements for quantum computing to effectively solve real-world problems.

1.2 Analog Quantum Computing

Analog Quantum Computing (AnQC) relies on continuous evolution of the system leveraging the analog nature of quantum mechanics. AnQC focuses on the evolution of a Hamiltonian by modifying the system energies and interactions until a desired final Hamiltonian, \mathcal{H}_f is reached. The solution to the problem is usually encoded in the ground state of \mathcal{H}_f . Interestingly, there exist known methods to express optimization problems into Hamiltonians suitable for AnQC[Glo18].

AnQC is commonly confused with Adiabatic Quantum Computation (AdQC) and Quantum Annealing (QA)*. They are all similar terms, and, in some situations, no distinction is required. AnQC is the most general of all, and only imposes continuous evolution as the algorithmic driving force. AdQC, on the other hand, is a well-developed quantum computing paradigm, that requires this analog evolution to be strictly adiabatic [Dam01; Far00a; Alb16]. Finally, QA is a heuristic method which consists on sweeping the control fluxes of Ising Hamiltonians until the final state is the solution to an optimization problem

*For the rest of the thesis after this chapter, no clear distinction will be formulated between AnQC, AdQC, and QA, since, from the experimental point of view in the context of superconducting qubits, they have many similarities. AQC (Analog Quantum Computing) will determine Analog Quantum Computing in the context of the Adiabatic and Quantum Annealing formalism.

[Apo89; Kad98; Cro20]. In this sense, QA is an algorithm inside AnQC that, if performed sufficiently slow, may operate as AdQC.

Analog Quantum Computing, however, is not only reduced to the AdQC model of computation. Some other paradigms exist, such as quantum reservoir computing [Fuj16], quantum simulations [Alt19], quantum walks, etc. However, throughout this thesis only the AdQC and QA versions of analog quantum computing will be considered.

1.2.1 Adiabatic Quantum Computing

AdQC has been proven to efficiently simulate any digital quantum algorithm [Aha04], thus ensuring universal computation also at the analog level. AdQC bases its predictions on the adiabatic theorem [Bor28; Kat50; Mes61], which ensures that, if a system starts at its ground state and evolves at a slow enough pace, the instantaneous $|g\rangle$ is not escaped during the evolution, successfully ending with the ground state of a final Hamiltonian, \mathcal{H}_f . The whole body of AdQC consists of determining how slow this evolution needs to be, defined by the final time, t_f . This mostly depends on the minimal gap along the evolution, defined as

$$\Delta \equiv \min_{t \in [0, t_f]} \Delta(t) = \min_{t \in [0, 1]} (\varepsilon_1(t) - \varepsilon_0(t)), \quad (1.1)$$

where $\varepsilon_{0,1}(t)$ are the instantaneous energies of the ground (0) and excited states (1). Thus, the final time must satisfy [Alb16]

$$t_f \gg \frac{1}{\Delta^2}, \quad (1.2)$$

in order to ensure that the system stays in the ground state[†].

However, the exact determination of Δ is hard, making the amount of known adiabatic quantum algorithms that hold quantum advantage a very reduced number [Alb16].

Moreover, AdQC considers the system as closed, which is not true in real quantum processors. Predictions from AdQC have to be then extended to open systems where decoherence alters the pure adiabatic evolution of the system.

1.2.2 Quantum Annealing

QA comes as a pragmatic approach to AdQC, since it follows its overall methodology to find optimal realistic algorithms. Although QA has not theoretically been proven to yield a quantum advantage, it is believed that it can lead to quantum advantage even without such a mathematical demonstration, similarly to neural networks in classical computing.

The name of quantum annealing [Kad98] comes as an analogy to simulated annealing [Kir83], which is a classical algorithm used to solve optimization problems in which the simulated temperature is initially increased to avoid

[†]A more rigorous version of this statement can be found in [Alb16].

metastable states, and then it is reduced until the ground state of the desired Hamiltonian is found. Simulated annealing itself takes its name from the metal annealing used in metallurgy, where metals are heated and then cooled in order to change their microscopic structure, reducing impurities in the grain.

Standard quantum annealing is an algorithm that consists in preparing the ground state of a Hamiltonian which is easy to prepare, and interpolate it into another Hamiltonian, whose ground state encodes the solution to a certain problem. QA is commonly used for solving combinatorial problems, which are represented in Ising Hamiltonians. The spin glass Hamiltonian is expressed as

$$\mathcal{H}_f = \sum_i h_i \sigma_{z,i} + \sum_{i < j} J_{ij} \sigma_{z,i} \sigma_{z,j}, \quad (1.3)$$

where $\sigma_{z,i}$ is the Z Pauli matrix of qubit i , and h_i and J_{ij} are the single-qubit and two-qubit Ising terms, respectively. The subscript in \mathcal{H}_f is to show that this is the shape of the final Hamiltonian. Spin glass problems represented by this Hamiltonian are known to be hard problems.

The initial Hamiltonian, \mathcal{H}_0 , is commonly taken as

$$\mathcal{H}_0 = \sum_i h_{x,i} \sigma_{x,i}, \quad (1.4)$$

whose ground state is the product state with equal superposition of all the states. Thus, it is a convenient starting point as it naturally explores all the available classical Hilbert space.

The annealing algorithm or *annealing schedule*, evolves the initial \mathcal{H}_0 into \mathcal{H}_f

$$\mathcal{H}(t) = A(t)\mathcal{H}_0 + B(t)\mathcal{H}_f, \quad (1.5)$$

where $A(t)$ and $B(t)$ are the amplitudes of the initial and final Hamiltonians. $A(t)$ goes from 1 to 0 as time evolves, and $B(t)$ evolves inversely.

Often, a normalized time variable is used, $s(t)$, which goes from $s(t=0) = 0$ to $s(t=t_f) = 1$. $s(t)$ captures the evolution rate of the Hamiltonians, which should be slowed down when approaching the minimum gap, Δ . However, the exact location of Δ is not generally known. Equation (1.5) can be rewritten as

$$\mathcal{H}(s) = (1-s)\mathcal{H}_0 + s\mathcal{H}_f. \quad (1.6)$$

1.2.3 Beyond Standard Quantum Annealing

The simple structure of Eq. (1.5) can be further extended in real-case scenarios. First, the sequence in Eq. (1.5) assumes that the Hamiltonians are tuned uniformly. However, each qubit can be discretely targeted by *inhomogeneous driving* of Hamiltonians. These drivings may avoid first-order phase transitions that may otherwise occur at the middle of the anneal, thus considerably increasing Δ . This approach, however, is highly problem-dependent [Sus18].

Other approaches consist in adding extra terms in the standard annealing sequence. Some of the more relevant are introduced here:

- *Catalysts.* Adding a catalyst [Alb17], \mathcal{H}_C , that vanishes both at the start and at the end of the anneal,

$$\mathcal{H}(s, \lambda) = (1 - s)\mathcal{H}_0 + s\mathcal{H}_f + (1 - s)\lambda\mathcal{H}_C, \quad (1.7)$$

where λ is another normalized time variable that also goes from 0 to 1 as time evolves. The addition \mathcal{H}_C could change a first-order transition to a second-order one.

- *Reverse annealing.* Reverse annealing consists of starting the annealing sequence at an initial state, \mathcal{H}_r , that contains partial information about the final desired state [Per08]. The reverse annealing sequence is described by

$$\mathcal{H}(s, \lambda) = (1 - s)\lambda\mathcal{H}_0 + s\mathcal{H}_f + (1 - \lambda)\mathcal{H}_r. \quad (1.8)$$

\mathcal{H}_r is detuned with λ while the transverse field \mathcal{H}_0 , initially at zero, is increased and then reduced. This way, the system explores the region around the initial proposed solution, which can be a more efficient way than exploring the whole parameter space.

- *Shortcuts to adiabaticity.* Adiabaticity imposes a severe restriction on the algorithm time. However, quantum annealing does not need to fulfill adiabaticity. Therefore, shorter paths than the adiabatic one leading to the optimal solution may be explored [Sal16]. This is now known as diabatic annealing [Cro20].
- *Counter-diabatic driving.* In the same direction as the previous point, sometimes, extra counter-diabatic terms are added, which counteract the diabatic behavior due to a fast anneal [Dem03].

Moreover, the final Hamiltonian considered so far, the Spin Glass Hamiltonian, is a stoquastic Hamiltonian [Sin09]. Stoquastic Hamiltonians are defined as having a matrix representation with all off-diagonal elements being non-positive in the considered basis. Stoquasticity is important as a classical simulation method known as quantum Montecarlo is believed to be inefficient when simulating non-stoquastic Hamiltonians, because of a limitation called *the sign problem*. However, the sign problem does not occur for stoquastic Hamiltonians, making them easier to simulate. However, it is uncertain whether non-stoquasticity is needed to provide quantum advantage [Cia20; Hal20].

A non-stoquastic Hamiltonian can be achieved by adding $\sigma_X\sigma_X$ interaction between the qubits. Apart from introducing $\sigma_X\sigma_X$ interactions, other interesting interactions are many-qubit couplings [Cha16; Men19], such as $\sigma_Z\sigma_Z\sigma_Z\sigma_Z$, which may enhance the annealer capabilities.

In a more pragmatic level, increasing the number of coupled qubits is also desired, as all-to-all coupling is not easily achieved in superconducting qubit annealers. Therefore, the original problem Hamiltonian has to be embedded into the physically available processor. Finding an optimal embedding can itself be a very hard problem.

Finally, the LHZ (Lechner-Hauke-Zoller) scheme is an alternative method for quantum annealing, where the optimization problem is encoded in the local fields acting on the qubits [Lec15]. This scheme allows for all-to-all coupling, but all the interactions are 4-body terms acting on nearest neighbors. The LHZ scheme can actually be implemented in many qubit technologies.

1.2.4 Comparison between Analog and Digital Quantum Computing

Digital quantum computing (DQC) is similar to digital classical computing as it relies on the application of logical gates to their individual components. However, unlike many of their classical counterparts, quantum logical gates are reversible, since they follow a unitary evolution. In general, quantum logic is qualitatively different from classical logic.

Although DQC and AnQC can be based upon the same qubits, and both can leverage their quantum properties to solve the same problem, the methodology is considerably different. Technically DQC is also analog as the discrete logic gates consist of continuous voltages or currents applied to the qubits [Mot09]. However, these continuous rotations are encapsulated as gates, and a digital abstraction is based upon these.

Digital algorithms also typically start in the ground state of the system, but their evolution rapidly deviates into highly excited states. These states are much more subject to decoherence than following adiabatic evolution such as in AdQC. One of the main decoherence mechanisms is relaxation to the ground state, which in annealing is usually favourable, while in DQC it destroys the algorithm. The other main decoherence mechanism, dephasing, typically occurs in the energy basis of the system, which is the computational basis in DQC. However, the dephasing in the energy basis is much less harmful in quantum annealing. In general, one of the main promises of the analog method is that it may be less impacted by decoherence than DQC [Alb15].

1.3 Implementations of Quantum Annealers

The only successful approach to build quantum annealers has been the technology of superconducting flux qubits. These qubits are particularly suitable for quantum annealing, as their ground state can hold two persistent current states in opposite directions, which are the computational states. Controlling the flux threading the superconducting loops, the annealing sequence can be performed.

Much of the development of quantum annealers is focused on increasing the coherence of the individual qubits, which for early demonstration was very low. Other paths of development are increasing the number of qubits, increasing the connectivity of the annealer, improving readout efficiency, etc.

The most prominent quantum annealer implementation has been made by the company D-Wave [Har09a; Joh09]. D-Wave annealers are, by far, the superconducting quantum processors with most qubits, currently. The last generation

yields more than 5,000 qubits. However, the qubit quality is not as good as the gate-model quantum computers [Ozf19].

D-Wave qubits have short coherence, and it has recently been clear that implementing coherent annealing with D-Wave systems is extremely challenging [Kin22]. Moreover, the connectivity of the qubits is limited. The current Pegasus architecture has each qubit coupled to 15 different qubits. This connectivity, although remarkable from the engineering point of view, requires embedding the original Hamiltonian, thus reducing significantly the total amount of logical qubits. Finally, only two-qubit stoquastic couplings are available in the current configuration.

Other proposals of coherent quantum annealers have been developed, such as a recent 25-qubit flux qubit quantum annealer built by MIT-Lincoln Labs [Yan15; Web17], where a multilayer chip structure has been implemented. One of the key aspects of this work is to use qubits with higher coherence as the building blocks. However, the progress to 25 qubits has not shown the translation of this single-qubit high coherence to such a many-qubit system.

The LHZ [Lec15] scheme can also be implemented with various superconducting qubit platforms, which is another promising alternative of the standard models of quantum annealing [Yam08; Yam22; Pur16]. A first prototype has been developed recently at NEC using superconducting parametric oscillators as qubits, where the unit cell of a LHZ annealer has been successfully developed.

In this context, Qilimanjaro Quantum Tech has emerged as a new player pursuing the goal of a coherent quantum annealer [Can21]. Qilimanjaro has the more general purpose of developing analog quantum computers, not only focusing on quantum annealing.

This thesis aims to start another route towards coherent quantum annealers, starting from the very basic foundation: the design of flux qubits. These flux qubits are designed to deploy long coherence times compared to D-Wave systems. The flux qubits developed in this thesis are intended to serve as building blocks of future annealer designs which incorporate non-stoquastic couplers as well as to perform alternative to the traditional annealing sequences while preserving coherence throughout the process.

1.4 Thesis overview

The main goal of this thesis is to initiate another path to coherent quantum annealers based on superconducting qubits. Therefore, in this thesis many techniques and methods have been developed for the first time in the newly established QCT lab at IFAE. The results represent the first coherent control of superconducting qubits in the QCT group.

The theoretical building blocks of superconducting qubits is given in Chapter 2. There, two types of qubits are introduced: transmons and flux qubits. The former are one of the simplest superconducting qubits, and they are used to introduce superconducting qubit experiments in this thesis Chapter 4. On the other hand, flux qubits are superconducting qubits particularly suitable to per-

form annealing schedules, where its ground state can hold superpositions of persistent current states, which act as computational states. Apart from the qubit introduction, an overview on the qubit operation, coupling and measurement is also given, as well as the main noise mechanisms affecting superconducting qubits.

The experimental setup used throughout the thesis is described in Chapter 3. Three types of experiments have been performed: transmon qubit experiments (Chapter 4), flux qubit experiments (Chapter 6) and resonator measurements (Chapter 7). Each experiment has different requirements, being the flux qubits the most fragile due to the special sensitivity to flux noise. However, the setup is mostly similar in all experiments.

The transmon qubit experiments described in Chapter 4 are primarily used to develop the time-domain measurement techniques in the QCT lab, and to set a superconducting quantum computing setup ready to perform quantum algorithms. Indeed, a Universal Approximant algorithm is run on a transmon qubit to experimentally demonstrate the approximation capabilities of a single-qubit quantum algorithm [Pér21].

Flux qubits are more complex circuits than transmon qubits, as they typically involve many Josephson junctions, increasing the number of variables to describe the system. In Chapter 5, the Hamiltonian design of flux qubits is developed so that it can be used as the basis to build a coherent quantum annealer. Moreover, a comparison among many types of flux qubits is performed. The dispersive interaction with a resonator is also designed, as it is required for both qubit control and readout. An initial qubit-qubit coupling scheme is proposed, along with a basic method to perform annealing schedules with flux qubits, although such an experiment was not implemented at the time of writing this thesis.

In Chapter 6 the flux qubits theoretically engineered in Chapter 5 are physically designed, while the manufacturing was performed by collaborators. The flux qubits are characterized via spectroscopic measurements, which provides initial information of the qubit parameters and quality. Coherent control of flux qubits is achieved, which constitutes one of the most important results of this thesis. The results using these flux qubits constitute an important benchmark in the development of a quantum annealer and provides very valuable information on how to improve flux qubits for future iterations of quantum annealer processors.

In parallel to the development of qubit experiments, some focus has been also set on studying fundamental properties from a very common material used in superconducting qubits: aluminum. In Chapter 7, the magnetic penetration depth, λ , of thin film superconducting Al is studied as a function of the film thickness. This calibration, not previously performed in the literature, is especially relevant for the design of flux-sensitive devices, such as flux qubits. λ is closely related to the kinetic inductance, which is a significant portion of the total inductance in superconductors. This study [Lóp23] allows for a better design determination of the inductance in superconducting circuits. Moreover, it points to the possibility of a change in superconductivity type of Al in the

typical range of thicknesses used in superconducting circuit experiments.

Finally, thanks to a brief stay in NTT (Japan), a quantum-limited amplifier has been redesigned to improve its usability in Chapter 8. The quantum-limited amplifier is theoretically identical as the one developed in [Ran21], which consists on an array of SNAIL's (Superconducting Nonlinear Asymmetric Inductive eLement). The SNAIL circuit is identical to that of the flux qubit, but operated in a different parameter regime. The work developed here will be continued with the fabrication of the actual devices.

Chapter 2

Superconducting Qubits

A quantum computer can be based on many possible technologies[Bur23; Slu19; Wu21]. Among them, superconducting qubits are arguably the most prominent technology at this moment [Kra19; Bla21]. Their relative ease of fabrication and their design tunability overcome drawbacks of the technology such as the decoherence effects due to their large size.

In this chapter, the superconducting circuit formalism is introduced in Section 2.1, detailing how these circuits can be utilized as qubits. Two types of superconducting qubits are explored: first, the transmon qubit[Koc07], due to its simplicity and its prevalent use in Digital Quantum Computing (DQC) in Section 2.2, and, next, the flux qubits [Yan15], which are the key ingredient of Analog Quantum Computing (AQC) in Section 2.3. Both these types of qubits will later be employed in subsequent experiments within this thesis.

Then, a concise overview is provided on how to couple qubits (Section 2.4), how to control them (Section 2.5), and which are the usual measurement techniques (Section 2.6). Finally, a dedicated section on noise in superconducting qubits is included (Section 2.7).

2.1 Superconducting Circuits

A superconducting circuit can be thought of an integrated circuit made out of a superconducting material. The inclusion of superconductivity dramatically changes the circuit behavior, since classical variables become quantum operators. Thus, the current I of the circuit is no longer a scalar variable but has to be expressed as an operator, \hat{I} , acting on the circuit wavefunction, $|\Phi\rangle$. Then, for instance, a superposition of two current states flowing in opposite directions can occur in a quantum circuit.

The superconducting circuits can be engineered as qubits thanks to their low dissipation, low noise susceptibility and nonlinearity. Moreover, these circuits are designed by scientists, instead of being *fixed by nature*, such as atoms. Often referred as artificial atoms, these circuits allow for detailed tailoring of

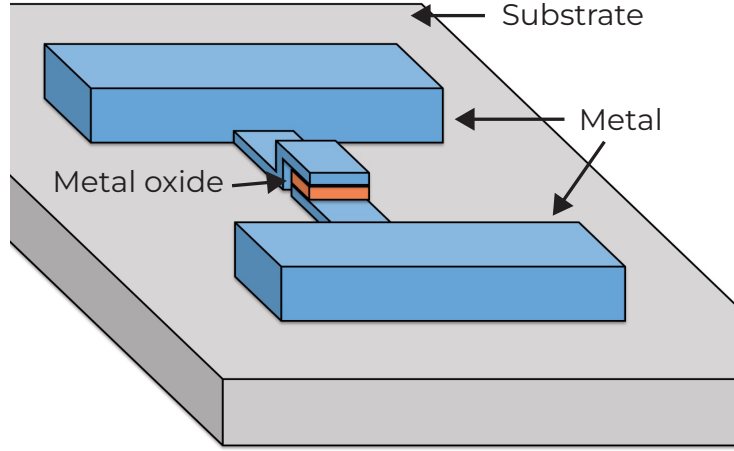


Figure 2.1: Schematic drawing of a transmon qubit. Two superconducting metallic pads are sitting on top of a dielectric substrate. The two pads are connected via a thin dielectric metal oxide layer that allows tunneling of the Cooper pairs.

their parameters within ranges that are challenging, if not impossible, in natural atoms [For18]. However, this design flexibility has some drawbacks since circuit contain more imperfections, and reproducibility of devices becomes a very important metric. Moreover, circuit defects can cause noise which diminishes qubit coherence. Despite these a priori insurmountable obstacles, the success of this technology is evident[Bla21]. The longer-term development and difficulties to build larger system are still to be seen.

2.1.1 The transmon qubit as an example of a superconducting quantum circuit

Transmon qubits provide the simplest approach in order to understand how a superconducting qubit works. The transmon qubit is depicted in Fig. 2.1. It consists of a thin piece of aluminum wire sitting on top of a silicon substrate, interrupted by a thin aluminum oxide layer and ended in two aluminum pads* [Koc07].

This transmon qubit is placed in a dilution refrigerator at temperatures around 10 mK. At these temperatures, the aluminum of the transmon turns superconductor. The paired electrons, named *Cooper pairs*, travel through the metal in a dissipationless state[†]. The lack of dissipation is key for quantum

*This is just a representative image. Some transmons are not made out of aluminum, have different geometries, etc.

[†]This is only strictly true for DC voltage due to dielectric and phase-slip processes. However, this new state has considerably less dissipation than normal metals at AC also.

computing applications, otherwise decoherence would quickly destroy the qubit state.

The many-body dynamics of the entire superconductor can be described by a single macroscopic wavefunction, [Tin04; Or191]

$$\Psi(\vec{r}, t) = |\Psi_0| e^{i\varphi(\vec{r}, t)}, \quad (2.1)$$

where $|\Psi_0|$ is the wavefunction amplitude, which depends on the density of paired electrons. The many-body dynamics can be described by the wavefunction phase φ , which allows for easy analytical treatment of the superconductor physics.

The other key element is the oxide layer in between the metal pads, which forms a Josephson junction, a dissipationless nonlinear element [Jos62]. The non-linearity is needed to break harmonicity and have uneven levels that can be targeted separately by external radiation, as with natural atoms.

In order to provide the qubit a suitable working scenario, a dilution refrigerator offers a vacuum, shielded and low temperature environment for the qubit, which heavily reduces environmental noise, thus increasing qubit coherence. The low temperatures are required not only for the metal to be superconductor, but to reduce thermal noise that would otherwise excite the qubit, and to initialize the qubit. The photon thermal frequency can be computed by

$$\omega = \frac{k_B T}{\hbar}, \quad (2.2)$$

where k_B and \hbar are the Boltzmann and the reduced Planck constant respectively. The ~ 20 mK temperature of the fridge corresponds to ~ 400 MHz, which implies that the transmon qubit energies should lie well above this frequency. The thermal excitation probability is

$$P_e = \frac{1}{1 + e^{\hbar\omega_q/k_B T}}, \quad (2.3)$$

with ω_q the qubit frequency. For a typical $\omega_q = 4 \times (2\pi \times \text{GHz})$, $P_e < 0.1\%$. However, as seen later, effective qubit temperatures can be higher than 20 mK, thus leading to higher thermal populations, $P_e \approx 10\%$.

Although focused on the transmon, the same principles presented above apply to all superconducting qubits.

2.1.2 LC Circuit

A LC harmonic oscillator is the simplest superconducting circuit, depicted in Fig. 2.2 [Voo16]. The Hamiltonian of such a circuit is

$$\hat{\mathcal{H}}_{\text{LC}} = \frac{\hat{q}^2}{2C} + \frac{\hat{\Phi}^2}{2L}, \quad (2.4)$$

where \hat{q} , is the charge at the capacitor and the $\hat{\Phi}$ is the flux at the inductor. \hat{q} and $\hat{\Phi}$ are canonically conjugate operators and follow the commutation relation $[\hat{\Phi}, \hat{q}] = i\hbar$, analog to position and momentum in a mechanical oscillator.

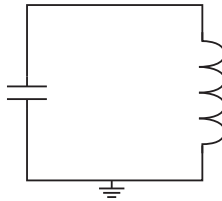


Figure 2.2: LC oscillator circuit schematic.

Another set of variables typically used are the number of charge, \hat{n} , and the phase of the superconducting wavefunction $\hat{\varphi}$, related to the previous variables

$$\hat{q} = 2e\hat{n}, \quad (2.5)$$

$$\hat{\Phi} = \frac{\Phi_0}{2\pi}\hat{\varphi}, \quad (2.6)$$

which fulfill $[\hat{\varphi}, \hat{n}] = i$. Therefore, the variables used are left to convenience.

Similarly to the mechanical oscillation, the LC circuit Hamiltonian can be rewritten in terms of ladder operators,

$$\mathcal{H}_{LC}/\hbar = \omega_{LC}\hat{a}^\dagger\hat{a}, \quad (2.7)$$

where $\omega_{LC} = \sqrt{\frac{1}{LC}}$ is the oscillator frequency. The ladder operator is defined as[‡]

$$a^\dagger = \frac{1}{2} \left(\frac{\hat{\varphi}}{\varphi_{\text{zpf}}} + i \frac{\hat{n}}{n_{\text{zpf}}} \right). \quad (2.8)$$

φ_{zpf} and n_{zpf} are the zero-point fluctuation of the phase and number operators respectively, defined as

$$\varphi_{\text{zpf}} = \sqrt{\frac{\pi Z_0}{R_q}} \quad (2.9)$$

$$n_{\text{zpf}} = \frac{1}{2} \sqrt{\frac{R_q}{\pi Z_0}}, \quad (2.10)$$

where $Z_0 = \sqrt{L/C}$ is the oscillator impedance and $R_q = h/(2e)^2$ is the resistance quantum.

The spectrum of this circuit is purely harmonic since no nonlinear element has been introduced. Therefore, the introduction of Josephson junctions are needed to design a qubit. However, it is possible to use the harmonic modes of an oscillator as qubits, as long as they are coupled to a superconducting circuit with Josephson junctions, that enables non-classical state preparation in the LC oscillator[Slu19].

[‡]From now on, hats are removed from operators, unless they are used to differentiate between variables and operators.

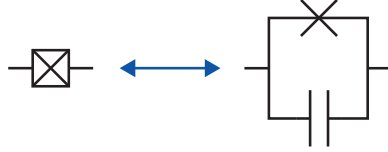


Figure 2.3: A Josephson junction (boxed cross) consists of a pure Josephson junction nonlinear inductance (cross) in parallel with a capacitance.

2.1.3 Basics of Superconducting Circuits

Superconducting circuits can be engineered out of the combinations of three core circuit elements: inductances, capacitances, and Josephson junctions [Koc07; Man09; Yan15]. The first two are essentially classical. The Josephson junction, on the other hand, is a purely quantum element and the key of the existence of superconducting circuits.

As explained in Section 2.1.1, a Josephson junction consists of a thin dielectric layer in between two superconducting metals. The dielectric is so thin that the macroscopic wavefunction in Eq. (2.1) can tunnel through it. The Josephson effect depends on the difference between the phases of the superconducting wavefunctions at both sides of the dielectric, $\varphi \equiv \varphi_1 - \varphi_2$. The first and second Josephson relations are

$$I(t) = I_C \sin \varphi(t), \quad (2.11)$$

$$V(t) = \frac{\Phi_0}{2\pi} \frac{\partial \varphi}{\partial t}, \quad (2.12)$$

where $\Phi_0 = h/2e$ is the superconducting flux quantum. Combining these two equations together, the following current-voltage relation arises

$$V = L_J(\varphi) \frac{\partial I}{\partial t}, \quad (2.13)$$

where the Josephson inductance is defined as

$$L_J(I) = \frac{L_{J,0}}{\cos \varphi(I)} \equiv \frac{\Phi_0}{2\pi I_c \cos \varphi(I)} = \frac{\Phi_0}{2\pi I_c \sqrt{1 - (I/I_c)^2}}. \quad (2.14)$$

The last relation shows that the Josephson junction behaves as a nonlinear inductance. This nonlinearity is of utmost importance for superconducting quantum devices. It is important to note that the Josephson junction is composed of an ideal Josephson junction and a stray capacitance in parallel (see Fig. 2.3).

The critical current, I_C , is the parameter that defines the behavior of the Josephson junction. Above this current, the Josephson effect vanishes and current of unpaired electrons fully passes through the junction, causing ohmic dissipation.

Each of the three circuit elements mentioned has a typical energy scale associated. An analysis of the energies of the circuit gives a great insight to the circuit behavior. If, for example, the charging energy dominates, the wavefunction is well approximated by a pure charge number state $|N\rangle$. The three energies are defined as[§]

$$\begin{aligned} E_C &= \frac{e^2}{2C}, \\ E_L &= \left(\frac{\Phi_0}{2\pi}\right)^2 \frac{1}{L}, \\ E_J &= \frac{\Phi_0}{2\pi} I_C. \end{aligned} \tag{2.15}$$

The relative strengths of these energies determines the regime over which the circuit operates. Two qubits with equivalent circuits can behave very different if their energies are different, such as fluxoniums and flux qubits, as explained in Section 2.3.4. Both qubits considered in this thesis, the transmon and the flux qubit, function within the flux regime, with $E_J \gg E_C$. In this regime, the states closely resemble pure phase states and their charge susceptibility is considerably reduced. Additionally, in both qubits E_L is usually neglected, although it is very large, as $L \ll L_J$. However, the equivalent mode is frozen, so its dynamics do not play a role.

2.1.4 Superconducting circuits as qubits

The design of a qubit requires of a nonlinear energy spectrum, so that two levels can be isolated from the rest. At the low temperatures inside a dilution refrigerator, a circuit with resonances in the few GHz-range, naturally relaxes to $|g\rangle$. Therefore, it is easy to confine the circuit dynamics to the two lowest energy states, by controlling transitions between $|g\rangle$ and $|e\rangle$, whose frequency is $\omega_q = (E_e - E_g)/\hbar$, with $E_{g,e}$ the energies to the ground and excited state.

In DQC, $|g\rangle$ and $|e\rangle$ are commonly used as the computational basis, labelled as $|0\rangle$ and $|1\rangle$ respectively. This is different for AQC, as is discussed in Section 2.3.1. From now on in this section, the two-lowest energy states are considered the computational basis.

For aluminum-based circuits, the Cooper pairs will begin to break at frequencies higher than 80 GHz, which sets an upper limit to ω_q . Moreover, GHz technology is much more accessible than THz one, so typically these circuits do not operate above 10 – 15 GHz. On the lower frequency side, the fridge temperature has a thermal energy of 0.4 GHz, as previously noted. This thermal energy could easily cause incoherent qubit transitions[Zmu12]. Moreover, the low-frequency noise is usually high since it has a $1/f$ spectrum [Yos06], so a very low ω_q is usually not desired.

[§]Note that E_C corresponds to the charging energy of one electron, while a more convenient definition for Cooper pairs would be $E'_C = (2e)^2/(2C)$. However, in order to be coherent with the literature, the single-electron definition is kept, which usually causes a term $4E_C$ in the charging energy terms of the circuit \mathcal{H} .

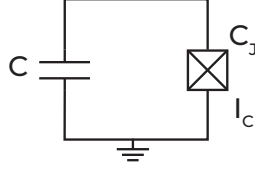


Figure 2.4: Transmon circuit schematic.

Another relevant aspect in designing qubits is their susceptibility to noise, a topic that will be covered in Section 2.7. For example, it is common to avoid detrimental charge noise, which can be achieved by reducing E_C [Koc07; Yan15]. Passive protection from noise can be obtained by circuit parameter design.

Qubits are not isolated but interact to other qubits, couplers, readout components, etc. The strength and type of these interactions has to be also considered in the design. Superconducting circuits easily interact with each other by sharing a capacitance, an inductance or a Josephson Junction [Kaf16; Web17].

Finally, when designing complex circuits involving many components, the circuit Hamiltonian is not known beforehand. \mathcal{H} is usually obtained by a process called circuit quantization [Voo16], which consists of applying Kirchhoff laws on the electrical circuit and later quantizing it. A brief explanation of the procedure is given in Appendix A, and a detailed development on superconducting circuits can be found in [Rip22].

2.2 Transmon Qubits

The transmon qubit circuit has already been introduced in Section 2.1.1 [Koc07]. However, a more formal understanding is still pending.

The transmon circuit is shown in Fig. 2.4. It resembles an LC circuit (Fig. 2.2) where L has been substituted by the nonlinear Josephson inductance. The Hamiltonian of the transmon is

$$\mathcal{H} = 4E_C n^2 - E_J \cos \varphi, \quad (2.16)$$

where n , is the number of Cooper pairs transferred through the Josephson junction and the φ is the wavefunction phase difference between both sides of the junction. $E_C = e^2/(2C_\Sigma)$ is the total capacitive energy of the transmon, with $C_\Sigma = C + C_J$.

The transmon operates in the flux regime, with $E_J/E_C \approx 50$. Therefore, the transmons are dominated by E_J , which reduces considerably their susceptibility to charge noise, which was the main limitations of its predecessor, the Cooper pair box [Bou98], with a much lower $E_J/E_C \approx 1$.

As the qubit will normally stay at the bottom of the potential energy where $\langle \varphi \rangle \ll 1$, the Josephson terms of the transmon can be expanded in Taylor series:

$$\mathcal{H} \approx 4E_C n^2 + \frac{E_J}{2} \varphi^2 - \frac{E_J}{24} \varphi^4. \quad (2.17)$$

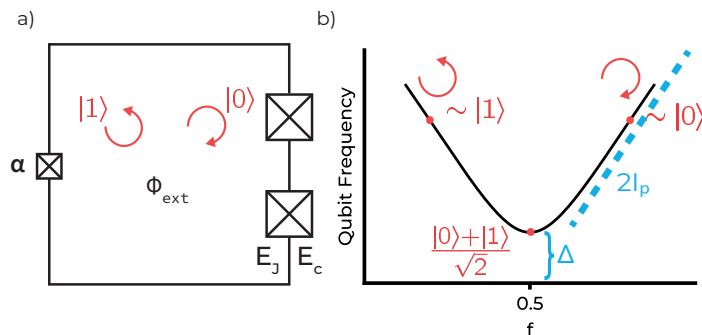


Figure 2.5: a) Flux qubit circuit. b) Lower-energy spectrum of the flux qubit. The qubit gap, Δ , and the persistent current, I_P , are visually identified.

The first two terms correspond to a harmonic oscillator (Eq. (2.4)). The third term is the leading Josephson nonlinearity, which causes anharmonicity in the qubit spectrum such that different transitions have different energies. This Hamiltonian can be rewritten in terms of ladder operators,

$$\mathcal{H}/\hbar = \omega_q a^\dagger a + \frac{\delta}{2} a^\dagger a^\dagger a a. \quad (2.18)$$

ω_q is the qubit frequency, and $\delta = \omega_{12} - \omega_{01}$ is the anharmonicity of the system, with ω_{ij} the frequency of the transition between states $|i\rangle$ and $|j\rangle$. In the transmon, both ω_q and δ can be directly obtained from the circuit energies, since

$$\hbar\omega_q = \sqrt{8E_J E_C} - E_C, \quad (2.19)$$

$$\hbar\delta = -E_C. \quad (2.20)$$

If only the two lowest energy states are considered, the Hamiltonian is simply,

$$\mathcal{H}/\hbar = \frac{\omega_q}{2} \sigma_Z. \quad (2.21)$$

2.3 Flux Qubits

There are many different circuits that fall into the definition of a flux qubit [Sil67; Orl99; Yan15; Rug06; Pol08; Pop24; Ste14]. In terms of the circuit definition, they all have a Josephson junction in parallel to another inductive element forming a loop. Under the appropriate external flux threading the loop and ratio between the energies of the Josephson junction and the inductive element, the two lowest-energy states can be described by superpositions of current states flowing around the loop in opposite directions.

An example of a flux qubit is shown in Fig. 2.5a), following the original work of [Orl99]. The circuit consists of a small Josephson junction on one side of the

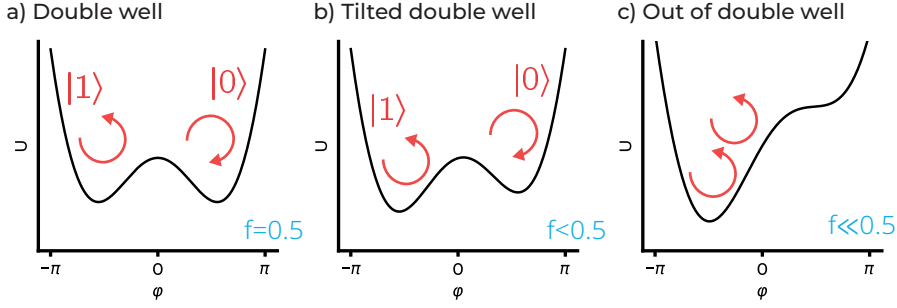


Figure 2.6: Symmetric potentials of the flux qubit considering $\alpha > 0.5$. a) In the sweet spot, $f = 0.5$, the potential is a symmetric double well. b) A small tilt promotes one of the persistent current states. c) When the tilt is too high, there is no double well and both $|0\rangle$ and $|1\rangle$ are located in the same well.

loop and two large junctions on the other side. The ratio between the small and big junction I_C 's is defined as $\alpha = I_{C,\alpha}/I_C$, which strongly influences the behavior of the qubits.

For a closed loop such as the one in Fig. 2.5a), the wavefunction must be single-valued so that it is continuous, causing a total phase accumulated around the loop of $n\pi$, with n an integer value. Due to the phase-flux relation expressed in Eq. (2.6), this corresponds to a number of trapped fluxoids $n\Phi_0$. The fluxoid quantization permits the reduction of one of the three node variables as $\varphi_3 = \varphi_1 + \varphi_2 + 2\pi f$, where $\varphi_{1,2}$ are the wavefunction phase differences across the big junctions, and φ_3 corresponds to the small junction.

The Hamiltonian of this circuit is

$$\mathcal{H} = 4E_C \left[\frac{1+\alpha}{1+2\alpha}(n_1^2 + n_2^2) + \frac{2\alpha}{1+2\alpha}n_1n_2 \right] - E_J [\cos(\varphi_1) + \cos(\varphi_2) + \alpha \cos(\varphi_1 + \varphi_2 + 2\pi f)], \quad (2.22)$$

where hats have been removed from the operators. Both E_J and E_C (see Eq. (2.15)) are referred to the energies of a large junction. The first term is the capacitive term, and represents the kinetic energy. The second term denotes the potential energy arising from the presence of Josephson junctions. The external flux trapped in the qubit loop, Φ_{ext} , is introduced through $f = \Phi_{\text{ext}}/\Phi_0$.

When the external flux is $\Phi_0/2$, or $f = 0.5$, the system is frustrated as classically there is equal energy in generating current in one direction or the other in order to have $n\Phi_0$ or $(n+1)\Phi_0$ trapped fluxoids. In this situation, for $1 > \alpha > 0.5$, $|g\rangle$ is an equal superposition of the persistent current states in both directions

$$|g\rangle = \frac{|0\rangle + |1\rangle}{\sqrt{2}}, \quad (2.23)$$

as shown in Fig. 2.6a). $|0\rangle$ and $|1\rangle$ are the clockwise and counter-clockwise persistent-current states respectively. This half-flux point is also called the

sweet spot, as the qubit is insensitive to flux at this point, to first order. When f deviates from the sweet spot, one of the two current directions becomes energetically favorable. For a sufficiently high flux bias, $|g\rangle \approx |0\rangle$ ($|1\rangle$) for $f > 0.5$ ($f < 0.5$), as seen in Fig. 2.6b). However, for a very large flux bias, both the two-lowest energy states fall inside the same well because the double-well regime is destroyed, depicted in Fig. 2.6c).

The behavior described previously occurs for $\alpha > 0.5$. To understand that, let's investigate the potential from Eq. (2.22), U ,

$$U/E_J = -\cos\varphi_1 - \cos\varphi_2 - \alpha\cos(\varphi_1 + \varphi_2 + 2\pi f), \quad (2.24)$$

It is more convenient to change to the variables to $\varphi_{\pm} = (\varphi_1 \pm \varphi_2)/2$. In the symmetric case, where $\varphi_1 = \varphi_2$, thus $\varphi_- = 0$, the potential is

$$U_+/E_J = -\cos\varphi_+ - \alpha\cos(\varphi_+ + 2\pi f). \quad (2.25)$$

U_+ represents the main mode of the qubit, since U minima occur at $\varphi_1 = \varphi_2$. U_+ is shown in Fig. 2.7 for different values of α at $f = 0.5$. When $1 > \alpha > 0.5$, there exist a double well, with two energy minima corresponding each to a persistent-current state. For $\alpha = 0.5$, the circuit is in the *quarton* regime [Yan20], where $U \propto \varphi^4$, and, in general, for $\alpha \leq 0.5$ the potential has a single well [Yan15]. While in all the regimes the circuit can be used as a qubit, the double-well regime is the only suitable for quantum annealing as will be explained in Section 2.3.1.

When in the double-well regime and near $f = 0.5$, the two-lowest energy levels of the flux qubit can be expressed as a spin 1/2-particle under a magnetic field with parallel (σ_Z) and transverse components (σ_X)

$$\mathcal{H} = \frac{\hbar\Delta}{2}\sigma_X + 2I_P\Phi_b\sigma_Z. \quad (2.26)$$

Here, σ_i are the Pauli matrices, Δ is the *qubit gap* and I_P is the qubit *persistent current*. Δ determines the qubit energy at the sweet spot, and I_P determines the slope at which the qubit energy changes with flux, as can be seen in Fig. 2.5b). I_P corresponds to the expectation value of the current of each of the persistent current states, $|0\rangle$ and $|1\rangle$. Both Δ and I_P are the defining parameters of the flux qubit.

2.3.1 Flux Qubits for Quantum Annealing

Quantum annealing, as described in Section 1.2.2, is a quantum computing algorithm where quantum system is continuously evolved from a known ground state to the ground state of a problem Hamiltonian [Hau19; Alb16]. From this definition it becomes clear that the energy states are not a good computational basis, since the system should remain in its ground state[¶].

In quantum annealing, each qubit $|g\rangle$ should encode the computational basis. This is exactly what occurs in the flux qubit in the double well regime, where the computational states are the persistent-current states $|0\rangle$ and $|1\rangle$.

[¶]In such a system, there is no single-qubit ground state, but a global system ground state.

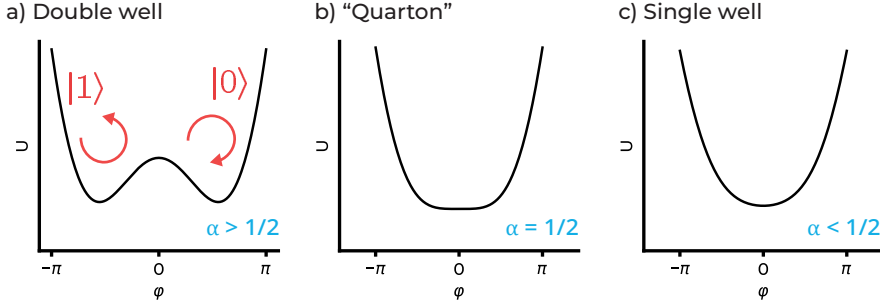


Figure 2.7: Symmetric potential energy of the flux qubits as a function of φ_+ (see text) for different values of α at $f = 0.5$. a) When $\alpha > 1/2$, a double well exists. b) The quarton regime occurs at $\alpha = 1/2$ where the double-well vanishes. c) Single well regime for $\alpha < 1/2$.

The persistent-current states are very convenient, since at the sweet spot, $|g\rangle$ is an equal superposition of $|0\rangle$ and $|1\rangle$, which is the common initial configuration in quantum annealing. By increasing the flux over time, the qubits are brought to either $|0\rangle$ or $|1\rangle$, depending on the algorithm schedule.

The transverse Ising Hamiltonian commonly used in quantum annealing is

$$\begin{aligned} \mathcal{H}_f = & \sum h_{X,i}(t)\sigma_{X,i} + \sum h_{Z,i}(t)\sigma_{Z,i} + \\ & + \sum_{i<j} J_{ij}(t)\sigma_{Z,i}\sigma_{Z,j}, \end{aligned} \quad (2.27)$$

where $h_{X,i}(t)$ are maximal at the beginning of the schedule and go to 0 at the end, and $h_{Z,i}(t)$ and J_{ij} follow the opposite behavior. Comparing Eq. (2.27) and Eq. (2.33), the relation between the $h_{X,Z}$ Ising coefficients and the single-qubit terms, the relation is

$$h_{X,i} = \frac{\hbar\Delta_i}{2}, \quad (2.28)$$

$$h_{Z,i} = 2I_{P,i}\Phi_{b,i}, \quad (2.29)$$

The ZZ terms in the Ising Hamiltonian can be obtained by coupling two qubits inductively [Web17; Kaf16], so that the flux in one qubit induces flux in the other qubits. This interaction depends on I_P and the mutual inductance between qubits. Tunable interactions can be achieved by using a coupler between the qubits, as will be explained in Section 2.4.

2.3.2 C-Shunted Flux Qubit

The flux qubit shown in Fig. 2.5a) is one of the original flux qubit designs. However, an improvement was proposed in [Yan15], which consists of the addition of a shunting capacitance, C_{sh} , followed by the reduction of I_P . The so-called C-shunted flux qubit can be seen in Fig. 2.8a).

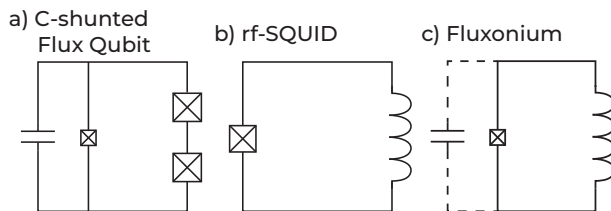


Figure 2.8: Circuit schematics of a) C-shunted Flux Qubit, b) rf-SQUID, and c) Fluxonium. Heavy fluxonium has an extra capacitance, while original fluxoniums do not.

The addition of C_{sh} reduces the sensitivity to charge noise since E_C of the α junction is reduced. Dielectric noise is also reduced as the electric field is now distributed over a larger area around the capacitor pad, reducing its intensity and coupling more weakly to surface defects. Moreover, it also allows for better parameter reproducibility since C_{sh} is easier to control compared to the Josephson junction capacitances.

The reduction of I_P with previous devices is also of utmost importance. Early flux qubits in quantum annealers had $I_P \geq 1 \mu\text{A}$ [Har09b], while in the C-shunted flux qubit, the current is almost two order of magnitude lower, $I_P \approx 50 \text{ nA}$. This strongly reduces sensitivity to flux noise, since the decoherence rate scales with I_P^2 , which significantly increases qubit coherence times.

The Hamiltonian of this flux qubit is equivalent to that of Eq. (2.22) by changing $\alpha \rightarrow \alpha + C_{\text{sh}}/C_J$. However, it is common to write the capacitance term in a matrix fashion

$$\mathcal{H} = \frac{1}{2} \vec{q}^T \mathbf{C}^{-1} \vec{q} - E_J [\cos(\varphi_1) + \cos(\varphi_2) + \alpha \cos(\varphi_1 + \varphi_2 + 2\pi f)], \quad (2.30)$$

where \vec{q} is the charge vector, and \mathbf{C} is the capacitance matrix.

Finally, the C-shunted flux qubit, can have more than 2 big junctions. In general, N large junctions can be placed, which modifies the range of values of α over which a double-well regime exists. This is detailed further in Section 5.2.

2.3.3 rf-SQUID

A rf-SQUID [Sil67] is a somewhat old version of a flux qubit and could be thought of the simplest of flux qubits, where the large junctions are replaced by a single linear inductance, as seen in Fig. 2.8b). The Hamiltonian of the rf-SQUID is

$$\mathcal{H} = 4E_C n^2 + \frac{E_L}{(2\pi)^2} \frac{\varphi^2}{2} + E_J \cos(\varphi + 2\pi f), \quad (2.31)$$

with E_C , E_L and E_J defined in Eq. (2.15).

The rf-SQUID is important as a historical circuit element, since it was developed as magnetic detector [Sil67] before being used as a qubit. Moreover,

it is still very actively operated as a flux qubit and as a coupler in quantum annealers [Har09b; Web17; Pop24].

2.3.4 Fluxonium

The circuit in Fig. 2.8c) corresponds to the fluxonium qubit [Man09; Ear18]. The fluxonium Hamiltonian is the same as the one for the rf-SQUID (Eq. (2.31)). However, the parameter regime is quite different. In both $E_L < E_J$, which implies that there exists a double-well potential which allows for quantum annealing formalism to operate. However, the large inductance in the fluxonium causes $E_L \ll E_J$, which results in a sub-nA I_P , not making this a suitable choice for quantum annealing, since the coupling energy $J \propto I_P^2$ (see Section 2.4.1).

2.4 Coupling Qubits

Quantum computing relies as much on individual qubit superpositions as in the coherent interaction between qubits. Qubit coupling can be achieved in many different flavors: inductive or capacitive, direct or indirect, tunable or fixed, etc. [Web17; Kaf16; McK16b; Hit21; Men19; DiC10]

The coupling enters in \mathcal{H} via a coupling operator. For example, a capacitive coupling between transmons is expressed as the $n_1 n_2$. Usually, a coupling Hamiltonian appears as

$$\mathcal{H} = \mathcal{H}_1 + \mathcal{H}_2 + \mathcal{H}_{\text{int}}, \quad (2.32)$$

where the first two terms represent the uncoupled qubit Hamiltonians and the interaction is captured in \mathcal{H}_{int} .

Regardless on how this interaction occurs, the coupling effect on the system depends on how it is represented in the two-level qubit description. In this sense, it is important to differentiate between longitudinal coupling in the axes of the computational states, $\sigma_{Z,1}\sigma_{Z,2}$ [Web17], and transverse coupling, for example $\sigma_{X,1}\sigma_{X,2}$ [Cho11]. The former introduces entanglement without energy exchange, while the second can lead to both excitation swapping between both systems and entanglement[Maj07].

Directly coupling two qubits, however, may involve an always *on* interaction that introduces an undesired evolution during the whole algorithm[Roy21]. Another circuit can be added in between the qubits to mediate this interaction. This *coupler* element may be tuned so that the interaction is switched off when desired[Web17].

2.4.1 Coupling in AQC

The coupling required in AQC is more specific than in DQC, where any entangling interaction that can be efficiently performed is valid. In AQC, the target Ising Hamiltonian forces the coupling requirements[Hau19]. When a transverse Ising Hamiltonian such as in Eq. (1.3) is needed, a ZZ interaction must be engineered.

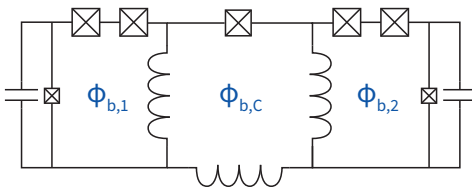


Figure 2.9: Two flux qubits inductively coupled by a rf-SQUID.

Moreover, in AQC, the coupling needs to be highly tunable, with the possibility of switching it off at the beginning of the anneal, and even changing sign for different problems. The coupling strength must also be comparable to the qubit energies, unlike in DQC where it is perturbative. In Eq. (2.27), the J terms at the end of the anneal must be equal in magnitude to the h_Z ones.

The circuit shown in Fig. 2.9 represents two C-shunted flux, coupled by a rf-SQUID coupler[Har09b], which is an example of a quantum annealing two-qubit coupling. The bias flux $\Phi_{b,1}$ in qubit 1 induces flux in the coupler, which, in turn, induces flux in the qubit 2, resulting in an effective $\sigma_{Z1}\sigma_{Z2}$ interaction. The coupled qubit Hamiltonian can be expressed as

$$\mathcal{H} = \sum_{i=1,2} \left(\frac{\hbar\Delta_i}{2} \sigma_{X,i} + 2I_{P,i} \Phi_{b,i} \sigma_Z \right) + \hbar g(\Phi_{b,1}, \Phi_{b,2}, \Phi_{b,C}) \sigma_{Z,1} \sigma_{Z,2}, \quad (2.33)$$

where $i = 1, 2, C$ correspond to the qubit 1, qubit 2 and coupler respectively. The coupling $g(\Phi_{b,1}, \Phi_{b,2}, \Phi_{b,C})$ depends on all the fluxes in the circuit, though. In practice, g depends mostly on $\Phi_{b,c}$ near the symmetry point of the qubits.

Equation (2.33) may seem a longitudinal coupling, but it depends on the state of the anneal. It is only at the end of the anneal, where the σ_Z terms dominate over the σ_X terms, when this is a purely longitudinal coupling.

Although this is the most standard coupling in AQC, it would be desirable to have more types of coupling. XX coupling for example would lead to non-stoquastic Hamiltonians [Hit21; Ozf19]. Many qubit couplings, such as $ZZZZ$ would also be interesting to perform other type of annealing sequences [Men19; Lec15] and quantum simulations.

2.5 Qubit Control

The two most common ways to control qubits is either by microwave pulses [Mot09], prevalent in DQC, or flux control [Khe20], the default implementation in AQC. The microwave pulses at frequencies around ω_q drive rotations around the Bloch sphere (see Section 1.1). Z rotations are usually controlled via software phase correction [McK16a]. Two-qubit gates can also be controlled via

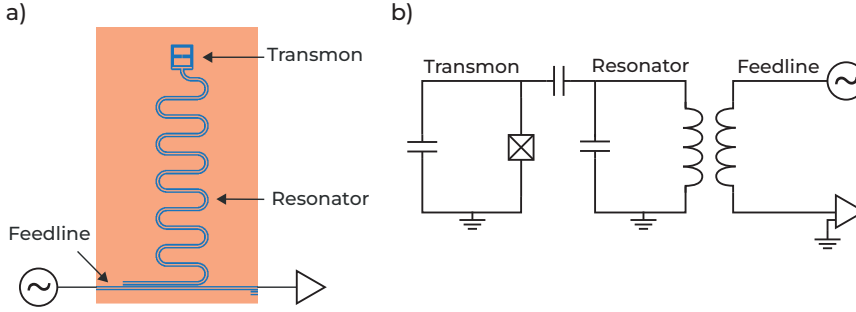


Figure 2.10: a) Transmon capacitively coupled to a $\lambda/4$ coplanar waveguide resonator, which is inductively coupled to the transmission line, from which the qubit driving signal is applied. b) Circuit schematic of the transmon-resonator-feedline system, where the resonator is modelled as an LC oscillator.

microwave pulses [Rig10]. Flux control can either be static to tune qubit parameters [Koc07] or dynamic to evolve the single-qubit and the two-qubit Hamiltonian such as in quantum annealing [Nov18].

Qubit control introduces new elements into the circuit structure, such as control lines and readout resonators. These elements introduce extra noise into the system as they ultimately couple the qubit with the external environment. A careful design is to be implemented in order to mitigate the undesired uncontrolled interactions, while strong and fast qubit operations can be performed. The error the control lines introduce is commonly characterized following randomized benchmarking [Kni07], cross-entropy benchmarking [Boi16] or other gate benchmarking in DQC. In AQC, the control errors are usually integrated into a flux crosstalk calibration [Dai21].

2.5.1 Driving Qubits with Microwave Pulses

In this section, the transmon control with microwave pulses is developed as an example on how these drives affect the qubit state. The extrapolation to flux qubits is conceptually equivalent, although it is more involved as flux qubits are not a single-variable circuit.

A transmon qubit may be coupled to a transmission line, through which the control and measurement pulses are transmitted. In Fig. 2.10, this coupling is not direct, but mediated through a resonator. There are two reasons for that: first, the resonator acts as a filter in order to protect the state of the qubit from noise coming from the signal lines; the second reason is that this same resonator can be used for dispersive readout of the qubit, as explained in Section 2.6.1. However, antennas to directly drive the qubit without the mediating resonators are also common. In general, no resonators are needed for driving the qubit.

A usual control pulse is a sinusoidal signal with a Gaussian envelope, which

drives the transmon to the target quantum state. Mathematically, the pulse

$$V_d(t) = V_E(t) \sin(\omega_d t + \phi(t)), \quad (2.34)$$

where $V_E(t)$ is the voltage envelope, a Gaussian in the simple case, ω_d is the driving frequency and $\phi(t)$ is the pulse phase. ω_d is usually close to the transmon frequency, ω_q .

The control drive line is capacitively coupled to the qubit, thus the driving Hamiltonian is then [Rip22]

$$\mathcal{H}_d/\hbar = \omega_q a^\dagger a + \delta a^\dagger a^\dagger a a + i\kappa V_d(t)(a - a^\dagger), \quad (2.35)$$

where the constant κ encapsulates the coupling and transmon details. A truncation to the two lowest-energy levels, leaves the Hamiltonian as

$$\mathcal{H}_d/\hbar = \frac{\omega_q}{2} \sigma_z + \kappa V_d(t) \sigma_y. \quad (2.36)$$

In the absence of a drive, the free evolution of the qubit is determined by the first term. In that case, the evolution operator, $\hat{U} = e^{-\frac{i}{\hbar} \mathcal{H}_d t}$, will result in a precession of the relative phase of the states $|0\rangle$ and $|1\rangle$. That is, the phase of the state $|\Psi\rangle = a|0\rangle + b e^{i\varphi(t)}|1\rangle$, will rotate at speed ω_q . Then, it is useful to move into a frame rotating at this speed so that all modifications of the qubit state depend on the drive. The Hamiltonian in this rotating frame reads

$$\mathcal{H}'_d/\hbar = -\frac{\kappa}{2} V_E(t) (I \sigma_x + Q \sigma_y), \quad (2.37)$$

where $I \equiv \sin \phi$, $Q \equiv \cos \phi$ are the in-phase and out-of-phase drive components, and we have considered the drive to be at the qubit frequency, $\omega_d = \omega_q$. Equation (2.37) is the starting point into operating the qubit.

2.5.2 Single-qubit rotations/gates

The choice of phase ϕ in Eq. (2.37) determines which is the axis of rotation. For example, if $\phi = 0$, then the drive will only have a σ_x component and the system will rotate around the X axis. Any axis across the XY plane is achievable just by tuning ϕ . However, this is not a global phase, but the relative phase between the pulse and the qubit phase, which is completely undetermined. Then, usually in the first pulse $\phi = 0$ is assumed to correspond to rotations around the X axis, as seen in Eq. (2.37). Subsequent pulses will take into account this initial value and relative phases will be consistent with it.

A single-qubit rotation has two variables: the rotation axis, σ_i , and the rotation angle, θ . The latter is determined by the prefactor of Eq. (2.37). κ is determined by design and fabrication, so it is a constant value, thus leaving $V_E(t)$ the only tunable parameter. A larger rotation angle θ can be obtained by increasing either the amplitude of the voltage envelope or its duration. In

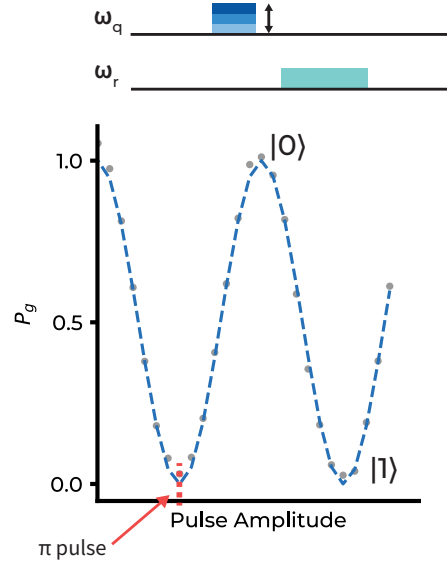


Figure 2.11: Rabi oscillations performed with varying amplitude, with the π pulse location marked. The pulse sequence is shown on top. Data taken from Chapter 4.

general, by using the time-dependent Schrödinger equation, the following expression is obtained for the total rotation angle

$$\theta(t) = -\Omega \int_0^t V_E(t') dt'. \quad (2.38)$$

The coupling details encapsulated in κ are set by design, and the pulse V_E is distorted and attenuated along the signal lines before it reaches the qubit. Therefore, a calibration protocol to drive the desired rotations is needed. A method to calibrate the signal at the qubit is implemented using the so-called *Rabi oscillations*.

2.5.2.1 Rabi experiment

If the qubit is left at rest and measured, the result should be $|0\rangle$, disregarding noise and thermal excitations. On the other hand, if a pulse is applied at a frequency ω_d close to the ω_q with a determined voltage amplitude and duration and the qubit is later measured, the results will be $|0\rangle$ with some probability P_g and $|1\rangle$ with probability $1 - P_g$. For a varying duration pulse, the resulting P_e is

$$P_e(t) = \frac{\Omega^2}{\Omega^2 + \Delta^2} \left[\sin^2 \left(\sqrt{\Omega^2 + \Delta^2} t \right) \right], \quad (2.39)$$

where $\Delta \equiv \omega_d - \omega_q$ is the drive detuning, and Ω is known as the Rabi frequency. The power delivered by the pulse can be also modified by changing the

amplitude, A , of the driving pulse voltage envelope, V_E , instead of the duration. In both cases, the resulting oscillations, shown in Fig. 2.11, are called *Rabi oscillations*.

The Rabi oscillations are the first time-domain experiment performed in most qubit experiments. Thanks to this experiment, the single-qubit gates are calibrated and, then, arbitrary rotation pulses can be performed by adjusting the pulse amplitude to the desired rotation angle θ .

The Rabi oscillations in amplitude as shown in Fig. 2.11, are expressed, for $\omega_q = \omega_d$, as

$$P_e(A) = \sin^2 \left(\frac{\Omega_A A}{2} \right), \quad (2.40)$$

where Ω_A is the Rabi amplitude frequency. A π pulse is achieved at amplitude $A_\pi = \pi/\Omega_A$, so $P_e = 1$.

2.5.2.2 X and Y gates

Once Rabi pulses can be controlled, X - and Y -gates may be implemented. By setting $\phi = 0$ in Eq. (2.37), X gates are applied. Instead, with $\phi = \pi/2$, Y gates are applied. Arbitrary rotations axes are easily performed with the appropriate relative phase ϕ .

Rabi oscillations provide a calibration for desired rotation angle. By using Eq. (2.40), for a general rotation θ , the required amplitude is

$$A_\theta = \frac{\theta}{\Omega_A}. \quad (2.41)$$

2.5.2.3 Z gates

Rotations around the Z -axis behave quite differently than the X - and Y -axes. As explained in Section 2.5.1, the qubit phase rotates around the Z axis in the laboratory frame. In order to effectively cancel this rotation, the rotating frame is used. If ω_q is modified for some time while staying in this same rotation frame, a relative phase in the qubit state will accumulate. By the time ω_q returns to its original value, the state would have rotated around the Z axis depending on the duration and the amount of the frequency deviation.

However, there is a simpler approach to perform Z rotations with no errors, known as the virtual Z gate (VZ gate)[McK16a]. In Fig. 2.12, the VZ gate sequence is shown, where a Z -rotation of angle φ is performed by changing the X - and Y -axes. This is easy to perform experimentally, since the exact definition of X - and Y -axes is arbitrary and can be modified by changing the relative phase of the pulses, as can be seen in Eq. (2.37).

These virtual Z rotations are *perfect* in the sense that they have no error associated as no actual pulse is implemented. A VZ gate means adding an extra phase ϕ_z on the subsequent pulse definition, so that the pulse quadratures are modified by $I' = \cos(\phi + \phi_z)$ and $Q' = \sin(\phi + \phi_z)$.

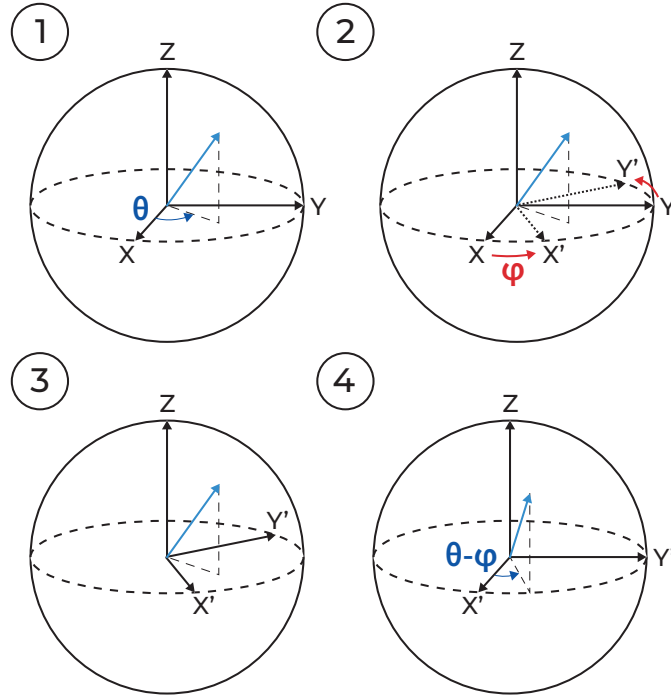


Figure 2.12: Sequence of a virtual Z gate. The state is rotated an angle φ by modifying the axis of the Bloch sphere, without performing any operation on the qubit to explicitly rotate around Z. The state has initially a Z-phase of $\theta(1)$. Then, the axis are rotated φ around the Z-axis (2), which leaves the state with a new relative phase to the new axes (3). When rotating with the new axis, the state has now a $\theta - \varphi$ Z-phase.

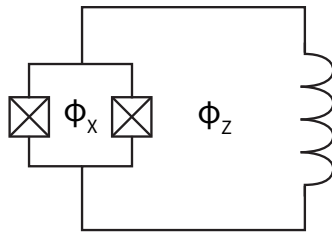


Figure 2.13: rf SQUID where the small junction has been replaced by a DC SQUID so that the effective E_J can be controlled via the flux Φ_X passing through the junction loop.

2.5.3 Flux Control

The magnetic flux is a common way to control the qubit behavior in flux-tunable circuits, both in AQC and DQC. Flux control is sometimes static and it is used

to set many circuit parameters. For example, it is common that qubits such as transmons or flux qubits substitute one of their junctions by a DC-SQUID, which consist of two junctions in parallel [Koc07; Har09b]. By modifying the flux inside the loop an effective $E_J(\Phi) = 2I_C |\cos(\pi\Phi/\Phi_0)|$ is obtained for identical junctions. This can be used, for example, to correct for possible fabrication variations.

In quantum annealing, however, the flux control is the key driving force of the algorithm. A mathematical description of flux control is simpler than qubit gates, since the fluxes already appear in the Hamiltonian, such as in Eq. (2.33). In general, all the annealing algorithms are controlled by the external fluxes, as expressed in

$$\begin{aligned} \mathcal{H}_f = & \sum h_{X,i}(\Phi_i)\sigma_{X,i} + \sum h_{Z,i}(\Phi_i)\sigma_{Z,i} + \\ & + \sum_{i<j} J_{ij}(\Phi_i, \Phi_j, \Phi_{C,ij})\sigma_{Z,i}\sigma_{Z,j}, \end{aligned} \quad (2.42)$$

where Φ_i corresponds to the fluxes applied to qubit i and $\Phi_{C,ij}$ to the coupler between qubits i and j .

As already noted in Section 2.3.1, the relation between the qubit and Ising parameters is

$$h_{X,i} = \frac{\hbar\Delta_i}{2}, \quad (2.43)$$

$$h_{Z,i} = 2I_{P,i}\Phi_{b,i}, \quad (2.44)$$

$$J_{ij} = \hbar g_{ij}. \quad (2.45)$$

However, this is an oversimplification, because of the crosstalk. For example, the flux bias on qubit i , depends not only on $\Phi_{b,i}$, but on the flux in the neighboring couplers, qubits and their control lines.

Moreover, the relation between g and J in Eq. (2.45) depends on the specific coupler design, the flux biases of the coupled qubits, coupler and neighboring elements. For large couplings such as the ones required in annealing, the full coupled system needs to be analyzed as a whole, thus making the circuit analysis more complex.

One of the most fundamental tasks in AQC is to calibrate the flux crosstalk [Dai21], encompassing both classical and quantum components. Classical crosstalk appears from control lines that induce flux not only in the intended components but also in neighboring elements. Quantum crosstalk corresponds to the effective interaction between the circuit elements. The phase quantization in each loop depends on the flux held in each of the neighboring qubits and couplers.

The flux crosstalk calibration consists of solving the following equation

$$\mathbf{f} = \mathbf{M}\mathbf{I} + \mathbf{f}_0 \quad (2.46)$$

where \mathbf{f} is the reduced flux vector with $f_i = \Phi_i/\Phi_0$ on each circuit loop, \mathbf{f}_0 is the reduced flux offset, and the current vector, \mathbf{I} , is the current applied on each

control line. The matrix \mathbf{M} is the mutual inductance matrix that describes the coupling between bias lines and flux loops. Every non-diagonal element on that matrix represents crosstalk. The crosstalk calibration means finding \mathbf{M} , so that the currents can be designed to output the desired fluxes[Khe20].

2.6 Qubit Readout

Similarly to qubit control, each individual qubit state must be measured, which requires either a dedicated readout line for each qubit or a way to identify each qubit in a global measurement line. The latter is the common readout implementation in superconducting circuits [Bla04], with each qubit coupled to a resonator with a different frequency, ω_r . The resonator response ultimately depends on the state of the qubit it is coupled to. Each measurement line contains several resonators coupled to their corresponding qubit. This method is called frequency *multiplexed* readout.

The resonator coupled to the qubit acts also as a filter to reduce the qubit deexcitation to the feedline, as ω_r is highly detuned from ω_q . However, this deexcitation is not fully suppressed, and the qubit can still decay to the feedline in a process called *Purcell decay*[Van03]. Sometimes *Purcell filters* [Set15] are added to further reduce this decay, which consists of an extra resonator between the readout resonator and the feedline, further detuned from ω_q , acting as a band-pass filter centered on the Purcell resonator frequency, ω_P .

2.6.1 Dispersive Readout

A resonator coupled to a qubit is the most common method of qubit-state readout[Bla04]. A transmon qubit coupled to a resonator is depicted in Fig. 2.10, and it is described by the following Hamiltonian

$$\mathcal{H}/\hbar = \frac{\omega_q}{2}\sigma_Z + \omega_r \left(a^\dagger a + \frac{1}{2} \right) + g (\sigma_+ a + \sigma_- a^\dagger), \quad (2.47)$$

where the Pauli matrices σ_Z and σ_\pm refer to the qubit operators, and the ladder operators a and a^\dagger refer to resonator operators. The first and second terms are the uncoupled qubit and resonator Hamiltonians, respectively. The last term corresponds to the qubit-resonator interaction, which, when the qubit and the resonator are resonant, may cause excitation to swap between the resonator and the qubit. σ_+ (σ_-) results in an excitation (deexcitation) of the qubit.

If the qubit-resonator interaction is small with respect with the detuning, $|g| \ll |\omega_q - \omega_r|$, it can be treated as a perturbation. In this case, the *dispersive* Hamiltonian, up to order g/Δ , becomes

$$\mathcal{H}/\hbar \simeq \frac{\omega_q}{2}\sigma_Z + \omega_r \left(a^\dagger a + \frac{1}{2} \right) + \chi \sigma_Z a^\dagger a, \quad (2.48)$$

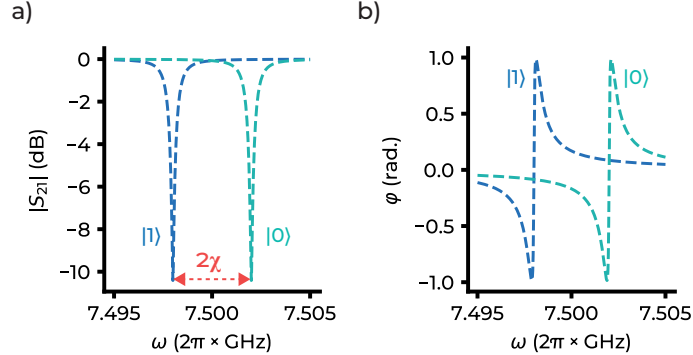


Figure 2.14: a) Ideal $|S_{21}|$ response of a hanging resonator when the qubit is at $|0\rangle$ and $|1\rangle$. The difference in resonance frequencies is 2χ . b) Ideal S_{21} phase response for the two qubit states.

where $chi \equiv g^2/\Delta$ is known as dispersive shift. Equation (2.48) can be rewritten in a more convenient form, disregarding constant terms

$$\mathcal{H}/\hbar \simeq \frac{\omega_q}{2} \sigma_Z + (\omega_r + \chi \sigma_Z) a^\dagger a, \quad (2.49)$$

where now the effect of the qubit-resonator interaction is seen as a change in the resonator frequency, $\omega'_{r,\pm} = \omega_r \pm \chi$, whose sign depends on the qubit state. By probing the resonator, the qubit state can be determined from $\omega'_{r,\pm}$.

2.6.1.1 Measurement pulses

The circuit shown in Fig. 2.10 is so-called a hanging $\lambda/4$ coplanar waveguide resonator, so transmission is measured, although the signal is technically reflected from the qubit-resonator system.

In order to perform a measurement of the qubit state, a pulse with a frequency close to ω_r is sent through the transmission line. The S_{21} response of the resonator ideally follows a Lorentzian shape

$$S_{21} = 1 - \frac{Q_L/|Q_c|}{1 + 2iQ_L(\omega/\omega_r - 1)}, \quad (2.50)$$

where Q_L and Q_c are, respectively, the loaded and coupling quality factors. Q_L is defined as

$$\frac{1}{Q_L} = \frac{1}{Q_c} + \frac{1}{Q_{\text{int}}}, \quad (2.51)$$

where Q_{int} is the internal quality factor of the resonator, describing internal losses. Q_c is also sometimes referred as Q_{ext} , as it corresponds to the external coupling to the readout line.

An ideal resonator response is shown in Fig. 2.14. The readout can be performed by probing at the frequency $\omega_{r,+}$, which corresponds to $|0\rangle$ in Fig. 2.14.

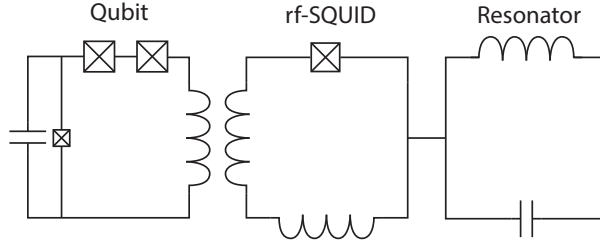


Figure 2.15: Current-based readout. The resonator has a rf-SQUID on the end, whose state depends on the state of the qubit.

High transmission means the qubit state is $|1\rangle$, and for low transmission the qubit is in state $|0\rangle$. 2χ defined in Section 2.6.1 can be extracted from $|S_{21}|$ measurements as it corresponds the difference of resonance frequencies between qubit in $|0\rangle$ and in $|1\rangle$.

An alternative to amplitude measurement is to read the phase of the pulse, as shown in Fig. 2.14b). Ideally, by measuring at exactly half distance between the $\omega_{r,+}$ and $\omega_{r,-}$, the phase difference between both states is maximized. In reality, the optimal phase frequency for phase measurements has to be calibrated. Finally, the signal-to-noise ratio (SNR) is known to be better for phase measurements than amplitude measurements [Jef14].

2.6.2 Current-based Readout

In AQC, the computational basis is not the energy but the current basis, as explained in Section 2.3.1. Therefore, the measurements have to be performed in this basis. A typical way to read out this operator is to replace the capacitor pad at the end of the resonator in the dispersive readout by a flux-sensitive element, such as a SQUID.

In Fig. 2.15, a resonator is ended with a rf-SQUID [Nov18]. The distributed resonator has a current maximum at the location of the rf-SQUID, thus maximizing its flux dependence. By careful design, the rf-SQUID-resonator resonance frequency strongly depends on the qubit flux. The rest of the readout process is identical to the standard dispersive readout.

2.6.3 Quantum-limited Amplifiers

Qubit measurements are typically performed at very low powers, as low as the single-photon regime[Bla04]. In this scenario, the output signal must be amplified significantly so that it can be read out by the available instrumentation.

Classical amplifiers provide large amplifications, achieving ~ 40 dB of amplification. However, they also add a considerable amount of noise. Noise temperature, T_N , is a usual noise benchmark of amplifiers, and is related to noise

power, N_N

$$N_N = k_b T_N. \quad (2.52)$$

The added-noise number, n_n , is defined as

$$n_n = \frac{N_N}{hf}, \quad (2.53)$$

where f is the photon frequency. n_n has units of number of photons, and can be compared to the amount of photons coming out of the resonator during readout, which is typically kept of order 1.

The quantum limit of noise is $1/2$ for single-mode detectors [Aum20]. However, real quantum-limited amplifiers have noise temperatures of $\sim 300\text{--}500$ mK [Ran21], corresponding to $n_n = 1 - 2$. HEMT amplifiers, on the other hand, have noise temperatures around 5 K, which correspond to $n_n \sim 20$ [Aum20].

Without a quantum amplifier, therefore, a correct state determination requires several averages in order to reduce the statistical fluctuations of the noise to properly identify the signal. Moreover, by averaging many measurements, no *single-shot* measurement is possible. This means that the exact measured qubit state is not accessed, but the averaged qubit population instead, and no feedback techniques are possible.

The quantum-limited amplifiers are very often designed using superconducting circuits [Esp21], as will be detailed in Chapter 8. Its behavior, however, is considerably different to standard superconducting qubit circuits.

2.7 Noise in Superconducting Qubits

The environment couples noise to the qubit similarly than the other circuit elements,

$$\mathcal{H}_{\text{noise}}/\hbar = \kappa_\lambda \hat{O}_q \hat{O}_\lambda, \quad (2.54)$$

where the noise operator is represented by \hat{O}_λ , while the qubit coupling operator is \hat{O}_q . The coupling strength of the noise κ_λ depends on the susceptibility of the qubit to noise, expressed as $\frac{\partial \mathcal{H}_q}{\partial \lambda}$, and the noise intensity at a given frequency.

\hat{O}_q determines the qubit-noise coupling type. When a transmon qubit is coupled to charge noise, $\hat{O}_q \propto (a - a^\dagger)$, which, in the qubit basis is expressed as σ_Y . Such a noise can induce qubit transitions, particularly qubit decay. The noise that can cause excitations or deexcitations is called *transverse noise*, as it is represented in the X or Y axis in the Bloch sphere. If the noise couples through σ_Z , then it is called *longitudinal noise*. Longitudinal noise causes fluctuations in ω_q , thus dephasing the qubit state in the Bloch sphere.

Two main approaches can be taken to decrease noise, either to minimize the qubit sensitivity to certain types of noise, or to reduce the noise strength. The former is usually implemented by design [Bro13], while the second one requires setup and qubit material improvements [Oli13]. Another option is to modify the qubit circuit so that it couples through a more convenient operator, \hat{O}_q .

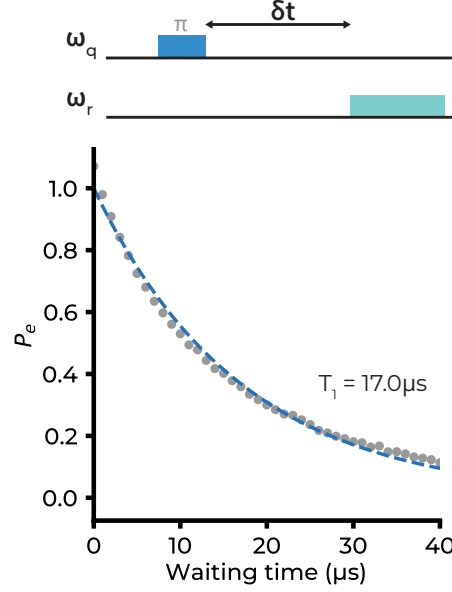


Figure 2.16: T_1 measurement (sequence on top). Data taken from Chapter 4.

2.7.1 Qubit Decay and T_1

Transverse noise at the qubit frequency can cause excitations at a rate $\Gamma_{1,\uparrow}$ and deexcitations at $\Gamma_{1,\downarrow}$, such that $\Gamma_1 = \Gamma_{1,\downarrow} + \Gamma_{1,\uparrow}$. However, the ratio between them is

$$\frac{\Gamma_{1,\uparrow}}{\Gamma_{1,\downarrow}} = e^{-\hbar\omega_q/k_B T}, \quad (2.55)$$

which at the working qubit temperatures is a very low number, $\Gamma_{1,\uparrow}/\Gamma_{1,\downarrow} < 0.1$. Therefore, transverse noise mostly causes qubit decay.

Γ_1 is defined as (following Fermi's golden rule)

$$\Gamma_1 = \frac{1}{\hbar^2} |\langle 0 | \frac{\partial \hat{H}_q}{\partial \lambda} | 1 \rangle|^2 S_\lambda(\omega_q), \quad (2.56)$$

where $S_\lambda(\omega_q)$ is the noise power spectral density at ω_q . If S_λ is white around ω_q , which is a common scenario, the qubit decay is exponential. Quasiparticle noise, on the other hand, cause Poissonian fluctuations, as their number on the qubit islands varies randomly. In that case, S_λ is not white and decay is not exponential[Gus16]. However, in most cases an exponential decay is a good approximation, and it is defined by the decay time $T_1 = 1/\Gamma_1$

T_1 is one of the key qubit coherence benchmarks in a quantum processor, and it is measured through a standard experimental sequence, called T_1 measurement. As seen on top of Fig. 2.16, the T_1 sequence consists of a π pulse

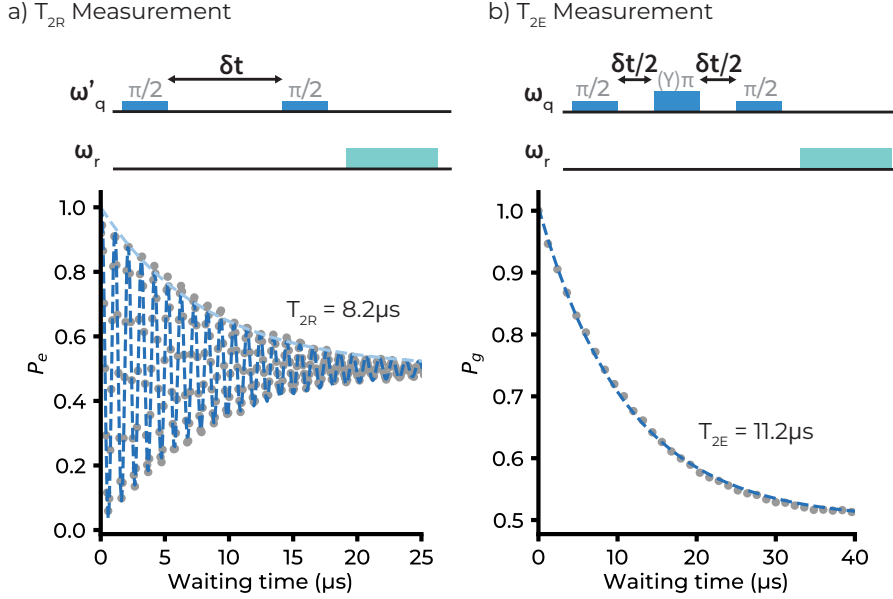


Figure 2.17: Sequence on top. Data is taken from Chapter 4. a) Ramsey measurement. b) Spin-echo measurement.

in X -axis that bring the qubit population to $|1\rangle$. Then a measurement is performed after a varying time, where the qubit would have decayed to $|0\rangle$. For white noise, the resulting P_1 population follows the form

$$P_1(t) = e^{-t/T_1}. \quad (2.57)$$

In Fig. 2.16 an example of a T_1 measurement is shown. Typical T_1 in superconducting qubits ranges from sub- μs to, so far, as long as ~ 8 ms [Pop14].

T_1 is known to change over time [Kli18] due to the modification of the noise environment. Thus, several T_1 measurements must be performed to obtain a histogram that correctly described the T_1 distribution of values.

T_1 measurements are performed in both transmon experiments in Chapter 4 and flux qubit experiments in Chapter 6, and are one of the coherence time figures of merit of both experiments.

2.7.2 Dephasing and T_2

Noise coupled longitudinally at frequencies lower than the qubit frequency ω_q , can cause ω_q fluctuations, $\delta\omega_q$, captured by the *pure dephasing rate*, Γ_φ . Dephasing is an energy-preserving error, as it corresponds to a loss of information of the quantum state. As there is no energy loss, dephasing noise can be compensated by proper pulse sequences to invert the dephasing dynamics[Vio98].

However, qubit decay causes also phase information loss, so that the total loss of coherence of a superposition state is described by

$$\Gamma_2 = \frac{\Gamma_1}{2} + \Gamma_\varphi. \quad (2.58)$$

This expression assumes that both decay functions are exponential. While this is generally true for Γ_1 , the dephasing noise is not generally white noise, which leads to slight modifications of this expression [Fal04].

Γ_2 corresponds to a transverse decay time T_2 , known as decoherence or dephasing time, which is another coherence time benchmark in superconducting qubits. T_2 is usually measured with the *Ramsey measurement* sequence, shown on top of Fig. 2.17 a). Ramsey measurement consists of sending two $\pi/2$ pulses to the qubit with a varying spacing between them. In absence of dephasing or decay, the final population would always be $|1\rangle$, which happens for very short times. However, for large times, the qubit is either completely dephased or has already decayed to $|0\rangle$ (whichever happens first). In both cases, on average, the second $\pi/2$ pulse brings the qubit population to the equator.

A common way to perform a Ramsey measurement is to slightly detune the two qubit pulses, at ω'_q , as in Fig. 2.17a). This introduces an extra precession in between the pulses in this new rotating frame, which causes decaying oscillations, expressed as[†]

$$P_1 = \frac{1 + \cos^2(\Delta\omega_q) e^{-t/T_{2R}}}{2}, \quad (2.59)$$

where $\Delta\omega_q = \omega'_q - \omega_q$. These oscillations are easier to fit than the previous decay, since the amplitude is higher. This technique is also used to correctly calibrate ω_q . When exactly on resonance, there are no oscillations.

$T_\varphi = 1/\Gamma_\varphi$ can be obtained once T_{2R} and T_1 have been measured via Eq. (2.58). T_{2R} is limited by $2T_1$, so even when the dephasing time is very long, the phase loss cannot be pushed further than $2T_1$, since decay is an incoherent process. On the other hand, pure dephasing is a coherent process with no energy exchange, which can be reversed.

A common way to reduce Γ_φ is to introduce an extra π pulse in the Y axis in the middle of the Ramsey sequence, which refocuses the qubit and completely removes the low frequency noise (see Fig. 2.17b)) that was constant in the time of the pulse sequence. If the qubit has a constant frequency shift which causes the qubit to precess at $\omega_q + \delta\omega_q$, then the extra refocusing Y pulse mirrors the phase accumulation caused by $\delta\omega_q$ at exactly the middle of the precession. By the end of the sequence, the qubit is back to the original point. This sequence is called (*Spin-*)*Echo measurement* [Hah50] and outputs a decay time $T_{2E} > T_{2R}$, described by

$$P_1 = \frac{1 + e^{-t/T_{2E}}}{2}. \quad (2.60)$$

[†]Note that $T_2 \equiv T_{2R}$ to differentiate between Ramsey and Spin-Echo decay times

The difference between the two coherence times, T_{2E} and T_{2R} , provides information about the noise nature. If low frequency noise is dominant, $T_{2E} \gg T_{2R}$. Extra pulses can be added in between to further filter the noise [Vio98].

2.7.3 Sources of noise

There are many possible sources of noise in superconducting circuits and many are not fully understood. Noise understanding and mitigation is an active topic of research [McR20; Oli13]. The most common sources of noise are:

- *Dielectric noise.* The materials used in superconducting circuits are not perfect and contain imperfections that can couple to the qubit. These defects are modelled as two-level systems (TLS) [Phi87; Mar05], causing dissipation as they couple capacitively to qubits through electric dipole interaction. The dielectric noise, also referred as charge noise, is the main limitation in transmon qubits and flux qubits operated at the symmetry point. TLS can also lead to flux noise, as stated in the next point. Better materials like Ta are needed to mitigate this noise.
- *Flux noise.* Flux noise is of utmost importance in flux qubits, and can be caused by different origins. The microscopic flux noise generated locally around the qubit has an almost universal $1/f$ dependence [Yos06]. The origin of this noise is suspected to come from unpaired spins on the superconductor surface [Sen08]. However, trapped vortices or fluctuations in the flux control also contribute to this noise [Nsa14]. Thorough material research and cleaner fabrication is needed to mitigate flux noise.
- *Quasiparticles.* Quasiparticle cause both relaxation by tunneling through the qubit junction(s), and charge noise in charge-sensitive devices. At low temperatures, thermal quasiparticles (qp) should be strongly suppressed. However, it is known that the effective electronic temperature of the qubit is higher than the nominal 20 mK of the refrigerator, thus increasing the quasiparticle density [Zmu12]. Moreover, quasiparticles can be excited by the microwave tone used to control or measure the qubit [Gol12], and also by stray radiation, either from the electromagnetic environment or by high-energy particles [Bar11; Kar19]. Quasiparticle trapping is the best known mitigation strategy, but is far from established cause [Wan14].
- *Resonator photons.* The stray photons in the resonator couple to the qubit via the qubit-resonator dispersive interaction. This causes a shift in the qubit frequency of $\delta\omega_q \propto \chi n_{\text{photons}}$. Fluctuations in the number of photons, thus, causes dephasing noise [Gam06]. These extra photons can also induce qubit transitions, thus causing decay [Sli12]. Proper thermalization and filtering helps suppress these photons.
- *Purcell decay.* The resonator acts as a filter that prevents the qubit to fully decay by emitting a photon at ω_q to the feedline. However, this

mechanism is not completely suppressed, and qubits may emit into the resonator mode. Purcell filters [Set15] can help in reducing this decay mechanism.

- *Parasitic modes.* An improper microwave environment can create unwanted on-chip and off-chip (box) modes that couple to the qubit causing hybridization and severely damaging qubit performance at the mode frequency [She17; Hou08].
- *Control lines noise.* The control lines couple the qubit to the environment, thus introducing noise in the system. This can be flux ohmic noise and charge ohmic noise, both increasing with frequency [Van03; Ith05]. A proper coupling of the qubit to these lines needs to be set to establish the limits on T_1 and T_2 . Improving the filtering can also help to reduce decoherence from control lines.

Chapter 3

Superconducting Circuit Measurements

In this chapter the basic equipment and techniques needed to measure superconducting circuits are explained. The experimental setup described here will be used in the following chapters to run qubit experiments. In Section 3.1, the fridge setup will be shown, with a special emphasis on the cabling & wiring configuration and the magnetic shielding. Then, in Section 3.2, the measurement setup including all the external equipment will be presented for the measurements performed throughout this thesis. Also in this section, a brief introduction to IQ mixing is given, as will be used later in Chapters 4 and 6.

3.1 Setup

A superconducting circuit experimental setup is characterized by the presence of a dilution refrigerator, which shapes the surrounding environment. The dilution refrigerator isolates and cools down the quantum the processor and through its interior the cables connect the processor with the exterior world. In this section, the setup around the refrigerator is described, and in Section 3.2 the measurement instrumentation will be added.

3.1.1 Refrigerator

A dilution refrigerator is a complex system whose main role is to cool down a part of its interior to $\sim 10 - 20$ mK or even lower. It does so by the use of liquid helium. By pumping ^4He the refrigerator is pre-cooled to around 4 K by evaporation techniques. Then, a mixture of ^3He and ^4He is used, which can be further cooled down through evaporation methods to < 1 K. Around 870 mK there is a phase separation, with a ^3He -rich phase (concentrated) and a ^3He -poor phase (diluted).

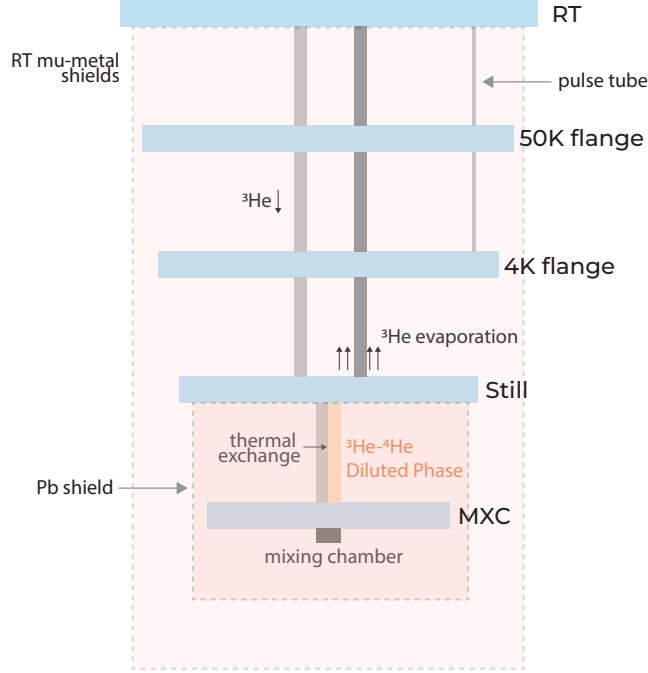


Figure 3.1: Refrigerator structure, with some of its most relevant parts. The extra magnetic shields are also labeled: the superconducting Pb shield at the still and the mu-metal shields: one thick inside the vacuum RT can and another made of thin mu-metal foil outside the same can.

The diluted phase is lighter than the concentrated phase, so it will sit on top. However, a tube can be connected from the lower part, so the ^3He -poor phase can be pumped. The ^3He poor has only around 6.6% of ^3He at the lowest temperatures. However, due to the large zero-point fluctuations of the ^3He , this isotope has a much higher vapour pressure than ^4He . When pumping the diluted phase, ^3He is mostly removed from the mixture. Then, ^3He from the concentrated phase, which is almost pure ^3He at low temperatures, moves towards the diluted phase to restore the equilibrium 6.6% concentration. This ^3He transition removes energy from the environment, effectively reducing the system temperature, which is the driving force of the dilution refrigerator.

The process where ^3He removes thermal energy from the environment takes place at the *mixing chamber* (MXC) in Fig. 3.1. The quantum processor is attached to the MXC, so that it thermally stabilizes to \sim mK. From the MXC a tube is connected to an upper stage called the *still* chamber. There, the diluted phase is pumped in a process similar to alcoholic *distillation*, which

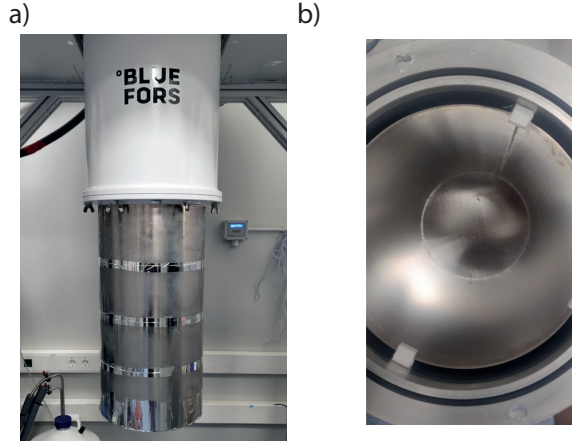


Figure 3.2: a) Outer mu-metal thin film shield. b) Inner thick mu-metal shield.

gives the name to this plate. The tube connecting the MXC and the still is thermally connected to the incoming tube bringing the evaporated ^3He back down to the MXC. Both tubes are connected through heat exchangers, which pre-cool the incoming ^3He . The amount and efficiency of this heat exchangers is one of the main differences between refrigerators that achieve lower or higher temperatures.

The refrigerator used in this work is a Bluefors SD dilution refrigerator. The SD fridge has another two flanges: one at ~ 4 K where the pulse tube that pre-cools the system at 4 K with ^4He is attached, and another one at around 50 K. There are thermometers at each stage, and heaters at the two lowest-temperature stages that can be used to attain higher temperatures to perform temperature-dependent measurements, such as those carried out in Chapter 7.

Finally, the refrigerator does not only cool down the processor, but it also isolates it. The refrigerator comes with many isolating layers per default. The larger one is the vacuum can which holds the vacuum inside the fridge, which can go as low as 10^{-9} bar. The others radiation shields are intended to isolated thermically between stages and to reflect incoming thermal radiation from the exterior. Extra shields can be placed to provide further isolation.

3.1.2 Magnetic shielding

Some types of qubits are not very dependent to flux noise, such as fixed-frequency transmons. However, flux qubits are specially sensitive to external magnetic flux. Indeed, flux qubits are so sensitive, that some of them are commonly used a magnetic detectors [Ste06].

In order to reduce flux noise effects on flux qubits, extra shieldings are placed to the refrigerator, whose schematic is shown on Fig. 3.1. A mu-metal thin lamina is placed outside the vacuum can and a mu-metal thick shield is placed

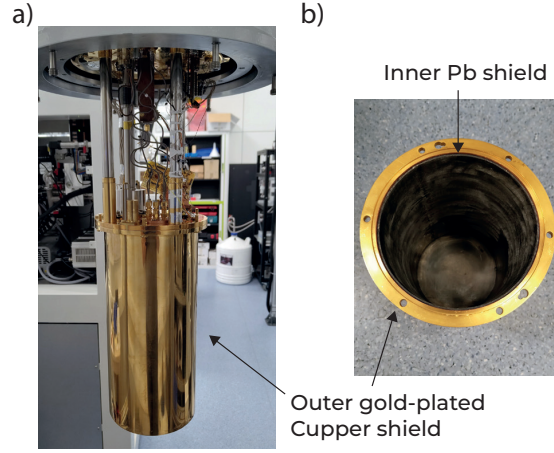


Figure 3.3: a) Outer gold-plated copper shield placed at the still stage. b) Top vision of the gold-plated copper shield with the Pb magnetic shield inside.

inside the same can. The mu-metal is a high permeability material that redirects magnetic flux lines through its interior, effectively shielding the inside of the mu-metal can. A full enclosure with a narrow slit to run the cables is the most optimal design for shielding. Mu-metal permeability is $\mu = 80,000 - 100,000$, an order of magnitude higher than other metals. This μ starts to drop at around 230 K, so it has to be placed at room temperature. These mu-metal shields are shown in Fig. 3.2.

At the still shield a 2 mm-thick Pb shield is placed, as shown in Fig. 3.3. This magnetic shielding operates differently than the mu-metal one, since at the temperatures of the still, ~ 1 K, lead is a superconductor. This shield operates because of the Meissner effect, as superconductors expel magnetic fields from their interior.

In the future, yet another shield will be placed at the MXC stage, to isolate it from all the components placed inside the still and MXC can, such as circulators, quantum amplifiers, etc which could disturb the qubit.

3.1.3 Cabling & Wiring

The quantum processors, along with other components, must be controlled from room temperature instrumentation. Apart from the fridge-related wiring, which operates heaters and thermometers, rf-signals, flux control and DC measurements and operations require proper wiring through the fridge.

3.1.3.1 rf signals

Many qubit operations, such as qubit state measurements and quantum gates, require rf signals. These signals, either pulses or continuous tones, are typically

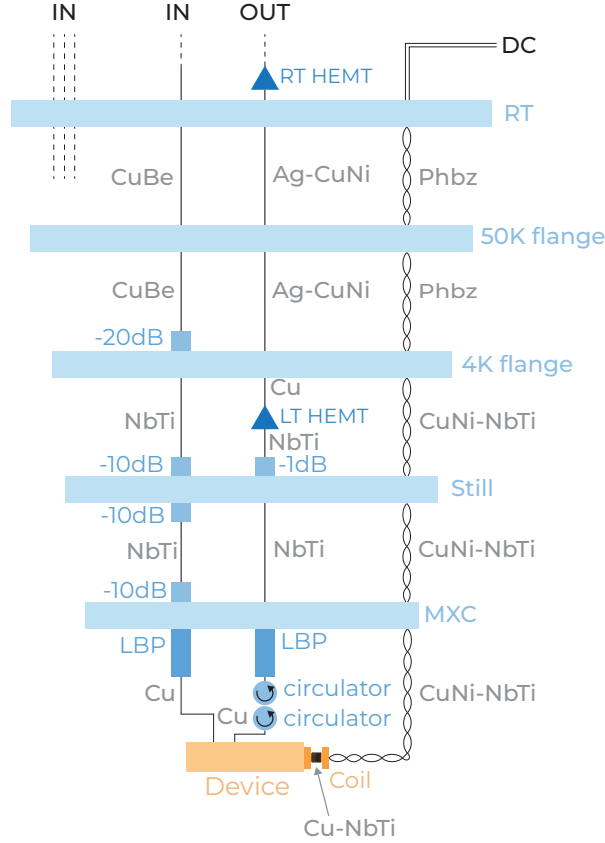


Figure 3.4: Wiring configuration inside the fridge. IN/OUT represent the input and output lines for rf signals. The cable or wire material is written next to it with XX-YY meaning YY metal with XX coating for wires or outer conductor for cables. Phbz stands for phosphor bronze, LBP is Low Band Pass filters and LT(RT) HEMT are the low temperature (room temperature) HEMT amplifiers. The DC flux control is only shown in flux dependent measurements.

in the 1 – 10 GHz range. The cables involved in these signal must, therefore, have low losses in this whole range. Usually < 20 dB S_{11} reflection is a good benchmark to cable quality.

The cables used to route rf-signal are coaxial cables assembled in-house with different materials, depending on the exact location, which can be seen in Fig. 3.4. The rf lines are divided into input and output lines, depending on the direction of the signal. There is only one output line, since there is only one amplifier, required to read out the outgoing signals. The rest of lines are input lines, which allow to control different qubit and couplers or to perform different

experiments at the same cooldown.

The input lines are heavily attenuated so that the signal can arrive at the single-photon level at the quantum processor. These attenuators also thermally connect the lines to the refrigerator flanges, which reduces the noise to the temperatures of that flange. A total of ~ 50 dB attenuation occurs inside the fridge due to these attenuators, while further attenuation is provided by the cables, the imperfect connections and the extra outside attenuation.

The cables going from the room temperature (RT) until the 4K stage are made of CuBe, while the cables between the 4K stage until the MXC are made out of NbTi. The latter is superconducting at temperatures below 7 K. While superconductors are very low loss materials, NbTi here is mainly used due to the poor thermal conductivity as a superconductor. The NbTi cables effectively decouple thermally the 4K, Still and MXC stages. The flexible cables inside the mixing chamber are made out of copper, as inside the MXC thermal conductivity is welcomed to connect all the elements to the flange.

At the MXC, the signals are filtered with low-pass filter (< 8 GHz) to remove high-frequency noise. The signal is then routed into the device. The outgoing signal from the device is then routed to two circulators, working in the 4–8 GHz regime. The circulators provide directionality so that there is little entering the device from the outgoing line, each giving -17 dB to signal in opposite direction. Then, this signal is further filtered and routed through the output line.

If more than one experiment is to be performed during the same cooldown, switches are needed to route only one of the signals to the output line. If there were more amplifiers, this would not be needed and each experiment could have a dedicated output line. The switches receive two signals as input and only allow one of them to go at the output. This is performed via DC control with a standard voltage or current source.

The output cable from MXC to the still is also made out of NbTi. In between the still and the 4 K flange, a low temperature (LT) high-energy mobility transistor amplifier (HEMT) is placed. The HEMT amplifies the signal by about 40 dB in the 4–8 GHz range. The cable below the HEMT is made from NbTi while the one above connecting to the 4 K plate is made from Cu. This way, the HEMT amplifier is thermally connected to the 4 K flange and decoupled from the still. There is a 1 dB attenuator before the amplifier to suppress possible standing waves in the lines, since neither the circulators nor the amplifier are well-matched to the line. This 1 dB attenuation also serves for further reducing the possible input from the amplifier to the qubit. The cables from 4 K to RT are made from silver-coated CuNi.

The output line is further amplified with another RT HEMT, that provided another 40 dB amplification, and a Pasternack amplifier which amplifies ~ 20 dB. The cables outside the fridge until the instrumentation are made from rigid Cu. These provide a stable setup, so that the specific cabling configuration is controlled by more flexible cables.

3.1.3.2 Flux Lines

Annealing sequences require dynamic flux control. This is performed by time-varying currents, which can be routed through the same cables as the rf signals described in Section 3.1.3.1. However, usually no more than 1 GHz is needed for these sequences, so other cables can be used with lower high-frequency requirements. The annealing sequence can be routed through more flexible and compact cabling.

Static flux control is performed via DC signals, which are not modified during a sequence. These DC lines only require to transmit DC signals. As can be seen in Fig. 3.4, the cables consist of twisted phosphor bronze pairs, which go all the way from the RT flange to the MXC without any attenuation. However, the lines are thermally connected at every stage in the refrigerator to remove thermal noise and for proper thermalization.

In this setup, the magnetic flux is generated by current passing through a coil. Since this is very close to the qubit, the potential thermal heat generated from the charge carriers could heat the qubit, thus causing excitations. Moreover, the $\sim 5 - 10$ mA used in the coil to generate the required magnetic flux, if passed through resistive wires that connect the local flux line, could heat the cryostat so much that it could not be operated.

Then, the wires from the MXC to the coil and in the coil itself are made from NbTi, the same superconductor material from the rf-signal cables. The wire from the MXC to the coil has CuNi cladding and the coil wire has Cu cladding over the NbTi core. CuNi has lower thermal conductivity, which helps to separate stages.

3.1.3.3 DC Measurement & Control Lines

In order to perform DC measurements, the same phosphor bronze wires of Section 3.1.3.2 are used. However, in this case the superconducting end is not needed. DC measurements are performed at temperatures above the superconducting state of the material or at the edge in order to spot the superconducting transition.

The control of components such as the microwave switches is performed via these same phosphor bronze wires. However, in this case, there is no need to use twisted pairs and single wires could be used, since noise is not important for this kind of control.

3.1.4 Grounding & Earthing

Grounding and earthing are two different, yet similar, concepts. Earthing refers to connecting the setup to the physical earth ground and it is mainly used in case of sudden charges outburst to provide a safe path to a lower (zero) voltage. Grounding, on the other hand, means providing a common voltage reference between all instruments and a common electrostatic mass providing a stable reference electric potential. The larger this mass, the better, since that implies larger electrostatic capacitance.

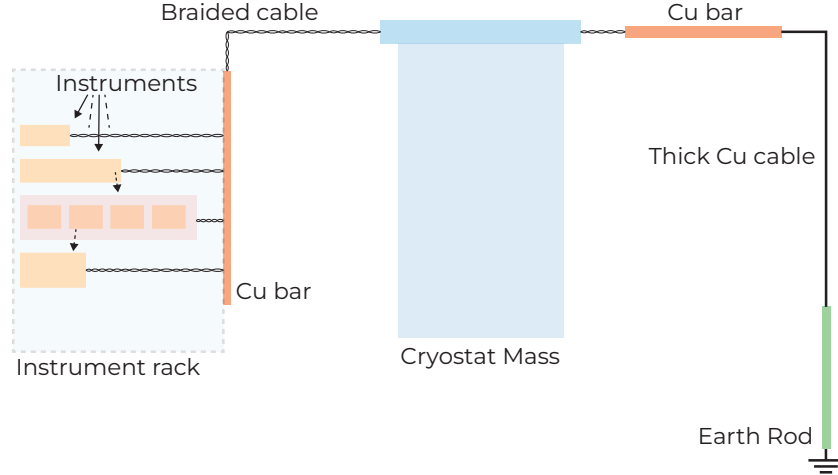


Figure 3.5: Grounding and earthing scheme used in the experiments. The instruments are connected to a common Cu bar that is then connected to the large cryostat mass that provided the grounding reference. All these connections are done via a braided Cu cable. Then, the cryostat mass is earthed to a dedicated earth rod via another Cu bar to provide a safe place to the earth ground for sudden discharges.

In order to provide a good earthing, there is a dedicated earth ground rod for the superconducting circuit experiments. This ground rod is intended to isolate the instruments from nearby labs, such as a mechanical workshop with very power-demanding machines. This earth rod is connected to the common ground (described below) through a copper bar, which should be the only connection to this clean earth ground.

For proper grounding, all instruments' chassis are connected to the common ground. The common ground provides a good potential reference with a large mass. This electrostatic mass is defined through the refrigerators, instruments, and rack chassis. The cryostat mass, being the biggest, is the one providing this stable potential reference.

The full grounding setup is depicted in Fig. 3.5. All the instruments are connected to a common copper bar in the instrument rack with braided cables. These cables are used because they have very low resistance. The copper bar is connected to the cryostat mass. Then, the cryostat mass itself is linked to another copper bar which then connects to the earth's ground. This last link provides a safe path for electrostatic discharges and should be the only path to the earth's ground.

Furthermore, the power provided to the instruments is filtered to remove transients, spikes, and harmonic (caused by engines, machines, switches...) from the ideal sinusoidal of 50 Hz.

Ideally, the instrumentation used for the experiments should be decoupled

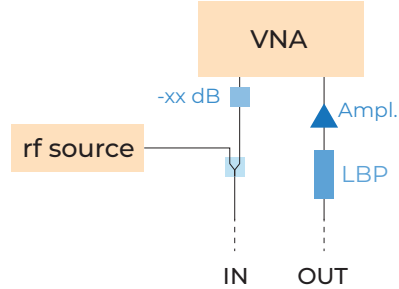


Figure 3.6: Spectroscopy measurement setup, consisting on a VNA and a rf-source. The low-band pass filter filters out frequencies below 8 GHz

from more noisy equipment, such as the refrigerator gas handling system controls or the computers. While the former is achieved through dielectric interruption between the metallic pieces, the second has not been implemented yet. Thus, for instance, the computer is still connected to the Keysight PXI rack through the PCIe cable, which introduces noise in the setup. Moreover, fridge temperature spikes have been correlated with large machinery being switched on/off in the neighbouring lab. Thus, further improvement must be performed in this regard.

3.1.5 Software

The instruments have been controlled with Labber software, a Keysight owned software specifically aimed at superconducting qubit experiments. This software allows to control all the different instruments and to generate the pulse sequence for the experiments. By using this software, most calibration can be performed without scripting and automatic documentation of the instrument parameters is saved.

However, scripting is required to generate more complex sequences, such as the ones commented at Section 4.4 on the Universal Approximant algorithm. In that case, Python scripts are written as well by making use of the Labber API. Direct control of the instruments through SCPI commands or their Python drivers has been also used to perform minor tasks or to debug the instrumentation. Moreover, several new Labber drivers have been developed to add new instrumentation to the setup.

3.2 Measurements

The measurement setup described in this section corresponds to the instrumentation and wiring outside the refrigerator, which can be usually modified during the same cooldown.

3.2.1 Spectroscopy Measurements

The quantum processor is usually first characterized in the frequency domain. These measurements provide initial characterization of the frequencies and energies of the qubits, resonators, and couplers. Obtaining these parameters with spectroscopy is simpler and faster than with time-domain measurements.

A Vector Network Analyzer (VNA) is the main instrument for spectroscopy measurements. This instrument sends a continuous radiofrequency tone and reads the reflected and transmitted scattering parameters, S_{ij} , in phase and amplitude. The frequency and power range depends on the specific device, but should operate in between the 1 – 10 GHz to be used in cQED experiments. The VNA used in the experiments is an Agilent E5071B VNA Network Analyzer, which works in the range 300 kHz – 8.5 GHz.

The signal sent with the VNA is typically attenuated with external attenuation, so that the few-photon level is obtained at the device. Some measurements such as the *punchout* measurement described in Section 4.2.2, require higher powers, so some attenuation may be removed.

For experiments that require two tones, such as the qubit spectrum obtained with two-tone measurements (Sections 4.2.2 and 6.3), a rf-source is added to the setup. This rf-source sends a continuous tone at GHz frequencies, that is combined with a rf splitter with the VNA tone. Usually the rf-source tone is sent to excite the qubit while the VNA is probing the resonator response. This rf source is a Rohde&Schwarz SGS100A SGMA RF source.

3.2.2 Time-domain Measurements

In order to perform quantum algorithms, a precise time control is needed on the qubits. This requires different instruments than for spectroscopy instruments. The measurement setup is shown in Fig. 3.7. The signals sent into the fridge are now pulses instead of continuous tones, so an Arbitrary Waveform Generator (AWG) is needed. In our setup, it corresponds to Keysight M3202A PXIe AWG, which is located inside a M9010A PXIe Chassis. Two different AWG modules are used, one for the qubit and another for the readout pulses.

The pulses are IQ modulated, which implies that an arbitrary modulated pulse is generated by two different pulses which are 90 degrees shifted: the in-phase (I) and the quadrature (Q) components. The general modulation is

$$A(t) \sin(\omega t + \varphi(t)) = A_I(t) \sin(\omega_{IQ} t) + A_Q(t) \cos(\omega_{IQ} t), \quad (3.1)$$

where A is the total pulse amplitude, A_I and A_Q the I and Q amplitudes respectively, ω_{IQ} is the modulation frequency and φ the phase. IQ modulation allows for complete amplitude and phase control obtained only with amplitude modulation, which is much easier to achieve precisely with the instrumentation used.

However, the AWG has a 1 GS/s sampling rate, which cannot directly output the necessary GHz pulses. Therefore, these pulses are upconverted with an IQ mixer. An IQ mixer is a 4-port component that receives the I and Q quadratures

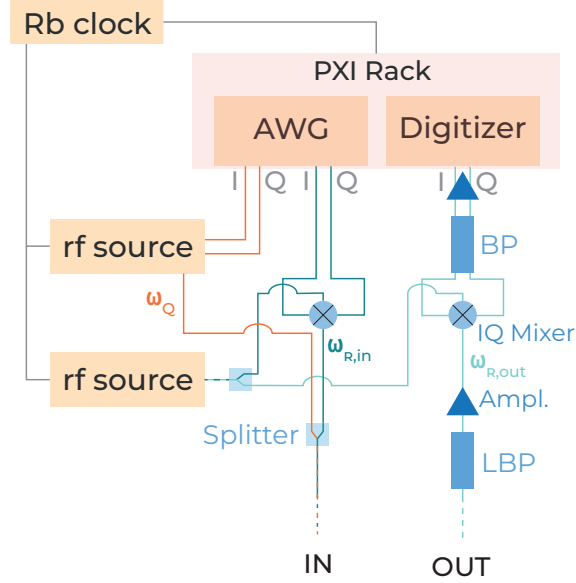


Figure 3.7: Time-domain measurement setup. The AWG generates the IQ signals of the qubit (ω_Q) and resonator pulses ($\omega_{R,in}$). The qubit pulse is upconverted by the internal IQ mixer of a rf source. The readout pulse is upconverted with an IQ mixer and a tone generated by another rf source. This same rf-source is used to demodulate the readout signal coming from the fridge ($\omega_{R,out}$). The $\omega_{R,out}$ signal is filtered and amplified before and after the downconversion, and then read out by the digitizer. A stable reference signal generated by a Rb-stabilizer source is distributed to all equipment, daisy-chained. The low-band pass filter filters out frequencies below 8 GHz, and the band-pass is centered at the modulation frequency, which is 70 MHz.

of the desired pulse and a continuous rf tone at another intermediate frequency ω_{LO} (LO: local oscillator). The resulting pulse (RF) has the shape of the IQ pulse and may output either of the frequencies $\omega_{LO} \pm \omega_{IQ}$. The sign depends on the exact configuration of the pulses.

IQ mixer upconversion works by receiving $I(t)$ and $Q(t)$ signals at the I and Q ports, with any kind of modulation. On the LO port, a continuous tone is received, $LO(t) = \cos(\omega_{LO}t)$. The resulting pulse, V_d , can be expressed as

$$\begin{aligned} V_d(t) &= I(t) \cos(\omega_{LO}t) + Q(t) \cos(\omega_{LO}t + \pi/2) \\ &= I(t) \cos(\omega_{LO}t) - Q(t) \sin(\omega_{LO}t) \end{aligned} \quad (3.2)$$

The desired pulse should have a shape

$$V_d(t) = V_0 s(t) \sin(\omega_d t) \quad (3.3)$$

where V_0 is the pulse amplitude and $s(t)$ the envelope function that shapes the

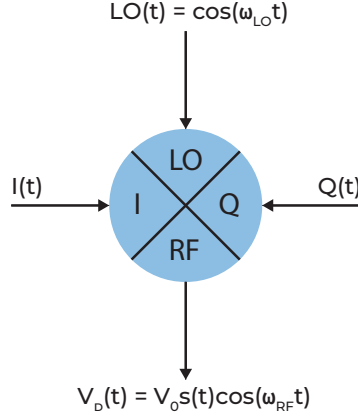


Figure 3.8: IQ mixer upconversion scheme. The input I and Q signals at ω_{IQ} are upconverted with the rf source at ω_{LO} to the resulting ω_{RF} . $\omega_{RF} = \omega_{LO} \pm \omega_{IQ}$ depending on the I and Q signals. The resulting voltage has a V_0 amplitude and an envelope functions $s(t)$ define by the I and Q shapes.

pulse. In order to obtain Eq. (3.3), these are the $I(t)$ and $Q(t)$ needed

$$I(t) = V_0 s(t) \sin(\omega_{IQ} t), \quad (3.4)$$

$$Q(t) = -V_0 s(t) \cos(\omega_{IQ} t). \quad (3.5)$$

The sign choice in the $Q(t)$ expression is what determines that the resulting frequency is $\omega_d = \omega_{LO} + \omega_{IQ}$.

The qubit pulse is upconverted at ω_Q at the internal mixer of the Rohde&Schwarz SGS100A SGMA rf source, which has an IQ mixing option. The readout pulse, on the other hand, is upconverted to $\omega_{R,in}$ via an external IQ mixer with the LO generated by another rf source of the same model without the IQ mixing option. Both signals are then combined via a Splitter/Combiner and routed to the Input port of the refrigerator in the same wire. The schematic is depicted in Fig. 3.7.

The readout signal coming from the fridge is further amplified and the high-frequency noise filtered. Then, it is downconverted with an IQ mixer working in the reverse way. In this situation, the IQ mixer receives the RF signal and the LO tone, and it outputs the two demodulated I and Q quadratures. The same LO used for upconverting the tone has to be used for downconverting. Otherwise, a phase drift between the LO sources would cause a continuous phase drift on the resulting readout signals, thus forbidding phase measurements. Once the signal is downconverted it is further amplified and filtered with 70 MHz band pass filters around the demodulated frequency, which in the experiment throughout the thesis was $\omega_{IQ}/2\pi = 70$ MHz.

The digitizer used is a Keysight M3102A PXIe digitizer that is located in the same chassis as the AWG. This is convenient, since very precise timing control

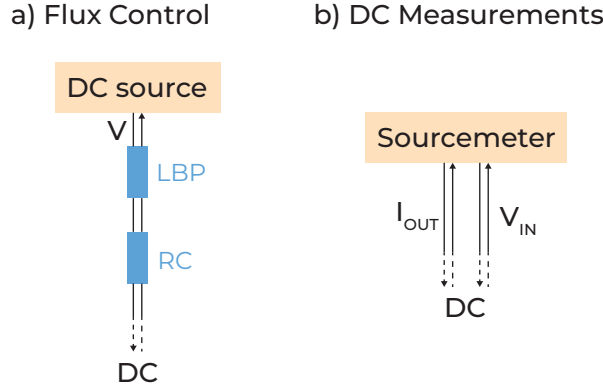


Figure 3.9: a) Static flux control achieved through a filtered voltage DC source. b) Resistance measurements are performed via a Sourcemeter. It outputs a current I_{out} and reads the voltage drop V_{in} so resistance can be computed.

is needed to trigger both with the desired detuning. The whole pulse sequence takes a few μs to travel from the AWG to the Digitizer. The digitizer then receives the I and Q signals at the modulation frequency ω_{IQ} . The signals are then integrated in order to receive the complex magnitude, $A = I + jQ$. If the readout is performed by magnitude, $|A| = \sqrt{I^2 + Q^2}$ is used; if it is a phase measurement, $\varphi = \arctan(Q/I)$ is used instead.

All the instruments are referenced to a Rubidium reference source that outputs a 10 MHz-stable reference tone. This is required to keep the internal clocks of the instruments referenced to the same stable clock, otherwise phase drifts would damage the experiment performance.

3.2.3 Flux Control

The static flux control is obtained via a Yokogawa GS200 DC Source. This instrument outputs a very stable DC voltage or current. The flux can be obtained by a fixed I which will generate the magnetic flux when turning in the coil in Fig. 3.4. The Yokogawa is a floating source, so the current comes back to the instrument without running through the fridge ground.

In the setup, the flux is generated via a stable voltage source. This DC voltage is first filtered with a LBP filter below 10 MHz and then further filtered with a home-built RC filter with a cutoff below 50 Hz, as can be seen in Fig. 3.9a).

Dynamic flux control, not used throughout this thesis, would be attained with similar structure as microwave pulse driving shown in Fig. 3.7. However, in that scenario, only the AWG would suffice, since required frequencies are not so high. Moreover, IQ modulation would not be required, and the digitizer is not used for flux control. Thus, it would consist of just AWG channels outputting the flux sequences to the required fridge input ports.

3.2.4 DC measurement and Control

The four-probe measurements performed in Chapter 7 use a Keithley 2634B Source Measurement Unit, which can output and read very low voltages and currents. The measurement is performed by generating a current and reading the voltage drop. In order to remove the cable resistance, an $I-V$ curve is taken, and the resistance is obtained by fitting the response to a linear regression. The setup can be seen in Fig. 3.9b).

DC control of equipment, such as the switches, only requires discrete voltages of > 12 V at very occasional times. This can be performed via power sources used to power amplifiers or with the same equipment used for generating flux or DC measurements.

Chapter 4

Transmon Qubit Experiments

ADRIÁN PÉREZ-SALINAS, DAVID LÓPEZ-NÚÑEZ, ARTUR GARCÍA-SÁEZ, P. FORN-DÍAZ, JOSÉ I. LATORRE *

4.1 Introduction

In this chapter, the experimental implementation of the Universal Approximant (UA) algorithm in a transmon qubit is described. This experiment paved the way for all the following experiments in the IFAE QCT group, thus many techniques are initially developed during this chapter work. These techniques are thus used throughout the rest of the thesis, and also served as the basis for other works in the QCT group. For this reason, Section 4.2 serves as an introductory guide on how to use a superconducting quantum computing setup and the instrumentation required.

In Section 4.3, the quantum Universal Approximant theorem is sketched and its quantum algorithm implementation presented. This work was developed together with other members of the Quantic group at BSC and is already published [Pér21]. The theoretical demonstration is overviewed here, although the work was fully developed by Dr. Adrián Pérez-Salinas and Prof. J.I. Latorre.

The experimental implementation of the UA algorithm is explained in Section 4.4, and the result is discussed in Section 4.5. Final conclusions are given in Section 4.6.

4.2 Controlling and Characterizing a Transmon Qubit

This section describes how to set up a quantum computing experiment using superconducting qubits ready to perform algorithms. This section is written

*Part of the contents of this chapter have been published in Phys. Rev. A 104, 012405

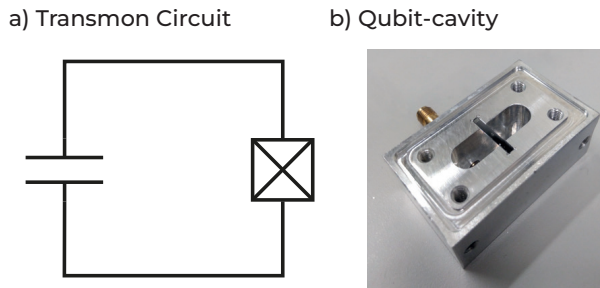


Figure 4.1: a) Transmon circuit schematic. b) Image of the opened cavity with the transmon chip inside.

as an introductory tutorial on how to use a quantum computing setup and the instrumentation required.

In Section 4.2.1, the transmon-cavity system and the setup used in the experiment are presented. Then, in Section 4.2.2 the basic qubit-cavity system properties are obtained with spectroscopy measurements. Time-domain measurements are described in Section 4.2.3, and Section 4.2.4 develops further on time-domain calibration and optimization.

4.2.1 System & Setup

To initiate superconducting qubits experiments, a 3D transmon qubit was used [Pai11], arguably the simplest and most reliable design of superconducting qubit. This simplicity and robustness is very convenient to characterize any superconducting qubit experimental setup.

A 3D transmon consists on a transmon qubit coupled to the lowest mode of a superconducting cavity. The transmon is formed by a single Josephson junction shunted by a parallel plate capacitor (see Fig. 4.1 a))[Koc07]. The superconducting cavity is made of aluminum, and the transmon is placed at its center, as can be seen in Fig. 4.1 b).

The cavity can be approximated as a rectangular cavity of width a (\hat{x}), height b (\hat{y}) and length d (\hat{z}), with $d > b > a$. In this case, the fundamental mode electric field, \vec{E} , is

$$\vec{E} = \hat{x}E_0 \sin \frac{\pi y}{b} \sin \frac{\pi z}{d}, \quad (4.1)$$

with E_0 the electric field amplitude. At the center of the cavity the electric field of the fundamental resonant mode is maximal, thus maximizing the coupling with the transmon, that is placed at the cavity center. Most of \vec{E} stays in vacuum, minimizing dielectric losses from the substrate, which is typical in qubits coupled to coplanar waveguide (CPW) resonators [Gao08; OCo08].

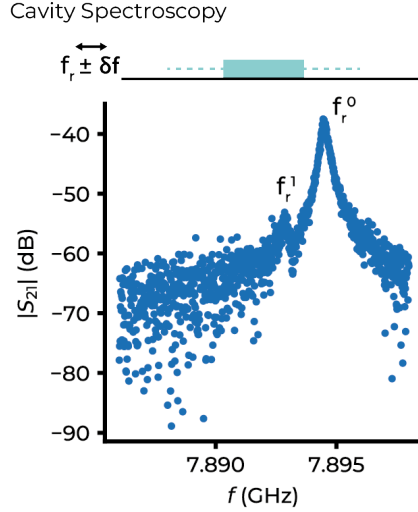


Figure 4.2: Cavity spectroscopy with sequence on top. The resonance peak is clearly seen, $f_r^0 = 7.895$ GHz, and some qubit thermal population lead to a second peak, $f_r^1 = 7.893$ GHz

The cavity resonance mode loaded quality factor, Q_L , is defined as

$$\frac{1}{Q_L} = \frac{1}{Q_{\text{int}}} + \frac{1}{Q_{\text{ext}}}, \quad (4.2)$$

where Q_{int} and Q_{ext} are the internal and the external quality factors respectively. If $Q_{\text{ext}} \gg Q_{\text{int}}$, internal losses dominate the quality factor, meaning that the cavity mode is undercoupled to the external circuitry. On the other hand, the cavity is said to be overcoupled when $Q_{\text{ext}} \ll Q_{\text{int}}$.

The cavity is coupled to the external world via two ports, input and output. In order to provide good directionality, the input port is undercoupled compared to the output port. This configuration cause most of the signal that enters into the cavity to exit through the output port. Typically, $Q_{\text{ext}}^{\text{in}}/Q_{\text{ext}}^{\text{out}} \approx 10$, which causes $P_{\text{out}} \approx 100P_{\text{in}}$, where P_{out} and P_{in} are the input and output power at the cavity, respectively.

4.2.2 Spectroscopy Measurements

Spectroscopy measurements provide the initial characterization of the qubit-cavity system. These measurements are performed in the frequency domain, and typically only require steady-state frequency and power sweeps. Spectroscopy measurements can be performed in a relatively fast manner, since they do not require precise timing control. This initial characterization allows one to start time-domain measurements, such as Rabi oscillations (Section 2.5.2.1), with a prior knowledge of the qubit and cavity properties.

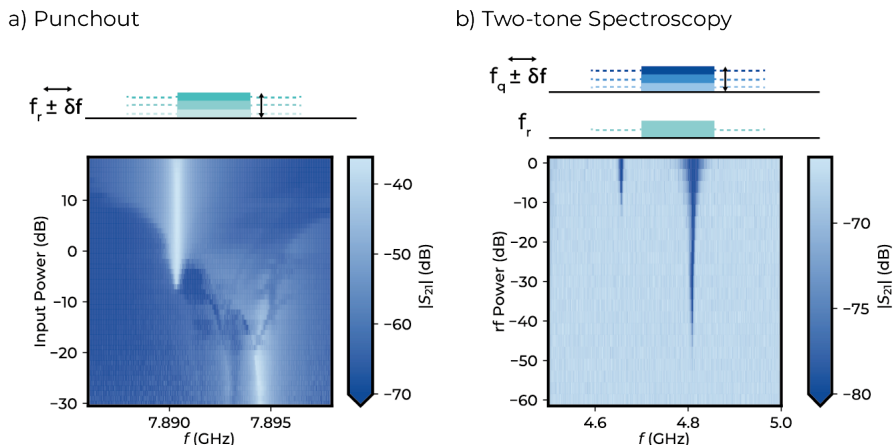


Figure 4.3: a) Punchout measurement (Sequence on top). The power of the readout pulse until the effect of the qubit is vanished. The frequency on top of the plot corresponds to the bare resonance, while the lower corresponds to f_r^0 . b) Two-tone spectroscopy (Sequence on top). The qubit frequency is observed at $\omega_q = 4.81$ GHz. When the qubit tone power is increased, an extra dip is observed which corresponds to half the frequency of the $0 - 2$ transition, $\omega_{02}/2 = 4.66$ GHz.

A frequency scan of the system returns the cavity transmission S_{21} , defined as

$$S_{21}(f) = \frac{Q_L}{Q_{\text{ext}}} \frac{1}{1 + 2jQ_L \left(\frac{f-f_r}{f_r} \right)}, \quad (4.3)$$

where f_r is the resonant mode frequency. The magnitude response, $|S_{21}|$, is shown in Fig. 4.2. The response has a peak at $f_r^0 \approx 7.895$ GHz, since the signal is admitted at the cavity at this frequency and exits through the overcoupled output port. For an off-resonant tone, most signal is reflected, thus significantly lowering $|S_{21}|$.

This is a simple experiment which only requires sending a weak tone to the cavity while monitoring the transmitted signal. Moreover, the same aluminum cavity can be used to test different qubit chips.

The resonance measured in this experiment, if performed at low power, does not correspond to the bare aluminum resonant frequency, but the displaced resonance due to the dispersive interaction with the qubit (see Section 2.6.1). Indeed, in Eq. (4.1), a small second peak at $f_r^1 \approx 7.893$ GHz to the left of the main peak is caused by the thermal population of $|1\rangle$ state. The difference in frequency between these two peaks yields the dispersive shift,

$$f_r^0 - f_r^1 = \frac{2\chi}{2\pi} = 1.5\text{MHz}, \quad (4.4)$$

where $\chi = g^2/\Delta$, with g being the qubit-cavity coupling strength, while $\Delta/(2\pi) = f_q - f_r$ is the difference between cavity and qubit resonance frequencies. The

Transmon level structure

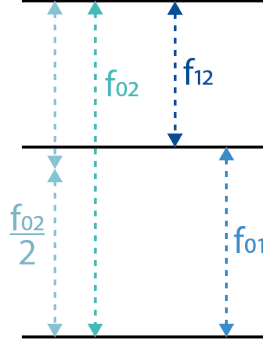


Figure 4.4: Transmon lowest energy level structure

limit of the dispersive regime is set by the critical number of photons, $n_{\text{crit}} = \Delta^2/(4g^2)$. At n_{crit} the photon-induced energy splitting of the qubit states, $2g\sqrt{n}$, is equal to Δ , which breaks the dispersive approximation [Bla04].

If this same measurement is performed at higher powers, above n_{crit} , the bare cavity resonant frequency will be measured. In this scenario, the energy difference of the dressed states $|N\rangle$ and $|N+1\rangle$ is equal or larger to the cavity linewidth, so the system becomes harmonic, effectively *punching out* the qubit.

In Fig. 4.3 a so-called punchout measurement is shown, consisting of performing a power sweep of a cavity resonance trace. The change in the cavity resonant frequency at high powers is the benchmark of the presence of a qubit in a cavity. By performing this measurement, f_r^0 at low powers is found to be 7.8945 GHz $\equiv f_r$, while $f_r' = 7.8902$ GHz appears at high powers.

In order to obtain the qubit frequency, $f_q \equiv f_{01}$ and the qubit anharmonicity*, $\delta \equiv f_{12} - f_{01}$, a two-tone spectroscopy-type measurement is required. This experiment consists of sending a low-power tone at f_r , corresponding to the resonance peak in the low power part of the punchout measurement. Simultaneously, a second tone whose frequency is swept is sent to the qubit-cavity system to find f_q . Once f_q is found, the qubit is in a driven steady state, with half its population in $|0\rangle$ and the other half in $|1\rangle$. Consequently, the peak in S_{21} transmission is reduced, effectively showing a dip in the qubit frequency scan at f_q .

Figure 4.3 b) shows the two-tone spectroscopy measurement performed at different powers. At low powers, the qubit frequency is found to be $f_q = 4.81$ GHz. Increasing the power shows a second dip at a slightly lower frequency.

*The common symbol α for anharmonicity is not used, since this will lead to confusion when flux qubits are introduced, since α is saved for the ratio between junction areas. Moreover, the anharmonicity will be now defined in frequency, unlike previous chapter which was in angular frequency.

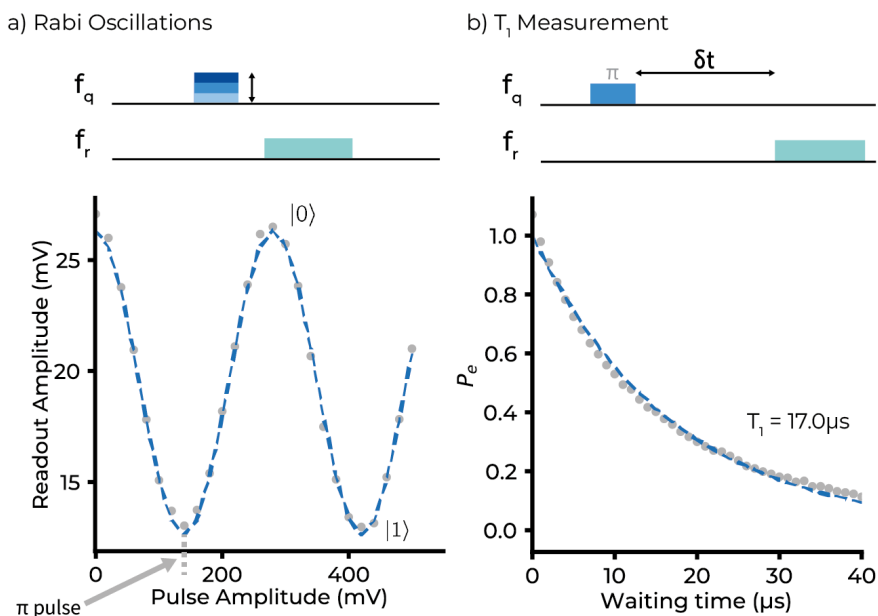


Figure 4.5: Qubit coherent control. Both figures show data points on grey and fits on dashed blue line. Pulse sequence is shown on top. a) Rabi Oscillations show qubit coherent control, while serving as a calibration for the π pulse and to set the $|0\rangle$ and $|1\rangle$ readout points. b) T_1 Measurement. $T_1 = 17.9 \mu\text{s}$ is long enough for performing many gates, as π -pulse time is $T_\pi = 30 \text{ ns}$.

This peak corresponds to $f_{02}/2$ (see Fig. 4.4), as it is a two-photon process from $|0\rangle$ to $|2\rangle$ which, since it is less probable than a one-photon process, requires higher powers to excite. Anharmonicity can be obtained by $\delta = 2(f_{02}/2 - f_{01})$. For this experiment, $f_{02}/2 = 4.66 \text{ GHz}$ which leads to $\delta = -324 \text{ MHz}$.

4.2.3 Qubit Coherent Control and Characterization

4.2.3.1 Rabi oscillations

Prior to observing Rabi oscillations, a preliminary pulsed readout of the cavity was performed. The readout pulse was set to $2 \mu\text{s}$ long, larger than cavity rise time, $\tau = 0.507 \mu\text{s}$. The pulse has $f_{IQ} = 70 \text{ MHz}$ modulation frequency, chosen to avoid $1/f$ noise that would have been present if homodyne detection was performed at 0 Hz modulation. The specific value of the f_{IQ} was chosen as it lies well within the bandwidth of the AWG used in the experiment.

Rabi oscillations (see Section 2.5.2.1) were performed with a 30 ns Gaussian pulse envelope at 70 MHz modulation frequency. The pulse amplitude is swept in order to rotate the qubit in the Bloch sphere. The amount of qubit state rotation is proportional to the energy delivered to the qubit, $\varphi \propto \int_0^t V_0 s(t') dt'$, where V_0 is the pulse amplitude and $s(t')$ the time envelope. Rabi oscillations in

amplitude were characterized instead of time-domain oscillations since fixing the pulse duration time allows setting the same timing control when many pulses are applied, such as in the Universal Approximant algorithm (see Section 4.4). The pulse sequence and the Rabi oscillations are shown in Fig. 4.5 a). It is worth stating that these oscillations were the first-ever observed on a superconducting qubit in Southern Europe.

With Rabi oscillations, the readout signal amplitude, A_{read} is mapped to $|0\rangle$ and $|1\rangle$ states. The signal received when no qubit pulse is sent corresponds to the qubit in $|0\rangle$, while the lowest amplitude of the oscillations corresponds to $|1\rangle$. A π -pulse is also determined by Rabi oscillations, as seen in Fig. 4.5 a). The precise determination of these quantities is obtained by fitting A_{read} to

$$A_{\text{read}} = A_{\text{Rabi}} \cos^2(\Omega A_{\text{pulse}}/2) + c, \quad (4.5)$$

where A_{pulse} corresponds to the applied qubit pulse amplitude and the rest are fitting parameters. Equation (4.5) is then compared to the Rabi oscillations formula

$$P_e(t) = \sin^2\left(\frac{\Omega t}{2}\right), \quad (4.6)$$

where Ω is the Rabi frequency, common in both expressions. Then, the population of the ground state is obtained by $P_g = (A_{\text{read}} - c)/A_{\text{Rabi}}$, and $P_e = 1 - P_g$. A π -pulse amplitude is defined as $A_{\text{pulse},\pi} = \pi/\Omega$, so the qubit population is rotated 100% to $|1\rangle$.

Up to this point, it is assumed that the initial qubit state is exactly $|0\rangle$, with no initial thermal population, and the Rabi pulse is exactly at f_q , which both cause complete Rabi oscillation between $|0\rangle$ and $|1\rangle$. A closer look on a more realistic scenario with imperfect state preparation and inexact drive parameters will be taken at Section 4.2.4.4 and Section 4.2.4.2.

It is important to note that, due to the lack of a quantum limited amplifier, no single-shot readout capability was available in this experiment. Thus, the measurement results consisted of averaging multiple single shots, typically 5,000, although it could be as high as 50,000 when smooth data was desired.

4.2.3.2 Coherence time characterization

After calibrating the π -pulse and the readout of the state population, the qubit coherence times characterization is performed (see Sections 2.7.1 and 2.7.2). First, T_1 is measured, which indicates the relaxation time of the qubit from the excited state to the ground state. The T_1 pulse sequence and the results can be seen in Fig. 4.5 b). T_1 is obtained by fitting the population to a decaying exponential, $P_e(t) = e^{-t/T_1}$, which for the qubit in the 3D cavity resulted on $T_1 = 17.0 \mu\text{s}$. Compared to the 30 ns π -pulse duration, $T_1/T_\pi \sim 10^3$, allowing to perform multiple gates before decay dominates.

For the dephasing time characterization, a Ramsey measurement is performed. Ramsey measurement consists of sweeping the spacing between two consecutive $\pi/2$ pulses applied to the qubit, which led to $T_{2R} = 8.2 \mu\text{s}$, as seen

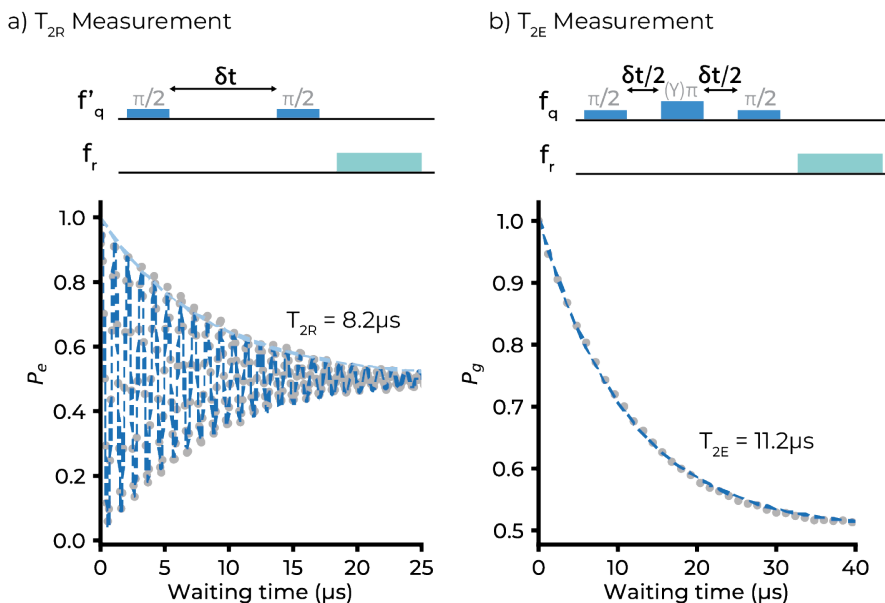


Figure 4.6: Qubit coherence times. Both figures show data points on grey and fits on dashed blue line. Pulse sequence is shown on top. a) Ramsey T_{2R} measurement. The value of $T_{2R} = 8.2 \mu\text{s}$ shows that the qubit coherence is not T_1 limited. b) Echo T_{2E} measurement. In the sequence it is specified that echo pulse is in the Y-axis, unlike the other pulses, along the X-axis, unless otherwise noted. The value of $T_{2E} = 11.2 \mu\text{s}$ is still far from $2T_1$, which indicates the high frequency noise is not negligible.

in Fig. 4.6 a). These pulses have the same shape and duration of the π pulses used for T_1 , but the amplitude is halved. If the pulse frequency is slightly detuned from f_q , the resulting trace will be a decaying sinusoidal. T_{2R} is obtained by fitting the data to

$$P_e = \cos^2(\delta f t) e^{-t/T_{2R}}, \quad (4.7)$$

where $\delta f = f_{pulse} - f_q$. The Ramsey decay time is defined as $\frac{1}{T_{2R}} = \frac{1}{2T_1} + \frac{1}{T_\varphi}$, where T_φ is the pure dephasing time. Since $T_{2R} < 2T_1$, it shows that T_{2R} is not limited by decay, but by dephasing time, $T_\varphi = 10.8 \mu\text{s}$.

The spin echo sequence adds an extra Y-axis π -pulse in between both $\pi/2$ pulses from the Ramsey sequence. The π -pulse suppresses low-frequency dephasing noise by mirroring the state along the Y-axis at the middle of the sequence. T_{2E} is obtained by fitting

$$P_e(t) = 1/2 + e^{-t/T_{2E}}/2. \quad (4.8)$$

As expected, $T_{2E} = 11.2 \mu\text{s}$, is higher than T_{2R} , but still lower than $2T_1$, which indicates that higher frequency noise dephasing still affects this decay. Both the spin Echo sequence and the measured results can be seen on Fig. 4.6.

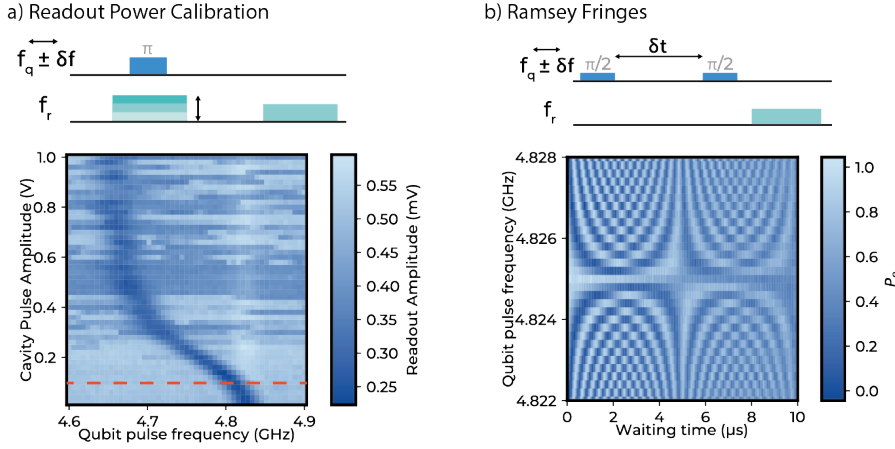


Figure 4.7: Readout and control pulse calibration. Both figures show their pulse sequence on top of the main graph. a) Readout Power Calibration. A pulse identical to the readout pulse is sent at the same time as the qubit drive. Increased power shows the dispersive shift of the qubit frequency and, at high enough powers, the tone starts to induce undesired qubit transitions to higher levels. The red dashed line marks the safe amplitude used in the experiments. b) Qubit frequency calibration. Ramsey fringes consist of the Ramsey measurement repeated at different qubit drive frequencies. Qubit frequency can be targeted to sub-MHz levels with this sequence.

The coherence times obtained are already sufficient for the goal of implementing the Universal Approximant algorithm, even when no further optimization has been applied to the readout and control pulses. However, there are still several improvements that need to be implemented in order to enhance readout efficiency and reduce pulse errors, which will be covered in the following section.

4.2.4 Control and readout optimization

4.2.4.1 Readout Calibration

All the measurements in this chapter have been performed in magnitude, which means that the qubit state is determined by $|S_{21}|$ from Eq. (4.3). The frequency of the readout pulse was set at f_r , which is the dressed frequency of the resonator when the qubit is in $|0\rangle$.

The most relevant calibration procedure in the readout is to ensure that the readout pulse power is not causing photon-induced transitions in the qubit[Sli12], which severely limits readout efficiency, as the qubit state can change during the measurement. These photon-induced transitions occur when the readout photons recombine with noise at $f_{ro} = f'_r - f_q$ at a rate $\Gamma_{\uparrow,\downarrow,PI}$ [Sli12]

$$\Gamma_{\uparrow,\downarrow,PI} = 4 \frac{g^2}{\Delta_{ro}^2} \nu^2 S(\mp \Delta_{ro}) \bar{n}, \quad (4.9)$$

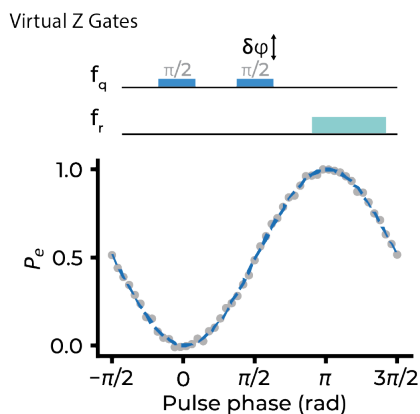


Figure 4.8: Virtual Z-gates are performed on the second gate (sequence on top). φ refers to the rotation axis, thus $\varphi = 0$ corresponds to the same axis as the original pulse and π reverses the original pulse.

where g and ν are the qubit-cavity and the qubit-noise coupling, respectively, and $\Delta_{\text{ro}} = f_{\text{ro}}/(2\pi)$. $S_{\varphi}(\Delta_{\text{ro}})$ is the spectral density of dephasing noise at the detuning frequency, and \bar{n} is the average photon occupation of the cavity. The latter is the only controllable parameter during the experiment. Thus, the readout pulse amplitude, A_{rp} , has to be kept at a low value so \bar{n} is also low.

A_{rp} calibration [San16] is shown in Fig. 4.7 a). The calibration sequence consists of sending a qubit π -pulse at varying frequency and, simultaneously, a pulse at the readout frequency and varying amplitude. After $\sim 1 \mu\text{s}$, the qubit is measured with a standard readout tone with weak amplitude. When the first cavity pulse has zero amplitude, the qubit π -pulse sets the qubit in $|1\rangle$ when the frequency is f_q , thus observing a dip in cavity transmission (see Section 4.2.3). At other frequencies, the qubit pulse does not excite the qubit and the transmission is kept high. However, when the cavity pulse has nonzero amplitude, it populates the cavity with photons, which induces a Stark shift on the qubit frequency of $\Delta f_q = 2\chi\bar{n}/2\pi$. If \bar{n} is too large, photon-induced transitions in the qubit are triggered. These are mainly seen as dips in the measured amplitude, while far from f_q . To stay on the safe side, the resonator amplitude is set at half the amplitude the first jumps are seen, around 0.1 V.

4.2.4.2 Qubit Frequency

The qubit frequency obtained with two-tone spectroscopy in Section 4.2.2 is not very precise, since it can be Stark-shifted from the presence of large amounts of photons in the cavity. In general, time-domain control is always a more precise way of determining qubit and cavity properties.

Ramsey decay is a standard approach to finding a precise f_q . As explained in Section 4.2.3, Ramsey decay oscillates at a frequency equal to the detuning,

δf , between the f_q and the frequency of the Ramsey pulses. Thus, repeating the Ramsey decay experiment at different frequencies will determine f_q , the frequency at which the decay shows no oscillations. This experiment, known as Ramsey fringes, is shown at Fig. 4.7 b), and can give sub-MHz precision. For this experiment, $f_q = 4.8250 \pm 0.0002$ GHz.

However, Ramsey fringes can be a rather long experiment, taking tens of minutes, and a single trace can already give a good determination of f_q . A single fit of a detuned Ramsey trace determines δf , as it corresponds to the oscillation frequency. This method requires that T_{2R} is large enough so that many oscillations can be accurately fitted, and an operation point where many oscillations occur at high visibility before decaying. In this case, a 2 MHz detuning is a good operation point, because the oscillations have high enough amplitude to be correctly fitted. Moreover, as there is no way to identify the sign of the detuning, so the operation point should be placed far enough so that fluctuations are always lower than the detuning.

4.2.4.3 Virtual Z-gates

All the qubit pulses discussed so far have been in the X - or Y -axis of the Bloch sphere, which change the population of the qubit. The Rabi oscillations, as defined in Eq. (4.6), are indeed oscillations along any axis perpendicular to the equator of the Bloch sphere. The standard approach to perform rotations in the Z -axis is by applying virtual Z -gates [McK16a] as discussed in Section 2.5.2.3. Virtual Z -gates consist of modifying the subsequent phases of the qubit pulses effectively rotating the X - and Y -axes.

In Fig. 4.8, an example of a sequence that leverages the use of the virtual Z -gates is shown, where two $\pi/2$ -pulses are placed one after the other and a virtual Z pulse is added in between which, effectively, consists of changing the axis of the second pulse. When $\varphi = 0$, the two $\pi/2$ -pulses bring the qubit to $|1\rangle$, and when $\varphi = \pi$, the qubit is back to $|0\rangle$.

4.2.4.4 Thermal Population

Thermal population of the first-excited (and higher) states of the qubit can considerably reduce the fidelity of the quantum gates and the readout efficiency. Calibration of the thermal population can be performed by using the 1-2 qubit transition. First, a calibration of f_{12} must be performed via similar Ramsey measurements as the f_{01} using as an initial guess the obtained f_{12} from the two-tone spectroscopy measurement (see Fig. 4.4 for a schematic of the transmon lowest-level structure).

A sequence for calibrating the thermal population of $|1\rangle$ is shown in Fig. 4.9 a)[Gee12]. The sequence consists of performing Rabi oscillations on the 1-2 transition, then applying a π -pulse to project $|1\rangle$ into $|0\rangle$. In the absence of thermal population, no oscillations would be seen. However, small oscillations are usually observed. The thermal population is obtained via Maxwell-Boltzmann statistics[Jin14]

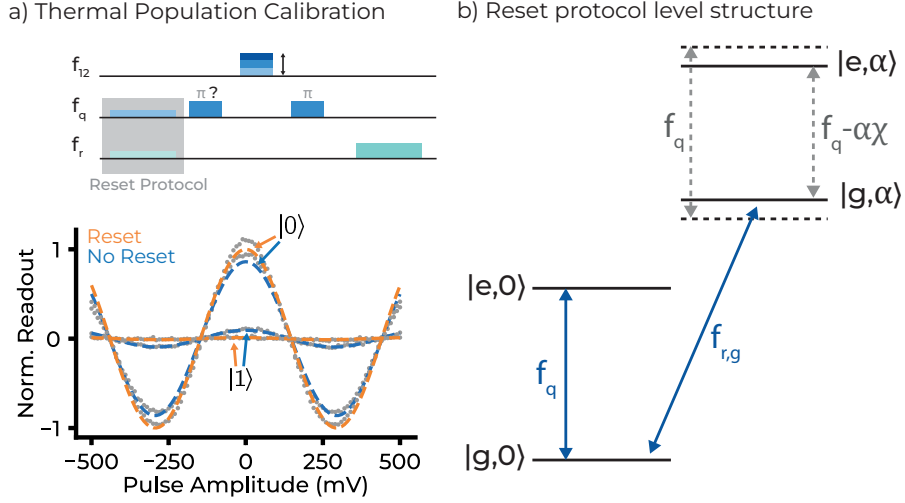


Figure 4.9: a) Thermal Population Calibration. Pulse sequence on top of the main graph. Data points are plotted in gray and fits in dashed colored line. A Rabi sequence in the 1-2 transition is performed before a π pulse. In case of thermally excited states, the $|1\rangle$ population oscillates. If a π pulse is applied prior to the Rabi sequence, the same behaviour can be seen on the $|0\rangle$ initial population. This corresponds to the *No Reset* dark blue dashed lines. If a reset protocol is performed previous to this sequence, the excited population is considerably reduced, and the ground population state increased, as can be seen in the *Reset* light orange dashed lines. b) Level structure involved in the qubit reset protocol. $|g/e, 0\rangle$ is the ground/excited of the qubit with no photons in the cavity and $|g/e, \alpha\rangle$ refer to the ground/excited state of the qubit and the coherent state $|\alpha\rangle$ in the cavity. In solid blue lines the driven transition, while the dashed are only marked for reference. The level differences are not to scale.

$$P_e = \frac{e^{-\frac{\hbar f_{01}}{k_B T_{\text{eff}}}}}{1 + e^{-\frac{\hbar f_{12}}{k_B T_{\text{eff}}}} + e^{-\frac{\hbar f_{01}}{k_B T_{\text{eff}}}}} . \quad (4.10)$$

For $f_{01} = 4.825$ GHz and $f_{12} = 4.490$ GHz, a $T_{\text{eff}} = 20$ mK, would correspond to $P_e < 0.0001$. However, it is common to have $P_e \approx 0.1$, which correspond to $T_{\text{eff}} \approx 110$ mK. To calculate the amount of $|1\rangle$ population, the same sequence is performed, but with a π -pulse at the beginning, thus observing the same 1-2 oscillations of the $|0\rangle$ population. Assuming there is no population in higher excited states, the thermal population can be obtained from

$$P_e = \frac{A_e}{A_e + A_g} , \quad (4.11)$$

where A_g and A_e are the amplitude of the oscillations in the ground and excited states, respectively. The resulting value seen in Fig. 4.9a) from this experiment shows a 10% of thermal population, which indicates $T_{\text{eff}} = 110$ mK.

If single-shot readout was available, simple heralding would suffice to make sure this thermal population does not damage gate efficiency and readout fidelity. Heralding consists of measuring the qubit state prior to starting the algorithm and discarding all measured states different from $|0\rangle$, thus ensuring a proper initialization. However, this was not possible in the experiment due to the lack of a quantum-limited amplifier. Instead, a reset protocol was used, which is a sequence that reduces thermal population by driving the initial state to $|0\rangle$.

The reset protocol[Gee12] used in this experiment consists of two simultaneous drives sent to the qubit-cavity system, schematically shown on Fig. 4.9b). The first drive is a low-power tone at the qubit frequency, f_q , thus starting a slow oscillation between $|g\rangle$ and $|e\rangle$. The second pulse is sent at the cavity frequency when the qubit is at $|g\rangle$, $f_{r,g}$, which is the readout frequency used so far. The role of this second drive is to populate the cavity with photons, as long as the qubit is in $|0\rangle$. As the number of photons keeps increasing, these causes a Stark shift on the qubit frequency, so that the first pulse stops being resonant with the qubit, thus leaving the qubit unaffected. The end result of this sequence is that the qubit-cavity system ends in $|0, \alpha\rangle$, where α represent the coherent cavity state with $\bar{n} = |\alpha|^2$.

When the system is already at $|0, \alpha\rangle$, the drives are stopped, and photons escape from the cavity, returning to $|0, 0\rangle$. This protocol relies on the photon decay rate τ^{-1} being much higher than the qubit excitation rate, Γ_{\uparrow} , which is achieved in most superconducting circuit experiments. In this experiment, $\tau^{-1} = 1.86$ MHz, and Γ_{\uparrow} can be estimated by

$$\Gamma_{\uparrow} = \Gamma_{\downarrow} e^{-hf_{01}/k_B T}, \quad (4.12)$$

where T is the effective temperature obtained from the excited population and Γ_{\downarrow} is approximated as $1/T_1$. This results on $\Gamma_{\uparrow}/2\pi \approx 6$ kHz $\ll \tau^{-1}$.

The results from this reset sequence applied prior to the thermal population calibration are shown superposed to previous P_e calibration in Fig. 4.9 a). There, by applying Eq. (4.11), thermal population is reduced to $< 1\%$, with $T_{\text{eff}} < 50$ mK. Both pulses are 2 μ s long and there is a 2 μ s waiting time before sequence starts.

Yet another benefit is obtained from using this sequence. Before starting any new experiment, one should typically wait around $10 - 20 \times T_1$ times in order to ensure the qubit has decayed in $|0\rangle$. However, this reset protocol brings the qubit to $|0\rangle$ irrespective of the initial state. Therefore, instead of waiting ~ 200 μ s, this waiting time is reduced to the 4 μ s the protocol lasts, which is almost a 2-order of magnitude improvement in sequence time.

4.2.4.5 Qubit Pulse Optimization

In order to optimally control the qubit state, Gaussian pulses can lead to errors if they are shortened too much, as there is a wider spread in frequencies when the pulse duration is reduced. If the pulse is short enough, there can be a

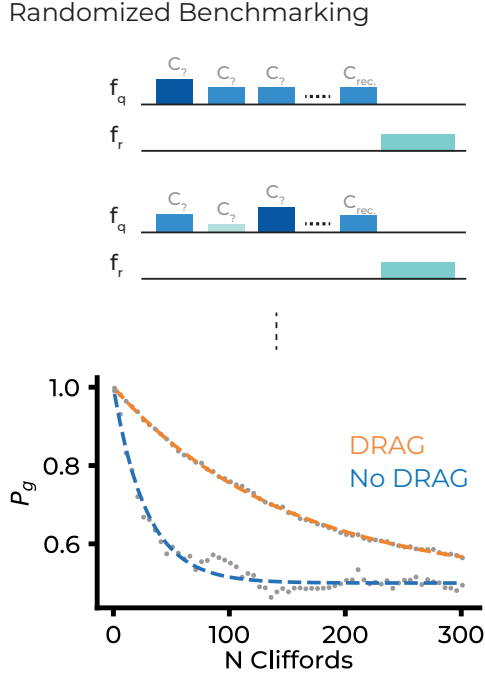


Figure 4.10: Randomized benchmarking. The sequence is shown on top of the main graph. Fit of randomized benchmarking of normal Gaussian pulses in dark blue dashed lines (*No DRAG*), or pulses with the DRAG correction applied in light orange dashed line (*DRAG*), while data is shown in gray points. Each point corresponds to 40 different random sequences of N number of Clifford gates, each averaged 5,000 times. After the sequence, a recovery pulse is sent in order to bring the state to the ground state. Pulse fidelity is $p = 0.993$.

non-negligible contribution at the qubit anharmonicity, $f = \delta$, which can cause excitations up to $|2\rangle$ in the qubit, thus exiting the computational qubit subspace and leading to gate errors.

Gate error characterization is obtained with a Randomized Benchmarking (RB)[Kni07] sequence. This sequence measures the error on Clifford gates, which are the set of gates that, starting at $|0\rangle$, move the qubit around the six vertices of the three main axes of the Bloch sphere. A single sequence of the RB protocol consists of applying N Clifford gates selected at random to $|0\rangle$ and, afterwards, applying a last recovery gate that brings the qubit back to $|0\rangle$. This last gate is another Clifford gate and can be easily calculated from the random sequence. The final state will be closer to $|0\rangle$ if little error is accumulated during the gate sequence.

The RB protocol consists of applying this last sequence for a varying number of N Clifford gates, and several randomized sequences for each N . Each single sequence is averaged over many shots to reduce sampling error, or to increase readout fidelity if there is no single-shot readout. For low N , the final probability

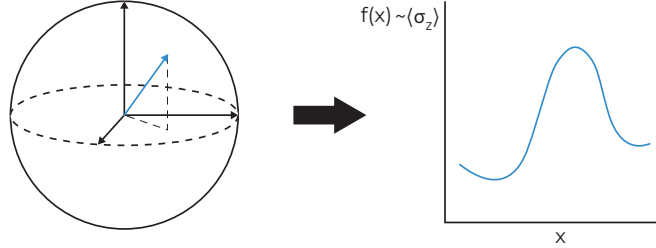


Figure 4.11: Can a single-qubit circuit approximate any bounded function?

to recover $|0\rangle$ is $P_g \approx 1$, since little error is accumulated. For very large N , the acquired error will have spread the quantum state at any point in the Bloch sphere, thus outputting $P_g = 1/2$ when averaging all traces.

In Fig. 4.10, the randomized benchmarking of the original simple Gaussian pulse is shown, with a single-qubit gate fidelity of ≈ 0.96 , which is a bit low for usual standards, tending to fidelities of > 0.99 . The gate fidelity, p is obtained by fitting the RB decay to $P_g = \frac{p^N}{2} + 1/2$.

A standard Gaussian pulse can improve in fidelity by applying a DRAG (Derivate Removal by Adiabatic Gate) correction[Mot09]. DRAG consists of applying the derivative of the Gaussian pulse in the out-of-phase quadrature, multiplied by a factor, β , that depends on the anharmonicity. If the Gaussian pulse in the X -axis is described as $\xi_x(t)$, the DRAG correction would be

$$\xi_y(t) = \beta \dot{\xi}_x(t), \quad (4.13)$$

where β is a parameter that inversely depends on the anharmonicity and has to be optimized.

The gate fidelity of the DRAG-corrected pulse can be seen in Fig. 4.10. The improvement in fidelity is substantial, achieving a gate fidelity $p = 0.993$.

4.3 One Qubit as a Universal Approximant

In collaboration with the UB-BSC group of quantum computing, called Quantic, a suitable algorithm to program on the IFAE/QCT transmon qubit was identified. The algorithm is the implementation of the quantum version of the Universal Approximant Theorem (qUAT). The simple question answered by qUAT is whether a single-qubit circuit can encode any bounded mathematical function in its gates (Fig. 4.11).

This section summarizes the demonstration of the positive answer to this inquiry, along with its algorithmic description. However, for more detail, the paper [Pér21] provides the full demonstrations[†].

[†]This part of the work was developed by Dr. Adrián Pérez-Salinas, and it is summarized

4.3.1 Universality of a single-qubit approximant

A single qubit can be in any state on the surface of a Bloch sphere, thus it can represent any point in the $[0, 1] \otimes [0, 1]$ plane. Any complex number can be thus represented by a qubit state up to a rescaling. However, it is not evident that a single-qubit quantum circuit that receives an independent variable x as an input, can represent any bounded function, $f(x)$, in the qubit state population, after a proper rescaling. In order to do so, a quantum algorithm only dependent on x should correctly approximate any $g(x)$ by $\langle \sigma_z \rangle \approx g(x)$, where $g(x) = af(x)$ is the rescaled function of any bounded function $f(x)$ in the $[0, 1]$ range.

The work in [Pér21] shows that, indeed, a single-qubit circuit is capable to universally approximate any bounded complex function, $z(x)$, in the degrees of freedom of the gates in the circuit. Note that the function in the proof include complex input variables compared to $f(x)$ stated previously, making the theorem more general. Two alternative demonstrations were performed by using the Fourier theorem and the classical UAT. Each demonstration is proved with its corresponding quantum algorithm, and have a different range of their applicability.

The demonstration of the quantum UAT implies that more complex theorems can build upon it to develop new theorems, in the same way that the Universal Approximation Theorem (UAT) is used in machine learning. Moreover, the algorithms proved in [Pér21] can be included in more complex quantum algorithms as subroutines.

4.3.2 Proofs of universality

4.3.2.1 Quantum Fourier

The Fourier series theorem states that any bounded complex function[‡], $z(x)$ can be convergently approximated by a series of complex exponentials.

The classical Fourier approximated function $z_N(x)$ after N steps, where each step is another term of the Fourier series, is defined as

$$z_N(x) = \sum_{n=-N}^N c_n e^{i \frac{2\pi n x}{P}}, \quad (4.14)$$

where

$$c_n = \frac{1}{P} \int_P z(x) e^{-i \frac{2\pi n x}{P}} dx \quad (4.15)$$

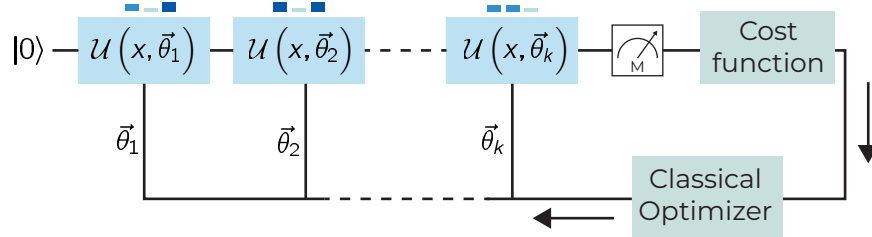
and P is the length the function $z(x)$ is to be approximated.

The *Quantum Fourier Theorem* is obtained by using a gate sequence that can be mapped to the complex exponentials of the Fourier series. The quantum Fourier gate sequence, $\mathcal{U}_{\mathcal{F}}$, represents a single term in the Fourier series, which

here for completeness.

[‡]The exact details of the function definition are omitted. In reality, the Fourier theorem only allows functions with a finite number of finite discontinuities in the interval of interest. However, the reader is referred to [Pér21] for exact details of the mathematical developments.

Optimization Protocol

Figure 4.12: Optimization protocol used for obtaining the optimal parameters, $\vec{\theta}_i$.

depends on several parameters to be optimized, $\vec{\theta}_i$, and the independent variable, x . The repetition of this sequence convergently approximates the target function $z(x)$. $\mathcal{U}_{\mathcal{F}}$, is defined as

$$\mathcal{U}_{\mathcal{F}}(x; \omega, \alpha, \beta, \varphi, \gamma) = R_z(\alpha + \beta)R_y(2\lambda)R_z(\alpha - \beta)R_z(2\omega x)R_y(2\varphi), \quad (4.16)$$

where $\vec{\theta} = (\omega, \alpha, \beta, \varphi, \gamma)$ are the parameters to be optimized and are related to the coefficients of a Fourier step.

4.3.2.2 Quantum UAT

The UAT states that any continuous function of m -dimensional variables can be approximated by a sum of a set of non-constant bounded functions, defined as σ , with adjustable parameters. The approximated function after N steps is

$$f_N = \sum_{n=1}^N \alpha_n \sigma(\vec{\omega}_n \cdot \vec{x} + b_n), \quad (4.17)$$

where $\vec{\omega}_n$, α_n and β_n are the parameters to be optimized. For the extension of this theorem to a complex function $z(x)$, please read [Pér21].

The *Quantum UAT* relies on replicating the classical theorem by using a gate sequence that corresponds to the non-constant bounded functions σ used in the theorem. The specific sequence, \mathcal{U}_{UAT} is

$$\mathcal{U}_{UAT}(\vec{x}; \vec{\omega}, \alpha, \varphi) = R_y(2\varphi)R_z(2\vec{\omega} \cdot \vec{x} + \alpha), \quad (4.18)$$

where $\vec{\omega}$, α and φ are now the parameters left for optimization.

4.3.3 Classical Numerical optimization

The UAT confirms that there is a set of parameters that approximates the target function $z(x)$. However, unlike the classical Fourier theorem [Eq. (4.15)],

no prescription is given to obtain them. Thus, the parameters are to be obtained with classical optimization.

For classical UAT, SciPy implementation of gradient-based algorithms is used to obtain the optimization parameters. The algorithms used are the BFGS (Broyden–Fletcher–Goldfarb–Shanno) and the L-BFGS (Limited-memory Broyden–Fletcher–Goldfarb–Shanno) algorithms. These algorithms rely on using the gradients to obtain the descent direction to obtain the function minimum.

The quantum implementation is performed on a noiseless quantum simulator that contains sampling uncertainty. The sampling uncertainty consists of averaging the result of the simulated quantum measurements instead on directly using the expected Pauli values, $\langle \sigma_i \rangle$. Then, the cost function is calculated with these simulated measurement average. At each cost function evaluation step, the classical algorithm proposes new parameters based on the current and previous results. This process is shown in Fig. 4.12.

The cost function driving the optimization is

$$\chi^2 = \frac{1}{M} \sum_{j=1}^M (\langle \sigma_z(x_j) \rangle - f(x_j))^2, \quad (4.19)$$

where M is the total number of samples of x . The complex version is analogous to this expression.

The L-BFGS method used in classical optimization is also chosen for the quantum version, along with the genetic optimization algorithm CMA (Covariance Matrix Adaptation). Genetic algorithms explore large regions of the parameter space and, most importantly, do not depend on gradients. This last property can be beneficial because sampling noise and real data hinders the task of gradient-based optimizers. However, genetic algorithms tend to require many more function evaluations. In this work, the best fit between the two methods is selected. Quantum optimization is more complex because the landscape of the cost functions is unknown, so it is unclear which optimizer is the best choice.

Several selected functions are approximated to prove the validity of the quantum Fourier and the quantum UAT algorithms. The single-variable approximations are benchmarked against the following functions:

$$\text{ReLU}(x) = \max(0, x), \quad (4.20)$$

$$\tanh(ax) \quad \text{for } a = 5, \quad (4.21)$$

$$\text{step}(x) = x/|x|; \quad 0 \text{ if } x = 0, \quad (4.22)$$

$$\text{poly}(x) = |3x^2(1 - x^4)|. \quad (4.23)$$

The first two functions are chosen for their importance in neural networks. The last two display non-trigonometric behavior, which prove that the algorithm can approximate polynomial dependencies as well as discontinuities. These functions are also used to encode the real and imaginary part of approximated complex functions, $z(x)$.

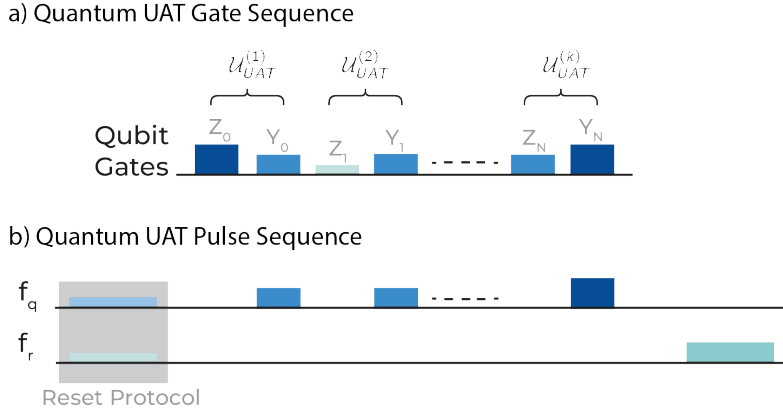


Figure 4.13: a) The gate sequence of the Quantum UAT algorithm is shown on top. b) The actual pulses of the sequence, with the prior reset protocol and the readout measurement. Note that only Y gates are performed, while Z gates are virtual.

Four functions of two variables, $f(x, y)$, are used for benchmarking multivariate functions. The functions are the known 2D functions named as *adjiman*, *brent*, *himmelblau*, and *threehump*. Definitions of these functions can be seen in [The20].

4.4 Universal Approximant Experiment

The experimental implementation of the Universal Approximant was performed at two different labs, ICN2 and IFAE, with very similar setups. The experimental setup is explained in Chapter 3.

The Quantum Fourier and the quantum UAT algorithms are both similar, but differ in the specific gate sequence, as seen in Eq. (4.16) and Eq. (4.18). Both consist of a series of R_Y and R_Z gates dependent on the independent variables and the optimized parameters. These parameters are $\vec{\theta}_i = (\omega, \alpha, \beta, \varphi, \gamma)$ for the i step of the Fourier series, and $\vec{\omega}_i$, α_i and β_i in the case of the UAT. The gate schematics of the Quantum UAT algorithm are shown in Fig. 4.13 a) as an example.

The optimal parameters used in the gate sequences are the ones obtained through the quantum simulation optimization described in Section 4.3.3. The functions are approximated in a specific range, which for the real and complex functions is $x \in [-1, 1]$. For a complete function evaluation, this range is discretized into 31 points distributed linearly along the range. Each individual sequence was averaged over 10,000 times for noise reduction.

The Y gates were implemented using Gaussian pulses with DRAG correction, as explained in Section 4.2.4.5, and rotations around the Z-axis were virtual Z-gates (see Section 4.2.4.3). The different phase of the Y-rotations are achieved

with different pulse amplitudes, for a fixed time pulse of 21 ns.

The reset protocol detailed in Section 4.2.4.4 is applied before each sequence to increase the fidelity and to allow a faster 10 μ s-repetition rate. The readout consisted of a 2 μ s pulse at f_r , thus measuring in amplitude. Rabi oscillations are used to calibrate the $|0\rangle$ and $|1\rangle$ readout voltage, together with the relation between pulse amplitude and Y -phase rotation. The Rabi calibration, together with a frequency calibration, as explained in Section 4.2.4.2, were performed prior the algorithm implementation. The complete experimental pulse sequence for qUAT is shown in Fig. 4.13 b).

The optimization of the gate sequence parameters was not successfully performed on the actual device. The main limiting factor was that each full function evaluation lasted around 10 s, due to the large averaging and the fact that the function had to be evaluated in several points along the x axis. The genetic algorithm CMA required several evaluations of the function to obtain the minimum, typically on the order of 10^6 , which lead to very large optimization times. The sequence time could be considerably reduced with the addition of a quantum limited amplifier, leading to single-shot readout. Still, with single-shot readout, several measurements should be performed to reduce sampling noise, with an overall reduction in function evaluation of 2 orders of magnitude.

Gradient-based algorithms were also tried, since they are known to lead to optimized results with a considerably reduced number of evaluations. However, these do not perform well in this experiment, probably due to noise affecting gradient search.

4.5 Results & Discussion

In order to prove the approximation capabilities of the Universal Approximant algorithms, the following function approximations were implemented:

- Four real single-variable functions defined in Eqs. (4.20) to (4.23).
- The sixteen combinations of these single-variable functions used for the real and imaginary components of a complex function.
- The four two-variable functions defined in Section 4.3.

All these functions have been approximated with both methods, Fourier and UAT, classically and with a quantum simulator, with the exception of two-dimensional functions, which can only be approximated with UAT. The experimental implementation of the quantum approximation has been realized for all the single-variable functions, four of the complex functions and the *himmelblau* two-dimensional function.

4.5.1 Single variable functions

Figure 4.14 shows all the single variable real functions considered in the study, as defined in Eqs. (4.20) to (4.23). In the plot, the case for $N = 5$ layers is

Single Variable Real Functions

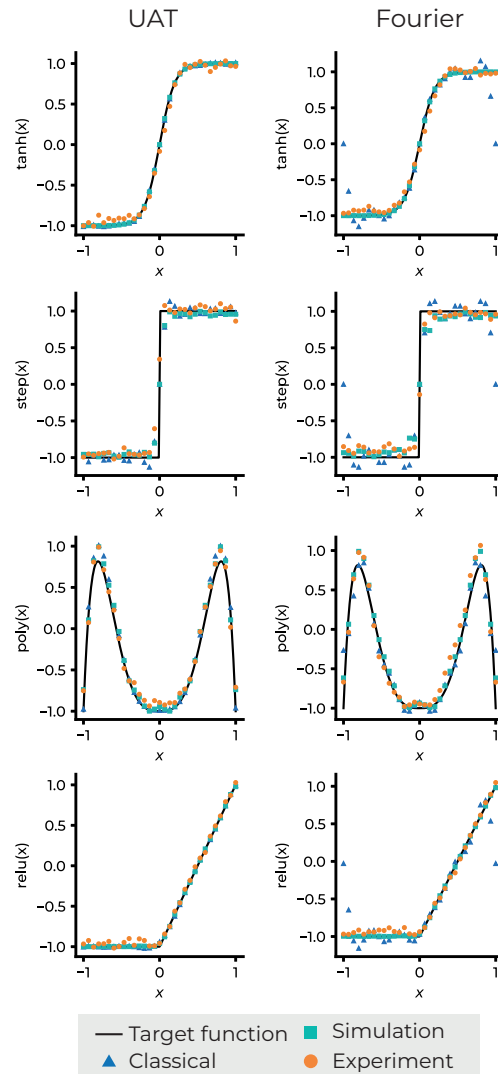


Figure 4.14: Single variable real functions reproduced by classical (dark blue triangles), simulation (turquoise squares) and experiment (orange squares). The target function is shown in black line. Four functions are reproduced, each in one column. The two approximation methods, Fourier and UAT are displayed in columns. All the results are for five layers.

displayed (see below for discussion on the number layers). The target function is displayed with a black-solid line and all three methods show good overall agreement: classical, quantum simulation and experiment. It is important to note that the function values have been rescaled to $[-1, 1]$ instead of $[0, 1]$ so

Optimal parameters	p_0	p_1	p_2	p_3	p_4	p_5	p_6	p_7	p_8	p_9	p_{10}	p_{11}
	-2.501	1.685	1.757	2.105	3.822	-1.788	-1.507	-4.640	0.430	1.875	5.038	-1.906
Rotational angles*	Z_0	Y_0	Z_1	Y_1	Z_2	Y_2	Z_3	Y_3				
	$p_0 + p_1x$	p_2	$p_3 + p_4x$	p_5	$p_6 + p_7x$	p_8	$p_9 + p_{10}x$	p_{11}				
$x = -0.5$	2.939	1.757	0.194	4.495	0.813	0.430	5.639	4.377				
$x = 0$	3.782	1.757	2.105	4.495	4.776	0.430	1.875	4.377				
$x = 1$	5.467	1.757	5.927	4.495	0.136	0.430	0.630	4.377				

* Angles between 0 and 2π

Table 4.1: Optimal parameters and angles obtained for the quantum approximation $\text{relu}(x)$ with qUAT and 4 layers. Above, the 12 parameters that define the rotational angles obtained through simulations. Below, the corresponding angles of the 8 rotations for three different values of x according to Eq. (4.18). Note that Y -rotations are not x -dependent, hence they are equal for all three x values.

that the output of $\langle \sigma_z \rangle$ is the approximated result.

The Fourier classical approximation relies purely on cosine terms and the approximations fail at the functions ends due their simple periodic nature. This method has the advantage over rest of allowing analytical calculations of the parameters instead of optimizing them, which makes the approximation considerably faster. In general, the classical UAT method outperforms the Fourier method, although sometimes the UAT fails to deliver a good approximation at the first optimization trial and has to be repeated.

The quantum simulation provides the best results of all methods. This is mainly due to the fact that the quantum version has more parameters than the classical versions. This allows a higher approximation capability for an equivalent number of layers. However, sampling errors can hinder the correct parameter optimization and, similar to the classical UAT method, both the quantum Fourier and UAT approximations sometimes output suboptimal parameters.

The experimental approximation using the optimal parameters obtained from the quantum simulation is, by definition, bounded by the quantum simulation results, up to some noise. The experimental methods show good agreement with the target functions for all the considered cases. There is no strong difference between Fourier and UAT, even taking into account the fact that the Fourier sequence has double the number of gates, implying an equivalent increase in time. Thus, the coherence time seems to be long enough and the pulse quality good enough for implementing all approximation methods successfully.

It is important to note that, in all method considered, not all functions are equally well approximated. The hyperbolic tangent and the step function have a similar shape, but the approximation quality differs, as the hyperbolic tangent is considerably better approximated than the $\text{step}(x)$. This difference shows that discontinuities make the approximation harder in all methods. Also, linear features such as the ones in $\text{step}(x)$ on the negative part or $\text{relu}(x)$ are difficult to reproduce. Finally, non-trigonometric characteristics, such as the polynomial nature of $\text{poly}(x)$, lead to discrepancies, especially at the extreme points at the maximum value of the function. However, these deviations, except for the classical Fourier, are minor and are well reproduced by the approximations.

N	p_0	p_1	p_2	p_3	p_4	p_5	p_6	p_7	p_8	p_9	p_{10}	p_{11}	p_{12}	...
1	2.35	-1.60	-1.57											
2	0.86	1.42	-1.97	-1.43	2.85	2.55								
3	0.82	1.57	16.92	2.99	-5.84	6.15	-1.41	8.88	-8.85					
4	-2.50	1.69	1.76	2.10	3.82	-1.79	-1.51	-4.64	0.43	1.87	5.04	-1.91		
5	-5.23	1.51	1.95	1.61	4.64	3.93	0.67	9.85	-0.21	-0.25	-4.55	-0.46	-3.58	...
6	-2.19	1.71	-2.30	-0.86	1.80	-1.83	-0.14	-1.22	1.25	0.92	5.48	1.56	0.92	...

Table 4.2: Optimal parameters for the quantum approximation $\text{relu}(x)$ with qUAT for different amount of layers.

Further analysis on the accuracy is discussed in Section 4.5.2.

An example of the parameters used for the sequence is shown in Table 4.1 for the $\text{relu}(x)$ function for the case of four layers and approximated via qUAT. A total of 12 parameters have to be obtained, since each layer has three parameters, as seen in Eq. (4.18). These parameters define the sequence together with the independent variable x . The Y -rotations are independent of x , so the pulses are the same. However, all Z -gates are different. The optimization protocol becomes more complicated as more layers are added. Each quantum Fourier step has 5 parameters (see Eq. (4.16)), compared to the 3 in qUAT.

4.5.2 Number of layers

Figure 4.15 shows χ^2 of the single-variable functions described in Fig. 4.14 for different number of layers. In general, χ^2 is reduced as N is increased, as predicted by each theorem.

In most cases, as mentioned in previous sections, the quantum simulation provides the best results for all the N range, except in the classical UAT approximation of $\text{poly}(x)$. The experimental implementation should not give a lower value of χ^2 than the quantum simulation, since the same optimized parameters are used.

As already noted in Section 4.5.1, the classical Fourier approximation requires a higher number of layers to reproduce similar results than the other methods. The cost function reduction with increasing number of layers is the smallest of all, and is systematically outperformed by their quantum counterparts and the UAT method.

The experiment performs considerably well. None of the functions reaches a value lower than 10^{-3} , which suggests that this value represents the noise plateau. It is expected that, for a large enough N , χ^2 increases. This would be caused either by longer sequences which expose the qubit state to decoherence a longer time, or by a larger amount of pulses which accumulate more error in the algorithm. In some functions, such as the UAT approximation of $\tanh(x)$, χ^2 is higher for larger N . However, since this is not a consistent trend compared to the other functions, the increase in χ^2 may be caused by statistical fluctuations and that the limit at which χ^2 starts increasing has not been reached.

Finally, $\tanh(x)$ is the best approximated function, probably because it does not show abrupt features. This would suggest that the functions with smoother

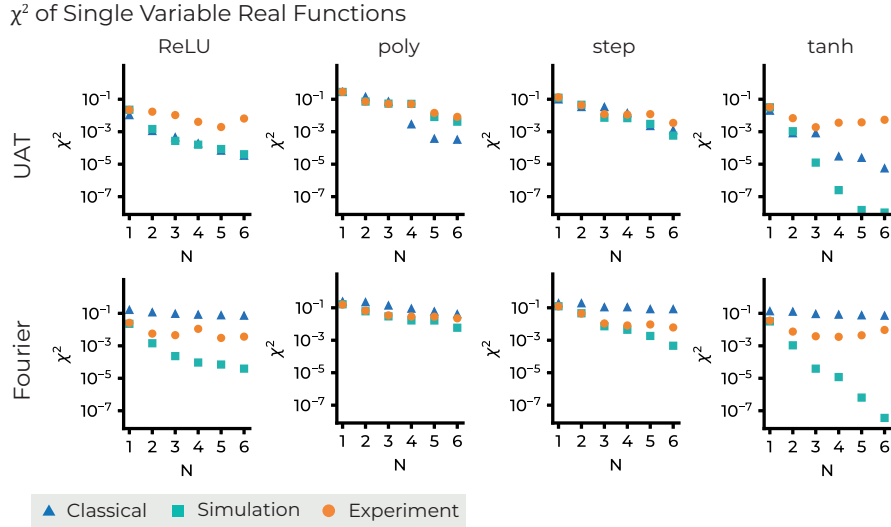


Figure 4.15: χ^2 for the single variable functions displayed in Fig. 4.14 as a function of the number of layers. Classical (dark blue triangles), simulation (turquoise squares) and experiment (orange squares) cost function is shown.

behavior are easier to approximate, as expected. Although not proven here, it is also expected that trigonometric functions are the easiest to reproduce due to the trigonometric functionality of quantum gates. X - and Y -gates have sinusoidal dependence on the pulse parameters, as can be seen from the Rabi oscillation expression, Eq. (4.6), thus naturally incorporating the trigonometric dependence on a possible input variable.

Table 4.2 shows the optimized parameters for the $\text{relu}(x)$ for the qUAT method for a varying number of layers. It is important to note that the unbounded optimization of the parameters sometimes output high values, such as $p_2^3 = 16.92$ in 3 layers for the angle of a Y rotation which, normalized to $[-\pi, \pi]$, is $p_2^3 = -1.92$.

Interestingly, the approximated values for $M - 1$ layers tend not to provide good estimates for the M -layer approximation. In the case of 2 and 3 layers, the first layers (parameters p_0 to p_2), do share strong similarities. However, as this similarity is not the common trend, sequential optimization, where optimized parameters in the $M - 1$ layer are used as initial parameters for the M layers, is not expected to yield better performance.

4.5.3 Two-variable functions

In Fig. 4.16, the himmelblau function is reproduced for the three approximation methods, along with the target function. In this case, only the UAT is considered, since no proof of the Fourier approximation for multivariate functions is

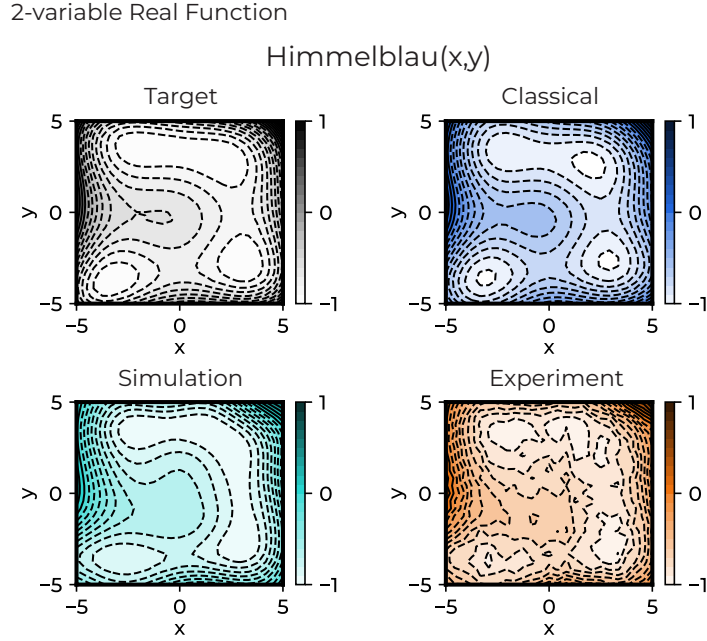


Figure 4.16: Himmelblau function approximation. In the top left panel, in grayscale, the original target function is displayed as a 2D map. Approximation with classical obtained parameters (top right, blue), quantum simulation obtained parameters (bottom left, turquoise) and experiment with quantum simulation obtained parameters (bottom right, orange) are shown. All the results are for five layers.

known.

The range of the independent variables has been extended to $[-5, 5]$ to capture some local maxima and minima in the studied range. The discretization of the range has been set at 25 points in each variable. The rest of the implementation is equivalent to the single-variable functions exposed in Section 4.5.1. The results shown in the figure are also for five layers.

In the case of the himmelblau, all the methods perform rather well, being the classical method the worst, since $\chi^2 = 2 \cdot 10^{-3}$, while the quantum simulation outputs $\chi^2 = 5 \cdot 10^{-3}$ and the experimental implementation $\chi^2 = 7 \cdot 10^{-3}$. The cost function evolution with N is similar to the single-variable case, with the experimental implementation reaching a plateau at around $N = 4$, while quantum and classical methods χ steadily decreasing with N .

4.5.4 Complex functions

The complex function approximation is shown in Fig. 4.17. The function shown is $z(x) = \tanh(5x) + j\text{relu}(x)$, although the four combinations between these two single-variable functions in the real and imaginary parts have been realized

Complex Functions

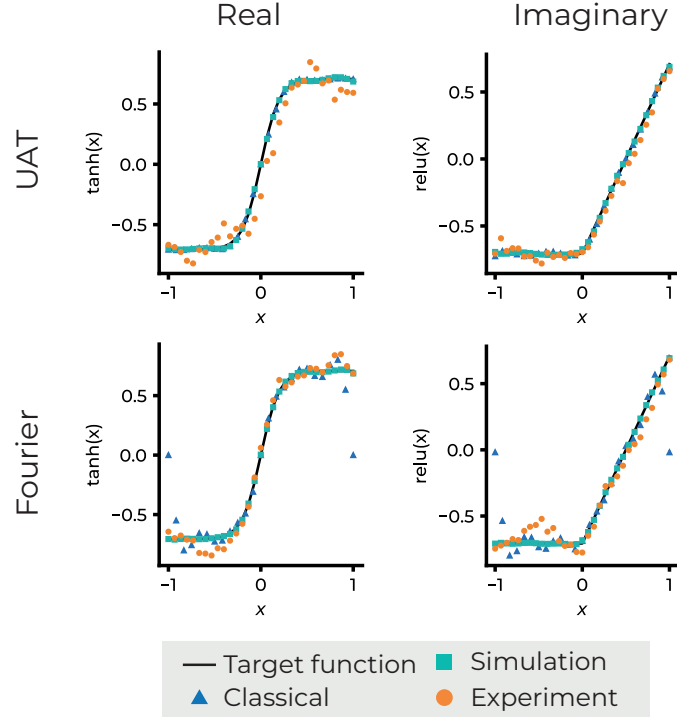


Figure 4.17: Complex function. In rows the two different approximation, Fourier and UAT; in columns the real and imaginary part of the function. The function is reproduced by classical (dark blue triangles), simulation (turquoise squares) and experiment (orange squares). All the results are for five layers. The target function is shown in black line.

experimentally as well. The twelve other combinations of the single-variable functions have been only simulated.

As shown in Fig. 4.17, the function values range from $[-1/\sqrt{2}, 1/\sqrt{2}]$, instead of the $[-1, 1]$ in the previous function to reflect that fact that the function is encoded in the both the X and the Y axes and the theoretical observables are $\langle \sigma_x \rangle$ and $\langle \sigma_y \rangle$. Otherwise, for the values where $\langle \sigma_x \rangle = \pm 1$, $\langle \sigma_y \rangle$ would be completely undetermined as these observables do not commute, and the value would always be $1/2$, and vice versa. Obviously, the function can easily be rescaled to the previous $[-1, 1]$ range.

The results are qualitatively analogous to the single-variable functions, as one would expect. From the experimental point of view, only an extra pulse is added to the sequence, where the $\langle \sigma_{x,y} \rangle$ population is rotated towards the Z axis, where the measurement is performed. This extra pulse should not introduce a considerable amount of error. The instrument effective resolution is reduced

because the population range does not go from -1 to 1 as before, but between $-1/\sqrt{2}$ and $1/\sqrt{2}$. Finally, this approximation requires double the amount of sequences since both axes have to be measured independently.

However, although the overall same behavior is observed in the complex and real single-variable functions, larger discrepancies can be seen in some regions, specially the negative values of x for the Fourier method. For this last case, the experiment $\chi^2 \approx 6e - 2$ is very close to classical Fourier, $\chi^2 \approx 8e - 2$ which is usually the poorest approximation. This discrepancy is expected to be caused by the fact that not every sequence is exposed equally to decoherence. Different sequences imply different pulses, and randomized benchmarking has only been optimized for the Clifford group, so it could be that gates further away from a Clifford gate have larger error. Moreover, decoherence mechanisms do not affect equally the points on the Bloch sphere. For example, the decay rate has a stronger effect for qubit states with larger $|1\rangle$ population. Finally, there may be some unknown systematic errors in the pulses that affect specific rotations differently.

4.6 Conclusions

Overall, in this chapter it is shown that the one-qubit circuit approximation works for all the chosen functions, regardless of its specific shape. The universal approximant algorithm for a single qubit does not represent any quantum advantage, but could be used in more complex algorithms as a subroutine. The extension of the algorithm to multiple qubits has not yet been studied, where entanglement could play a relevant role. There are known ways to introduce an independent variable inside an algorithm, which could make use of the quantum universal approximant as a classifier inside a larger algorithm. Moreover, the theoretical proofs can serve as the building block to further developments in quantum information theory.

Decoherence and gate uncertainty did not affect significantly the experimental implementation of the algorithm on the 3D transmon used, which validates the calibration and optimization methods shown in this chapter. The noise imposed an upper bound to the value of the cost function to $\sim 10^{-3}$, not allowing to get to better approximations.

The optimization of the gate parameters directly performed with the qubit could not be implemented due to the large amount of measurements required for the optimization protocol to converge, largely exceeding the timescales of experimental work. This could be improved with single-shot readout fidelity and better software optimization, along with the development of faster optimizers not based on gradients.

Finally, this chapter introduced the experimental techniques that will be similarly employed in subsequent sections.

Chapter 5

Engineering Flux Qubit Hamiltonians

DAVID LÓPEZ-NÚÑEZ, P. FORN-DÍAZ

Most of the work in this chapter is devoted to designing a quantum annealing processor prototype. The designed processor, whose schematic is shown in Fig. 5.1, will later be fabricated and measured, with the results shown on Chapter 6. Characterizing coherent flux qubits is the primary goal of this thesis, and the theoretical work to achieve such a goal is developed throughout this chapter.

A brief schematic of the processor prototype is provided in Section 5.1, where the main design decisions are explained. The flux qubits of the prototype are presented in Section 5.2. This section relies on the flux qubit theory from Section 2.3 to investigate the specific case of four-josephson C-shunted flux qubits (4J-CFQ) designed to perform coherent quantum annealing sequences. These qubits have been chosen mostly due to fabrication constraints, but other types of flux qubits could be potentially used. Then, prior to targeting other parts of the quantum analog processor, a comparison between the 4J-CFQ and alternative versions of flux qubits is made in Section 5.3.

The design of the processor requires more than the individual flux qubit simulations. Indeed, the qubit-resonator coupling required for both readout and control is defined in Section 5.4. Although the measured processor consists of an uncoupled qubit device, a qubit-qubit coupling is later analyzed in Section 5.5, as a coupled processor has also been designed, but not measured. Finally, Section 5.6 describes how to perform single- and two-qubit annealing schedules with the proposed design.

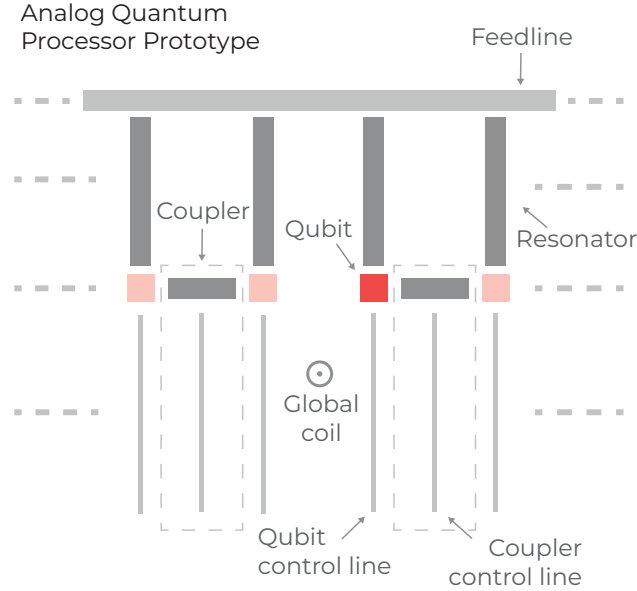


Figure 5.1: Quantum annealing processor prototype, which consists of flux qubits coupled dispersively to a readout resonator, this latter connected to a common feedline. The qubits are controlled via local flux control lines and by a global flux set by an external coil. Two prototypes are designed, either with uncoupled qubits or with coupled qubits in pairs. The qubits are coupled via a coupler whose flux is controlled by another local flux line.

5.1 Analog Quantum Processor Prototype

The primary ingredient of an analog quantum processor based on superconducting circuits are flux qubits* [Yan15; Or199]. These qubits, however, need to be controlled, measured and connected between them by different circuit elements, which combined shape the full quantum processor.

Figure 5.1 shows the schematics of the prototype of a quantum annealing processor that will be developed in the rest of the chapter and measured in Chapter 6. The primary goal of this prototype is to benchmark the qubit design developed throughout this chapter and the measurement setup.

The processor is based on flux qubits, which are controlled via two different flux sources. First, an external coil delivers a global flux bias, which is sufficient to control the uncoupled flux qubits. However, local qubit control lines are also added, which enable flux control at the single-qubit level.

A quarter-wave distributed resonator is coupled to each flux qubit, and also coupled to a coplanar waveguide feedline common to all resonators. These resonators allow both to measure the qubit in the energy basis and to control the qubit state with pulses. Typical coherence characterization techniques, such as

*There exist alternative designs based on transmons[Lec15], but those require quantum error correction and are thus out of reach.

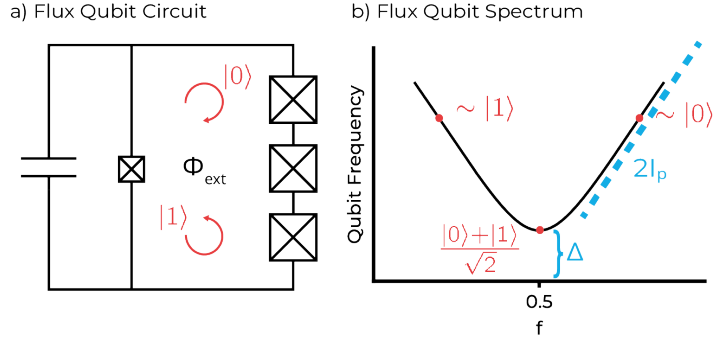


Figure 5.2: a) Four-Josephson junction C-shunted flux qubit circuit. The computational states correspond to the persistent-current states in different directions. b) Schematic spectrum of the 4J-CFQ, which is analogous to any flux qubit in the double-well regime.

T_1 and T_2 measurement, require quantum gates and dispersive readout (Section 2.6.1).

When dealing with single- or two-qubit annealing schedules, current-based readout (Section 2.6.2) is not indispensable to track the qubit state, as it is simple to differentiate between $|0\rangle$ and $|1\rangle$ by computing the local fluxes. Therefore, while many-qubit quantum annealer designs are expected to incorporate current-based readout, dispersive readout is more convenient for coherence characterization.

The initial processor consists of several uncoupled qubits. However, as shown in dashed box inside Fig. 5.1, a coupler has been also designed for another prototype with coupled devices. This coupled prototype has been designed, manufactured, but not measured at the time of the writing.

The specific physical design of the qubit circuit along with its measurement techniques and results is left for Chapter 6.

5.2 Coherent Flux Qubits Design

5.2.1 Four-Josephson Junction C-Shunted Flux Qubit

Figure 5.2a) shows the four-Josephson junction C-shunted flux qubit, which consists of three big junctions in series with a small junction, shunted by a large capacitance, C_{sh} . The 4J-CFQ is analogous to the traditional (three-Josephson junction) C-shunted flux qubit (3J-CFQ) more common in the literature [Yan15; Or199] (see Section 2.3.2). The addition of the extra junction does not change the shape of the spectrum, which is the same as any flux qubit in the double well regime, as seen in Fig. 5.2b).

The main modification introduced by an extra large junction is the change in the available values of α to have a localized double-well potential, with α being the ratio between the small and the large junctions critical current. For the

flux qubit to operate in the double-well regime needed for quantum annealing, $\alpha > 1/3$, compared to the 3J-CFQ, which is $\alpha > 1/2$. In general, $\alpha > 1/N$, where N is the number of large junctions.

The Hamiltonian of the 4J-CFQ is (omitting hats on operators)

$$\mathcal{H} = \frac{1}{2} \vec{q}^T \mathbf{M}^{-1} \vec{q} - E_J \left[\sum_{i=1}^3 \cos(\phi_i) + \alpha \cos \left(\sum_{i=1}^3 \phi_i + 2\pi f \right) \right], \quad (5.1)$$

where the first term corresponds to the charging energy of the circuit, with \vec{q} the charge variables at each node and \mathbf{M} is the capacitance matrix. The second term corresponds to the Josephson energy of the junctions. E_J refers to the Josephson energy of the big junctions, ϕ_i is the gauge-invariant phase difference around big junction i and f is the magnetic frustration defined as the ratio between the external applied flux, Φ_{ext} and the superconducting flux quantum, $f \equiv \frac{\Phi_{\text{ext}}}{\Phi_0}$.

The capacitive term on Eq. (5.1) is defined as

$$\frac{1}{2} \vec{q}^T \mathbf{M}^{-1} \vec{q} = 4E_C [\kappa_1 (n_1^2 + n_2^2 + n_3^2) + \kappa_2 (n_1 n_2 + n_2 n_3 + n_3 n_1)], \quad (5.2)$$

where E_C is the total capacitive energy of the circuit, the total capacitance being $C_\Sigma = \alpha C'_J + C_{\text{sh}} + C'_J/3$, with C'_J the big junction capacitance. n_i are the conjugate momenta of φ and corresponds to the number of excess Cooper pairs in each circuit node. $\kappa_{1,2}$ are constants of order unity relating the capacitances of the circuit (see Appendix B for exact definition of these constants).

From the circuit Hamiltonian in Eq. (5.1), a 2-level description near $f = 1/2$ can be made [Orl99]

$$\mathcal{H} = \frac{\hbar\Delta}{2} \sigma_X + 2I_P \Phi_b \sigma_Z, \quad (5.3)$$

with the qubit gap Δ and the persistent current I_P being the two parameters that define the behavior of the flux qubit.

5.2.2 Design Parameters

The Hamiltonian in Eq. (5.1) has four degrees of freedom, but the exact definition of the free parameters can be determined at will. A convenient set of free parameters chosen would be I_C , α , C_{sh} and C_J . The main reason is that they are closer to the fabrication values than working with energy terms such as E_J , E_C ... Thus, fabrication limitations on the parameters are more easily introduced:

- J_C is the junction critical current density, which together with the junction area, A , define the junction critical current, $I_C = J_C \cdot A$. For this value realistic limits are set of $[1, 5] \mu\text{A} \mu\text{m}^{-2}$ [Chi03; Yan15]. The upper bound ($5 \mu\text{A} \mu\text{m}^{-2}$) is limited by fabrication and reproducibility of very thin junction tunnel barriers by dynamical oxidation. Junctions with thicker tunnel barrier and low J_C can be easily obtained by static oxidation.

However, lower J_C will result in too low I_p , which sets a self-imposed lower bound of $1 \mu\text{A} \mu\text{m}^{-2}$ in order to design large qubit-qubit coupling energies.

- A_{big} and A_{small} are areas of the big and small junctions, respectively. Assuming that both junctions have the same J_C , the ratio between them is defined by α . Since α is order 1, both types of junctions can be fabricated using the same fabrication procedure. Sometimes, when ratios between different junctions are high ($\alpha \lesssim 1$), such as in SNAILs (Superconducting Nonlinear Asymmetric Inductive Element)[Fra17], the different junctions must be fabricated with different methods. Here, we impose ourselves the limits $[0.02, 0.2] \mu\text{m}^2$. The lower is set by fabrication feasibility, while the upper bound is set to limit the junction self-capacitance (next point).
- S_C is the capacitance density that, together with $A_{\text{big,small}}$, defines the junction self-capacitance, $C_J = S_C \cdot A$. This term is not easy to characterize and is highly dependent on the junction oxide thickness. According to other literature values[Yan15], we set it to $50 \text{ fF} \mu\text{m}^{-2}$.
- C_{sh} can be tuned across a very large range, from few to hundreds of fF, especially for single-qubit devices. In the processor design in this chapter, only a lower bound is set to 1 fF, which is already comparable to stray and junction capacitances in the circuit. Ideally, $C_{\text{sh}} \gg C_J$, so that the capacitance of the circuit is dominated by C_{sh} , thus making charging energy E_C more reproducible and reduce dielectric noise in the junction.

There are actually five fabrication parameters, although the Hamiltonian only has four. This is caused by the fact that three fabrication parameters define only two Hamiltonian parameters, $I_C = J_C A$ and $C_J = S_C A$, which enables fabrication to have some freedom to yield the same Hamiltonian. However, both S_C and J_C are connected through the junction oxide, limiting its independent control.

5.2.3 Annealing Constraints

The flux qubits studied in this chapter are intended to perform annealing schedules, which leads to some requirements on the circuit parameters:

- α . The most obvious constraint for the annealing processor is the lower bound of $\alpha > 1/3$ for the double-well potential to exist. Actually, α should be considerably above this value, otherwise whenever the external bias is not zero and the double-well is tilted, it will soon be that the two lowest states are localized in the same well, thus destroying the persistent-current description. Furthermore, $\alpha < 1$ as otherwise the qubit wavefunction would not be localized inside the double well and the qubit would be charge sensitive[Orl99]. This last is true when $C_{\text{sh}} = 0$, but $C_{\text{sh}} \neq 0$, $\alpha \lesssim 0.75$, but is highly dependent on the rest of parameters.

- The qubit frequency, ω_q , can dramatically change during the anneal. Moreover, as no transitions to the excited state are intended, its value is not so important in analog quantum computing. Usually, only the qubit frequency at the sweet spot, Δ , is considered.

The Hamiltonian of a single qubit in annealing is simplified to

$$\mathcal{H} = h_Z \sigma_Z + h_X \sigma_X, \quad (5.4)$$

where h_Z and h_X are the Ising terms. Since this processor has no σ_X control because Δ is not adjustable, a high h_Z must be achieved at the end of the anneal, so that $h_Z/h_X \gg 1$. To achieve such a large ratio, a low h_X helps, which in one qubit is $h_X = \Delta/2$. Thus lowering Δ is helpful for a successful annealing sequence.

On the other hand, a qubit with a low Δ suffers from thermal excitations, one of the main decoherence mechanism in quantum annealing, which is around 500 MHz for 25 mK, so a $\Delta > 0.5 \times (2\pi \times \text{MHz})$ would be required.

- I_p is the magnetic dipole which couples the qubit to flux noise, the most relevant source of decoherence for flux qubits. Then, a low I_p value is important for retaining coherence and control over the anneal schedule. However, it cannot be arbitrarily low, since h_Z is directly linked to this value and is therefore essential for the annealing schedules.

However, the coupling between qubits with SQUIDs (see Section 5.5), also depends directly on I_p . At the end of the anneal, the coupling terms, J , should be comparable to individual qubit terms h_Z . For that, large couplings are required, which are proportional to I_p^2 .

With all this into consideration, an I_p around 50 nA is targeted.

- A brief comment on anharmonicity, δ , is necessary, since it is a very important design requirement in digital quantum computing. Typically, δ is desired to be high so that there is no accidental excitations to higher states when applying control pulses to the qubit, which is not the case for annealing schedules. Nevertheless, flux qubits are inherently highly anharmonic, so the designs presented have high δ .

Related to this, higher levels do play an important role in coupling between the readout resonators and the qubit, which will be covered in Section 5.4.

5.2.4 Simulation Methods

The qubit parameters, mainly Δ and I_p , have been obtained by the standard method of exact diagonalization of the Hamiltonian on Eq. (5.1). A brief explanation of the method is given here, but more detailed explanation on how these simulations are performed is explained in Appendix C.

The Hamiltonian is written in its matrix form in the charge basis. The charge basis is used since the capacitance terms are diagonal in this basis, and

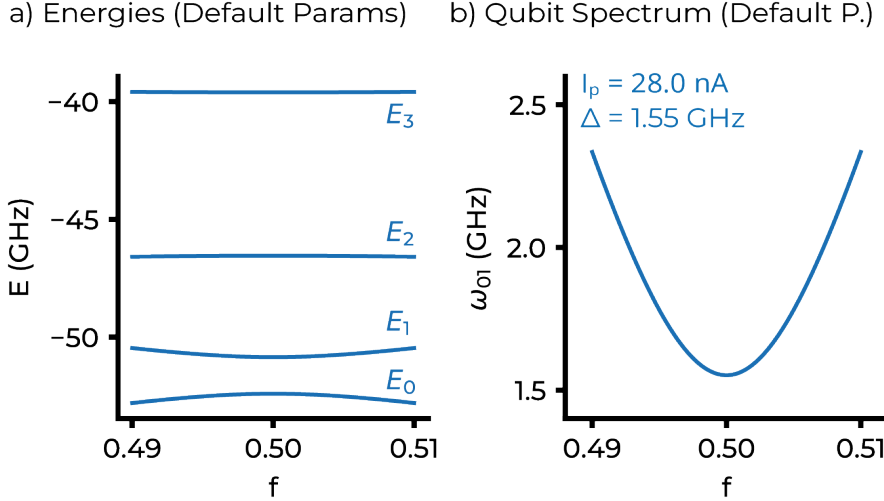


Figure 5.3: a) Flux qubit energies and b) flux qubit lower energy spectrum for default initial values.

the Josephson terms are mostly sparse, with only a few off-diagonal terms. The charge states are truncated at ± 8 number of charges in each node, after performing a convergence test. Then, an exact diagonalization is performed via Python SciPy library, and the qubit spectrum and eigenenergies are obtained. At $f = 0.5$, the qubit splitting directly gives the value of Δ .

The simulation is performed at various flux points around $f = 0.5$, as required for computing I_P , since it is related to $\partial\omega_{01}/\partial f$. The qubit frequency over the flux range is fitted to $\hbar\omega_q = \sqrt{(\hbar\Delta)^2 + (2I_p\Phi)^2}$ according to Eq. (5.3).

An example result from these simulations is seen in Fig. 5.3, where the energy spectrum is obtained for different flux points. The inherently large anharmonicity can be visually seen. By looking just at the first transition, both I_P and Δ can be obtained. A more detailed analysis of these results and the parameters used is given in the following section.

5.2.5 Qubit Simulations

The goal of the simulations explained in this section is to find the suitable values within the fabrication bounds defined in Section 5.2.2, that fulfill the annealing requirements defined in Section 5.2.3. Therefore, the qubit spectrum has been analyzed throughout the large parameter space to find an optimal configuration.

Instead of sweeping both A_{big} and A_{small} , only A_{big} has been swept along with α . This way, the potential energy shape was not qualitatively modified within the range of values attempted, and the simulations stayed in the double-well regime.

The variables explored are J_C , S_C , A_{big} , α , and C_{sh} . The dependence over

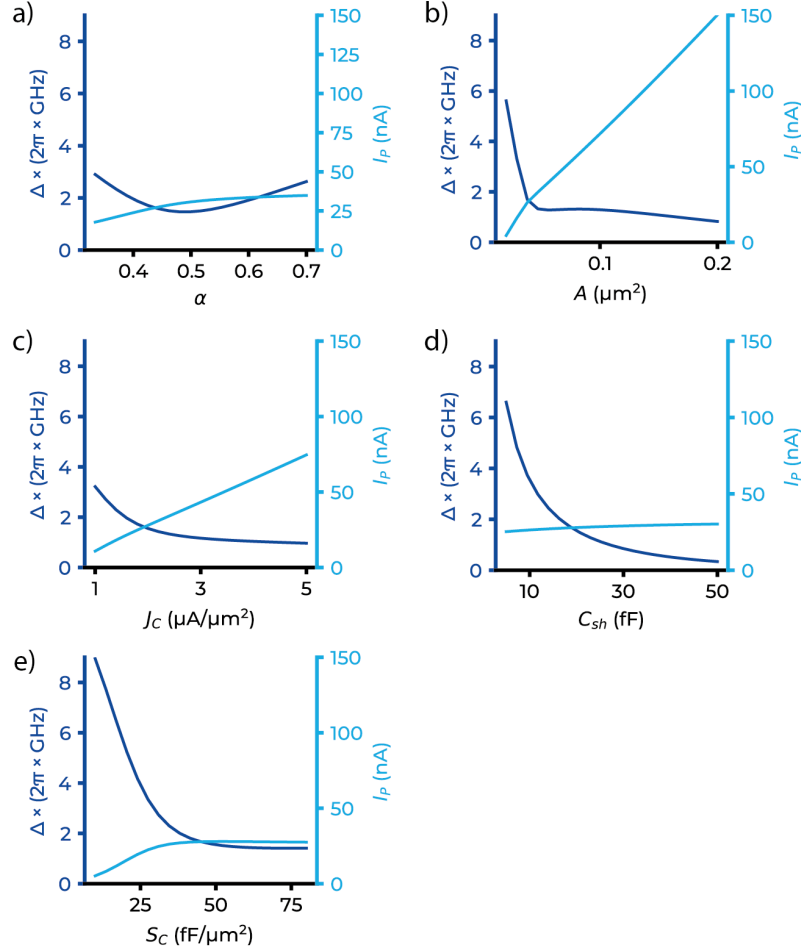


Figure 5.4: Qubit gap and persistent current with parameter sweeps. Each figure represents the qubit gap, Δ , on the left axis in dark blue, and the persistent current, I_P , on the right axis in light blue. All vertical axes are kept constant for easier parametrization. The parameters swept are: a) the small junction ratio, α ; b) the big junction area, A ; c) the critical current density, J_C ; d) the shunting capacitance, C_{sh} ; e) the junction capacitance per area, S_C .

S_C has been observed to see how sensitive is the qubit behavior to its value. However, the final design value has been set to $50 \text{ fF}/\mu\text{m}^2$.

Δ and I_P are the main outcomes of the simulations. Other important parameters, such as α and C_{sh}/C_J are already defined by the input Hamiltonian values. Moreover, although it is monitored, the anharmonicity is very large along all the parameter space. $E_J \gg E_C$ is also fulfilled, which ensures the qubit to be flux-dominated, thus highly insensitive to charge noise.

The original default values are shown in Table 5.1. These simulations correspond to $E_J/h = 42.0 \text{ GHz}$ and $E_C/h = 0.90 \text{ GHz}$ with this starting values.

α	A μm^2	S_C $\text{fF } \mu\text{m}^{-2}$	J_C $\mu\text{A } \mu\text{m}^{-2}$	C_{sh} fF	Δ $2\pi \times \text{GHz}$	I_P nA
0.45	0.04	50	2	20	1.55	28.0

Table 5.1: Default design values without optimization.

Δ is already in the desired range. However, I_P need to be increased. In Fig. 5.4 the behavior of both I_P and Δ for the different parameter sweeps is shown. In this figure, a single parameter is swept, while leaving the others in their default values. The same vertical limits have been set for easy comparison between different parameter sweeps.

Some conclusions can be extracted from these simulations:

- Higher I_C , which can be achieved either by increasing J_C or A_{big} , causes an increase in the persistent current as expected. Changing A_{big} also modifies the junction capacitance, so the trend is not as clean as with J_C . Inversely, this same increase in J_C and A_{big} causes a decrease in Δ . This is a consequence of the increase of the barrier height of the double well potential, which determines the coupling between the qubit states, and consequently Δ [Orl99].
- α contributes to a higher I_P , although at a smaller rate than I_C . Although Δ decreases with α at the initial values, it increases at larger values, where the wavefunction is delocalized and could be potentially susceptible to charge noise. In any case, the effect of α on Δ and I_P is considerably smaller than the other parameters in the available range. The minimum Δ with α is not at $\alpha = 1$ because $C_{\text{sh}}/C_J \approx 10$
- An increase in C_{sh} or S_C notably reduces the qubit gap, because the capacitance in the flux qubit plays a similar role as the mass in a harmonic potential. Larger mass localizes more the states, reducing the coupling between them, thus Δ [Ear18]. Although large C_{sh} is desired, the reduction in Δ is too large. For S_C around $50 \text{ fF}/\mu\text{m}^2$, the effect on Δ and I_P is low. However, the effect of S_C is not completely negligible, so further study should be performed to reduce or control its impact on the qubit parameters.

5.2.6 Final Design Parameters

In Table 5.2 the final design parameters are shown with the respective final target qubit properties. Two different designs have been used, which deviate only in C_{sh} . This results in two qubit designs with similar I_P 's but considerably different Δ . The flux qubit spectrum for these values can be seen in Fig. 5.5.

Both qubit designs have $\alpha = 0.55$, $A_{\text{big}} = 0.05 \mu\text{m}^2$ and $J_C = 2.18 \mu\text{A}/\mu\text{m}^2$. Qubit design #1 has $C_{\text{sh}} = 8 \text{ fF}$ and #2, $C_{\text{sh}} = 13 \text{ fF}$. I_P between 40 and 50 nA has been obtained for both designs, $I_P = 45.2 \text{ nA}$ for #1, and $I_P =$

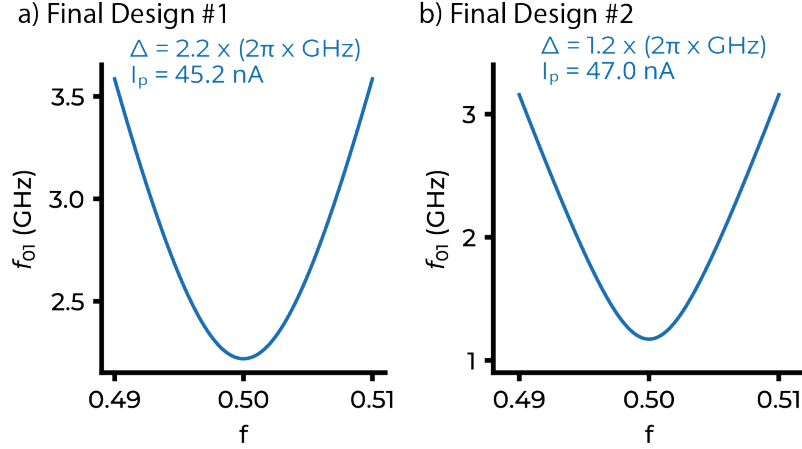


Figure 5.5: Lower qubit frequency for the two final designs, whose parameters are shown on Table 5.2. The value of Δ and I_P is also displayed for each qubit.

	α	A μm^2	S_C $\text{fF } \mu\text{m}^{-2}$	J_c $\mu\text{A } \mu\text{m}^{-2}$	C_{sh} fF	Δ $2\pi \times \text{GHz}$	δ $2\pi \times \text{GHz}$	I_P nA
#1	0.55	0.05	50	2.18	8	2.2	7.6	45.2
#2	0.55	0.05	50	2.18	13	1.2	7.5	47.0

Table 5.2: Final design values after parameter search is performed.

47.0 nA for #2. Both qubit gaps are above $1 \times (2\pi \times \text{GHz})$, which was a limit to not be limited by thermal excitations, although they are not completely suppressed. The qubit gaps are considerably different for both designs, with $\Delta = 2.2 \times (2\pi \times \text{GHz})$ in the design with $C_{\text{sh}} = 8 \text{ fF}$ and the second having a much lower $\Delta = 1.2 \times (2\pi \times \text{GHz})$ for $C_{\text{sh}} = 13 \text{ fF}$. This lower Δ would correspond to $P_e = 0.38$ if $T_{\text{eff}} = 100 \text{ mK}$, by using

$$P_e = \frac{1}{1 + e^{hf_q/k_B T}}, \quad (5.5)$$

so protocols to remove this thermal excitation may. Finally, a very large anharmonicity is reached, $\delta \gg \Delta$, for both designs.

With these two designs, it is possible to evaluate the impact of a low Δ on qubit coherence. However, a lower Δ is achieved by a higher C_{sh} , which reduces sensitivity to charge noise. Indeed, design #1 has $C_{\text{sh}}/C_J \approx 5$, which may be insufficient.

5.3 Comparison between flux qubit types

Four-Josephson junction C-shunted flux qubits (4J-CFQ) are actually not very common in the literature. Other flux qubits, such as the (three-josephson junction) C-shunted flux qubit[Web17] (3J-CFQ) or the rf-SQUID[Har09b] are much more common flux qubit designs. In this section, 4J-CFQ is compared to the 3J-CFQ and a C-shunted version of the rf-SQUID to evaluate whether they are completely analogous up to a renormalization of their variables.

All three qubits designs are also compared to an analytically simplified version of an N-junction flux qubit commonly used in the literature[Yan20]. The goal of this comparison is to evaluate whether the simulation requirements can be simplified to speed up the analysis, especially for many-qubit simulations.

However, as it is shown in Section 5.3.5, the N -junction approximation is not valid for the circuits in the current device target parameters, unlike previously reported in the literature. Moreover, all flux qubit types behave differently as function of circuit parameters, which means that no easy *swapping* between flux qubits can be performed from the circuit point of view.

5.3.1 Flux Qubit in the Symmetric Basis

The flux qubit Hamiltonian as expressed in Eq. (5.1) is very useful when comparing to the physical design and can be easily mapped to fabrication variables. However, this may not be the most useful description for an intuitive analysis how to compare it to other flux qubit types. For these other cases, it is more convenient to leverage the symmetries of the circuit and use symmetrical variables.

A new basis is defined in terms of the original variables, which are the phase differences across each of the junctions, φ_i . For a general number of big junctions, N , the new basis is

$$\begin{aligned}\phi &= \sum_i \phi_i, \\ \xi_\mu &= \sum_m W_{\mu m} \phi_m,\end{aligned}\tag{5.6}$$

where the sums over latin indices goes from 1 to N , and over greek indices from 1 to $N - 1$. The matrix coefficients $W_{\mu m}$ are

$$W_{\mu m} = \sqrt{\frac{2}{N}} \cos \left[\frac{\pi \mu (m - \frac{1}{2})}{N} \right].\tag{5.7}$$

The main variable, ϕ , is now the sum of the phase differences across all the big junctions, which represents the *sum mode*. The other variables, ξ_μ vanish when $\phi_1 = \phi_2 = \phi_3$, which happens at the minima of the potential energy. ξ_μ represent the *difference modes*. The most relevant physics of the circuit takes place in the sum mode, where, for example, the double-well potential is defined.

This mode can easily be compared among qubits. For large arrays of junctions, the difference modes are known to be negligible [Yan20],

For the 4J-CFQ, the exact expression of these new variables is

$$\begin{aligned}\phi &= \phi_1 + \phi_2 + \phi_3 \\ \xi_1 &= \frac{1}{\sqrt{2}}(\phi_1 - \phi_3) \\ \xi_2 &= \frac{1}{\sqrt{6}}(\phi_1 - 2\phi_2 + \phi_3).\end{aligned}\tag{5.8}$$

The new Hamiltonian in this basis is

$$\begin{aligned}\mathcal{H}_4 &= 4E_C n^2 + 4E'_C (n_1'^2 + n_2'^2) \\ &\quad - E_j \left[\sum_{i=1}^3 \gamma \cos(\phi/3 + \sum_{\mu} W_{\mu i} \xi_{\mu}) + \cos(\phi + 2\pi f) \right].\end{aligned}\tag{5.9}$$

The first two terms of the Hamiltonian correspond to the charge energy terms and the rest are the Josephson energy terms. $E_C = \frac{e^2}{2C_{\Sigma}}$ is the total capacitive energy in the circuit, with $C + C_{sh} + \frac{\gamma}{N}C$, and E'_C is now the charging energy of a big junction. $\gamma \equiv \frac{1}{\alpha}$ will now be used instead of α as it is more convenient for future comparisons. n is the conjugate moment of ϕ , and n'_{μ} is the conjugate moment of ξ_{μ} . The Josephson energy, $E_j = \alpha I_C / (2\pi)$ is the Josephson energy of the small junction, unlike previous E_J which was the Josephson energy of the large junctions.

In this new form of \mathcal{H} in Eq. (5.9) the sum mode behavior is clearly identified. Adding or subtracting large junctions in this Hamiltonian is an easy task and the main mode suffers minor modifications, which allows treating N as an extra variable. Moreover, the capacitive terms are better separated now and clearly separated between the sum and the difference modes.

This new basis provides a convenient notation to compare different flux qubits, since all flux qubits share the same sum mode term, up to leading order of the Taylor expansion of the cosine terms. If the difference modes are neglected, all flux qubits are equivalent up to this leading order if they have the same C_{Σ} , E_j and γ/N .

The main drawback is that the basis construction for simulation is not easy in this scenario. Natural limits of maximum n on the junctions nodes are not easily transferred to this basis (see Section 5.3.5). Furthermore, the relation between fabrication parameters and the Hamiltonian is not straightforward and physical constraints cannot be so directly imposed.

5.3.2 3-Junction C-Shunted Flux Qubit

Traditional C-shunted flux qubits (3J-CFQ) contain only two big junctions and a small one, as shown in Fig. 5.6 a). This qubit has already been described in Section 2.3.2. The behavior of 3J-CFQ is conceptually analogous to 4J-CFQ but, by having only two big junctions, the qubit is described with two variables,

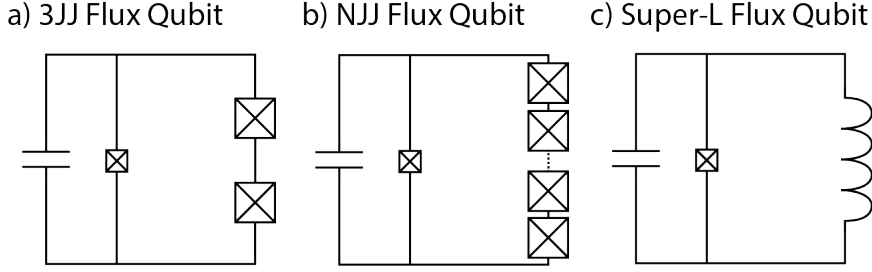


Figure 5.6: Different flux qubit designs compared with the 4J-CFQ design.

which considerably simplifies the analysis, the fabrication, and the simulation. In this qubit, with $N = 2$, the limit for the double-well regime is $\gamma < 2$ (or $\alpha > 1/2$).

The Hamiltonian in the symmetric variables is

$$\begin{aligned} \mathcal{H}_3 = & 4E_C n^2 + 4E'_C n'^2 \\ & - E_J \left[\sum_{i=1}^2 \gamma \cos(\phi/N + W_i \xi) + \cos(\phi + 2\pi f) \right], \end{aligned} \quad (5.10)$$

with $N = 2$. Exact definition of ξ and W_i can be computed with Eq. (5.6) and Eq. (5.7) respectively.

The Hamiltonians of 4J-CFQ and 3J-CFQ are very similar, but the role of an extra big junction is not straightforward in the low N regime. It is uncertain which value of N sets this low N regime.

5.3.3 N-Junction C-Shunted Flux Qubit

When extending the definition of flux qubit to an arbitrary number of junctions, N becomes an extra free parameter, as shown in Fig. 5.6 b). In this scenario, the relevant ratio for this N -junction C-shunted flux qubit (NJ-CFQ) between junctions is γ/N , instead of γ or α .

The Hamiltonian for an arbitrary N is

$$\begin{aligned} \mathcal{H}_N = & 4E_C n^2 + 4E'_C \sum_{\mu}^{N-1} n_{\mu}^2 \\ & - E_J \left[\sum_{i=1}^N \gamma \cos(\phi/N + \sum_{\mu}^{N-1} W_{\mu i} \xi_{\mu}) + \cos(\phi + 2\pi f) \right]. \end{aligned} \quad (5.11)$$

It has been shown that for large number of junctions the difference modes contribute negligibly to the final result, as they behave as a linear inductance.

Indeed, superinductors based on disordered superconductors [Mal18], such as granular Aluminum, are thought to be formed by large arrays of junctions. When this is the case, the Hamiltonian can be simplified to

$$\mathcal{H}_N \approx \mathcal{H}_{N,1V} = 4E_C n^2 - E_j [\gamma N \cos(\phi/N) + \cos(\phi + 2\pi f)] . \quad (5.12)$$

This is the single-variable simplification of the flux qubit Hamiltonian based only on the sum mode.

5.3.4 C-Shunted Superinductance Flux Qubit

When N is large, the first term in brackets of Eq. (5.12) can be expanded through Taylor formalism and the Josephson-array inductance is recovered

$$\mathcal{H}_N \approx \mathcal{H}_{SI} = 4E_C n^2 + E_j \left[\frac{\gamma}{2N} \phi^2 - \cos(\phi + 2\pi f) \right] , \quad (5.13)$$

where one could define the inductance energy as $E_L \equiv \frac{\gamma}{N} E_j$. The subscript in \mathcal{H}_{SI} represents that this is a SuperInductance C-shunted flux qubit (SI-CFQ).

The circuit in Fig. 5.6 c) corresponds to the SI-CFQ and is equivalent to either a fluxonium qubit [Man09] or to a rf-SQUID. SI-CFQ could indeed be considered as a capacitively shunted rf-SQUID. When working in the same energy scales as the previous qubits, SI-CFQ can be a perfectly suitable circuit for performing quantum annealers. SI-CFQ has the benefit of being inherently single-variable, which simplifies mathematical analysis.

The drawback is that superinductors are not typically available for fabrication in many labs. Achieving similar values with geometric inductance requires very large loops, which is detrimental for noise [Per21]. Finally, this superinductance can be achieved with very large number of junctions[Man09].

5.3.5 Comparison Between Flux Qubits

As commented before, performing the simulation in the symmetric basis, $|n_s\rangle$, is more complex because this is not the natural basis of the system. When imposing a maximum number of charges in the charge basis, $|n\rangle$, it does not translate directly to this basis. For example, if maximum number of charges is 10, then the maximum charge in the symmetric variable, which is $n = n_1 + n_2 + n_3$, would be 30. However, in this specific case, both difference charge variables are set to 0, because these are always 0 whenever $n_1 = n_2 = n_3$. In general, the number of charges in the symmetric basis cannot take arbitrary values, but they are all correlated, thus making basis construction more complex.

Finally, the four types of flux qubits commented in previous sections can be compared: 4J-CFQ, 3J-CFQ, NJ-CFQ and SI-CFQ. The comparison between qubit types is performed by making sure that the symmetric mode is equivalent in all of them up to leading order. That is, E_C is adjusted to be the same, which usually means tuning the shunting capacitance of the individual qubit so that the total capacitance, C_Σ , is equal. Also, γ/N is the same in all designs, along

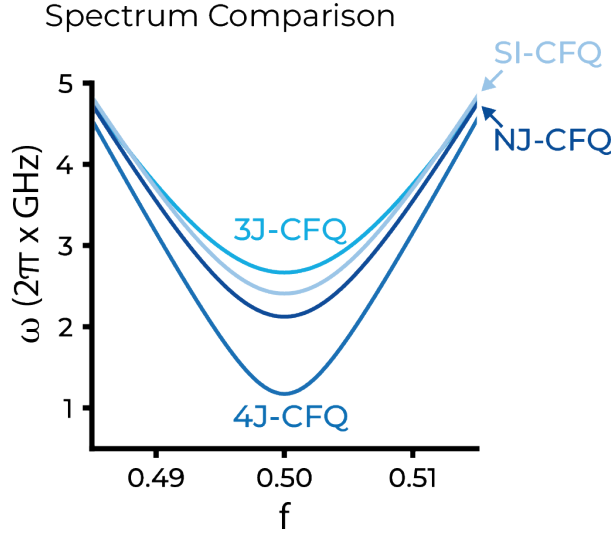


Figure 5.7: Comparison between the qubit spectrum of the four different flux qubit Hamiltonians considered in Section 5.3.

with the small junction Josephson energy, E_j . Thus, the only difference between the Hamiltonians comes from the difference modes and sub-leading order of the symmetric mode.

Fig. 5.7 shows clearly that all the flux qubits behave differently, where Δ can vary as much as $> 100\%$ among them and I_P is also noticeably different. This figure shows just a snapshot, but the qubits behave differently in general among all the parameter space explored. Moreover, the sorting of the qubit gaps and persistent currents is not consistent, with the lowest Δ qubit not always being the 4J-CFQ. In general, all qubits have a similar behavior and can be used as flux qubits, but with very different qubit parameters.

An important result is that the single-variable approximation, such as previously reported, is not valid in our 4J-CFQ design. The difference modes play such an important role that cannot be neglected.

5.3.6 Comparing potential energies

An analysis on the potential energy for the symmetric variable has been performed in order to understand if the potential energy had a relevant role on the difference between the flux qubits. A comparison of the potential of the sum mode is shown in Fig. 5.8 for the 4J-CFQ, 3J-CFQ and SI-CFQ. The potential energy of the simplified version is not analyzed here, as the comparison is focused on full Hamiltonian circuits.

The sum mode potential energy are defined from the Josephson terms of

Potential Comparison

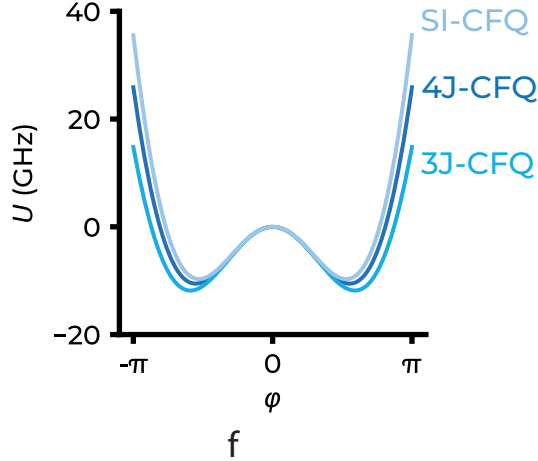


Figure 5.8: Comparison between the potential of three different qubit types.

their respective Hamiltonians neglecting the difference variables, ξ_μ

$$U_{4J} = -E_j (3\gamma \cos(\phi/3) + \cos(\phi + 2\pi f)) , \quad (5.14)$$

$$U_{3J} = -E_j (2\gamma \cos(\phi/2) + \cos(\phi + 2\pi f)) , \quad (5.15)$$

$$U_{SI} = E_L \left(1 - \frac{\phi^2}{2} \right) - E_j \cos(\phi + 2\pi f) . \quad (5.16)$$

These potential energies share the same E_j , which means that the last term is equivalent for all of them. The first term is only equal up to the quadratic term in the Taylor expansion, which correspond to the first term in U_{SI} . The difference in the potential energies comes, thus, from this higher order terms from the potential which are more important as it deviates from $\phi = 0$.

The two main features from the potential energies in Fig. 5.8 are the barrier height and the location of the minima. In order to check if any of the characteristics had any role on the observed difference in qubit spectra, an extra refactoring was applied on γ , so that the potential of the 3J-CFQ and the SI-CFQ was changed by modifying their γ to a γ' to match the minima location or the barrier height of the 4J-CFQ.

In Figs. 5.9 and 5.10 the effect of this modification of the potential energy can be seen for matching the minima location and the barrier height, respectively. The left panels show how the potential of the 3J-CFQ is modified. SI-CFQ potential has been modified similarly. In the right panels, the comparison between all three qubits is depicted, showing the spectrum before and after the modification.

In all cases the modification of U with the new γ' brought closer the spec-

Changing Potential Minima Location

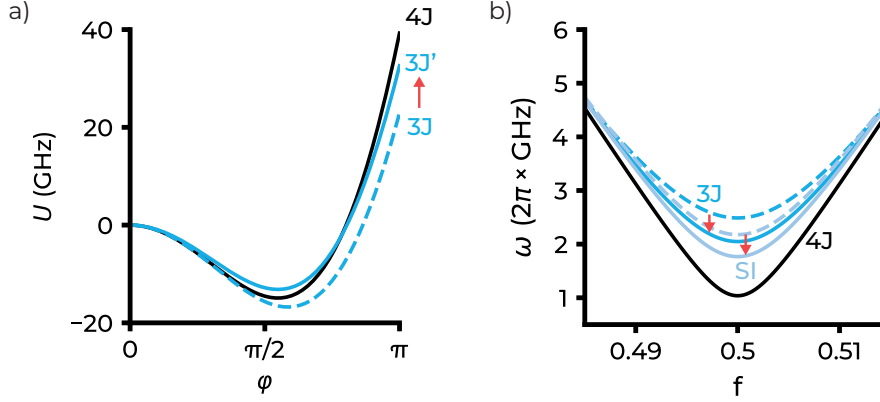


Figure 5.9: a) Positive part of the potential of the 4J-CFQ is shown in black. In blue dashed line the potential of 3J-CFQ is shown as used when comparing the flux qubits. In blue line the potential of 3J'-CFQ, when adapting γ' so that the minima are placed at the same location. b) Spectrum of the 4J-CFQ (black), 3J-CFQ (dashed blue) and SI-CFQ (dashed light blue) are shown as in Fig. 5.7. The 3J'-CFQ and SI-CFQ with the modified potential are shown in solid lines.

tra, but their numerical values still differ significantly. Therefore, the potential energy is not the only relevant aspect of this difference.

In order to discard the difference modes, a closer look to these modes is needed. If the plasma frequency of the difference modes is brought higher, it will probably mean that its contribution is locked to their lowest state and, thus, can be traced out. More work is required in order to understand the role of all the different modes in the circuit.

5.4 Qubit-Resonator System

The qubit readout design depends on which measured operator is desired. In digital quantum computing, measurements are performed in the energy basis to determine qubit population. There, a dispersive readout scheme is used, where resonator energy shift directly represent qubit state population. In quantum annealing, the relevant measurement basis is the persistent current basis to determine the qubit magnetization. Thus, a current-based readout is typically designed.

For the prototype studied in this work, whose main goal is to benchmark qubit coherence, it was more convenient to have the dispersive readout in place, as already commented in Section 5.1. Both control and readout pulses can be sent through the same resonator line. Moreover, dispersive readout is considerably simpler than persistent-current readout, since the latter typically requires

Changing Potential Barrier Height

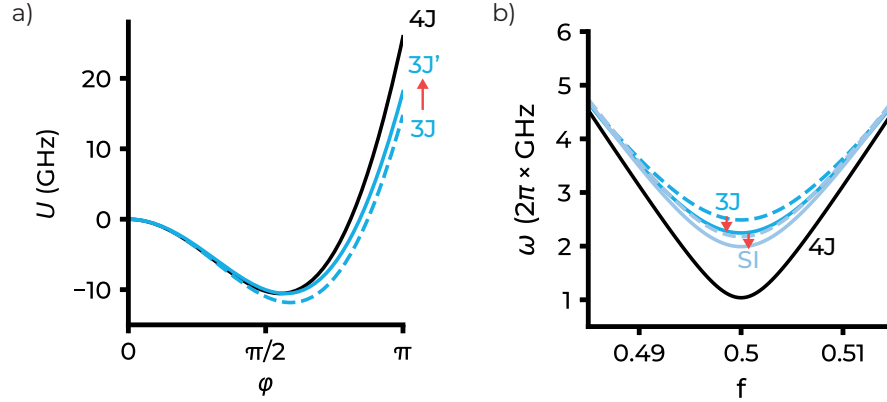


Figure 5.10: a) Positive part of the potential of the 4J-CFQ is shown in black. In blue dashed line the potential of 3J-CFQ is shown as used when comparing the flux qubits. In blue line the potential of 3J'-CFQ, when adapting γ' so that the potential barrier height is the same. b) Spectrum of the 4J-CFQ (black), 3J-CFQ (dashed blue) and SI-CFQ (dashed light blue) are shown as in Fig. 5.7. The 3J'-CFQ and SI-CFQ with the modified potential are shown in solid lines.

Qubit-Resonator Circuit

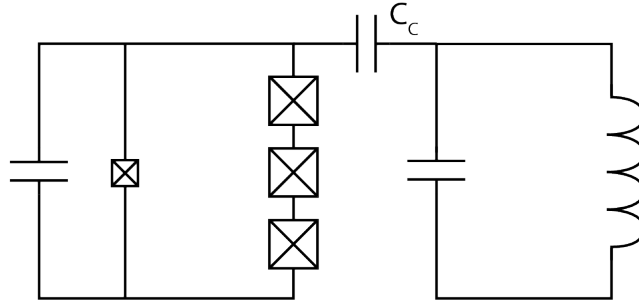


Figure 5.11: Qubit-Resonator Circuit

a resonator terminated with a SQUID[Gro20], requiring extra flux control.

5.4.1 Readout Circuit

In the design used, the flux qubit is coupled capacitively to a resonator as shown in Fig. 5.11. The resonator is a quarter-wave distributed resonator, modeled in the circuit as an LC resonator.

The exact derivation of the Hamiltonian can be found in the Appendix C.

A simplified explanation is given here. The Hamiltonian of the qubit-resonator system can be expressed as

$$\mathcal{H} = \mathcal{H}_q + \mathcal{H}_R + \mathcal{H}_C, \quad (5.17)$$

where \mathcal{H}_q , \mathcal{H}_R , and \mathcal{H}_C are the qubit, resonator, and coupling resonator respectively. \mathcal{H}_q is conceptually equivalent to Eq. (5.1), where some terms are loaded by the presence of the resonator. The resonator Hamiltonian is that of a simple harmonic oscillator, $\mathcal{H}_R/\hbar = \omega'_R (a^\dagger a + 1/2)$, where ω'_R is the resonator loaded resonance frequency. The coupling Hamiltonian is given by

$$\mathcal{H}_C = 2e \left(\frac{\Phi_0}{2\pi} \right) \frac{n_1 + n_2 + n_3}{m_c} p_R, \quad (5.18)$$

where n_1 , n_2 and n_3 are the charge number operators of the big qubit junction nodes, and p_R is the resonator momentum, related to the resonator electric field. m_c is an effective mass that can be expressed as

$$m_c = \left(\frac{\Phi_0}{2\pi} \right)^2 \eta C_C, \quad (5.19)$$

where η is a dimensionless parameter that depends on the capacitances of the system. Exact values of all the parameters are found on the Appendix C.

5.4.2 Dispersive shift derivation

Whenever the coupling is weak enough compared to both ω_q and ω_R , the system can be approximated as two separated system with a dispersive coupling, χ ,

$$\mathcal{H}'/\hbar = (\omega'_R - \chi\sigma_Z) a^\dagger a - \frac{\omega'_q}{2} \sigma_Z, \quad (5.20)$$

where ω'_R and ω'_q are the loaded resonator and qubit frequencies, respectively. In the dispersive regime, the resonator frequency is modified when the qubit changes state by a factor 2χ .

To obtain the dispersive approximation of Eq. (5.20), the qubit-resonator Hamiltonian on Eq. (5.17) is rewritten as $\mathcal{H}_0 + V$. The first term is the uncoupled Hamiltonian, $\mathcal{H}_0 = \mathcal{H}_R + \mathcal{H}_q$, and $V = \mathcal{H}_C$ is the coupling term, considered as a small perturbation. Since this term is small compared to \mathcal{H}_0 , a Schrieffer-Wolff transformation can be performed, which consists of transforming this small perturbation into the original uncoupled basis. The final Hamiltonian, after reduction of the flux qubit to the lowest two levels, is Eq. (5.20).

In the flux qubit-resonator system studied here, the dispersive shift obtained by this transformation is defined as

$$\chi = \frac{1}{2} \left(\sum_{j \neq 0} (\chi_{0j} - \chi_{j0}) - \sum_{j \neq 1} (\chi_{1j} - \chi_{j1}) \right). \quad (5.21)$$

The terms χ_{ij} are

$$\chi_{ij} = \frac{|g_{ij}|^2}{\omega_{ij} - \omega_R} \equiv \frac{|g_{ij}|^2}{\Delta_{ij}}, \quad (5.22)$$

where ω_{ij} is the qubit transition frequency between levels j and i keeping the corresponding sign. g_{ij} is the coupling element matrix for the qubit, defined as

$$g_{ij} \equiv \langle i | \kappa_C (n_1 + n_2 + n_3) | j \rangle, \quad (5.23)$$

where $\kappa_C = \frac{2e}{m_c} \left(\frac{\Phi_0}{2\pi} \right)$ is the coupling constant obtained from Eq. (5.18), and the states $|i\rangle$ are the uncoupled qubit eigenstates. Follow Appendix C for more details on this derivation.

By looking at Eq. (5.21), it can be noticed that higher qubit energy states can have a strong effect on the dispersive shift if a qubit transition frequency is close to ω'_R , since the denominator in Eq. (5.22) will be smaller. However, this applies only to the first excited states, since the terms ω_{0i} and ω_{1i} for $i > 3$ are rapidly detuned from the resonator frequency, thus vanishing for very high energy qubit states. However, g_{ij} goes up for these states, so this requires manual truncation or renormalization techniques[Par17].

5.4.3 Qubit-Resonator Simulations

In order to simulate the qubit-resonator system, a first separate treatment is performed in the uncoupled Hamiltonian. Full coupled system analysis is very costly computationally and can lead to very large matrices that Python may not handle. Moreover, when the subsystems are weakly coupled, a separate treatment is justified.

For obtaining the qubit states, the same procedure as in Section 5.2.4 is followed, after modifying the parameters by the resonator loading as in Eq. (5.18). \mathcal{H}_R has exact harmonic solutions, so analytical solutions using Hermite polynomials are used.

In order to simulate the coupling part of the Hamiltonian, the full system is described in the uncoupled basis. The basis states $|\Psi\rangle$ are constructed using the lowest energy states of the two subsystems. These states are defined as

$$|\Psi\rangle = |\psi_q\rangle \otimes |k\rangle, \quad (5.24)$$

where $|\psi_q\rangle$ are the qubit lowest energy eigenstates and $|k\rangle$ are the harmonic oscillator basis states.

\mathcal{H}_c in Eq. (5.18) can be exactly computed in the basis defined in Eq. (5.24). The qubit states have been diagonalized in the charge basis, so their charge basis representation is available. Then, the n_i operators are diagonal and can be easily computed. For the harmonic term, the harmonic oscillator momentum definition is known,

$$p_R = i \sqrt{\frac{\hbar m_R \omega_R}{2}} (a^\dagger - a), \quad (5.25)$$

where m_R is an effective mass dependent on the system capacitances.

The matrix representation of H_C is not sparse, and all terms are populated indeed. The 10 lowest eigenstates of the qubit and the 5 lowest harmonic modes are used, thus obtaining a 50×50 matrix. This matrix, together with diagonal \mathcal{H}_0 , describes now the full system.

Once the full-system matrix is diagonalized, it is useful to map the new coupled states to the uncoupled basis (see Fig. 5.12). This way, states can be numbered n, m , where n is the number of photons in the resonator and m is the qubit state in the uncoupled system. χ can be obtained by calculating the difference between f_r when the qubit is $|1\rangle$ and in $|0\rangle$. This can be expressed as

$$\hbar\chi = \frac{1}{2} [(E_{1,e} - E_{0,e}) - (E_{1,g} - E_{0,g})]. \quad (5.26)$$

χ can also be computed by solving Eq. (5.21), which is not needed for the full system circuit to be diagonalized, and can be obtained with the uncoupled results, but may require going up to higher qubit states to converge.

5.4.4 Results

In Fig. 5.12 the system spectrum is shown. Panel a) shows the bare qubit spectrum, where we can identify the $0 - 1$ and the $0 - 2$ transitions. The transitions are labelled according to the number of excitations they contain, thus $0 - 1$ is labelled as 1, and the $0 - 2$ as 2. In panel b), the uncoupled Hamiltonian spectrum is displayed. The previous qubit states can now be identified as $1 \otimes 0$ and $2 \otimes 0$, since they correspond to qubit excitations with no photon in the resonator, where the \otimes symbols represent that they are uncoupled transitions. The two pure photon states are easily identified since there is no flux dependence. Then, the last state in the plot contains an excitation in both the qubit and the resonator.

In panel c), the full coupled spectrum is shown. Visual inspection is enough to map between the uncoupled and coupled spectra. Now, the states are labelled in terms of the original uncoupled system. The coupling is very small compared to the transition frequencies, and can only be seen in the avoided level crossing, as shown in the inset.

The avoided level crossing provides the coupling between the first qubit level and the resonator by measuring the vertical distance between the levels, which is $g_{01} \approx 50 \times (2\pi \times \text{MHz})$ (note that g_{01} is flux-dependent). By applying Eq. (5.22), an estimate of the dispersive shift at the flux bias point can be performed, only taking into account this level, $\chi_{01} \approx 0.5 \times (2\pi \times \text{MHz})$.

In Fig. 5.13, the total dispersive shift is shown along with the individual χ_{ij} contributions. Panel a) shows the dispersive shift in the flux range that will be used during quantum annealing, and panel b) shows a wider range, coinciding with the one shown in Fig. 5.12.

The left panel clearly shows that the biggest contribution to the dispersive shift is χ_{12} , whose effect has a different sign and half the amplitude, as expressed in Eq. (5.21). This effect is understandable since $\omega_{12} \approx 9.5 \times (2\pi \times \text{GHz})$ is the closest transition to the resonator frequency, $\omega'_R \approx 7.8 \times (2\pi \times \text{GHz})$.

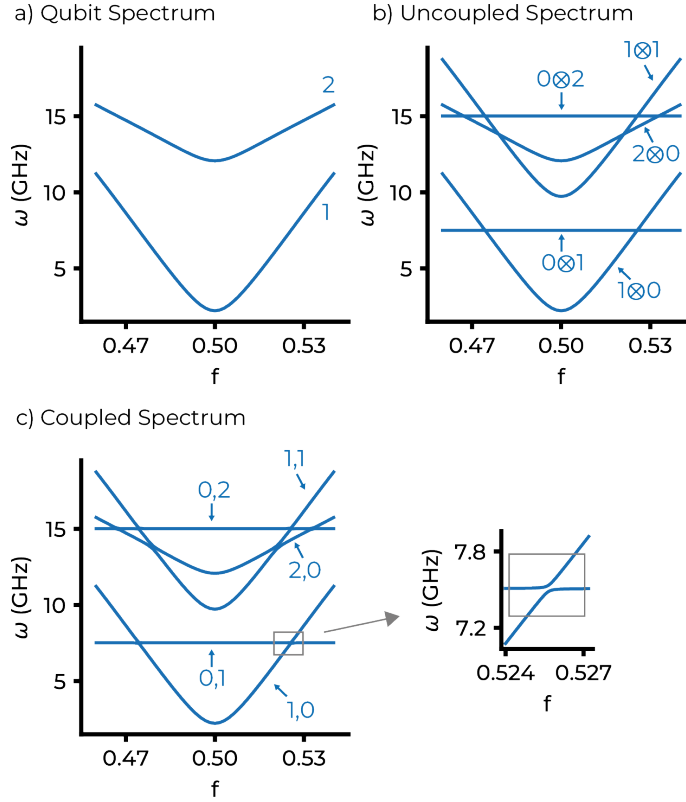


Figure 5.12: Qubit-Resonator Spectrum. a) The qubit low spectrum with the loaded values from the resonator coupling. The transitions are labelled as respect to the $|0\rangle$. b) The uncoupled spectrum of both the resonator and the qubit, where the transitions are labelled $n_q \otimes n_r$ in terms on how many excitations are in the qubit, n_q and resonator, n_r . The symbol \otimes indicate that this is the uncoupled spectrum. c) The coupled spectrum, where the states are labelled by comparing visually with the uncoupled spectrum. The only visible difference in this spectrum are the avoided level crossings, such as the shown in the inset.

In the sweet spot, $\chi \approx 4 \times (2\pi \times \text{MHz})$, an order of magnitude greater than the predicted by observing the avoided level crossing on the inset of Fig. 5.12c). Indeed, χ_{01} is much smaller than the total dispersive shift and has a negligible contribution. This justifies the need of considering higher levels in the calculation of the qubit-resonator interaction.

Another important aspect is that the dispersive shift does not vary dramatically during this annealing range, and it starts increasing at $f = 0.5 \pm 0.01$, which may not be surpassed in the analog computing schedules. This allows to use the dispersive readout along all this flux range, since the coupling is low at all times compared to the other system frequencies.

On the right panel of Fig. 5.13, the same dispersive shift is plotted in a wider range. In this range, two avoided divergences are seen. These happen

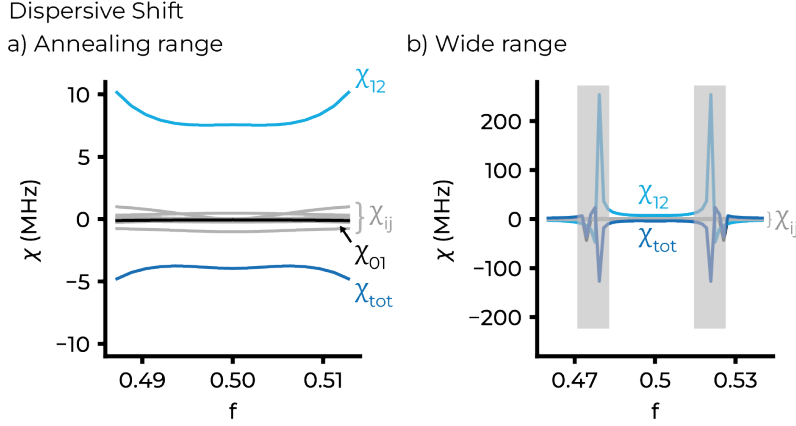


Figure 5.13: χ and χ_{ij} for different fluxes. a) takes into account the flux refine where usual annealing schedules take place, and b) a wider regime. The shaded region in b) shows region where the interaction is so strong that the dispersive regime is not valid, thus ξ .

when there exist frequency collisions. The first one occurs when ω_{12} is resonant with ω'_R , and the second one is the avoided level crossing shown in Fig. 5.12 c) inset. In these situations, the qubit-resonator interaction is so strong that the dispersive interaction is no longer valid.

The divergences in χ indicated hybridization between the qubit and the resonator, which would destroy the annealing sequence. Therefore, a plot like Fig. 5.13b) is needed to determine which is the maximum flux range that can be applied before qubit and resonators states hybridization occurs.

5.5 Coupling qubits

In the context of quantum annealing, coupling is a crucial element as explained in Section 2.4, and it is necessary that the couplings are tunable, with large couplings both for positive and negative interactions, and with possibility of switching it off completely.

For the qubit-qubit coupling on the coupled qubit prototype that was designed by the QCT team, a ZZ -coupling between flux qubits is proposed. The ZZ -interaction couples the qubits through σ_Z operators in Eq. (5.3), which corresponds to a coupling in the main qubit loop. The ZZ -coupling is a very common coupling scheme in quantum annealers due to its simplicity, and it leads to spin glass [Har18], which is a hard problem classically.

The simplest flux-tunable coupler for flux qubits is a rf-SQUID, already introduced in Section 2.3.3, which consists of a Josephson junction in series with an inductance in a loop, as seen in Fig. 5.14 a). The Hamiltonian is

$$\mathcal{H}_{\text{rf}} = 4E_C n^2 + E_L \frac{\phi^2}{2} - E_j \cos(\phi + 2\pi f). \quad (5.27)$$

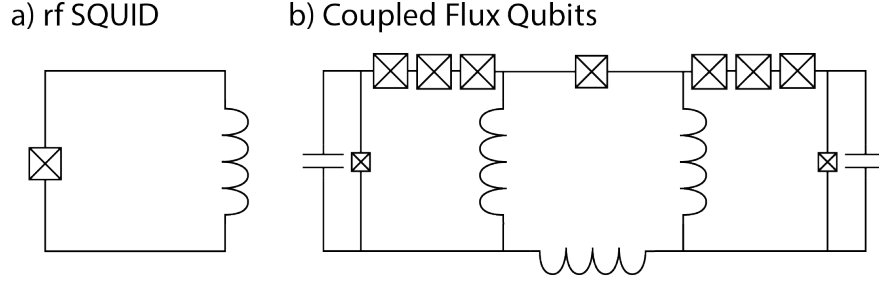


Figure 5.14: a) rf-SQUID, which is the coupler used in the processor prototype. b) Full coupled circuit, with two 4J-CFQ qubits on the sides and the rf-SQUID in the middle, all galvanically coupled.

The rf-SQUID can be itself used as a flux qubit, as in D-Wave processors [Har09b]. One of the main differences between the rf-SQUID working as a coupler is that couplers need to have a very large f_{01} compared to the qubits, so they always stay in $|g\rangle$. A large f_{01} transition ensures the coupler always in $|0\rangle$ and responds fast to the qubit changes, thus not participating in the system dynamics.

The schematic of the coupling is shown in Fig. 5.14 b). In this particular design, the two qubits are galvanically connected to the rf-SQUID coupler, coupled through a shared mutual inductance, M . A galvanic connection is chosen as it is easier to obtain a large coupling compared to geometric inductive coupling, which requires either bridges, so that the two loops overlap, or large loops.

The most important parameter of the coupler is its susceptibility, χ , which indicates how sensitive is the coupler current to a flux change. This is defined as

$$\chi \equiv \frac{1}{L_{\text{eff}}} = \frac{\partial I}{\partial \Phi_{\text{ext}}} = \frac{\partial^2 E_0}{\partial \Phi_{\text{ext}}^2}. \quad (5.28)$$

Here we also introduced the equivalent effective inductance, L_{eff} , the coupler represents as a circuit equivalent.

The coupler susceptibility as a function of the rf-SQUID flux is shown on Fig. 5.15. The coupler response can be tuned with the external flux threaded through the coupler loop, whose response can change sign and be turned off. This last aspect is crucial for an annealing schedule, since the start of the anneal should have the qubits decoupled. Sign change allows for ferromagnetic and antiferromagnetic couplings. For this simulation, the parameters were taken from [Web17], and listed in Table 5.3.

Apart from χ , the coupling strength depends on the mutual inductance between the rf-SQUID and the qubits, M , and the persistent current of the qubits, I_P . For low couplings, the effective coupling, $J \ll \omega_{01}$, with this coupler is

$$J = \chi M^2 I_P^2, \quad (5.29)$$

assuming identical qubits and M . This expression responds to a semiclassical

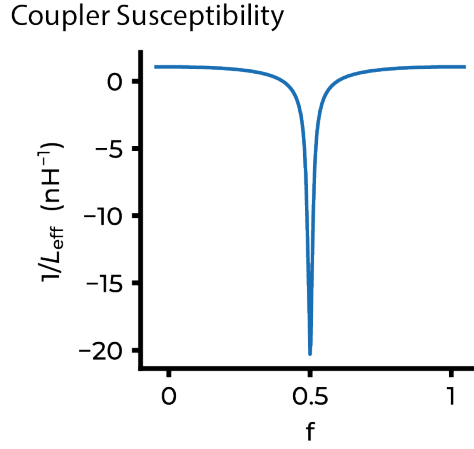


Figure 5.15: rf-SQUID Susceptibility as a function of the external flux.

L pH	A μm^2	S_C $\text{fF } \mu\text{m}^{-2}$	J_c $\mu\text{A } \mu\text{m}^{-2}$
467	0.26	50	2.78

Table 5.3: rf-SQUID design parameters.

analysis where the coupling, if small enough compared to ω_{01} , is treated classically, while the individual components are analyzed quantum mechanically. In this prototype, coupling is expected to be at least an order of magnitude lower than the qubit frequencies, thus validating this expression.

In order to enhance the coupling one can increase M , I_P or χ . Increasing I_P can reduce performance and decoherence due to increased susceptibility to flux noise, as explained in Section 2.3. A larger M is an easier path to increase the coupling. Nevertheless, if M is very high, it cannot be neglected in the flux qubit circuit schematic, unlike previously simulated. A different coupler than the rf-SQUID could be used to increase χ . In this design, the maximum absolute coupling has been optimized, which occurs for the ferromagnetic case.

An important remark, is that Eq. (5.29) is a semiclassical approximation of the coupling. When J is strong, as intended for quantum annealing, this expression is no longer valid, and the full circuit must be properly analyzed. In Section 5.6 this point is discussed.

5.6 Annealing Schedules

An annealing schedule is the analog version of a gate sequence in digital quantum computing. For the transversal Ising Hamiltonian schedule, the sequence is

defined as[Far00b]

$$\mathcal{H}(t) = \sum_i (h_{Z,i}(t)\sigma_{Z,i} + h_{X,i}(t)\sigma_{X,i}) + \sum_{i<j} J_{ij}(t)\sigma_{Z,i}\sigma_{Z,j}. \quad (5.30)$$

An annealing sequence usually starts with $h_{Z,i} = J_{i,j} = 0$, and $h_{X,i} \neq 0$. This corresponds with the initial state of the system being a complete superposition of all computational states. Then, as time evolves, h_X is tuned down and both h_Z and J are increased to their final value. The final state leads to the solution of an optimization problem, as explained in Section 1.2.2. The specific implementation of such a sequence on each device depends on the circuit properties and functionalities.

5.6.1 Single qubit Annealing

Understanding a single-qubit annealing sequence is very useful when considering larger systems. When the flux in the main qubit loop is swept, the energy levels change as seen in Fig. 5.16[†]. If starting the sequence in $|g\rangle$ at $f = 0.5$, and increasing f , $|g\rangle$ will follow the dark blue line.

It is important to remember than $|g\rangle$ is not a computational basis state, since in quantum annealing such a role is taken by the persistent current states, defined as $|0\rangle$ and $|1\rangle$. It is important to note here that the decision on which circulating direction has $|0\rangle$ and $|1\rangle$ is arbitrary.

The average circulating current, $\langle I_{\text{circ}} \rangle$ is obtained by the circulating current operator, $\hat{I}_{\text{circ}} = \frac{\partial \mathcal{H}}{\partial \Phi_{\text{ext}}}$. Figure 5.16 b) shows that $\langle I_{\text{circ}} \rangle$ in $|g\rangle$ changes from 0 when in $f = 0.5$ to a value that becomes close to the actual I_P , since double-well potential becomes so tilted it is nearly a single well potential. This is expected, since when the flux bias is large enough, $|g\rangle$ would be approximately equal to one of the two computational states, whose circulating current is exactly I_P .

In annealing schedules, it is common to write a normalized time, $s = t/t_f$, where t_f is the final time of the annealing sequence. A single-qubit annealing schedule could sweep the flux from 0.5 at $s = 0$ to 0.51 at $s = 1$ linearly. In such an annealing sweep, $|g\rangle$ will evolve from a complete superposition of $|0\rangle$ and $|1\rangle$ to the $|0\rangle$ state as the time evolves, as seen in Fig. 5.16c). The Ising coefficients h_X and h_Z , can be directly computed from the flux qubit two lowest-level description, since

$$\begin{aligned} \hbar\Delta/2 &= h_x, \\ 2I_P(f - 0.5) &= h_X, \end{aligned} \quad (5.31)$$

as can be inferred from Eq. (5.3). In Fig. 5.16 d), the evolution of the Ising coefficients in this annealing schedule is shown, which at the end it achieves a ratio $|h_Z/h_X| \approx 3$, which may be too weak.

In order to increase the ratio of $|h_Z/h_X|$ and final $|0\rangle$ population, a higher flux range can be explored. It is important to note that by increasing the flux

[†]Throughout this section, values from qubit design #2 from Section 5.2 are used.

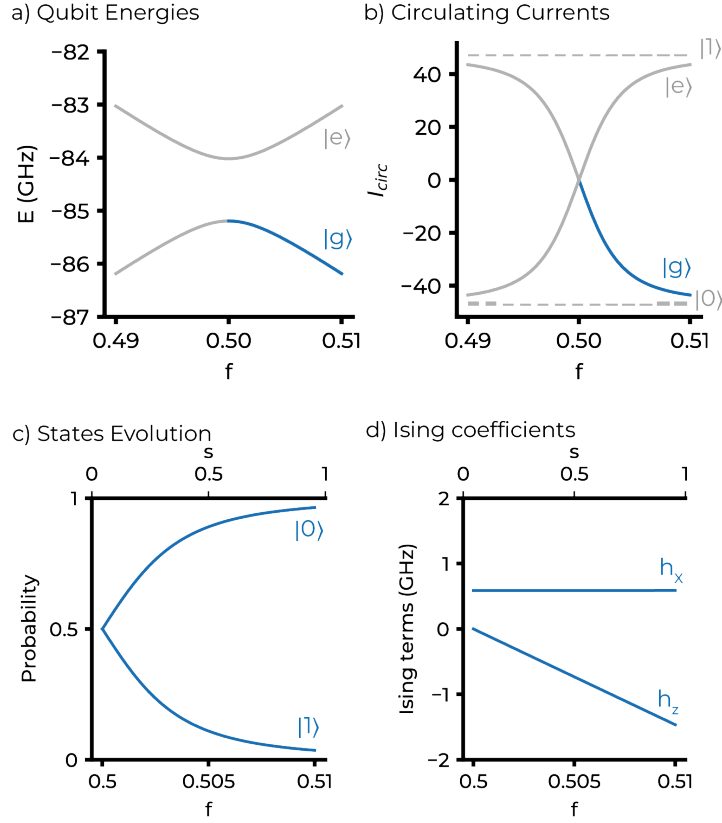


Figure 5.16: All these simulations are for flux qubit design #2 in Section 5.2. The dark blue colored parts correspond to what corresponds to a single qubit annealing sequence. Upper x axis in b) and c) shows the adimensional annealing time. a) Energy levels for varying external flux. b) Circulating currents obtained from the operator for both the ground and the first excited state. In dashed, the circulating current of the computational states, which corresponds to the persistent current. c) Probability of measuring one of the computational states as the qubit evolves along the ground state. d) Evolution of the Ising parameters when sweeping the flux.

beyond this range, the hyperbolic approximation of the 2-level flux qubit fails. Without the hyperbolic approximation the analysis is more complicated, since linear relations in Eq. (5.31) are no longer valid. An alternative is to design a Δ -tunable circuit.

Fig. 5.17 shows the plots from Fig. 5.16 in a wider flux range. By looking at the circulating current in Fig. 5.17 b), one can see that the excited state $\langle I_{\text{circ}} \rangle = 0$ around $f = 0.45$. After this point, both $|g\rangle$ and $|e\rangle$ have the same current direction, which is an invalid configuration for quantum annealing. Moreover, before this takes place, h_z/h_x and P_0 have already been maximized, as seen in Fig. 5.17c-d). Thus, the annealing sequence should be stopped at the maximum.

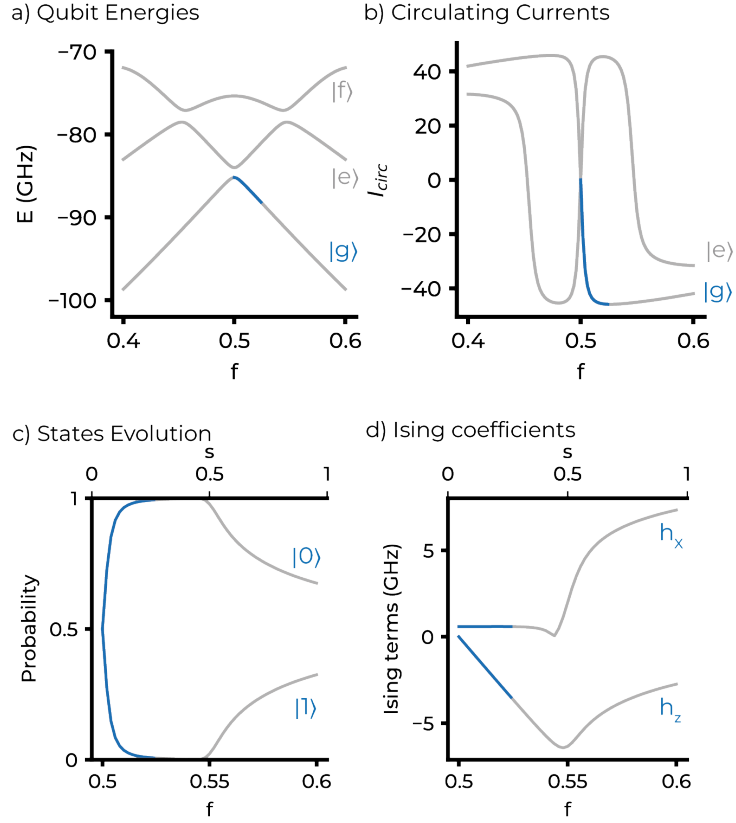


Figure 5.17: All these simulations are for flux qubit design #2 in Section 5.2. The dark blue coloured parts correspond to what corresponds to a single qubit annealing sequence. a) Energy levels for varying external flux. b) Circulating currents obtained from the operator for both the ground and the first excited state. c) Probability of measuring one of the computational states as the qubit evolves along the ground state. d) Evolution of the Ising parameters when sweeping the flux.

Figure 5.17c) shows that $|g\rangle$ can be, to a very good approximation, $|0\rangle$. Furthermore, in Fig. 5.17d), it is seen that the ratio between Ising parameters can be increased to $h_z/h_x \approx 10$. When many qubits are placed, the algorithm efficiency relies on measuring the correct state, which is proportional to P_0 , thus $P_0 \gg 0.9$ would be desirable at the end of the anneal.

5.6.2 Two-qubit Annealing

The two-qubit with a coupler system showed in Fig. 5.14 b) is considered. It consists of two flux qubits coupled inductively via a rf-SQUID. A complete analysis would require the simulation of this whole system. However, for a first approximation, the single-qubit results from previous section are considered

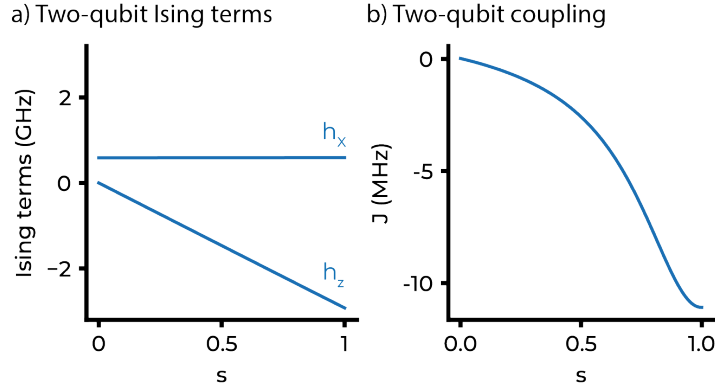


Figure 5.18: Two-qubit anneal schedule terms. Single qubit parameters on a) and two-qubit coupling J on b).

and the coupling is added semiclassically, as described in Section 5.5.

The two-qubit transverse Ising model is then expressed as

$$\mathcal{H} = \sum_{i=1}^2 (h_{Z,i}(t)\sigma_{Z,i} + h_{X,i}(t)\sigma_{X,i}) + J(t)\sigma_{Z,1}\sigma_{Z,2}, \quad (5.32)$$

where the subindices represent the two qubits. The coupler does not affect the dynamics and only determines J .

In Fig. 5.18, the one-qubit Ising parameters together with the coupling are shown. The Ising parameters have been computed by using the same qubit parameters as in Section 5.6.1, tuning the flux to values where the hyperbolic 2-level qubit regime stays valid.

The coupler has been simulated with the values used in Section 5.5, with a realistic qubit-coupler mutual inductance of $M = 43$ pH. The flux schedule consists of starting with the rf-SQUID at the zero susceptibility point and increasing it towards $f = 0.5$ where the interaction is maximized (see Fig. 5.15).

The final J with this approach is two orders of magnitude smaller than h_i . This means that future designs need to severely increase this value. Moreover, although coupling is much smaller than qubit energies, the results shown here should only be seen as an approximation. The real Ising parameters require a full system analysis instead of this semiclassical approximation. Finally, qubit crosstalk has not been considered, which may be very important. In general, crosstalk calibration is one of the most demanding tasks required to operate an annealing processor.

In this section the Ising parameters have been obtained from the flux applied to the system. However, in real scenarios, this should happen the other way around. For a defined annealing schedule, the applied fluxes must be found. This reverse problem must be solved using optimization techniques, as no analytical method is known.

Chapter 6

Flux Qubit Experiments

DAVID LÓPEZ-NÚÑEZ, FABIAN ZWIEHOFF, ELIA BERTOLDO, LUCA COZZOLINO, BARKAY GUTTEL, P. FORN-DÍAZ

This chapter presents the results of the flux qubit experiments performed with the prototype design introduced in Chapter 5, where the Hamiltonian design was developed. Here, in Section 6.1 the physical implementation of that Hamiltonian is explained, with all the necessary finite element simulations and capacitance and inductance analysis.

The device fabrication process is not thoroughly explained, since the designed devices are not fabricated in-house, but at the University of Glasgow at Prof. Martin Weides group, and at Superfab group led by Prof. Vladimir Antonov at the Royal Holloway University of London. The experimental setup has been already extensively introduced in Chapter 3, so only a few details on the chip packaging are given in Section 6.2.

Spectroscopy measurements are performed prior to coherent control to initially benchmark qubit parameters and quality. These measurements (Section 6.3) provide a prior characterization of qubit Δ and I_P , and also allow to map the current passing through the coil with the flux experienced by the qubits.

Coherent control of flux qubits is presented in Section 6.4, which constitutes one of the most relevant results from this thesis. Time-domain measurements show T_1 as large as 42 μs , but $T_{2R} \approx 15$ ns. This short T_{2R} probably indicates large flux noise. Moreover, the qubit is explored in various flux point, which gives insights about the origin on the noise. However, these results are still work in progress as qubit has not yet been controlled at the symmetry point. The coherence results indicate the path to continue to develop the following flux qubits in the group.

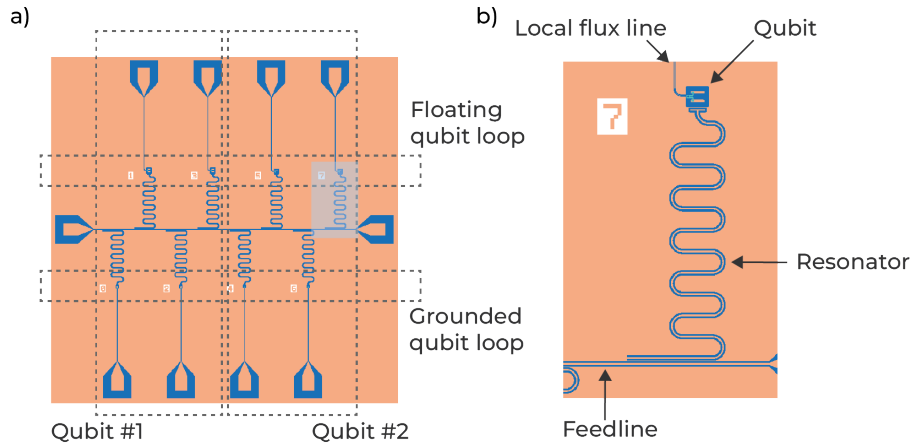


Figure 6.1: a) Layout of the chip with 8 individual flux qubits and their readout resonators coupled to a common transmission feedline. From the bottom and top of the chip, 8 flux bias lines emerge towards the qubit loops. b) Zoom on one of the qubits, with its dedicated readout resonator and local flux line.

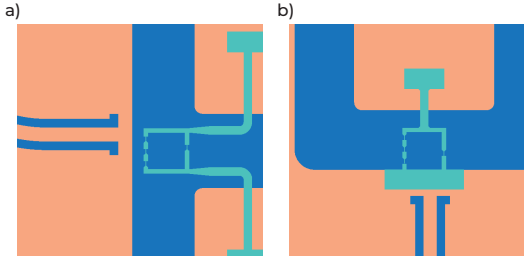


Figure 6.2: a) Floating qubit coupled to the local flux line. b) Grounded qubit coupled to the local flux line.

6.1 Chip Design

In this section, all parts of the flux qubit device presented in Chapter 5 are physically designed: readout resonators, local flux lines, qubit loops, etc. The methods described here cover many of the required steps in an actual quantum processor design.

6.1.1 Device overview

The full device design is shown in Fig. 6.1a). In the central part, a feedline with an input and output port is used for transmission-type measurements. A total of 8 readout resonators are inductively coupled to the feedline with 8 flux qubits, each one capacitively coupled to their respective resonator.

The qubits in this device correspond to the two theoretical designs exposed in Section 5.2.6. The 4 qubits on the left correspond to the design #1, and

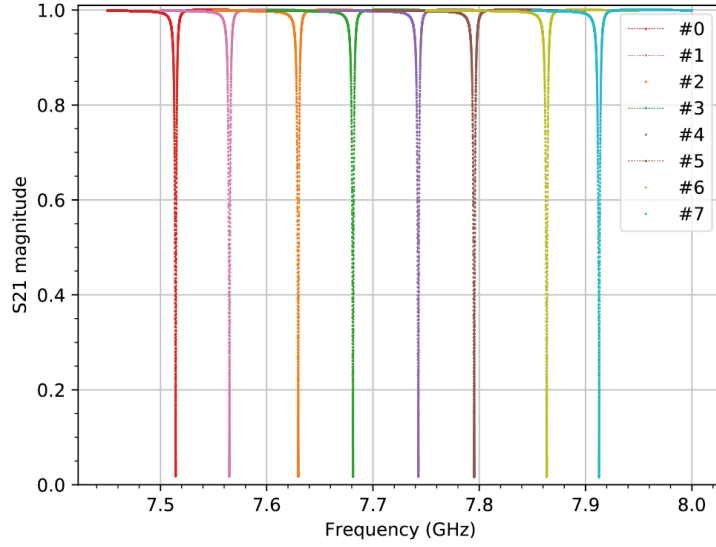


Figure 6.3: S_{21} magnitude of the resonators simulated with Sonnet.

the 4 on the right to design #2. Both designs consist in 4-Josephson junction C-shunted flux qubits with $I_C = 109$ nA and $C_J = 2.5$ fF, both referring to the large junction. The ratio between the small and the large junction is $\alpha = 0.55$. The only difference between the designs is the shunting capacitance, C_{sh} , which was 13 fF for design #1 and 8 fF for design #2.

Another variation is introduced in the qubit loops. The 4 qubits above the feedline are floating, thus disconnected from the circuit, and the 4 qubits below are galvanically attached to the circuit ground plane, as shown in Fig. 6.2. One of the goals of this device is to observe whether the loop configuration has any significant effect on the coherence.

A zoom on a single qubit device is shown in Fig. 6.1b). Each qubit is capacitively coupled to its own resonator, which is itself coupled inductively to the feedline. Each qubit is also coupled inductively to a flux bias line that is placed in close proximity to the qubit loop. This line allows for fine local flux control. Apart from the local flux lines, there is a global coil placed on top of the box containing the chip for biasing all the qubits.

The GDS layout file seen in Fig. 6.1 was created by a Python script based on the package GDSPy*. This package provides the basic geometrical forms upon which the final design is formed. The QCT lab developed its code on top of it to draw the specific processor parts.

#	Length	f_0	$f_{\lambda/4}$	δf_0	Δf	Q_L	Q_{ext}
	mm	GHz		MHz		10^3	
0	3.835	7.762	7.514		1.086	6.9	7.2
1	3.804	7.824	7.565	51	1.142	6.6	6.9
2	3.774	7.886	7.630	65	1.129	6.8	7.0
3	3.745	7.948	7.681	52	1.181	6.5	6.7
4	3.716	8.010	7.743	62	1.192	6.5	6.7
5	3.688	8.072	7.795	53	1.234	6.3	6.5
6	3.659	8.134	7.863	68	1.225	6.4	6.6
7	3.632	8.196	7.913	50	1.303	6.1	6.3

Table 6.1: Design parameters of the 8 resonators extracted from electromagnetic simulation in Sonnet: $f_{\lambda/4}$ is the bare resonance estimated from Eq. (6.1), f_0 is the simulated one, δf_0 is the spacing between the resonator and the previous one, Δf is the 3 dB bandwidth of the dip, Q_L and Q_{ext} are the loaded and external quality factors (see text).

6.1.2 Feedline and Resonators

Both the feedline and the resonators are designed as coplanar waveguides (CPW) with a center conductor width of 10 μm and a spacing of 6 μm to the surrounding ground plane to match to a 50 Ω impedance. This can be calculated from elliptical integrals already known for the CPW geometry [Wat94].

The feedline contains two launcher pads: the input port on the left end and the output port on the right end of the chip, as it is seen in Fig. 6.1a). These pads will be connected to the PCB via wire bonding.

The readout resonators are designed to be distributed-element $\lambda/4$ CPW resonators, since they are shorted on the feedline end and open on the qubit end (see Fig. 6.1b)). The open end has a small capacitor pad shape resulting, see Section 6.1.3b). The specific shape and strength of the qubit-resonator coupling depend on each qubit.

From the length $l = \lambda/4$ of the resonator, its bare resonance

$$f_{\lambda/4} = \frac{c_0}{\sqrt{\epsilon_{\text{eff}}}} \frac{1}{4l} \quad (6.1)$$

where c_0 is the speed of light in vacuum and ϵ_{eff} is the effective relative electric permittivity index of a CPW geometry sandwiched between two dielectric substrates. ϵ_{eff} can be estimated through $\epsilon_{\text{eff}} = \frac{1}{2}(\epsilon_1 + \epsilon_2) \approx 6.225$ with $\epsilon_1 = 11.45$ for Si and $\epsilon_2 = 1$ for air. $f_{\lambda/4}$ is a good estimation of the real resonance, f_0 . However, f_0 is shifted due to the interaction with the rest of the device and needs to be determined by electromagnetic simulation, e.g. with Sonnet.

From electromagnetic simulations with Sonnet, the actual resonance frequency, f_0 , and the -3dB bandwidth, Δf (full width at half maximum), can be extracted. With Δf , the resonator damping, $\kappa = 2\pi\Delta f$, can be computed.

*<https://gdspy.readthedocs.io>

Both are relevant parameters for the calculation of the desired dispersive qubit-resonator coupling χ . In qubit-resonator circuits, such as the one described here, an optimal signal-to-noise ratio (SNR) is achieved when χ satisfies [Gam07]

$$\chi = \frac{\kappa}{2}. \quad (6.2)$$

Furthermore, Δf determines the response time τ of the resonator

$$\tau = \frac{1}{2\pi\Delta f}. \quad (6.3)$$

An important measure for the performance of a resonator is its loaded quality factor Q_L that is composed of an internal and external contribution which can be directly inferred from the (measured/simulated) resonance f_0 and Δf :

$$\frac{1}{Q_L} = \frac{\Delta f}{f_0} = \frac{1}{Q_{\text{ext}}} + \frac{1}{Q_{\text{int}}}. \quad (6.4)$$

Q_{int} is determined by internal losses from the resonator, while Q_{ext} originates from the coupling to the external circuit elements, mainly the feedline. For the case of superconducting resonators, the dominant internal loss mechanism are two-level systems (TLS) residing in the interfaces and dielectrics of the CPW, such that the internal quality factor can be approximated as

$$\frac{1}{Q_{\text{int}}} \simeq \tan \delta, \quad (6.5)$$

with the dielectric loss tangent $\tan \delta = 5 \times 10^{-5}$ measured for Si CPW resonators at low temperatures and powers at which they are typically operated [Kru06]. Thus, $Q_{\text{int}} \simeq 5 \times 10^5$ is assumed for all resonators. Then, the quality factor Q_{ext} of the coupling between the feedline and the resonator can be extracted by using Eq. (6.4).

Table 6.1 gives an overview of the design parameters for the 8 resonators. The resonator frequencies are separated $\delta f_0 \approx 50$ MHz, so that they are easy to distinguish, as $\delta f_0 = f_{0,i+1} - f_{0,i} \gg \Delta f \approx 1$ MHz. The simulated magnitude response from the resonators, $|S_{21}|$, can be seen in Fig. 6.3.

In Sonnet, the metallization layer was set to be a lossless material. The Si substrate was defined to have a dielectric loss tangent of $\tan \delta = 5 \times 10^{-5}$ while the conductivity was set to be zero since high-resistivity wafers do not conduct at cryogenic temperatures.

6.1.3 Capacitance Network Analysis

In the Hamiltonian description, only C_{sh} and C_C are taken into account. C_{sh} defines the qubit α -junction effective shunting capacitance and C_c indicates the qubit-resonator capacitive coupling. However, in real circuits, capacitances are not isolated, but a full capacitive network has to be analyzed.

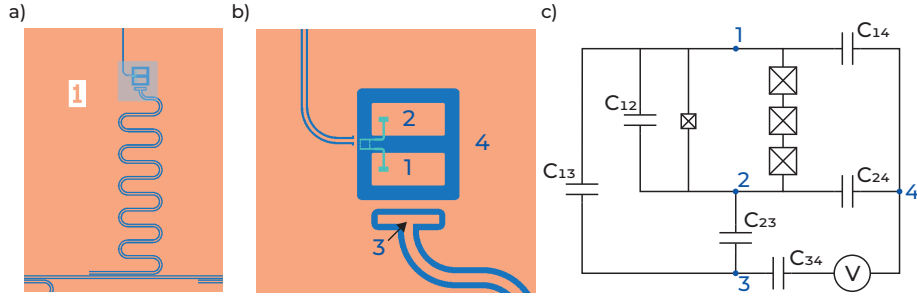


Figure 6.4: a) Shaded area is where the capacitance network analysis is performed. b) Floating qubit, coupled to the resonator and the flux line. Four separated metallic areas are defined: 1 and 2 are the qubit pads, 3 is the resonator center feedline and 4 is the ground plane. c) Circuit schematic of the capacitance network. Cross-capacitances with the Josephson junctions are not considered in the analysis.

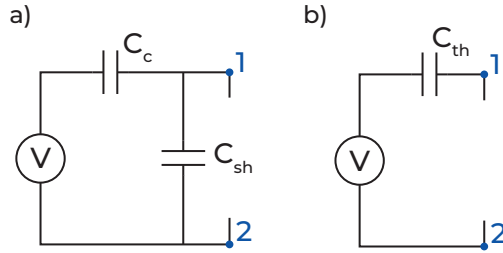


Figure 6.5: a) Final effective capacitance circuit, where V is the resonator voltage and the qubit loop with the Josephson junctions is between node 1 and 2. b) Thevenin effective circuit.

In Fig. 6.4, the capacitance network of the floating qubit device is shown[†]. In Fig. 6.4b), the four isolated metallic parts that create the capacitance network are shown. The two qubit pads, 1 and 2, the resonator center line, 3, and the qubit ground, 4, are the four nodes. In Fig. 6.4c), the corresponding circuit schematic is shown. It must be noted that in this circuit the cross-capacitances between the qubit islands and the other elements are not considered.

Two tasks are needed to design the circuit capacitances: first, to relate the full capacitive network to C_{sh} and C_C , and then to simulate the actual design until the desired parameter configuration is obtained.

6.1.3.1 C_{sh} and C_C extraction

The floating qubit considering all the capacitance is depicted in Fig. 6.4c). There are four nodes, with the ground plane considered as node 4. The voltage in the circuit represents the resonator voltage between the center line and the ground

[†]From here on, only the floating qubit configuration is shown. The grounded qubit, which is simpler, is analyzed in Appendix D

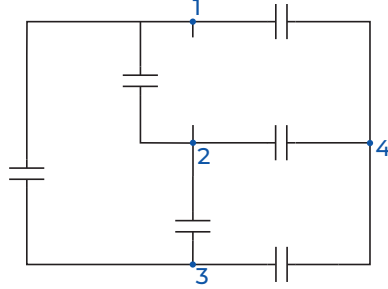


Figure 6.6: The capacitive network of the floating qubit considering only the capacitances, after removing the Josephson junctions.

plane. The capacitance reduction to obtain C_{sh} and C_C should not modify the qubit loop where the Josephson junction are placed. Thus, the procedure should leave untouched the connections between node 1 and 2 that are not purely capacitive. These nodes, 1 and 2, are considered the primary nodes.

The final expected circuit should have the shape of Fig. 6.5a), where the Josephson junction loop should be located between nodes 1 and 2. In order to find this effective circuit, Thevenin's theorem is used[Dor89].

The AC version of the Thevenin's theorem states that any circuit that connects two terminals which include resistances, capacitances, and inductances can be represented by an effective circuit consisting on a voltage source in series with an impedance. For this case, where only capacitances are considered, this effective impedance is a capacitance, called C_{th} . The Thevenin circuit is shown in Fig. 6.5b).

The first step towards finding the Thevenin circuit consists of removing the junctions in between the primary nodes 1 and 2 from Fig. 6.4c), and considering the voltage source as a short. This leaves the pure capacitive network as seen in Fig. 6.6.

Then, the node 4 is reduced via the $Y - \Delta$ conversion, shown in Fig. 6.7.

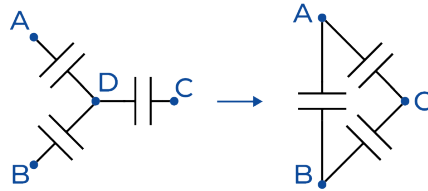


Figure 6.7: $Y - \Delta$ conversion can be used to remove a node only connected via capacitances.

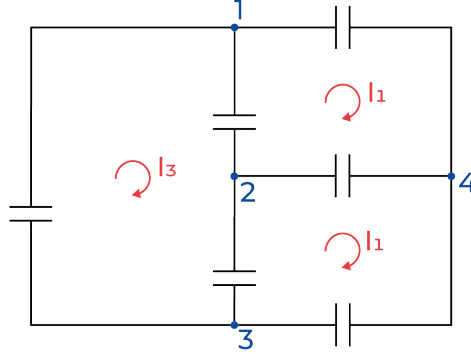


Figure 6.8: Capacitance network with considered currents for applying Kirchhoff voltage laws.

The resulting capacitances from the $Y - \Delta$ conversion are found as

$$\frac{1}{C'_{ij}} = \frac{\sum_k C_{k4}}{C_{i4}C_{j4}}, \quad (6.6)$$

where the indices i , j and k take any value from 1 to 3. C'_{ij} is the new capacitance obtained by the reduction of node 4, and C_{i4} are the circuit capacitance connecting any node to node 4.

Then, node 3 is removed by computing the resulting capacitances in series and parallel, and finally the system is reduced to a single capacitance between nodes 1 and 2, which is C_{th} .

The next step is to find the Thevenin voltage, V_{th} . Since the value of the resonator voltage is unknown, V_{th} will be related to an undefined voltage as $V_{th} = \beta V$. To find V_{th} , Kirchhoff voltage law must be used for the system, as depicted in Fig. 6.8.

The Thevenin effective circuit, as shown in Fig. 6.5b), is not the final circuit, but the circuit in Fig. 6.5a). The obtained C_{th} and V_{th} are related to C_C and C_{sh} by finding the effective Thevenin circuit of the final design Fig. 6.5b), which gives the following relations

$$C_{th} = C_c + C_{sh}, \quad (6.7)$$

$$V_{th} = \frac{C_c}{C_c + C_{sh}} V. \quad (6.8)$$

Then, by substituting the values obtained for C_{th} and V_{th} as function of C_{ij} in Fig. 6.4c), the effective values of C_{sh} and C_C are obtained. The exact expressions are rather complex, and are computed numerically.

6.1.3.2 Capacitance Network Design

The full capacitive network was simulated in COMSOL, where one may obtain all the individual capacitances: C_{12} , C_{13} , etc. on Fig. 6.4c).

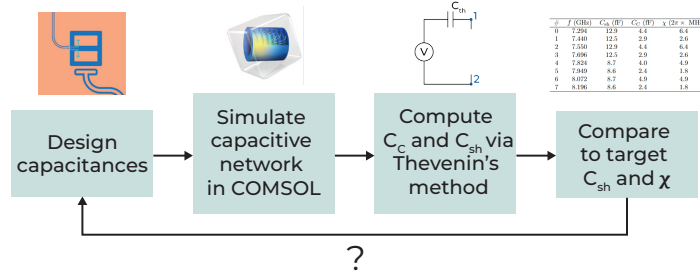


Figure 6.9: Method used to design the qubit-resonator capacitance network.

The target C_{sh} is defined by the qubit design, which is 13 fF for qubit #1 and 8 fF for qubit #2. However, C_C is still undefined. For a given resonator damping κ , an optimal value of the dispersive qubit-resonator coupling χ for qubit readout can be readily determined from Eq. (6.2). Finding suitable values of χ that satisfy this condition, however, requires to numerically solve the non-trivial problem Hamiltonian of the coupled qubit-resonator system, as explained in Section 5.4.

The simulations performed to obtain χ from the Hamiltonian circuit have C_C and C_{sh} as input variables, as well as the rest of qubit parameters. First, the qubit subsystem is diagonalized to obtain its lower-energy states. Then, the full system is diagonalized by using the lowest energy states of both qubit and resonator subsystems, thus obtaining the qubit-resonator coupled spectrum and χ .

The iterative process to obtain the optimal design is schematically shown in Fig. 6.9. The process consist of designing the capacitances of the circuit and simulate the full capacitive network in COMSOL. With the values of the capacitances, C_C and C_{sh} are extracted via the Thevenin reduction described in Section 6.1.3.1. Then, C_{sh} is compared to the target for the qubit designs and C_C is compared to the target one according to the χ simulations and the previous resonator simulations in Sonnet (Section 6.1.2). The process is iterated until de values of C_C and C_{sh} converge to our desired target. This optimization protocol is performed manually.

6.1.4 Flux bias lines

A flux bias line is added on each qubit to locally apply flux in the qubit loop. A coil is placed on top of the sample box containing the device to set a global flux to all the qubits, and then each qubit is locally biased. This is not strictly needed for the uncoupled devices. However, the inclusion of these local flux lines pave the way for future coupled qubit designs where local control is indispensable.

The design of the flux lines can be seen in Fig. 6.2 for both the floating and grounded qubit on panel a) and b) respectively. The flux bias lines consist of a 50Ω CPW geometry, with the end of the line shorted in close proximity to the

qubit loop, see Fig. 6.2. The flux line antenna is slightly displaced with respect to the symmetry axis of the qubit loop to attain a low mutual inductance, $M = 0.1 - 0.2$ pH. M is kept low in order not to couple the qubit too strongly to the ohmic environment coming from the line as discussed below.

The simulations to determine M are performed using FastHenry, a software that allows to compute inductance of superconductors, considering both geometric and kinetic contributions of the inductance. Kinetic inductance can be a significant part of the total inductance in superconductors, and is not usually considered in commercial finite-element software. The simulations can be seen on Fig. 6.10.

In the case of the floating qubit, a displacement of $4\ \mu\text{m}$ results in $M = 0.15$ pH. Using $\Phi = M \cdot I$, this yields a flux bias current of $I = 13$ mA required to induce a single flux quanta Φ_0 in the loop. In the experiment, however, a magnetic coil will set the global flux already close to the qubit sweet spot, $\frac{\Phi_0}{2}$, such that the bias lines will only be used to introduce small fluxes of $\approx 1\%$ Φ_0 or $\approx 130\ \mu\text{A}$, which is an acceptable current introduced into the system. This range is comparable to the range explored during an annealing sequence.

For the grounded qubit, the displacement is $1.5\ \mu\text{m}$ such that $M = 0.15$ pH. The distance between the qubit loop and the antenna is $5\ \mu\text{m}$ in both cases (measured from the center of the leads).

Lastly, similar to the resonator-induced Purcell loss, the inductive coupling of the qubit to the flux bias antenna represents another loss mechanism. The energy relaxation rate $\Gamma_{1,\text{ind}}$ and dephasing rate $\Gamma_{2,\text{ind}}$ through this channel can be estimated to be [Van03]

$$\Gamma_{1,\text{ind}} \approx \frac{2(\hbar\Delta)^2}{\hbar^3\omega_q} \frac{(MI_p)^2}{R} \coth\left(\frac{\hbar\omega_q}{2k_B T}\right), \quad (6.9)$$

$$\Gamma_{2,\text{ind}} \approx \frac{4}{\hbar^2} \frac{(MI_p)^2}{R} k_B T. \quad (6.10)$$

Here, Δ is the qubit tunnel splitting, $R = 50\ \Omega$ is the designed impedance of the inductively coupled flux bias antenna, k_B is the Boltzmann constant, $T = 20$ mK is the system temperature, and ω_q is the resonance frequency at which the qubit is operated. For the two qubit designs one can use $\Delta = 2\pi \times 1.2$ GHz and $2\pi \times 2.2$ GHz and their respective I_p from Table 5.2 to yield energy relaxation times of $T_{1,\text{ind}} = 7.0$ ms and 4.1 ms, respectively, as well as dephasing times of $T_{2,\text{ind}} = 10.1$ ms and 11.1 ms, respectively. For a more realistic $T_{\text{eff}} = 100$ mK, $T_{1,\text{ind}}$ remains mostly unchanged, but $T_{2,\text{ind}}$ reduces to 2.0 ms and 2.2 ms, for the lower and larger Δ design respectively. All these coherence times are well above the expected decoherence times, around tens of μs .

6.1.5 Qubit loops

A closer look to the qubit loops is given in Fig. 6.11. Both the grounded and floating loops are almost identical with inner horizontal and vertical dimensions

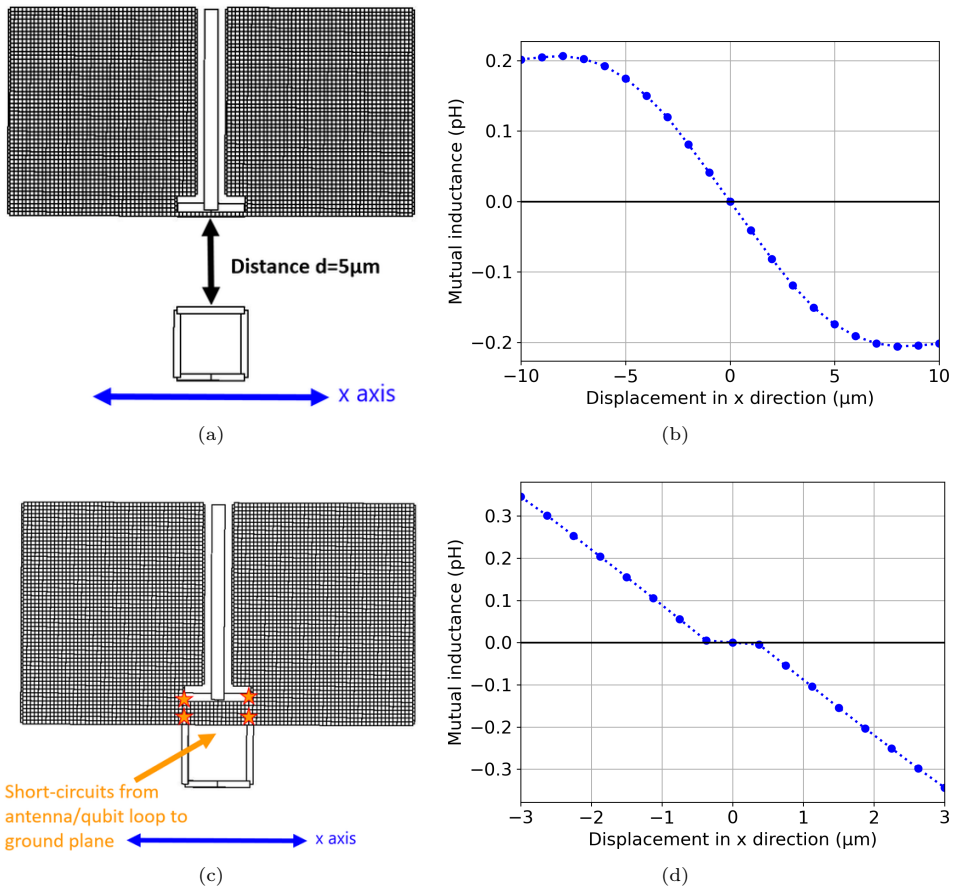


Figure 6.10: Simulation of the mutual inductance M between the flux bias antenna and the qubit loop based on FastHenry. 6.10a and 6.10c show the model for the floating and grounded qubit loop, respectively, while 6.10b and 6.10d show the results.

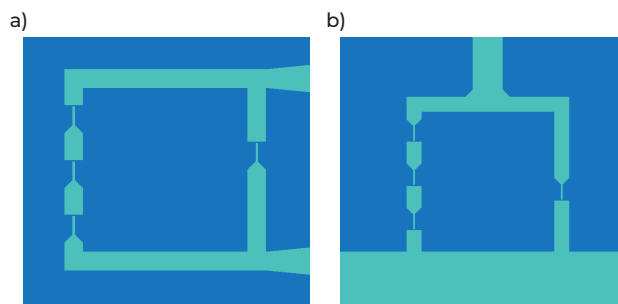


Figure 6.11: a) Floating qubit loop. b) Grounded qubit loop.

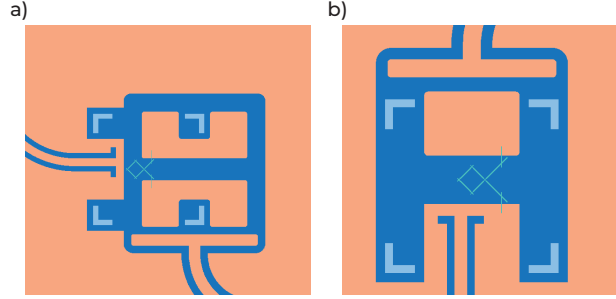


Figure 6.12: Redesign of a) floating qubit and b) grounded qubit.

of 9 μm , respectively, and a width 1 μm of the leads. In the case of the grounded qubit, the vertical dimension is 9.5 μm .

Resulting from the inductance simulations performed in Section 6.1.4, the qubit loops contain a geometric inductance L_{loop} between 26.5 and 28.5 pH, respectively. This value is much smaller than the Josephson inductance $L_J = \frac{\Phi_0}{2\pi I_c} = 3$ nH of the big junctions, for the designed $I_C = 109$ nA. Thus, it is reasonable to omit the loop inductance in the Hamiltonian as already claimed in Section 5.2.

6.1.6 Josephson Junction and Fabrication

The chip is fabricated on a 500 μm high-resistivity Si substrate, while the metal layer is 100 nm of Al. Fabrication has not been done in-house since junction fabrication was being developed at the time of these qubit designs. The fabrication of the first two generations was performed at the University of Glasgow (UG) by Dr. Paul Baity at Prof. Martin Weides group. The aluminum overlap junctions were defined by subtractive process on intrinsic Si substrate. The third and final design, was fabricated by Dr. Rais Shaikhaidarov at Superfab group led by Prof. Vladimir Antonov at the Royal Holloway University of London (RHUL).

The junction were shaped according to each manufacturing specific process. The design shown in Fig. 6.11 is produced, so that shadow evaporation is performed through the Dolan bridge technique [Dol77]. The exact A and J_C are specified according to the evaporation angle. However, the qubits manufactured in UG adapted the specific junction design to their fabrication technique.

6.1.7 Modifications on designs

A total of three different qubit batches were fabricated. The two first in Glasgow and the last one in London. The change in manufacturer, motivated by aluminum contamination in the Glasgow evaporator, caused a variation in the junction shape. However, most important, from the first to the second design, a higher C_C was targeted since the first qubits showed a weak dispersive shift.

#	f (GHz)	C_{sh} (fF)	C_C (fF)	χ ($2\pi \times$ MHz)
0	7.294	12.9	4.4	6.4
1	7.440	12.5	2.9	2.6
2	7.550	12.9	4.4	6.4
3	7.696	12.5	2.9	2.6
4	7.824	8.7	4.0	4.9
5	7.949	8.6	2.4	1.8
6	8.072	8.7	4.9	4.9
7	8.196	8.6	2.4	1.8

Table 6.2: Table with modified parameters of the designed capacitance, with the corresponding dispersive shift.

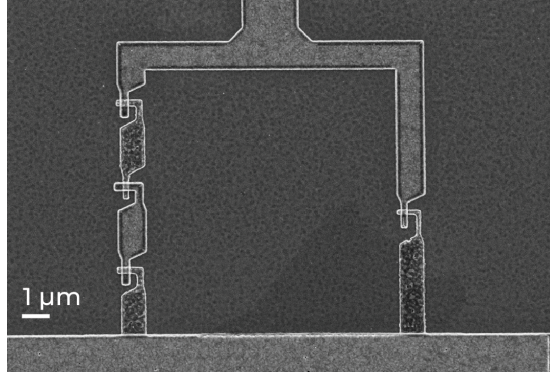


Figure 6.13: Grounded qubit loop of a design of the first generation of device, manufactured at the University of Glasgow.

The new design, as seen in Fig. 6.12, consisted on bringing the capacitance pad of the resonator closer to the qubit, compared to Fig. 6.4b). This caused an increase on C_C and, correspondingly, χ .

Moreover, extra space for the ebeam marks had to be given. This all led to a substantial modification of the capacitance network analysis, and new simulations had to be performed. The final values of C_C and χ are given in Table 6.2.

6.2 Device Inspection & Setup

The first devices were manufactured at the University of Glasgow. A qubit with aluminum overlap junctions can be seen in Fig. 6.13. The two different evaporation steps are seen with two different shades of the metals.

Figure 6.14a) shows a general image of a grounded qubit from the devices fabricated in RHUL. The qubit is coupled to a resonator and its dedicated local flux line. A zoom on the qubit loop can be seen in Fig. 6.14b). There, compared to Fig. 6.13, the number of junctions do not need to be even because they are not fabricated with the Dolan bridge technique. In Fig. 6.15, an image of the

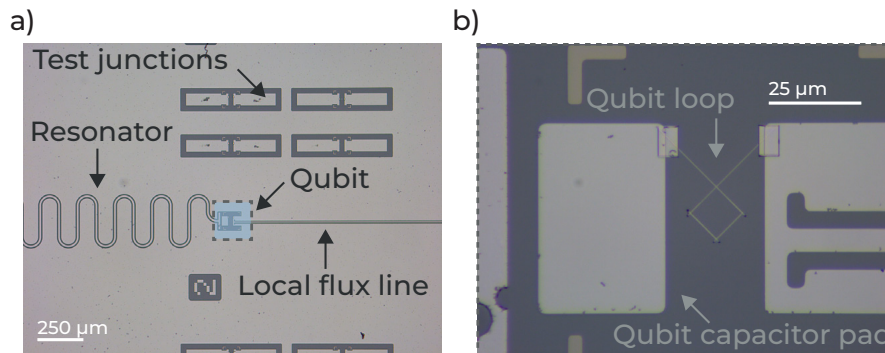


Figure 6.14: a) Microscopy image of one of the chips manufactured in RHUL. Image shows one of the grounded qubits coupled to a resonator and a dedicated local flux line. On top, some test junctions are seen. b) Zoom on the qubit loop.

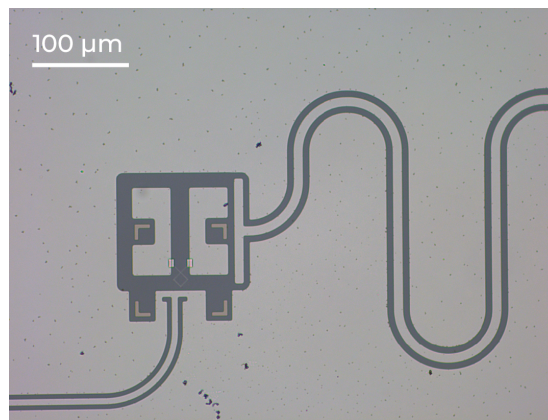


Figure 6.15: Microscopy image a floating qubit device. The e-beam marks are placed where the shunting capacitor should be. This modifies the shunting capacitance and, most importantly, the coupling between the qubit and the resonator.

floating qubit is shown.

6.2.1 Chip Packaging

The refrigerator setup can be seen in Chapter 3, with the magnetic shielding especially relevant for flux qubit experiments. The sample is wirebonded to a ceramic PCB. The wire bonds connect the central feedline pads and the flux line local lines (see Fig. 6.1), as well as the ground plane. The PCB is then placed inside a Cu sample box, which has a dedicated place for attaching a magnetic coil with a screw. The coil is placed at the center of the sample box, and sets a global magnetic flux for all qubits, as can be seen in Fig. 6.16. However, the

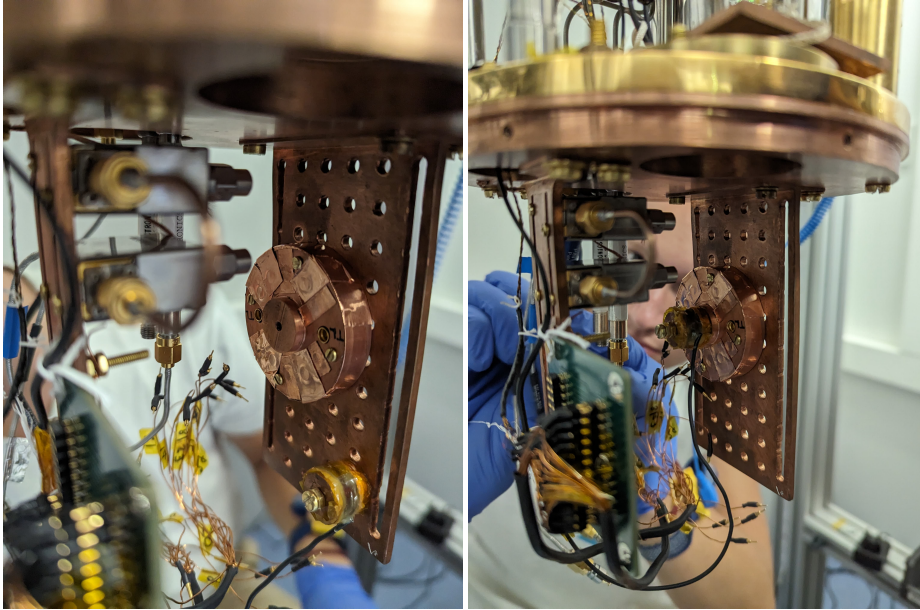


Figure 6.16: a) Copper sample box where the device is mounted, inside the mixing chamber stage of the dilution refrigerator. b) A coil is placed on top of the sample box. The coil sets the global magnetic flux for all qubits.

individual qubits will experience a different effective mutual inductance to the coil depending on their relative position and the size of the qubit loops.

6.3 Spectroscopy

6.3.1 First and Second Generation Devices

Spectroscopy measurements are performed prior to provide initial qubit and resonator frequency characterization. First, a frequency scan identifies the resonator frequency, f_r , plotted against different coil biases (Fig. 6.17). Qubit frequency, f_q , changes as the flux is swept by the coil current. When f_q is resonant with f_r , an avoided level crossing is observed, such as seen in Fig. 6.18. The qubit sweet spot is located in between the two avoided level crossings in Fig. 6.17.

In order to determine the presence of the qubits, the avoided level crossing with periodicity is identified, as seen in Fig. 6.19. This periodic avoided level crossing is the benchmark of a qubit, similar to punchout measurements in transmon experiments. Moreover, by observing a full Φ_0 period, a relation between current and flux can be established. Then, results can be expressed as a function of Φ , instead of current in the coil, as already implemented in Fig. 6.19.

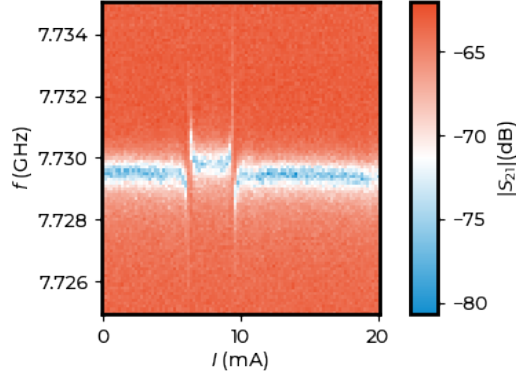


Figure 6.17: Resonator spectroscopy. The flux is tuned by modifying the current that flows through the coil. The flux qubit changes its frequency with I , and avoided level crossing occurs when qubit and resonator are resonant.

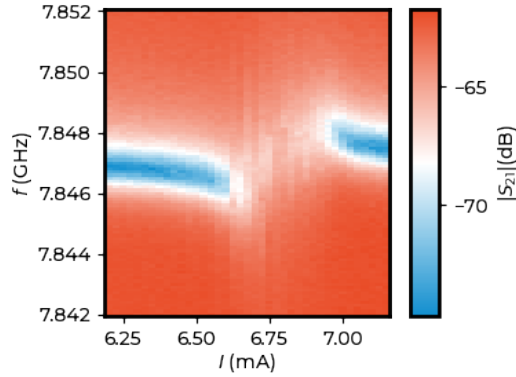


Figure 6.18: Zoom on the avoided level crossing between the flux qubit and the resonator.

An example of a two-tone measurement is shown in Fig. 6.20. Similarly to Section 4.2.2, the two-tone measurement consists on sending a varying frequency tone around the expected f_q , while weakly probing a tone with the VNA at f_r . By repeating this measurement at different Φ , the qubit gap, Δ , and the persistent current, I_P , can be determined by fitting

$$hf_{01} = \sqrt{(\hbar\Delta)^2 + (2I_P\Phi_b)^2}, \quad (6.11)$$

where $\Phi_b = \Phi - \Phi_0/2$ is the flux bias. Usually, $\hbar\epsilon \equiv 2I_P\Phi_b$ is defined.

Four qubits were correctly fitted, and their values are shown in Table 6.3. A systematic lower Δ and higher I_P than designed were measured, which could be both caused by a higher I_C of the qubit junctions.

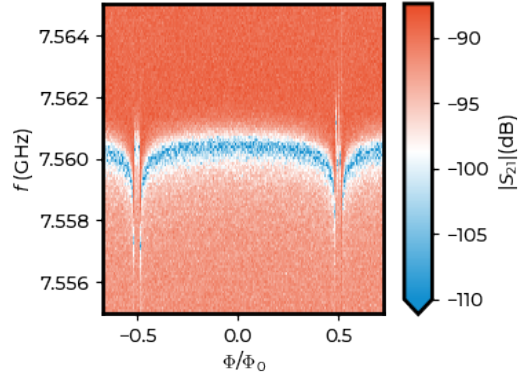


Figure 6.19: Periodicity of avoided level crossings is the benchmark of qubit presence. This also serves to map between I and Φ .

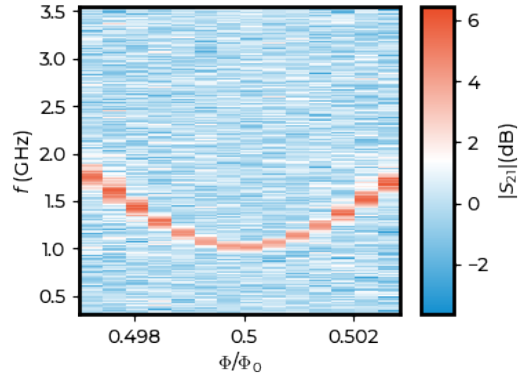


Figure 6.20: Two-tone spectroscopy for second generation chips. The qubit lowest transition, f_q , is observed. This qubit $\Delta = 1.02$ GHz and $I_P = 82$ nA.

The linewidth of the qubit spectrum observed in Fig. 6.20 is 220 MHz, which would result in a qubit coherence lifetime < 1 ns, using the uncertainty relation $\Delta E \Delta t \geq \hbar/2$. Indeed, in these devices, no successful time-domain measurement were achieved.

Later inspection of the fabrication process by the providers (UG) showed that the aluminum evaporator was contaminated with other metals. Aluminum T_C was measured to be under 1 K, compared with the expected aluminum T_C around 1.2 K. This discrepancy shows that the material used for this qubits was very dirty, which explains why qubit quality was so low.

	$\Delta_{\text{th.}}$ $2\pi \times \text{GHz}$	$\Delta_{\text{exp.}}$ $2\pi \times \text{GHz}$	$I_{P,\text{th.}}$ nA	$I_{P,\text{exp.}}$ nA
#1	1.17	1.01	47	82
#2	1.17	0.70	47	97
#3	1.17	0.80	47	-
#4	2.22	1.53	45	60

Table 6.3: Qubit spectroscopy results from second chip generation.

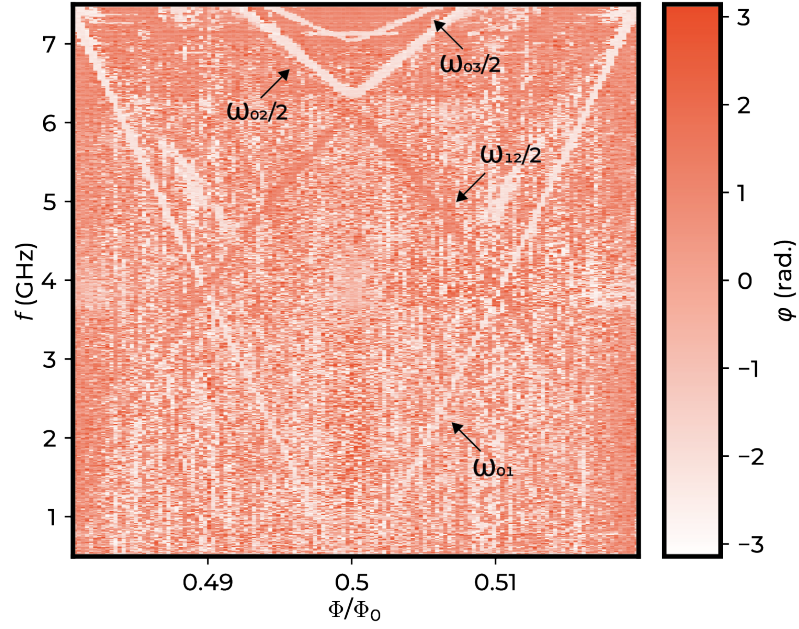


Figure 6.21: Two-tone spectroscopy of third generation devices. Several transitions can be identified. ω_{01} is much lower than expected, as it corresponds to $\Delta \approx 250$ MHz at the sweet spot. The other transitions that can be seen are a consequence of two-photon processes.

6.3.2 Third Generation Devices

For the third batch of chips, fabrication facilities were switched to RHUL. These chips, with almost identical design as the previous ones (see Section 6.1), showed functional qubits.

In Fig. 6.21, two-tone spectroscopy measurement of one of these devices is shown. The main feature that can be seen is the f_{01} transition that goes from 7 GHz to 0.25 GHz. Other transitions can be seen, such as $\omega_{02}/2$ and $\omega_{03}/2$. $\omega_{12}/2$ can also be seen, which is reduced as the qubit is more biased from the sweet spot, as it requires initial qubit population in $|1\rangle$. The strength in $\omega_{12}/2$ transition closer to the sweet spot, where f_q is lower, indicates more thermal

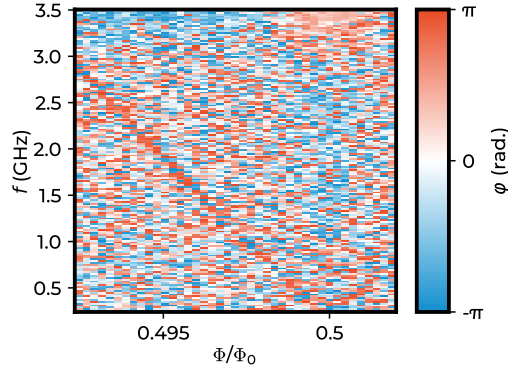


Figure 6.22: Zoom on sweet spot for two-tone spectroscopy.

population of $|1\rangle$.

A zoom on the sweet spot is seen in Fig. 6.22, where the resonance can be traced down to the sweet spot. For this device, the qubit frequency at the symmetry point is found to be around 250 MHz, much lower than the designed $\Delta = 1.2 \times (2\pi \times \text{GHz})$. Preliminary inspection of the devices indicates a higher I_C than designed, which could explain this gap deviation. Moreover, inspection of the junction areas show an expected $\alpha \approx 0.65$, which deviates by $> 10\%$ from the nominal value. I_p is fitted to 58.6 nA in this device, also higher than nominal 47 nA.

The spectroscopy results indicate that qubits are manufactured with a noticeable deviation from the designed Hamiltonian. This is specially significant in the qubit gap, Δ , that is reduced up to a few hundreds of MHz. For these frequencies, the qubit is expected to have a large thermal population, and its control can be more challenging.

Extracting the fabrication parameters from the results is not an easy task, unlike with transmon qubits. However, since several transitions have been identified, a full circuit analysis can be performed to predict the circuit parameters. At this point, María Hita at Dr. Juan José García Ripoll at CSIC is working on this parameter extraction.

6.4 Flux Qubit Coherent Control

6.4.1 Rabi oscillations

Similar to the transmon measurements in Section 4.2.3, the Rabi oscillations presented here are the first-ever time-domain experiments performed on flux qubits at IFAE. Thus, these oscillations constitute an important milestone in the project of building a quantum annealer.

In Fig. 6.23, Rabi oscillations for the qubit at 6.65 GHz and $f = 0.47$ external

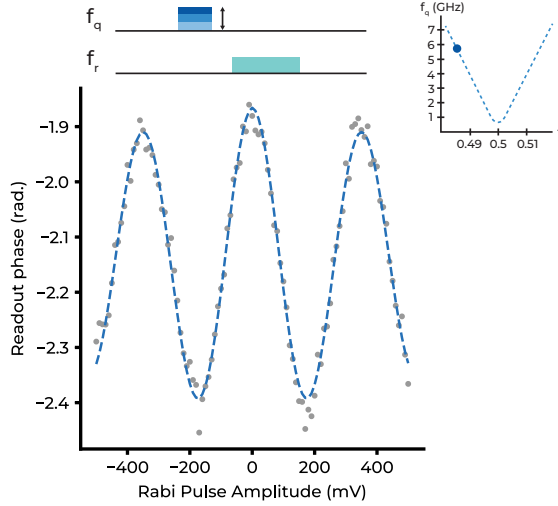


Figure 6.23: Rabi oscillations prior to any pulse optimization. Rabi sequence and flux location on top of the figure. Data points in gray circles and fit in dashed blue line.

flux are performed. These oscillations show that the 2π pulse does not return all the population to $|0\rangle$, meaning some loss by driven evolution, either through energy decay or dephasing. Studying the decay of these oscillations, as done in Section 6.4.4, would give insights of the dominant decay mechanism.

This first Rabi experiment allows for a preliminary π -pulse and f_q calibration. The readout setup is to be optimized prior to obtain the coherence characterization of the qubits.

6.4.2 Readout calibration

Once coherent control of the qubit is achieved, the readout pulse can be optimized. The main goals of this optimization are to increase the signal-to-noise ratio (SNR) and to ensure that the photon number in the resonator is low enough to avoid qubit excitations.

The readout calibrations shown below are obtained for $f \approx 0.486$, but has to be performed for every different flux. The qubit-resonator coupling is modified at the different flux locations, which changes the specific optimal readout location. This is especially relevant for the readout frequency, since it depends strongly on the dispersive change, which can change noticeably along the whole flux range.

6.4.2.1 Readout frequency calibration

The readout driving frequency, f_d , is optimized to yield the largest qubit signal by measuring a resonator trace with and without a π pulse on the qubit

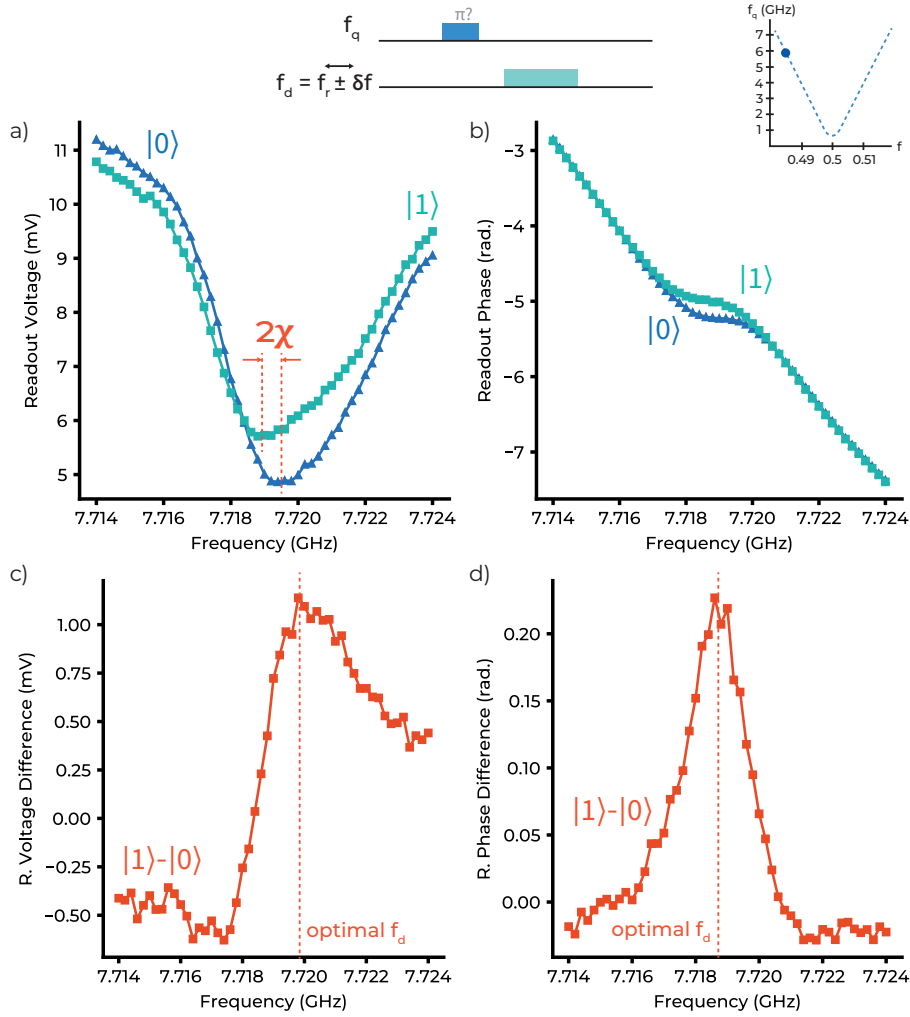


Figure 6.24: Readout frequency calibration. The pulse sequence (top) consists of reading out the qubit state at different readout frequencies and comparing the results when the qubit is at $|0\rangle$, and when a π pulse sets the qubit initially at $|1\rangle$. This calibration is performed at $f = 0.486$, as shown on top right. a) Readout voltage magnitude when the qubit is in $|0\rangle$ (dark blue triangles) and $|1\rangle$ (light blue squares). b) Readout phase when the qubit is in $|0\rangle$ (dark blue triangles) and $|1\rangle$ (light blue squares). c) Readout voltage magnitude difference between the qubit in $|0\rangle$ and in $|1\rangle$. d) Readout phase difference between the qubit in $|0\rangle$ and in $|1\rangle$.

(Fig. 6.24). At the top of the figure, the readout frequency calibration sequence is shown, where the complex readout response is measured at different f_f , with the qubit population in $|0\rangle$, and then with the qubit population in $|1\rangle$ after a π -pulse.

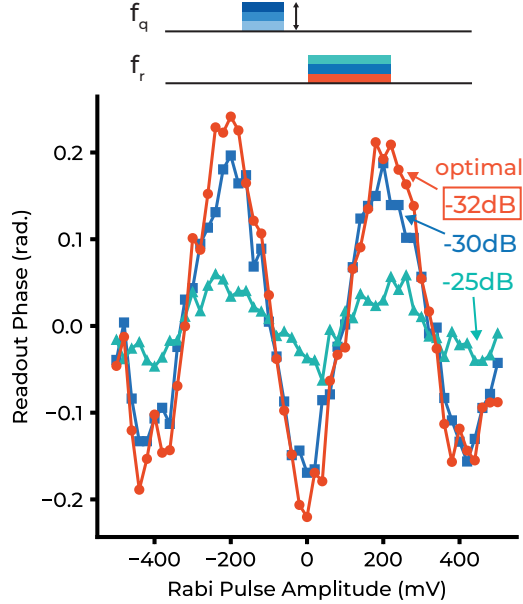


Figure 6.25: Readout power calibration. Rabi sequences at different readout powers, which shows better SNR for the lowest power, at -32 dB.

The transmitted signal for both cases is shown in Fig. 6.24a) and the phase response in Fig. 6.24b). By subtracting the two traces from different qubit populations, the optimal operation point is identified for both magnitude measurement (Fig. 6.24c)) and phase measurement (Fig. 6.24d)). The two optimal operation points are different and, indeed, the optimal phase difference is usually located where the magnitude measurement is minimal. Thus, only one of the two measurement types can be optimized. The phase measurement is chosen, since the SNR is known to be higher [Gam07] and already gave better results in spectroscopy for this device.

The f_r calibration also allows to measure the dispersive shift, χ , as will be explained in Section 6.4.3. In this measurement, $2\chi = 1.5 \times (2\pi \times \text{MHz})$.

6.4.2.2 Readout power calibration

Large readout pulse power can lead to more output signal, which could be better for higher SNR. However, too many photons in the resonator may induce qubit-state transitions that lead to lower measurement fidelity from decay or excitation during the measurement, as already explained in Section 4.2.4.1 for transmon qubits.

In Fig. 6.25, Rabi oscillations are seen for different input power attenuation. The attenuation is added after the pulse generation. Higher powers lead to

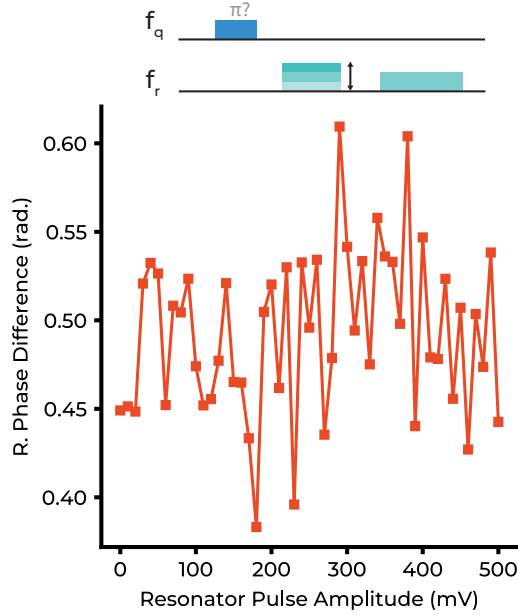


Figure 6.26: Readout amplitude calibration. Sequence on top, readout phase difference for states $|0\rangle$ and $|1\rangle$ is shown for varying a varying resonator amplitude pulse placed between qubit and readout pulses. No change in readout efficiency shows no photon-induced qubit transition are excited.

the lowest SNR, while for lower powers than -32 dB attenuation, the Rabi oscillations have the highest SNR.

In Fig. 6.26, a sequence is shown where the qubit population is initialized in $|0\rangle$ or in $|1\rangle$, this latter obtained with a π -pulse. Then, a resonator tone is sent at varying amplitude and, finally, the readout tone is sent. If the first fictitious readout tone caused any decay or excitations, this should be seen as a reduction on the phase difference. As shown in Fig. 6.26, no noticeable difference is seen over the whole range of amplitudes used, and the fluctuations are within the noise range. This implies that for this particular setup the readout power is fit for qubit measurements.

6.4.2.3 Readout duration calibration

In general, the shorter the readout pulse, the faster the sequence can be made and the faster the computer communication with both the digitizer and AWG will be. This reduction in time is very important, since, as no qubit reset is applied, the repetition time has to be increased to ensure that the qubit has fully decayed to $|0\rangle$.

In Fig. 6.27, the readout sequence is shown, together with the measured resonator response. Similar to readout power calibration, two sequences are

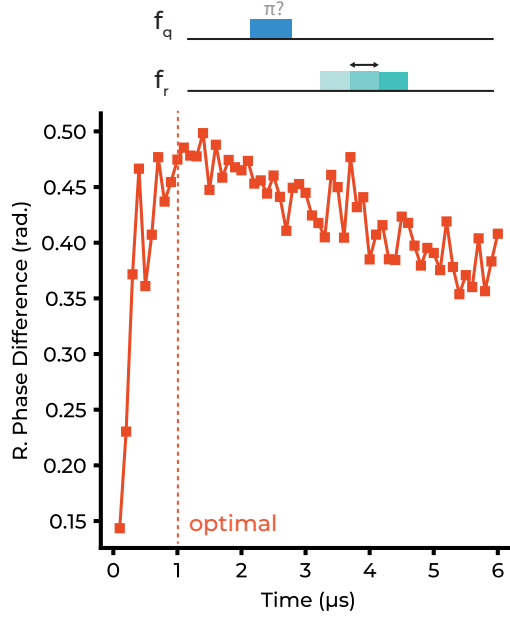


Figure 6.27: Readout pulse length calibration. Sequence on top, the difference in readout phase between qubit in $|0\rangle$ and in $|1\rangle$ for a readout pulse of varying duration. The optimal point is achieved around $1 \mu\text{s}$.

performed, one with an initial π pulse and the other one with the qubit left in $|0\rangle$. Then, the readout pulse is varied in length. Looking at the difference between both, the optimal pulse duration is set to be $1 \mu\text{s}$ for this experiment. At low readout duration, not enough signal is collected and both states output similar results. This readout difference increases until an optimal point, and then it starts to decrease, probably limited by qubit decay during readout.

6.4.3 Resonator Dispersive Shift

The calibration of the readout frequency also returns the value of χ , as seen in Section 6.4.2.1. In Fig. 6.28, χ is plotted for different flux biases, together with the qubit frequencies. As already showed in Section 5.4,

$$\chi = \frac{1}{2} \left(\sum_{j \neq 0} (\chi_{0j} - \chi_{j0}) - \sum_{j \neq 1} (\chi_{1j} - \chi_{j1}) \right), \quad (6.12)$$

with terms χ_{ij} are

$$\chi_{ij} = \frac{|g_{ij}|^2}{\omega_{ij} - \omega_R} \equiv \frac{|g_{ij}|^2}{\Delta_{ij}}, \quad (6.13)$$

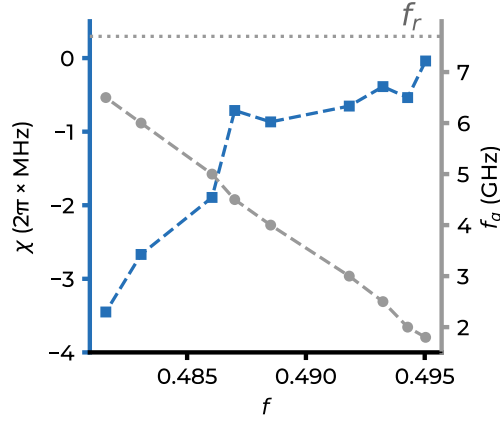


Figure 6.28: Resonator dispersive shift, χ , for different flux values in blue squares (left axis). In gray circles (right axis) the qubit frequency is also plotted, and the dotted gray line indicates the resonator frequency. As expected, the closer both frequencies get, the higher is the dispersive shift. Closer to the symmetry point, χ almost vanishes, making it very difficult to measure the qubit.

where ω_{ij} is the qubit transition frequency between levels j and i keeping the corresponding sign. g_{ij} is the coupling element matrix for the qubit-resonator system.

As seen in Fig. 6.28, χ increases in magnitude the closer f_q gets to f_r , which would indicate that term χ_{01} is dominant, unlike the simulations where χ_{12} was the most important term. This can be caused by the large deviation between measured qubit transitions and the designed ones. Moreover, χ vanishes when close to the symmetry point, which makes very challenging measuring the qubit state at that point.

6.4.4 Rabi oscillations decay time

In Fig. 6.29, time-domain Rabi oscillation are shown is seen at two different flux bias points of the qubit away from the symmetry point. The Rabi decay is considered to be

$$A(t) = A_{\text{Rabi}}(t) \cos(\Omega t + \phi_0), \quad (6.14)$$

where $A_{\text{Rabi}}(t)$ is an exponentially decaying envelopment, if quasistatic noise is neglected [Yos14], and Ω is the Rabi frequency and ϕ_0 the initial phase. A_{Rabi} decays as

$$A_{\text{Rabi}}(t) = A_0 \exp(-\Gamma_R t), \quad (6.15)$$

where A_0 is the initial Rabi oscillations amplitude and

$$\Gamma_R = \frac{3 - \eta^2}{4} \Gamma_1 + \Gamma_{f_{\text{Rabi}}} \quad (6.16)$$

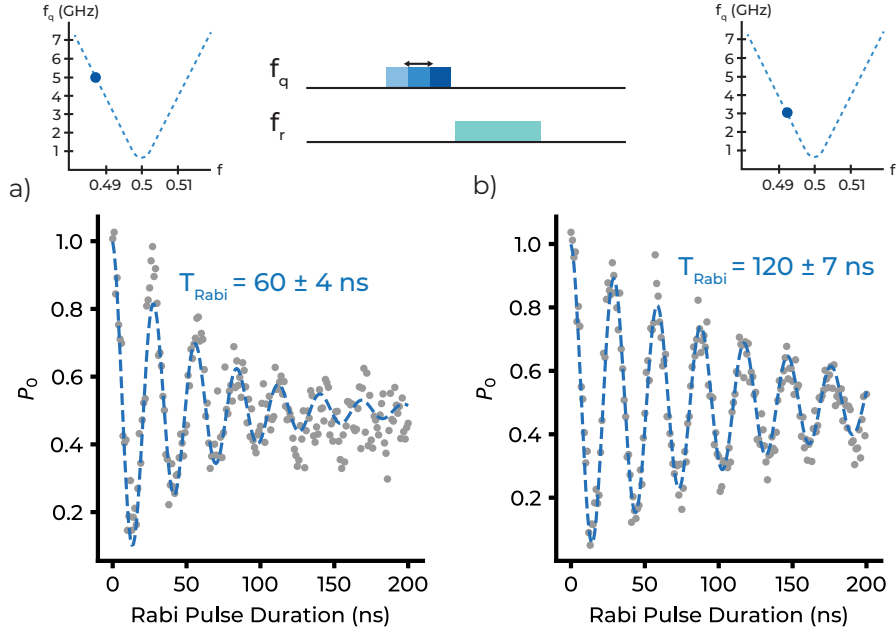


Figure 6.29: Two Rabi decay traces for different qubit frequencies: a) $f_q = 5$ GHz and b) $f_q = 3$ GHz. Both sequences consist in a Rabi sequence where the qubit pulse is changed in duration (see sequence on top), and the flux location is shown on top of the figures. Data points are shown as light gray circles, while fit is shown on blue dashed line.

with $\eta = \delta f / f_{\text{Rabi}}$ being the ratio between the detuning driving frequency, $\delta f = f_{\text{drive}} - f_q$, and the Rabi frequency, f_{Rabi} . $\Gamma_1 = 1/T_1$ is the qubit decay rate and $\Gamma_{f_{\text{Rabi}}}$ is the decay rate caused by the low frequency noise at f_{Rabi} . $\Gamma_{f_{\text{Rabi}}}$ contains low-frequency noise that causes dephasing. Therefore, it describes dephasing at different f_{Rabi} , so it can be used as a noise spectrometer in the kHz – MHz regime [By11].

For both flux points shown in Fig. 6.29, the Rabi decay is considerably fast, which could be caused either by Γ_1 or $\Gamma_{f_{\text{Rabi}}}$. The fact that there is a factor 2 in the decay rate between both qubit frequencies means that the qubit is more exposed to decoherence at 5 GHz, than at 3 GHz. It is expected that qubit T_1 increases for larger ϵ/ω_q as the qubit dipole to flux decreases [Yos06]. This implies that the term $\Gamma_{f_{\text{Rabi}}}$ dominates the decay, probably due to enhanced flux noise or Purcell emission to the resonator. For properly identifying the origin of decoherence, T_1 and T_2 measurements at different frequencies will be performed.

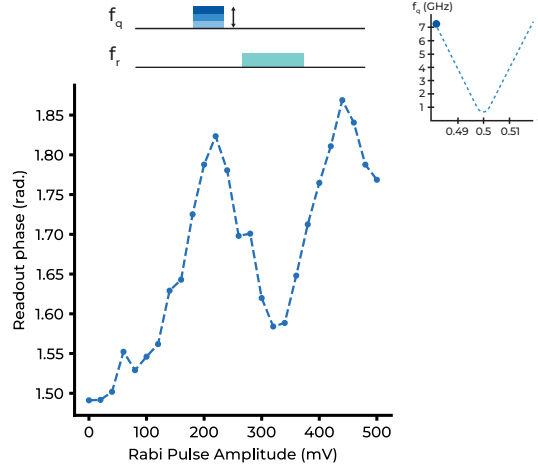


Figure 6.30: Rabi oscillations at $f_q = 7.1$ GHz. The behavior strongly deviates from usual Rabi oscillations, probably caused by the enhanced interaction with the resonator due to both frequencies being close together (see top right for flux location).

6.4.5 Rabi oscillations for different frequencies.

Rabi oscillations could not be observed throughout the whole qubit spectrum. At $f_q > 6.5$ GHz, oscillations are poor, and the behavior heavily deviates from a squared cosine as can be seen in Fig. 6.30. This can be caused due to the close proximity with resonator frequency, around 7.5 GHz, causing strong Purcell emission and even coherent dynamics with the resonator.

At very low qubit frequencies, lower than 1.6 GHz, no sign of Rabi oscillations is seen. The resonator naturally acts as a filter to frequencies away from the resonance. Very low frequencies are heavily filtered by the resonator, requiring more and more power to excite the qubit. At some point, the microwave source cannot produce more power and the qubit pulse is required to be very long. If Rabi decay, as shown before, is fast, long pulses are not effective. Thus, controlling the qubit at low frequencies becomes very challenging.

Another reason for not observing Rabi oscillations at low frequencies could be thermal excitations. 25 mK correspond to ~ 500 MHz, higher than the qubit gap. Moreover, it is believed [Zmu12] that real electronic temperature is higher than the measured one with usual thermometers, which could lead to a high excited state population, leading to Rabi oscillations with a very low contrast.

6.4.5.1 Reset protocol

Actively resetting the qubit population could be an alternative to detect qubit coherence at the symmetry point where $\Delta \lesssim k_B T$. However, the method [Gee12] used in transmon experiments in Section 4.2.4.4 could not be performed.

In Fig. 6.31, it is seen how f_q is modified when a π -pulse is applied at the

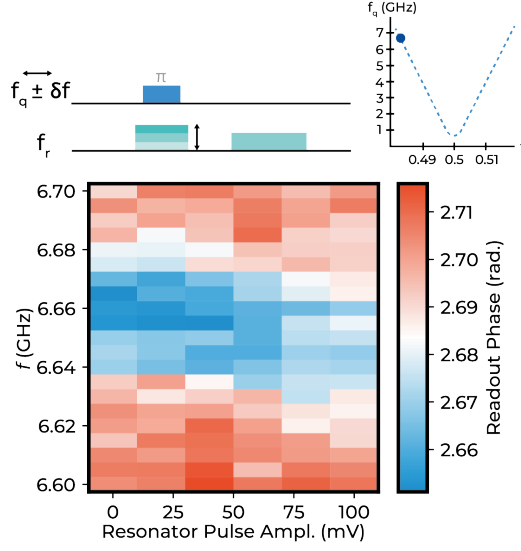


Figure 6.31: Qubit frequency modified by the resonator photons. The sequence consists on sending a π pulse at the same time as a resonator pulse, before the readout. The resonator pulse is varied in amplitude. For higher values, the qubit frequency gets Stark-shifted by the resonator photons, so the π pulse qubit frequency gets modified.

same time as a resonator pulse of increasing amplitude. The qubit is biased at $f \approx 0.481$, for leveraging the higher χ . When more photons are added into the resonator, $f_q \rightarrow f'_q = f_q + \delta f_q$ with

$$\delta f_q = \frac{2\chi n_{\text{photons}}}{2\pi}. \quad (6.17)$$

Then, the blue (low phase) part in Fig. 6.31, which corresponds to the excited population peak after the π -pulse, is obtained at f'_q . However, it can be seen that while f'_q is modified, there is also a strong reduction in amplitude.

The small dispersive shift, $2\chi \approx 1.5 \times (2 \times \text{MHz})$, compared to the qubit linewidth $\sim 5 \text{ MHz}$, requires many photons to modify noticeably f_q , as seen from Eq. (6.17). This large n_{photons} can induce qubit transitions, as commented in Section 6.4.2. A larger χ or a more coherent qubit for instance if one could measure at the symmetry point, could allow to perform the reset protocol.

6.4.6 T_1 measurements

A single trace of a T_1 measurement at $f_q = 3 \text{ GHz}$ is shown in Figure 6.32, with $T_1 = 14.5 \mu\text{s}$. However, T_1 is known to vary over time [Kli18] so, in order to have a good estimate for T_1 measurements, repeated measurements must be performed.

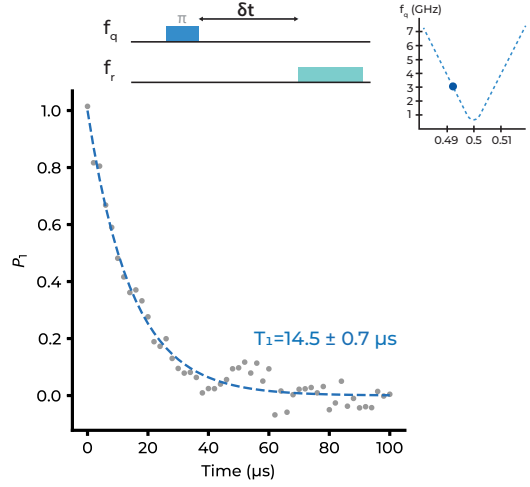


Figure 6.32: Single trace of a T_1 measurement performed at qubit frequency $f_q = 3$ GHz. The T_1 sequence is shown on top, along with the bias point where the qubit is operated.

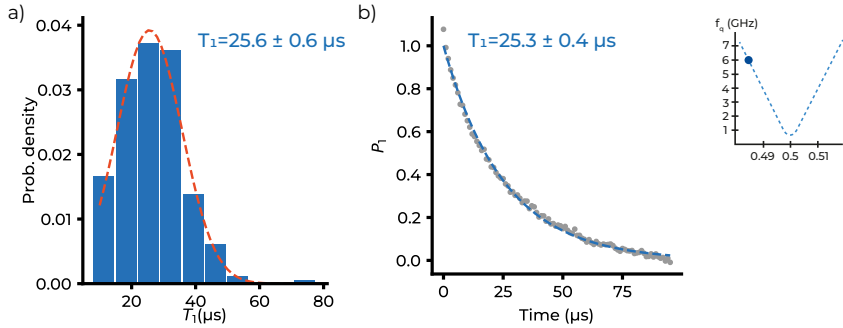


Figure 6.33: a) T_1 histogram for a $f_q = 6$ GHz. The T_1 measurement is repeated 256 times. b) Average of all the traces in the histogram. Flux location is shown on the right.

In Fig. 6.33a), the collected histogram of T_1 measurement for $f_q = 6$ GHz is shown. 256 measurements, each with 5000 averages, are plotted. The distribution resembles a Gaussian distribution, with a mean of $25.6 \mu\text{s}$. For this case, the fit of the average of all the traces Fig. 6.33b) gives nearly the same T_1 value.

Figure 6.34 shows the same plot as before, but for $f_q = 4$ GHz. In this case, the distribution deviates more strongly from a Gaussian, which leads to a higher fit uncertainty. The value obtained with the histogram fit, $T_1 = 30.6 \mu\text{s}$, deviates from the fit of the averages of 100 traces (each averaged 5000 times), which is $T_1 = 41.7 \mu\text{s}$. This can be explained due to asymmetry in the histogram distribution, which has some higher T_1 values.

T_1 measured for different f is shown in Fig. 6.35, for both the histogram

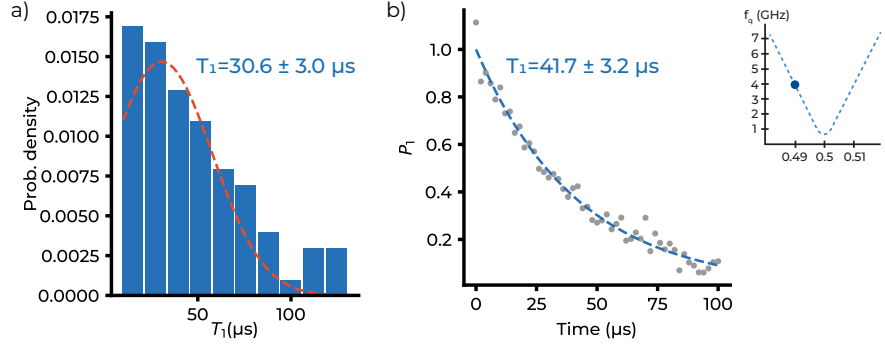


Figure 6.34: a) T_1 histogram for a $f_q = 4$ GHz. The T_1 measurement is repeated 100 times. b) Average of all the traces in the histogram. Flux location is shown on the right.

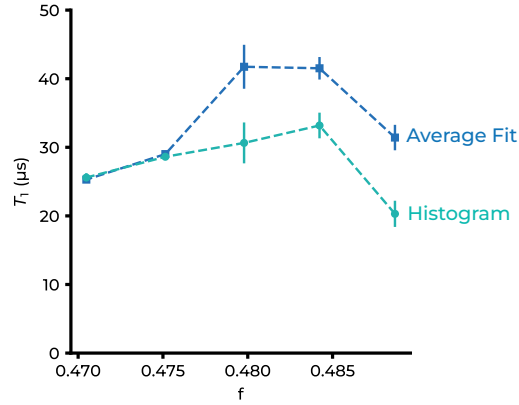


Figure 6.35: T_1 measurement for different qubit frequencies. Light blue circles represent the T_1 obtained by the histogram fit, while the dark blue squares represent the whole average fit.

method and the full average trace. The histogram method tends to give lower values, but both have the same non-monotonic behavior, where T_1 decreases in both extremes. For $f_q > 6$ GHz, qubit frequency is closer to the resonator one, $f_r \sim 7.719$ GHz. Therefore, the qubit-resonator coupling increases, potentially leading to Purcell-induced decay. Purcell decay rate, Γ_P , can be estimated as

$$\Gamma_P = \left(\frac{g}{\Delta_{qr}} \right)^2 \kappa, \quad (6.18)$$

where g is the qubit-resonator coupling, $\Delta_{qr} = f_q - f_r$ and κ is the resonator linewidth. For the $f = 0.47$ point in Fig. 6.35, $f_q = 6$ GHz and $\kappa = 3.6 \times (2\pi \times \text{MHz})$. g can be obtained from the dispersive shift, as $\chi = g^2/\Delta_{qr}$. At

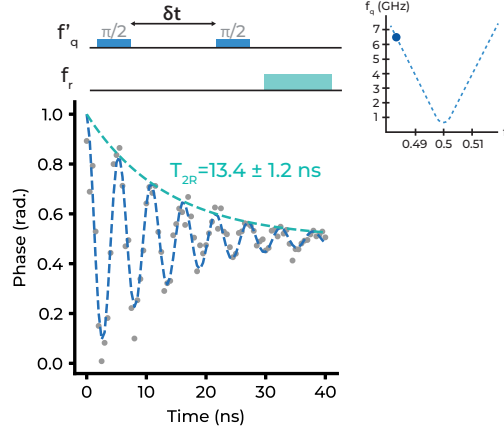


Figure 6.36: Ramsey oscillations measurement trace at qubit frequency $f_q = 6.4$ GHz. The Ramsey sequence is shown on top and the flux location on the top right.

that flux location, $\chi = -2.7 \times (2\pi \times \text{MHz})$. This corresponds to a Purcell decay $T_{1,P} \approx 28 \mu\text{s}$, consistent with the observed results.

For f closer to 0.5, a low $f_q < 2$ GHz has higher thermal population, which affects both excitation and decay mechanisms. The thermal relaxation rate, Γ_{th} , can be expressed as [For16]

$$\Gamma_{\text{th}} = \Gamma_0(1 + n_{\text{th}}), \quad (6.19)$$

where Γ_0 is the decay rate due to quantum noise and n_{th} is the thermal quasi-particle population, defined as

$$n_{\text{th}} = \frac{1}{e^{\hbar\omega/k_B T} - 1}. \quad (6.20)$$

For $\omega = 250 \times (2\pi \times \text{MHz})$ and considering $T_{\text{eff}} = 100$ mK, the natural decay is enhanced by a factor $1 + n_{\text{th}} \approx 9$. Moreover, at the symmetry point, the transition dipole is largest, and so is Γ_1 .

The obtained values of T_1 are comparable or better than typical results in flux qubits [Yan15; Byl11]. However, the value at the sweet spot is the lowest, and most of T_1 data in the literature has been obtained for this spot.

6.4.7 T_2 measurements

T_2 measurements are the standard approach to measure dephasing, as Ramsey decay depends on both T_1 and pure dephasing, T_φ . If both T_1 and T_φ are assumed to be exponential [Kra19],

$$\frac{1}{T_2} = \frac{1}{2T_1} + \frac{1}{T_\varphi}. \quad (6.21)$$

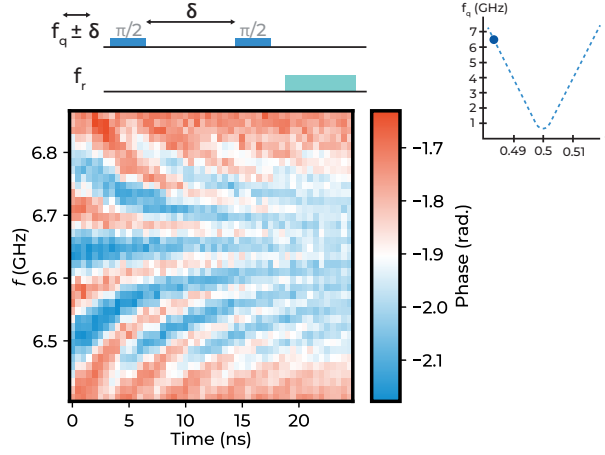


Figure 6.37: Ramsey fringes plot with sequence on top. It consists on Ramsey measurement traces for different qubit frequency pulses. Measurement shown Fig. 6.36 corresponds to a trace of this plot.

These measurements were much more challenging for these qubits as $T_2 \propto (\epsilon/f_q)^{-2}$. Far from the sweet spot, where all the successful Rabi measurements have been performed, T_2 is expected to be very low due to $1/f$ flux noise. This is also consistent with the assumption that the small T_{Rabi} is caused by the same noise that origins dephasing, since T_1 is very high.

Indeed, it was considerably difficult to perform a Ramsey measurement at many flux values. Moreover, typical Rabi pulses used for T_1 and amplitude Rabi oscillations were ~ 30 ns large, which represent a very long time for dephasing to degrade the qubit state. Instead, very short pulses were needed to perform Ramsey measurements. In Fig. 6.36, a Ramsey trace is shown, with the sequence shown on top (see Section 2.7.2). The fitted exponential decay leads to $T_{2R} = 13.4$ ns, which is a very low value. Since $T_1 \gg T_{2R}$, the dephasing time is $T_\varphi \approx T_{2R}$ (see Eq. (6.21)).

In Fig. 6.37, a Ramsey fringes experiment is shown. Ramsey fringes are a series of Ramsey measurements at different qubit driving frequencies, and used to identify the actual f_q , which is the point where no oscillations are observed as a function of time. The fact that very short pulses are needed for such a small decay time, causes a qubit resonance linewidth of ~ 40 MHz.

The rapid decay of the Ramsey fringes indicate that dephasing is very high, which is likely caused by flux noise. One solution would be to reduce I_P , whose value was higher than designed. Also, extra shielding in the setup could help to reduce overall flux noise. Finally, it is needed to observe these fringes at the sweet spot to have more insights about the origin of the noise.

6.5 Conclusions & Outlook

Flux qubits presented in the previous chapter have been physically designed and manufactured in two different fabrication facilities. In the third generation of devices, time-domain measurements have been successfully performed, which has given insights on how to improve the designed flux qubits.

Large T_1 over many parts of the qubit spectrum are a promising result for quantum annealing. However, low T_{2R} and the difficulty to measure at flux values close to the sweet spot indicate that some improvements must be implemented. A detailed flux-dependent noise analysis would give insights on which are the most prominent errors, although flux noise seems a plausible responsible given the low T_{2R} .

The qubit Δ strongly deviates from design, which indicates that there has probably been some fabrication deviation from nominal values. Therefore, the analysis on the thermal noise for the designed gaps as not been achieved. Moreover, the distinction between floating and grounded qubit loops is still work in progress, as only floating devices has been successfully characterized.

From the results, it is clear that a large Δ should be aimed to reduce potential thermal noise. However, it has been seen that the experiment would benefit from a higher χ , which can easily be obtained by increasing the coupling between the qubit and the resonator. Moreover, these large χ , together with higher coherence, could enable to perform a reset protocol that could enable to operate at the symmetry point, even for lower Δ .

The first improvement requires is to have a better fabrication process to attain qubit values closer to the nominal ones. Otherwise, it is difficult to analyze the Hamiltonian design, as the extraction of the parameters from the spectrum is not trivial. Then, in order to measure at the sweet spot, both χ and Δ has to be increased. Controlling the qubit through the flux line could also help in this regard to overcome the resonator filtering. Finally, it may be needed to further reduce I_P or increase the magnetic shielding environment to achieve larger dephasing times.

The results in this chapter pave the way for future designs of a quantum annealer processor. Coupling qubits can be achieved by adding a rf-SQUID in between two qubits[Web17], without modifying the rest of the physical design. Moreover, if the qubit can be measured at the sweet spot, single-qubit annealing schedules can be performed, and understand the noise mechanisms that affect the qubit during the anneal passage.

Chapter 7

Magnetic Penetration Depth of Aluminum

DAVID LÓPEZ-NÚÑEZ, QUERALT PORTELL MONTSERRAT, GEMMA RIUS, ELIA BERTOLDO, ALBA TORRAS-COLOMA, M. MARTÍNEZ, P. FORN-DÍAZ *

Superconducting aluminum is arguably the most used material in superconducting qubits [Bro23; Kim23; Bla21; Pér21]. However, its thin-film characteristics are not yet fully characterized. This chapter focuses on studying the magnetic penetration depth, λ , of aluminum as it changes with film thickness. λ is a very important parameter that defines the kinetic inductance, L_k , of the material, becoming very important in flux-sensitive devices, such as flux qubits and couplers. Moreover, along with the coherence length, ξ , it defines the type of superconductivity of the material.

Section 7.1 gives a brief recap on superconductivity theory. The focus of this introductory section is to define the superconducting length scales, λ and ξ , how their relation shapes the superconductivity type, and the thickness effects on them. Many of the concepts introduced in this section are usually overlooked in superconducting qubit circuit design, which sometimes leads to inaccuracies in the circuit parameters, particularly in circuits that depend on kinetic inductance value.

In Section 7.2, the experimental model is presented, and details how λ is determined from the measurements: both through resonator and 4-probe resistance measurement. This resonator model requires precise determination of the inductance and capacitance used to determine λ . These resonators are simulated with Sonnet in Section 7.3. Then, the final designs are shown in Section 7.4.

The experimental description along with the fitting analysis is explained

*Part of the contents of this chapter are being published, currently in preprint arXiv:2311.14119.

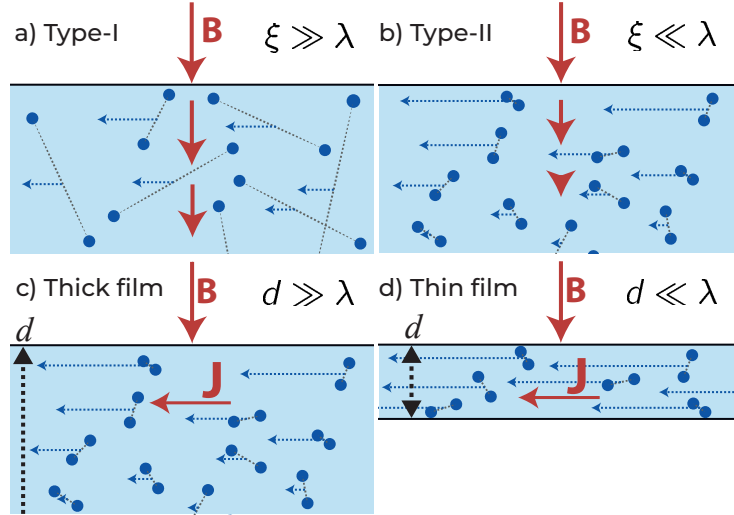


Figure 7.1: **a)** Type-I superconductors, where response to the external magnetic field is non-local. Each Cooper pair reacts to the magnetic field at its center of mass, since the average Cooper pair size ξ is much larger than the typical distance at which the magnetic field decays, λ . This effectively reduces the field response, allowing the magnetic field to penetrate further into the material, thus increasing the penetration depth. **b)** In type-II superconductors, ξ is smaller than λ , and the response is local, since both electrons of the Cooper pair are very close. **c)** Schematic representation of a local thick superconductor, where the London equations are valid. The current response to the magnetic field follows $\vec{j}_S = -\frac{e_0}{\lambda^2} \vec{A}_S$. **d)** In very thin films, the Cooper pair number density is lower, and each Cooper pair has to increase its velocity to provide the same supercurrent \vec{j}_S as in thicker films, since London equations are still valid. The kinetic inductance increases dramatically in this situation, as it is proportional to the squared velocity, $L_k \propto v^2$.

in Section 7.5. The results of the experiment are explained in Section 7.6, where λ dependence on thickness, d , is shown. Furthermore, an estimation on the critical thickness, d_{cr} , at which the superconducting types change for aluminum is given, along with an analysis of the design variability. The results are discussed in Section 7.7, and final conclusions and future work are detailed in Section 7.8.

7.1 Theoretical Background

In general, the superconductivity type exhibited by a given material reflects the interplay between the magnetic penetration depth λ and its coherence length ξ , which corresponds to the average distance between the electrons forming a Cooper pair [Pip53].

The thickness of a thin film affects its internal microscopic structure, modifying both λ and ξ and the rest of parameters that depend on them. In particular, the kinetic inductance L_k has a strong dependence on λ through [Rot16; Mat58;

Kau08; Tur91]

$$L_k = L_{k,s}N = \mu_0\lambda N, \quad (7.1)$$

where $L_{k,s}$ is the surface kinetic inductance, or kinetic inductance per square, which depends on the film thickness d . N is the number of squares of a given wire. For wires with constant cross section, we have $N = l/w$, where l and w are the wire length and width, respectively. Otherwise, N becomes a position-dependent parameter.

In bulk aluminum, the response of the superconductor to magnetic fields is non-local [a qualitative picture is given in Fig. 7.1a)], causing a larger value of λ than the one predicted by the London equations $\lambda_L = 15.7$ nm. Since the Al bulk coherence length is $\xi_0 = 1.6$ $\mu\text{m} \gg \lambda_L$, bulk aluminum is in the non-local limit. In the non-local limit, λ is modified by [Gen18]

$$\lambda = 0.65(\lambda_L^2\xi_0)^{1/3}, \quad (7.2)$$

which, in the case of aluminum, is $\lambda_{\text{bulk}} = 50$ nm [Gen18; Fab55]. Thus, bulk aluminum satisfies type-I superconductivity criteria, $\xi_0 > \lambda_{\text{bulk}}$.

However, decreasing the film thickness d eventually decreases the aluminum grain size as well [Mes71], thereby reducing the electron mean free path, l . In this regime, an effective coherence length $\xi < \xi_0$ at $T = 0$ K can be defined [Sai69; Gen18]

$$\frac{1}{\xi} = \frac{1}{\xi_0} + \frac{1}{l}, \quad (7.3)$$

which, in the dirty superconductor limit $\xi_0 \gg l$, also modifies λ as

$$\lambda = a\lambda_L\sqrt{\frac{\xi_0}{l}}. \quad (7.4)$$

a is of order unity which depends on the surface scattering type, being $4/3 \approx 1.33$ for diffusive scattering and $\sqrt{4/3} \approx 1.15$ for specular reflection [Tin04]. Eq. (7.4) is a reasonable approximation, particularly when $l \sim d$. Accordingly, by lowering d , one may reach the regime where $\xi < \lambda$, causing the film to become a type-II superconductor, where the response to external fields is local [see Fig. 7.1b)]. The transition between superconductivity regimes is determined by the Ginzburg-Landau parameter κ [Tin04]

$$\kappa \equiv \lambda/\xi. \quad (7.5)$$

Above $\kappa = 1/\sqrt{2}$, the superconductor can be categorized as type-II since the normal-superconductor interface energy becomes negative, thus allowing for the generation of normal paths (vortices) [Abr57]. For thick enough films, κ decreases below $1/\sqrt{2}$ and the film exhibits vortex-free behavior, thus entering the type-I superconductivity regime. By carefully choosing the thicknesses of different thin films, this boundary between superconductivity types occurring at a critical thickness d_c may be attained. In actual thin films, local fluctuations in κ are expected given the disordered nature of the film, thus leading to a spread of values of d_c over which the transition takes place.

For very thin films with thickness in the range of $d \lesssim \lambda$, the response of the film to external perpendicular magnetic fields follows the London equations, reacting with an opposing current \vec{j}_S to an incoming field \vec{A}_S . Since $d \lesssim \lambda$, \vec{A}_S fully penetrates the film. Nevertheless, the expression $\vec{j}_S = -\frac{\mu_0}{\lambda^2} \vec{A}_S$ remains valid [Pea64]. In this scenario, the supercurrent response to \vec{A}_S is the same regardless of the film thickness. However, as thinner films contain a lower amount of charge carriers, Cooper pairs are compelled to attain higher velocities, resulting in a substantial increase in L_k (see Fig. 7.1d), since $L_k \propto v^2$. The correction to $L_{k,s}$ due to this effect is given by [Kau08]

$$L_{k,s} = \mu_0 \lambda \coth \frac{d}{\lambda} \equiv \mu_0 \lambda_{\text{thin}}, \quad (7.6)$$

where λ_{thin} represents an effective penetration depth. For $d \gg \lambda$, $\lambda_{\text{thin}} \rightarrow \lambda$, while for $d \ll \lambda$, $\lambda_{\text{thin}} \rightarrow \frac{\lambda^2}{d}$, significantly enhancing $L_{k,s}$. Resonator measurements, as will be detailed in the next section, give direct access to L_k , which can be used to derive λ_{thin} through Eq. (7.6), and then used to calculate λ .

Finally, λ can be related to the normal metal properties of the thin film as it ultimately depends on the charge carrier properties. Specifically, in the dirty limit with $\xi_0, \lambda \gg l$, λ is related to the normal state resistivity ρ_n of the metal at $T = 0$ K, through [Hak67]

$$\lambda \simeq 105 \text{ nm} \sqrt{\frac{\rho_n (\text{m}\Omega \text{ cm}^{-1})}{T_c (\text{K})}}, \quad (7.7)$$

where T_c is the superconducting critical temperature. Therefore, for each given thickness d , the value of λ estimated through Eq. (7.6) can be validated against the values of resistance of thin films of the same nominal thickness d .

Equations (Eq. (7.6), Eq. (7.7)) allow a complete characterization of λ and L_k of thin superconducting films, and are the key expressions used in this chapter.

7.2 Methodology

Following from the previous section, two independent approaches are employed to measure λ in aluminum thin films, along with $L_{k,s}$. The first method involves resonator measurements combined with finite-element simulations, where the effect of λ is reflected in the measured resonance frequency. The second approach utilizes four-probe measurements on resistive aluminum meanders.

The resonator measurements give access to λ through λ_{thin} , while the resistance measurements give direct access to λ . Fabrication inaccuracies affect both methods differently. Discrepancies between nominal and real dimensions are much more difficult to track in resonators than in four-probe designs. λ_{thin} is also much more sensitive to deviations in the thickness d . Resistance measurements are, thus, more robust. However, we include resonators in this work as they represent a good benchmark of a real-case scenario where calibrated values of λ are used to predict the values of L_k of a resonator circuit. Therefore, the

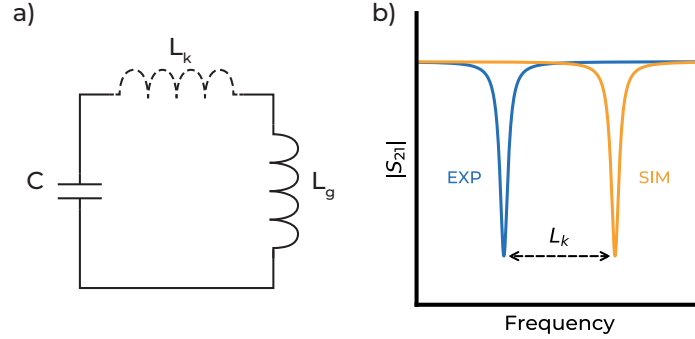


Figure 7.2: **a)** LC Resonator circuit schematic. In the simulations conducted, no kinetic inductance is considered, while in the experiment the kinetic inductance L_k contribution appears merged with the geometric inductance L_g . **b)** Simulated and experimental resonances are assumed to only deviate due to L_k .

resistance measurements in this study are in fact used to validate the resonator measurements.

7.2.1 Resonance Method

Lumped element LC resonators were chosen for this study in order to achieve a more controlled definition of their inductance L and capacitance C , compared to distributed resonators. LC resonators are characterized by their resonance frequency $\omega = (LC)^{-1/2}$, where C represents the capacitance and $L = L_g + L_k$ is the sum of geometric and kinetic inductances. As explained in Section 7.1, superconductors may exhibit a significantly high L_k , especially for thin films with $d \ll \lambda$.

In order to extract L_k , we first perform an accurate simulation of each resonator studied considering a perfect conductor, thus obtaining L_g and C that lead to a simulated resonance frequency f_{sim} [Figure 7.2 a) with $L_k = 0$]. Resonator measurements provide f_{meas} as they contain a total inductance $L = L_g + L_k$ [Figure 7.2 a)], so $f_{\text{sim}} > f_{\text{meas}}$. L_k may be then obtained with

$$L_k = L_g \left(\frac{f_{\text{sim}}^2}{f_{\text{meas}}^2} - 1 \right). \quad (7.8)$$

The L_k obtained in this way determines λ_{thin} using Equation (7.6). This method requires a precise simulation of the perfect conductor resonance f_{sim} (see Section 7.3).

7.2.2 Resistivity Method

Resistance measurements directly lead to λ through Eq. 7.7. Since ρ_n is the normal state resistivity at 0 K, it can only be measured by destroying the

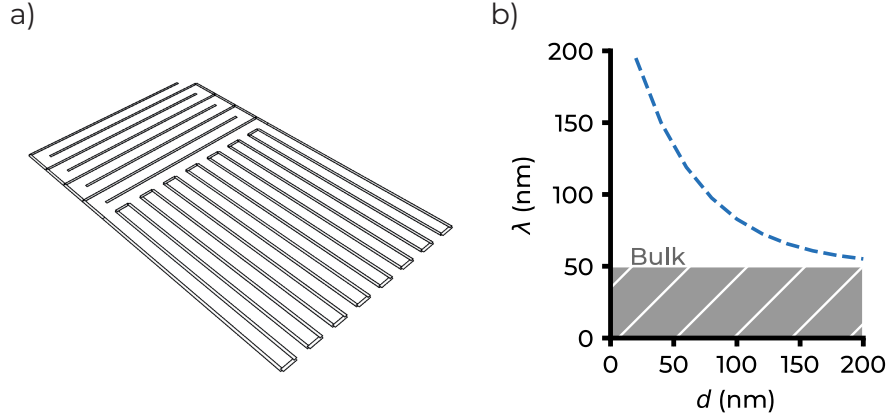


Figure 7.3: a) Initial LC resonator design in FastHenry for α predictions. b) Estimation of λ at different thickness for FastHenry simulations.

superconducting state with an external magnetic field. However, the aluminum resistivity is nearly constant at low temperatures, so we instead approximate ρ_n with the value at 4 K.

It is important to note that ρ_n is connected to λ and not to λ_{thin} as in the resonator method. ρ_n and λ are connected through the properties of the material, such as the charge carrier mass, the Cooper pair number density, and the electron mean free path. Thus, the thin-film effects described in Eq. (7.6) do not play a role in the determination of λ through ρ_n .

7.3 Resonator simulations

An accurate determination of λ through resonator measurement, requires precise simulations to obtain f_{sim} with Eq. (7.8). In this section, the whole body of simulations are exposed, which constitute an indispensable part of this work. Noticeably, these simulations highlight the role of the thickness on the L_g , which, similarly to L_k , increases for decreasing thicknesses.

The design of the resonators as described in Section 7.4 have been performed parallelly to results obtained through the simulations. Thus, some design decision are developed here, leaving the final design parameters for Section 7.4.

7.3.1 FastHenry Simulations

Resonance measurement allow to indirectly compute λ by the extracted value of L_k . Therefore, the kinetic inductance fraction of the resonators, $\alpha \equiv L_k/L$, need to be sufficiently high for a proper estimation of L_k . We work in the range $\alpha = 0.02 - 0.5$, as lower α can incur in big inaccuracies, while higher α leads to

frequencies lower than our experimental system bandwidth (4 – 8 GHz). This α restrictions have to be fulfilled for the full thickness range considered in the work, which would be between 25 nm and 200 nm.

Before the final design, a prior estimation of α has to be performed. These initial simulations are performed with FastHenry*, a software used for calculating inductance that includes London equations so that both L_g and L_k .

The initial design considered for these simulations is shown in Fig. 7.3a), which consists of an LC resonator with meander inductor and finger capacitances. At this point, the number of meanders and fingers, along with its exact dimensions are yet to be determined.

FastHenry needs λ as an initial parameter, which is the goal of the study. A prior assumption is made by using some previous internally estimated values of λ at 25 nm and 50 nm thickness, and the known $\lambda_{\text{bulk}} = 50$ nm. The functional behavior is considered to be a decaying exponential, as shown in Fig. 7.3b).

The outcomes of these simulations results in the determination of the inductor shape, which consists of 15 meanders of 4 μm width and gap between the lines. The capacitor fingers later simulated should add to a resonance frequency of $\approx 7 - 8$ GHz. This inductor shape results in $\alpha = 0.47$ for 25 nm thickness and $\alpha = 0.03$ for 200 nm. These resonators are labelled as medium resonators, (MR).

In order to have some flexibility in case prior λ estimation was considerably wrong or if future designs intend to explore thickness regions further away from the 25 – 200 nm, two extra designs are considered. The small resonators (SR) have 2 μm meander width and spacing, and the large resonators (LR) have 6 μm for the same dimensions; both SR and LR having also 15 meander. The SR resonators have a considerably larger α aiming at very thick designs where L_k is reduced due to the decrease of λ . Large resonators, on the other hand, are intended to very thin samples, where very large λ can bring the LC resonance lower than 4 GHz, thus not allowing for our experimental setup to measure it.

Finally, the design variation is also intended to reduce systematic deviations in the λ determination due to discrepancies between nominal and real design.

7.3.2 Sonnet Simulations

An entire resonator simulation to obtain the system transmission is run with Sonnet[†]. Sonnet is a 2D finite-element solver commonly used to simulate the rf response of superconducting circuit structures.

For the rest of the section, the simulation of the MR resonators is exposed, unless specified otherwise. Similar results are obtained for the SR and LR resonators. The specific design of all the resonators is described in Section 7.4.

*We use the version found in <http://www.wrcad.com/ftp/pub/fasthenry-3.0wr-071720.tar.gz> which takes into account the London equations and thus the penetration depth λ in the inductance calculations.

[†]<https://www.sonnetsoftware.com/>

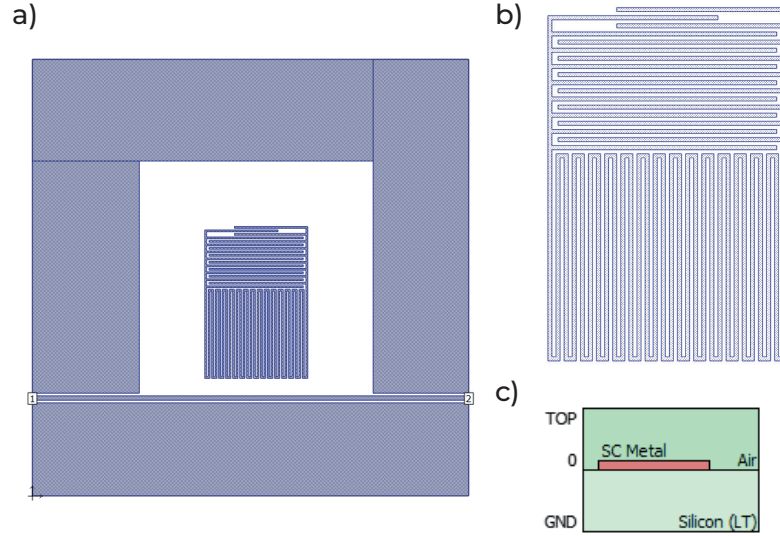


Figure 7.4: a) Simulated structure in Sonnet, consisting on a CPW feedline coupled to a LC resonator. Ports are located on the edges of the feedline. b) Zoom on the resonator structure. c) Sonnet layers, with Silicon at low temperature (LT) as the dielectric substrate and air on top. Aluminum is modelled as a perfect metal to model superconductivity.

7.3.2.1 Basic Simulation

The simulation design, as shown in Fig. 7.4a-b), consists of an LC resonator coupled inductively to a coplanar waveguide (CPW) feedline. The meander inductor from the resonator is the same as the decided with the FastHenry simulations. The capacitance fingers share the same dimensions with the meanders, $4 \mu\text{m}$ in width and spacing, and their number is to be determined so that the desired frequencies, $7-8 \text{ GHz}$ is obtained. The CPW feedline have $10 \mu\text{m}$ width and $6 \mu\text{m}$ gap for a characteristic impedance $Z_0 = 50 \Omega$.

The feedline and the resonator are inductively coupled, and placed $40 \mu\text{m}$ distance apart, so that mutual inductance is small so that it does not play a big role on the resonator inductance. Also, the resonator is considerably detached for the ground plane, at $150 \mu\text{m}$, so that also capacitance to ground can be disregarded, and the resonance is purely determined from resonators L and C .

The layer structure, shown in Fig. 7.4c), consists of high resistivity Silicon in the substrate, with aluminum, modelled as a 2D perfect metal layer, on top. Simulations performed with a perfect metal are a good approximation to the superconducting response with $L_k = 0$. Thus, the comparison between the simulations and the experiment can be considered to be caused by the effect of L_k .

The silicon used in the simulations has an $\epsilon_r = 11.45$, validated in ref. [Kru06]

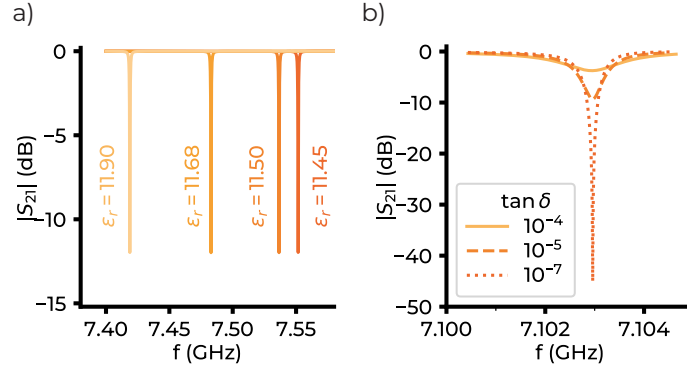


Figure 7.5: a) LC resonator response with varying Si relative permittivity, ϵ_r . Range of values is typically found in the literature. The actual value used in this work is $\epsilon_r = 11.45$ [Kru06]. b) Effect of Si loss tangent, $\tan \delta$, on the quality factor of LC resonators.

which was also the low-temperature value confirmed by the manufacturer[‡]. ϵ_r is very important, since different values of ϵ_r are found throughout the literature [Bru15; Göp08; Sat22; Web11], leading to a difference in the obtained λ of up to 100%. As seen in Fig. 7.5a), the value of a resonance changes noticeably for values of ϵ_r , where apart from $\epsilon_r = 11.45$, other values found in the literature are shown, 11.90 [Bru15], 11.68 [Web11], 11.6 [Göp08], and 11.50 [Sat22].

The silicon loss tangent, $\tan \delta$, is another important parameter to determine, which acquires a huge relevance when dealing with dielectric noise in qubits. However, in our study this value has no importance since it does not change the resonance of the device, just affecting its quality factor, as shown in Fig. 7.5b).

7.3.2.2 Determination of L_g and C

Sonnet simulations return the scattering matrix, with the focus of this work placed on S_{21} . The resonance frequency can be obtained by fitting a Lorentzian to the absolute value of the transmission. However, the specific value of each resonator L_g and C is not provided.

To separately determined L_g and C , the technique developed in [Doy08] is followed. It consists of adding a manual known sheet inductance (L_s) to the metallic layers, and repeating the simulation. This new resonance will only differ with the previous one by this inductance increase, $f'_{\text{sim}} = [(L_g + L_s)C]^{-1/2}$ (see Fig. 7.6a)). Therefore, there are two expressions with two unknown variables, L_g and C , which allow to calculate them. Sonnet can also return the current and charge distribution of the system, which is shown in Fig. 7.6b). There, it can be seen that most of the current is located in the meander, thus validating the lumped approximation of separate inductance and capacitance. However, an extra correction is performed for the accurate determination of the resonance,

[‡]<https://www.topsil.com/>

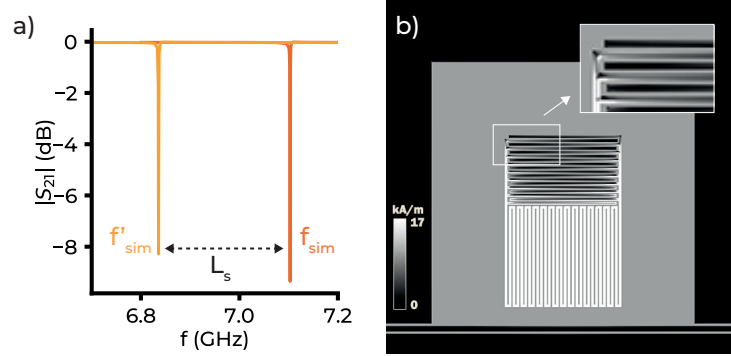


Figure 7.6: a) Basic MR Sonnet simulation (right) and simulation with an added sheet inductance, L_s . Both simulations, with known L_s allow for separate determination of L_g and C . b) Simulated current distribution of an LC resonator. The inset shows the current in the last capacitor fingers, where it is minimal.

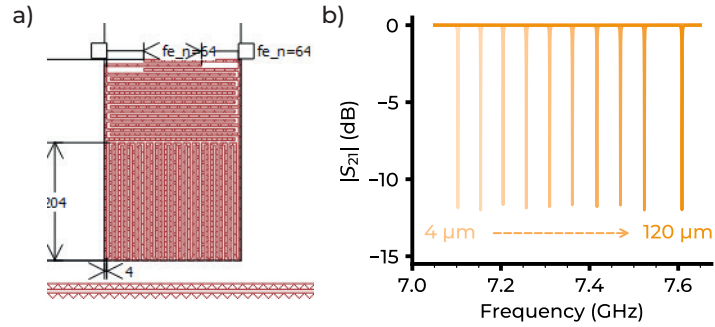


Figure 7.7: a) Sonnet picture of a simulated resonator. Only last three fingers (of M resonators) are changed to modify the resonator frequency. The finger lengths range from $4 \mu\text{m}$ to $120 \mu\text{m}$. b) Simulated resonator frequencies by modifying the spacing in the last fingers of the resonator. Resonances are separated $\propto 30 - 50$ MHz, enough to be distinguishable in the experiment.

as the effective length of the resonator is enhanced by a 2% obtained with this current simulations.

7.3.2.3 Frequency of the resonators

The desired simulated resonator frequency is around 7 – 8 GHz. The main limitation in the frequency is coming from the experimental setup (see Chapter 3), where some components only work in between 4 and 8 GHz, such as the circulators or the HEMT amplifiers. Thus, staying in the upper regime is desired, since the addition of kinetic inductance in real devices will lower the frequency, specially for the thinner devices.

The number of fingers in the capacitor with $4 \mu\text{m}$ width and spacing is then modified to fit this range, resulting in a total number of 18 fingers, for a

Table 7.1: Results of the MR simulations, for each last finger length, l . The frequency, quality factor, inductance, capacitance are obtained using the method developed in [Doy08].

l (μm)	f (GHz)	Q	L (nH)	C (fF)
4	7.10295	$1.26 \cdot 10^4$	1.99	252
16	7.15416	$1.25 \cdot 10^4$	1.99	248
28	7.20475	$1.25 \cdot 10^4$	1.99	245
40	7.25721	$1.25 \cdot 10^4$	1.99	242
52	7.30996	$1.25 \cdot 10^4$	1.99	238
64	7.36121	$1.25 \cdot 10^4$	1.99	235
76	7.41668	$1.24 \cdot 10^4$	1.99	232
88	7.46971	$1.24 \cdot 10^4$	1.99	229
100	7.52376	$1.25 \cdot 10^4$	1.99	225
124	7.60859	$1.25 \cdot 10^4$	1.99	221

simulated frequency of 7.1 GHz. However, in order to have better results, several different resonators are intended to be placed in a single chip, thus allowing to average the results to correct for individual device imperfections. Since the result target is L_k , the goal is to achieve different frequencies, while leaving L_k unaltered, thus changing only the capacitance.

Simulations of the current as seen in Fig. 7.6b) show that the least amount of current is placed in the last fingers, which makes these fingers suitable for modifying the frequency. By changing just the length of the last three fingers, the frequency can be increased until $f_{\text{sim}} \approx 7.6$ GHz, as shown in Fig. 7.7. This way, 10 resonators can be placed in the same chip with ≈ 50 MHz separation between them. A table with the results for the MR resonators is shown in Table 7.1

7.3.2.4 Thickness effects

So far, all Sonnet simulations have been performed considering the metal as a zero-thickness layer. Sonnet is actually a 2.5D software in the sense that it allows the implementation of thick layers as long as there is no patterning in the vertical dimension. However, Sonnet thick metals do not allow the addition of the extra L_s needed for L_g and C extraction, as explained in Section 7.3.2.2.

Nevertheless, the software allows for a manual implementation of the thickness[§] This method consists of placing an extra metallic layer on top of the original aluminum layer with the exact same pattern, and then electrically connecting both layers with vias along all the edges, as depicted in Fig. 7.8. The dielectric layer between them, modelled as air, has the desired metal thickness, d .

The addition of this thickness increases the resonance frequency by a 1–2%, which can lead to a 100% deviation in the final λ . The results are shown in

[§]This method was indeed suggested by Sonnet software support, which resembles the default thick metal method by Sonnet.

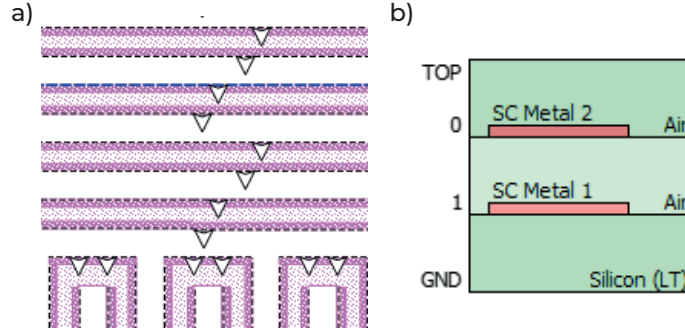


Figure 7.8: a) Zoom of the simulation design with the through vias used represented as white triangles in the fingers (upper wires) and meanders (bottom turning wires) to connect the two layers of metal used to emulate thickness. b) Sonnet layers for simulations with thickness, where two metallic layers are placed to simulate the film thickness.

Fig. 7.9a), where the frequency increases with thickness. In order to accurately determine the resonance frequency, this simulation will be repeated for the actual device measured thicknesses if they differ from the nominal ones. The results for the real thickness simulation for the MR resonators are shown in Table 7.2.

The same method as in Section 7.3.2.2 is used to determine L_g and C . In Fig. 7.9b), one can see that the relative change between the thick and 2D simulations in L_g and C . It can be seen that L_g decreases at a higher rate than the capacitance increase, thus leading to a decrease in the frequency.

These simulations take a couple of hours, so they have not been performed for all the resonators with different last finger length. Instead, a simulation for both the longest and shortest fingers and both have been compared. Since the resulting relative changes in L_g and C were less than 0.1%, the average between both relative changes is taken and used to convert 2D simulations into thick ones. The values depicted in Fig. 7.9b) correspond to this averaged results. In Table 7.2 the case for the lowest frequency MR resonator is shown.

7.4 Device Design and Fabrication

Most of the design decisions were performed iteratively with the results of the simulations performed in the previous sections. In this section, we describe the final device and chip designs of the different chips used in this experiment.

7.4.1 Resonator designs

As already commented in Section 7.3.1, three different resonator designs have been considered: small resonators (SR), medium resonators (MR), and large

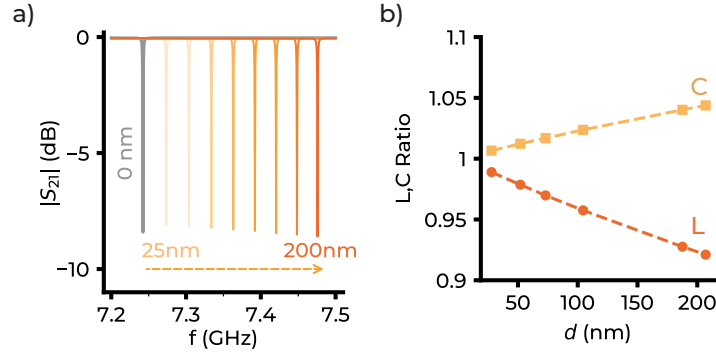


Figure 7.9: a) Sonnet simulations for resonator transmission. Grey curve represents the default response with no thickness. Yellow and increasing saturation color curves correspond to thicknesses ranging from 25 nm to 200 nm. b) Ratio of simulated L and C with and without thickness. L is reduced more rapidly than the increase on C . Points are on the real thickness MR devices.

Table 7.2: Simulated MR resonator with last finger length 4 μm for zero-thickness and for real measured thicknesses. d represents the thickness, and L and C ratios are compared to the zero-thickness simulation.

#	d (nm)	f (GHz)	L (nH)	C (fF)	L ratio	C ratio
	0	7.10295	1.994	251.8	1	1
	27.9	7.11846	1.972	253.5	0.989	1.007
	52	7.13588	1.952	254.9	0.979	1.012
	73.1	7.15092	1.934	256.1	0.970	1.017
	104.5	7.17278	1.91	257.8	0.958	1.024
	187.6	7.22861	1.85	262	0.927	1.040
	207	7.24124	1.837	262.9	0.921	1.044

resonators (LR). They differ in the size of their meander and finger structure. An image of the different devices design is shown in Fig. 7.10a-d).

The main dimensions of the SR, MR, and LR devices are 2, 4 and 6 μm in most of the meander and finger structures. While the number of meanders is kept constant, the number of fingers is adapted between the three designs so that the 7 – 8 GHz range is achieved. Also, the number of last fingers modified is also varied depending on the design, since each finger does not add the same capacitance in each design.

10 different resonators were designed for each resonator type, in order to have 10 different frequencies to add to each individual chip. Distributed resonators were also designed and measured, but their analysis is out of the scope of this work, because the extraction of the kinetic inductance require an extra geometric analysis, that will be left for future works.

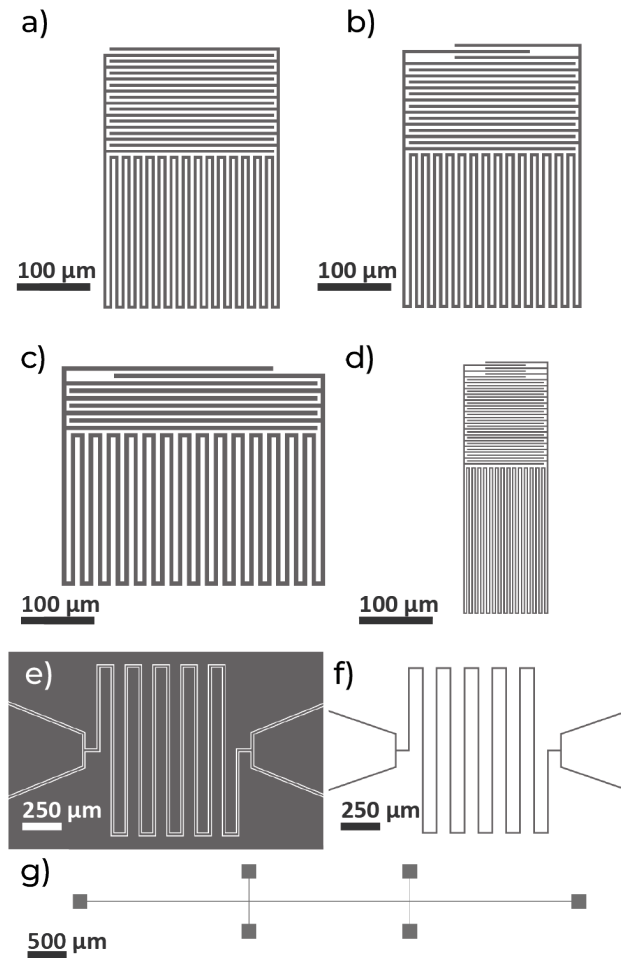


Figure 7.10: *LC* resonator device design variations: (a) medium (MR); (b) medium with modified finger capacitor; (c) large (LR), (d) and small (SR). Design of a 4-probe measurement meander with (e) and without (f) surrounding ground plane. (g) Design of a Hall-bar measurement.

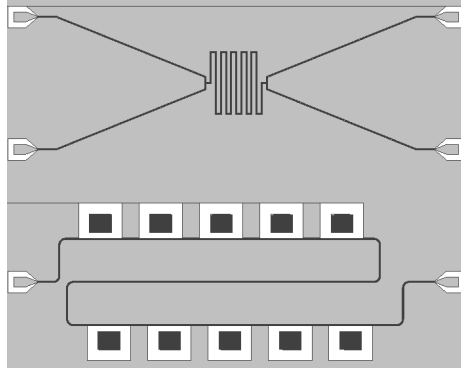


Figure 7.11: An example of a device design of the first generation of devices. A four-probe structure is placed on top and ten MR resonators in on the bottom line. There were analogous designs with SR and LR resonators were also.

7.4.2 Resistance structure designs

The resistance structures are meander-like structures as shown in Fig. 7.10e). The meander is designed to have a room temperature resistance in the range $100 - 1000 \Omega$, which falls well within instrument measurement range. The resistance is expected to drop by an order of magnitude at 4 K.

The meander in Fig. 7.10f) replicates the CPW design with $10 \mu\text{m}$ width and $6 \mu\text{m}$ gap, although only DC signal is used, so the ground should play no effect. An alternative design with no ground plane has also been measured, which is shown in Fig. 7.12. The first design is abbreviated as 4P-1 (four-probe, first design), and the second one 4P-2.

Finally, a third design, resembling a Hall bar structure (HB) is also fabricated and measured, depicted in Fig. 7.10g). In this structure the current flows from left to right, and the voltage drop is measured in the two pads on the bottom, leaving the pads on top unused.

7.4.3 Chip designs

The first generation of chips were designed so that each device had a series of resonators of the same type and a four-probe structure, as it is seen in Fig. 7.11. Four different devices were designed, with either MR, SR, LR or distributed resonators on it and the four-probe structure 4P-1. 10 different resonator designs were patterned to have good statistics of the measured L_k .

7.4.4 Studied thicknesses

The thicknesses d chosen for the study range from 25 nm to 200 nm. This range includes typical values found for superconducting qubit devices and radiation detectors (50 nm–100 nm). Including this range is indispensable for calibrating λ for real-scenario devices. $d < 50 \text{ nm} \sim \lambda_{\text{bulk}}$ is chosen to observe thin-film

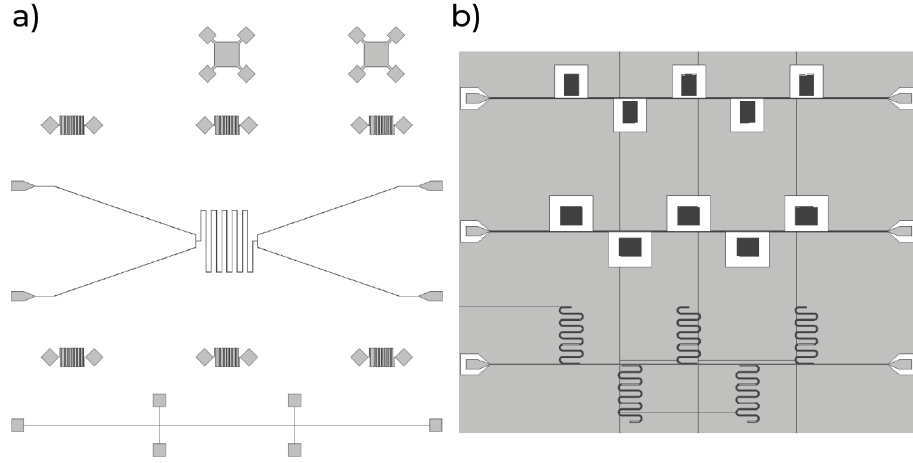


Figure 7.12: a) Four-probe structure in the second generation of devices were isolated in a separate device. Out of the several structures, only the meander and the Hall-bar were measured (see Fig. 7.10). b) Three lines with different resonator types: MR, LR and distributed. Each line had five resonators unevenly spaced in frequency. A separate chip with only SR structures was designed but not used.

effects, while $d > 100$ nm is chosen to explore the regime approaching bulk aluminum behavior. The actual thicknesses were accurately determined using Atomic Force Microscopy.

7.4.5 Fabrication

The devices were fabricated using photolithography on high resistivity silicon wafers from TOPSIL provider. Aluminum was deposited via metal evaporation. The devices were later diced and wirebonded to a ceramic PCB. The basic processing steps for patterning the electronic devices are as follows.

Samples are diced in quarter wafers and subsequently cleaned in acetone, rinsed in isopropanol and blown dry in N_2 stream. Substrates are dehydrated before photoresist deposition. LOR3A plus AZ6512 resists are spin coated and soft baked sequentially. A Karl Suss mask aligner is used for resist-stack exposure and then a standardized development sequence is applied. The pattern transfer consists in aluminum thin film deposition followed by a lift off of the resist in NMP solvent. The aluminum deposition was performed by e-beam evaporation for the given thicknesses. The remaining LOR3A is removed by mild oxygen plasma treatment. For electrical characterization, the samples were diced appropriately and mounted onto ceramic PCBs. Devices were wire-bonded with aluminum wires to either a sample holder for AC measurements or to chip carriers for DC measurements. Exemplary images of actual devices are shown in Fig. 7.13.

Two different evaporators, one Plassys at IFAE and another from Univex

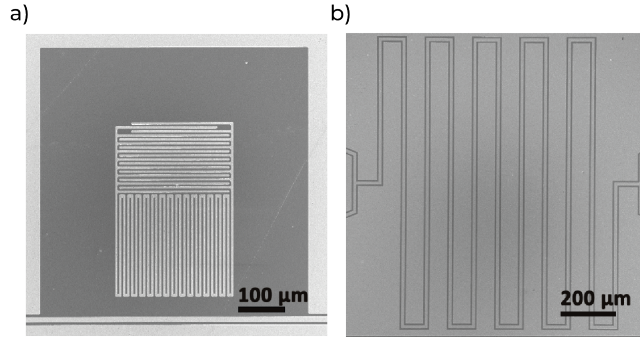


Figure 7.13: **a)** Scanning Electron Microscopy (SEM) of a *LC* resonator. **b)** SEM of a 4-probe measurement meander.

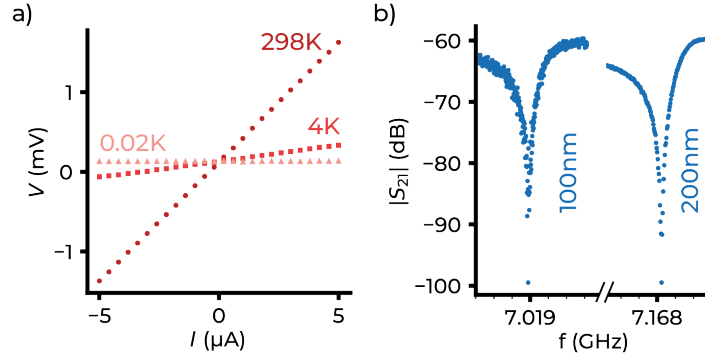


Figure 7.14: **a)** S_{21} data and fit of measured resonators with 100 nm and 200 nm thickness. Each minor tick corresponds to 1 MHz **b)** Resistance measurements at room temperature (RT), 4 K and 10 mK.

at CNM, were used in this study in order to account for possible fabrication dependencies on λ . While the IFAE evaporator is only used for aluminum, the CNM evaporator contains other metals and may thus lead to a higher amount of impurities.

Altogether, the different variety of designs and fabrication conditions account for potential systematic errors on λ , ensuring a more comprehensive analysis.

7.5 Experiment

All devices were mounted in a sample holder at the mixing chamber plate of a dilution refrigerator ($T = 20$ mK) and subjected to measurements using a Vector Network Analyzer (VNA) at power levels near the single photon regime. Full setup schematics can be found in Chapter 3. 4-probe structures were either located in the same chip as the resonators or in a separate chip, in which case

Table 7.3: Table with results of the fits from Fig. 7.15. All parameters are used in Eq. (7.9) to fit the resonator response. Parameter uncertainties are obtained using iminuit, as detailed in the main text.

f_r GHz	$ Q_c $ $\times 10^3$	Q_l $\times 10^3$	ϕ	α	a $\times 10^{-3}$	τ nHz
7.0056(10 ⁻⁶)	15.2(0.3)	9.2(2)	0.22(0.01)	-3.78(0.04)	1.01(0.01)	69.7(0.1)
7.0115(10 ⁻⁶)	3.47(0.01)	4.20(0.01)	-0.76(0.01)	-2.87(0.01)	8.17(0.01)	69.9(0.1)

they were located either at the mixing chamber or at the still plate of the dilution fridge, and measured with a sourcemeter.

7.5.1 Resistance measurements

Resistance measurements were performed at room temperature and at 4 K [see Fig. 7.14a)] and then the trace was fit to a linear regression. Then, a continuous measurement was run at a low current while sweeping the temperature around $T_{C,\text{bulk}} \sim 1.2$ K to find the critical temperature of the sample. T_C was determined at the midpoint where the resistance dropped by 50%.

7.5.2 Resonator measurements

A typical resonator measurement is shown in Fig. 7.14b) for two different resonator thicknesses.

The resonator response was fit to the following expression [Pro15]

$$S_{21} = ae^{i\alpha}e^{-2\pi if\tau} \left[1 - \frac{(Q_l/|Q_c|)e^{i\phi}}{1 + 2iQ_l(f/f_r - 1)} \right], \quad (7.9)$$

where the factor between brackets is the actual resonator response, while the pre-factor in front contains the response of the rest of the circuit. a is an attenuation constant, α represents a phase shift and τ is the electrical delay of the measurement line. Q_l is the loaded quality factor related to the complex coupling quality factor Q_c and internal quality factor Q_i , through $Q_l^{-1} = Q_i^{-1} + \text{Re}(Q_c^{-1})$. Finally, ϕ expresses the impedance mismatch, and f_r is the resonator frequency. Typical fits to the resonator response are shown in Fig. 7.15, where one can see that the impedance mismatch is correctly captured.

7.5.2.1 Resonator fitting routine

Our fitting process follows from a routine inspired by ref. [Pro15]. In that study, the data fitting is performed sequentially, until the full expression for S_{21} is obtained. However, with such a sequential process it is hard to propagate errors in the fitting, and correlations between parameters are lost. For that reason, we use the sequential procedure to yield our initial parameter guess. Standard SciPy optimization routines are employed for this method.

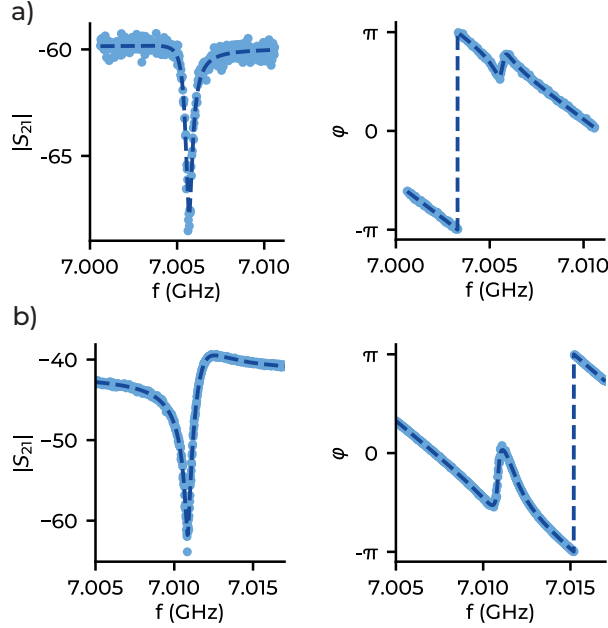


Figure 7.15: S_{21} resonator response in magnitude ($|S_{21}|$, left) and phase (φ , right). The fit using our procedure is superimposed to the light blue data points as a dark blue dashed line. **a)** 100 nm MR resonator. **b)** 200 nm MR resonator, with the same design as the device in **a)**.

Once a good initial set of parameters is obtained, we use the `iminuit` library [Dem20] for fitting the full S_{21} expression. `iminuit` is a library mainly used in the particle physics community, with a focus on error propagation and accurate uncertainty estimation. The S_{21} fit has seven parameters, which makes it a complex fit, and proper error estimation becomes relevant.

In most fits performed in this work, the initial guess provided by the sequential method and final fitting parameters were close. In general, having good initial parameters for `iminuit` is indispensable.

Table 7.3 shows fitted parameters from resonators in Figure 7.15, with the corresponding errors. The error in frequency δf_r is of order 10^{-6} , which is the most important parameter to extract λ . The resonator internal quality factor Q_i is not used in this study. In fact, the resonators in this work are designed with $Q_l \ll Q_i$ to maximize the signal strength, and therefore Q_i is not very accurately determined, lying in the range 50.000-100.000 showing no obvious thickness dependence.

Using `iminuit` one has access to the correlation matrix between variables, which is defined as

$$\rho_{ij} = \frac{\sigma_{ij}}{\sqrt{\sigma_{ii}\sigma_{jj}}}. \quad (7.10)$$

Here, σ_{ii} is the variance of variable i , and σ_{ij} is the covariance between variables i and j , if $i \neq j$.

Table 7.4: Table with correlation for fitting of resonator on Fig. 7.15a). Parameters can be seen in 7.9.

	a	α	τ	Q_L	$ Q_c $	ϕ	f_r
a	1	0	0	-0.3	-0.3	-0.1	0.1
α	0	1	1	0	0	-0	0
τ	0	1	1	0	0	-0	0
Q_L	-0.3	0	0	1	0.8	0	-0
$ Q_c $	-0.3	0	0	0.8	1	0	0
ϕ	-0.1	0	0	0	0	1	-0.7
f_r	0.1	0	0	-0	0	-0.7	1

When using the fitting formula for the transmission measurements S_{21} Eq. (7.9), both quality factors, Q_L and $|Q_c|$, show high correlation and, indeed, Q_L is bounded by Q_c . Other variables that are highly correlated are α with τ , and f_r with ϕ_0 . In both cases, a slight change in one of them, provokes adaptations in the other coupled variable to minimize the cost function, which indicates correlation. One could, in principle, parameterize the model in an alternative way to Eq. (7.9) to use purely independent variables. However, this parameterization will probably require the use of variables with little physical meaning, thus losing the benefits and information obtained from fitting the variables with actual physical meaning. In Table 7.4, correlations between parameters are shown for resonator in Fig. 7.15a).

7.5.2.2 Temperature and magnetic field measurements

The resonator measurements have been performed at different temperatures in order to follow the resonance change with temperature, which is known to depend on the superconducting type [Tin04]. London penetration depth temperature dependence is known to be $\lambda_L(T) \propto (1 - T/T_C)^{-1/2}$. This dependence is also valid for local superconductors. However, for nonlocal superconductors, $\lambda \propto (1 - T/T_C)^{-1/3}$, by using Eq. (7.2). In general, the exponent δ is expected to be between these two limits.

To perform these measurements, the temperature of the fridge was monitored and changed while letting the system to slowly thermalize. Then, resonator measurements as described previously were changed. The

Moreover, some measurements with external magnetic field were performed in order to observe any sizeable difference in the quality factor. For that, an external coil was placed on top of the resonator sample box, and different magnetic fields were applied. In between each different \vec{B} , the sample was heated above T_C to break superconductivity and then brought back to ~ 20 mK with the new magnetic field.

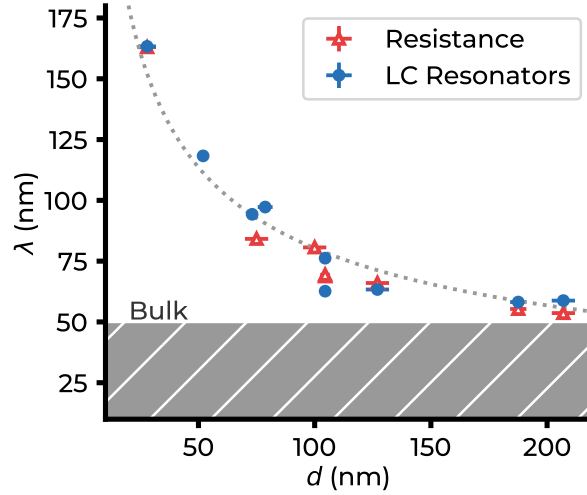


Figure 7.16: Measured penetration depth λ as function of device thickness d . Two measurement methods are shown: resistance measurements (red triangles) and *LC* resonator resonances (blue circles). Bulk penetration depth is shown as a lower limit. The thickness of samples is measured using atomic force microscopy. The fitting curve assumes the electron mean-free path to be proportional to the sample thickness, following from Eq. (7.3), Eq. (7.4).

7.6 Results

The obtained values of λ for each sample thickness d from both resonator and resistance measurements are plotted in Fig. 7.16. Each point of the resonator measurement consists of an average of several resonators on the same chip with varying capacitance and kinetic inductance ratio (see Table 7.5), as explained in Section 7.3. The vertical error bars correspond to the standard error of the mean, which is smaller than the marker size. The error in the horizontal axis corresponds to the uncertainty in AFM measurements to determine the actual film thickness. The resistance measurements consist of a single structure in each device, given the small error in the fitting of the resistance [Fig. 7.14].

Table 7.5 shows the full experimental results obtained for both the resonance and resistance measurements. A total of 70 structures have been analyzed, combining the two measurement methods (see Section 7.2), three different designs for each measurement method, along with eight different thicknesses and two evaporation facilities. This combination reduces considerably the possibility of a systematic error on the experiment, and provides a good statistical ensemble from which to extract conclusive values of λ .

The data in Fig. 7.16 exhibit a consistent trend, with λ increasing rapidly for $d < 100$ nm and approaching bulk values for $d \sim 200$ nm, validating the chosen thickness range. For very low thicknesses, it is common to assume that the electron mean-free path l is limited by surface scattering, leading to $l =$

Table 7.5: Results for both resistance and resonance frequency measurements. d_{nom} is the nominal target thickness, while d_{meas} is the measured thickness using atomic force microscopy. λ is the measured average penetration depth. Measurement type is "LC" for lumped resonators and "R" for 4-probe resistance measurements. "N" represents the number of devices measured for each particular thickness, which include small resonators (SR), medium resonators (MR), and large resonators (LR) for the resonance frequency measurements, and four-probe (4P) and Hall bar (HB) for the resistance measurements. The mask number is also specified, together with the fabrication facility. For resonator measurements, λ_{thin} is shown, together with surface kinetic inductance $L_{k,s}$. For resistance measurements, residual-resistance ratio, defined as $RRR = R_{\text{RT}}/R_{4\text{K}}$ and T_C are shown.

#	d_{nom} nm	d_{meas} nm	λ nm	Meas.	Design	N	Mask	Fab.	λ_{thin} nm	$L_{k,s}$ fH
1	25	28(4)	163.3(0.5)	LC	MR	9	1	IFAE	965(4)	1212(5)
3	50	52(2)	118.3(0.3)	LC	MR	9	1	IFAE	286(1)	359(2)
4	75	73(2)	94.3(0.6)	LC	MR	5	2	IFAE	145(2)	182(3)
6	75	78(3)	97.2(0.9)	LC	LR	9	1	IFAE	145(2)	182(3)
8	100	105(2)	76.2(0.9)	LC	MR	5	2	IFAE	87(2)	109(3)
9	100	105(2)	62.6(0.2)	LC	LR	5	2	IFAE	67(2)	84(3)
12	100	127(5)	63.3(1.1)	LC	SR	9	1	CNM	66(1)	83(2)
14	200	188(3)	58.1(1.1)	LC	MR	5	2	IFAE	58(1)	73(2)
16	200	207(5)	58.8(1.0)	LC	MR	6	1	CNM	59(1)	74(2)
#	d_{nom} nm	d_{meas} nm	λ nm	Meas.	Design	N	Mask	Fab.	RRR	T_C K
2	25	28(4)	162.9(1.2)	R	4P	1	1	IFAE	2.1(0.1)	1.32(0.03)
5	75	76(3)	84.1(0.7)	R	4P	1	2	CNM	6.1(0.1)	1.22(0.01)
7	100	97(3)	80.6(0.7)	R	4P	1	1	CNM	6.1(0.1)	1.27(0.02)
10	100	105(2)	69.4(0.6)	R	4P	1	2	IFAE	7.2(0.1)	-
11	100	105(2)	69.4(0.6)	R	HB	1	2	IFAE	7.2(0.1)	.
13	100	127(5)	68.7(0.6)	R	4P	1	1	CNM	7.4(0.1)	1.20(0.05)
15	200	188(3)	55.3(0.5)	R	4P	1	2	IFAE	11.6(0.1)	1.20(0.02)
17	200	207(5)	53.6(0.4)	R	4P	1	1	CNM	9.9(0.1)	1.20(0.05)

d [Tin04]. With this assumption, λ can be fitted to c7.4 leaving a as a fitting parameter. The fit yields $a = 1.26 \pm 0.03$, which lies in a regime of mixed scattering. It is important to note that Eq. (7.4) is only valid in the regime of a type-II superconductor, as the limit for large l is λ_L , and not λ_{bulk} . Using the fitted curve, $\lambda = \lambda_{\text{bulk}}$ at $d \simeq 250$ nm, which sets this thickness as an upper limit to the validity of the expression.

7.6.1 Kinetic inductance results

The resonance frequency method gives access to L_k through Equation (7.8), which is then converted to $L_{k,s}$ via Equation (7.1). $L_{k,s}$ is proportional to λ_{thin} , and both are shown in Figure 7.17. In this figure, only LC resonators are plotted, and the exponential increase at low thicknesses is more pronounced than the increase of λ in Figure 7.16, as expected.

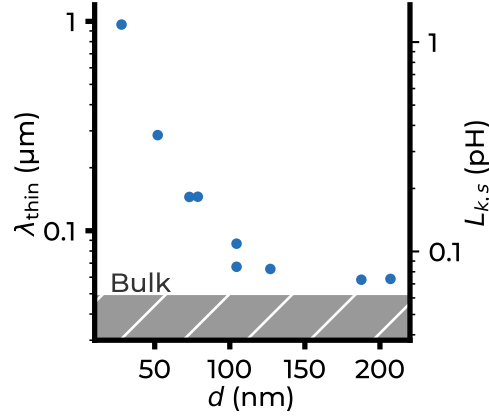


Figure 7.17: LC resonator response, plotted in two scales: λ_{thin} (left y-axis) and L_k (right y-axis), which are proportional, see Eq. (7.6).

Large $L_{k,s}$ values near ~ 10 pH are predicted for aluminum with $d = 10$ nm. Combined with a long enough meander, pure aluminum can attain L_k values comparable to those exhibited by superinductors [Mal18]. For example a thin wire of $2 \mu\text{m}$ with length of $200 \mu\text{m}$ would already provide an inductance of 1 nH, that could be increased by increasing the length of the wire.

7.6.2 Design variations

Figure 7.18 show variations on the design and deposition system for both resonance and resistance measurements, respectively. In Fig. 7.18a), λ from the three different resonator designs are shown. The devices fabricated at the different fabrication facilities do follow the overall trend, considering the differences in the two deposition systems. The noticeable difference at $d = 100$ nm may arise from a systematic difference in the device geometry between M and L resonators not accounted for.

Resistance measurements are displayed in Figure 7.18b). All values follow a consistent trend $\lambda \sim 1/\sqrt{d}$. Most data are obtained from 4-probe structures with (4P-1) and without (4P-2) surrounding ground plane. The single Hall bar value is consistent with a 4-probe measurement. Devices fabricated at different fabrication facilities did not show visible deviations in λ despite the difference in the residual resistance ratio RRR values (Table 7.5).

7.6.3 Critical thickness

The results obtained in this work allow us to provide estimates of the critical thickness d_c where aluminum turns from a type-I to a type-II superconductor. Such a transition is expected to occur for a value of $\kappa = 1/\sqrt{2}$ in

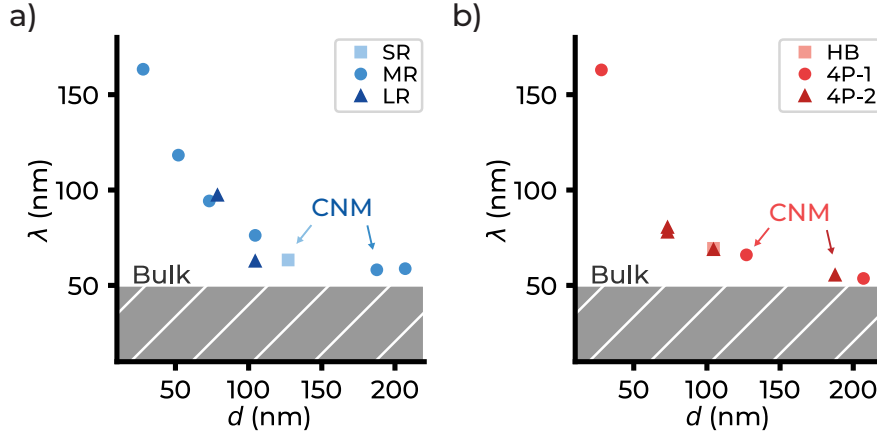


Figure 7.18: a) Measured λ by the resonance frequency method for different thicknesses. Different resonator types are shown. The devices fabricated in CNM evaporator are highlighted. b) Measured λ using the resistance method for different thicknesses. Different resistance structures are shown, the two types of four-probe, with (1) and without (2) ground plane, and the Hall bar. The devices fabricated in CNM evaporator are highlighted.

Eq. (7.5) [Abr57].

In Fig. 7.19, the values of λ obtained are compared to values of ξ obtained from two different assumptions on the dependence of the electron mean-free path l as function of thickness d . Our first method assumes $l = d$, which is a reasonable approximation for thin films as already argued, leading to a value ξ' estimated from Eq. (7.3). The thickness that satisfies $\xi = \sqrt{2}\lambda$ is $d_c^{(1)} \simeq 113$ nm. It is important to note that this fit, which assumes a linear dependence between d and l , fails for large d .

An alternative method to predict ξ is obtained by using the relation[Bra71; Rom82] $\rho \cdot l = 4 \cdot 10^{-12} \Omega \cdot \text{cm}^2$ known for aluminum. According to this relation, a different ξ'' is obtained through Eq. (7.3) and the ρ values obtained from the meanders, leading to $d_c^{(2)} \simeq 155$ nm. In either case, an exact description of l as function of d is outside of the scope of this work. Therefore, our assumptions allow us to define a region of critical thicknesses $d_c = 113$ nm–155 nm where the transition between superconductivity types may occur. As argued in Section 7.1, the actual transition between superconductivity types may take place over a certain range of values of d_c , given the intrinsic inhomogeneity of κ due to the disordered nature of thin films.

In summary, our results suggest that the thicker samples ($d > 150$ nm) may enter the regime towards type-I superconductivity [Bra71], unlike the thinner ones ($d < 50$ nm) which are more likely to behave as type-II local superconductors.

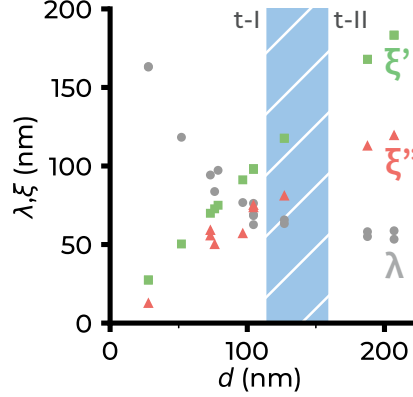


Figure 7.19: Estimated dependence of coherence length ξ on thickness using the fit from Fig. 7.16. ξ' is calculated assuming $l = d$ with Eq. (7.3). According to this fit, the transition between superconductivity regimes, when $\xi/\lambda = \sqrt{2}$ [Abr57], occurs at a critical thickness $d_c \simeq 113$ nm. ξ'' is calculated from l obtained from the relation $\rho \cdot l = 8 \cdot 10^{-12} \Omega \cdot \text{cm}^2$. The blue region is the predicted zone where d_c could fall according to these two methods.

7.6.4 Temperature dependence

Fig. 7.20 shows the temperature dependence of λ of a 200-nm thick MR resonator. These measurements, performed for several resonators, show how the penetration depths increases with the temperature. The cause of this change is the decrease in superconducting carrier density, n_s , causing an increase in λ , which follows [Tin04]

$$\lambda(T) = \lambda(0) (1 - T/T_C)^{-\delta}, \quad (7.11)$$

where δ is the relevant exponent which determines the superconductivity type, which is $1/2$ for local and $1/3$ for nonlocal superconductors. However, the best fit corresponds to $\delta = 0.045$, far from the predicted exponents. Moreover, the temperature dependence is not correctly fitted by Eq. (7.11). This can be caused by an incorrect determination of the temperature or that the model used to determine the temperature dependence is not correct.

Further work is needed to understand the results. Few samples have been studied, so more experiment should enable to understand if this behavior has any relation with thickness. Then, alternative determination of the temperature of the sample should be performed, as it could be that the effective temperature differs from the nominal one, as when computing qubit thermal population. Finally, more complex functionalities can be studied.

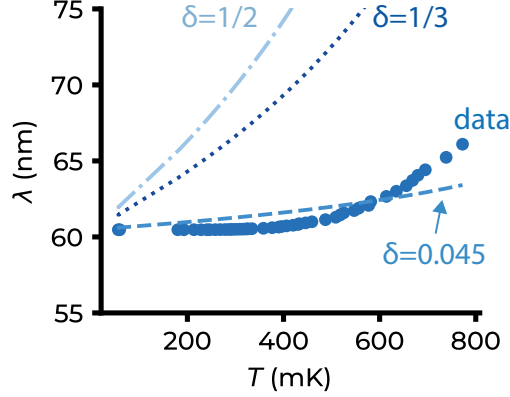


Figure 7.20: $\lambda(t)$ for a 200-nm thick MR resonator as a function of temperature. Data is plotted as circles and the best fit of Eq. (7.11) ($\delta = 0.045$) in dashed line. The expected exponents are $\delta = 1/2$ and $\delta = 1/3$ for local (dashed-dotted) and nonlocal (dotted) respectively. Results show high deviation between expected behavior and measured data.

7.6.5 Measurements with external magnetic field

An external coil was added to the setup to analyze the resonator response under an applied magnetic field. It was expected to observe a distinct behavior depending on the type of superconductor, since type-II superconductor should allow vortices to nucleate in the film. The main result of the added vortices was supposed to be a reduction in the quality factor caused by extra noise. However, as seen in a representative picture in Fig. 7.21, Q_i is mostly unaffected by the increase in current in the four resonators considered.

The main cause of Q_i not being modified by the current on the coil could be the imprecision in the determination of Q_i whose uncertainty may be larger than the effect of the vortices. Moreover, the experiment was not specifically designed for these measurements. A higher Q_i/Q_L should allow for a precise fitting of Q_i . Replicating the measurements presented [Nsa14], where a resonator is designed to trap flux in specific locations for different thicknesses, would be a suitable experiment.

7.7 Discussion

This study brings forward the relevance of including thickness effects in LC resonator designs where inductance plays an important role. For thinner films $d \sim 50$ nm, as those typically used in cQED, L_k is almost an order of magnitude higher than what would be expected from bulk aluminum.

Geometric inductance is also modified with thickness, as seen from Sonnet simulations. L_g follows the same trend and L_k , decreasing for thickest samples.

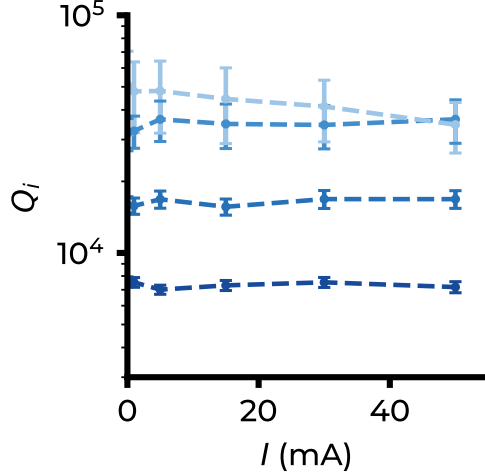


Figure 7.21: Q_i of four different MR resonators for different external current applied on the coil.

Depending on the specifics of the sample, a 2D simulation which gives a higher L_g than real could potentially compensate for not considering L_k into the simulation. However, this cannot be assumed, and accurate predictions require the exact determination from both L_g and L_k . Geometric inductance also depends strongly on the other dimensions of the device, which makes this analysis more important.

The results in this study are obtained from a diversity of samples, with the goal of capturing the overall trend of λ vs d without systematic deviations. However, the remaining deviations observed when combining all values of λ obtained in Fig. 7.16 may derive from variability in the fabrication process, as the complete set of devices was fabricated in a period of over a year, or variations of L_k not accounted for in the different resonator types.

The designs in this study were not optimized to characterize the resonator internal quality factors Q_i with precision. The Q_i values observed varied in the range $10^3 - 10^5$ and showed no clear dependence on d . We attribute this fact both to fabrication and measurement uncertainties and to the inaccuracy of the fitting procedure, as many devices had $Q_c \ll Q_i$, which led to high uncertainty in the determination of Q_i .

A targeted design to accurately determine Q_i could provide information on which role plays d on the system losses. Thicker samples could have no vortices, which, along with its reduced inductance, would reduce the flux-noise sensitivity. On the other hand, thicker samples have a larger surface, which can hold more microscopic defects and, thus, more noise. It is uncertain which mechanism would have a stronger effect.

The measured thickness range includes the expected crossover from a type-I to a type-II superconductor, as seen in Fig. 7.19. However, in order to properly identify the exact location, magnetic field measurements should be performed, which could show vortex trapping only in thinner samples. This would clearly identify the superconductivity type of the samples. Similar experiments have been already performed in Nb [Gub05].

The temperature dependence of the resonances and internal quality factors is another important source of information. Q_i and λ behave differently for local and non-local superconductors as temperature increase, which could provide an alternative differentiation of superconducting types. However, using T -dependence to discriminate between type-I and type-II superconductors poses additional challenges. Thicker samples would transition from non-local to local superconductivity at some temperature as λ increases with temperature, which could lead to a complex temperature dependence of the samples. Near T_c , all superconductors are local.

Thickness, in general, is a widely unexplored variable in superconducting qubit design, except for gap dependence on the Josephson Junction leads [Li22]. d is usually chosen because of fabrication constraints and reproducibility, and L_k is either disregarded or approximated from test structures of the same thickness. Using different thicknesses opens the path to both using thin aluminum as superinductor, and thicker aluminum for vortex-free materials which are less sensitive to flux noise. Another alternative to completely expel vortices is to use wires narrower than a critical width, which is known for Nb [Sta04], but not for Al. Thicker aluminum could, then, substitute ground planes with holes. Combining both thicknesses, thinner aluminum could capture vortices, serving as quasiparticle traps [Pan22] in more complex designs.

7.8 Conclusions and outlook

In summary, a characterization of the aluminum penetration depth λ was conducted for thicknesses in the range 25 – 200 nm, providing values ranging from 160 nm down to 54 nm, approaching the aluminum bulk value. Our measurements of λ vs thickness represent a guide to circuit designs where inductance plays a significant role, such as e.g. circuit QED and kinetic inductance detectors.

We have also introduced an accurate fitting procedure for resonators which can easily be extended to other experimental settings. For simultaneous parameter fits, sequential fitting can be a good process to obtain each parameter at a time. However, this process does not provide a good estimation of the fitting error and the correlations between parameters. Using the result of sequential fitting as the initial guess, we then fitted with the `iminuit` package, providing an accurate error estimation and, in particular instances, a better parameter prediction.

Our work has also enabled us to provide an estimation of the thickness range at which thin-film aluminum starts behaving as a type-II superconductor.

Further work is needed to explore the actual transition point and investigate potential new circuit functionalities in thicker aluminum films.

In future works, an accurate determination of this transition point will be targeted with experiments designed for trapping single flux quanta. Improvements in the design and setup to properly determine Q_i will be needed for these experiments. Moreover, a thorough analysis of the temperature variation of λ is to be performed to validate the current existing models, and to obtain alternative information on the type of superconductivity.

Chapter 8

Kerr-reversed TWPA

DAVID LÓPEZ-NÚÑEZ, IMRAN MAHBOOB

In this chapter the redesign of a Kerr-reversed Travelling-Wave Quantum-Limited Amplifier (TWPA) is presented. This amplifier[Ran21] was designed by Arpit Ranadive in Dr. Nicolas Roch group in the Néel Institute-CNRS (Grenoble), whose fabrication I briefly followed during a short stay in their group.

Section 8.1 introduces the concept of quantum-limited amplification and exposes the main goals in the designed amplifier. In Section 8.2, the TWPA amplification mechanism is introduced, along with the specific description of the Kerr-reversed TWPA (KrTWPA) used in the work.

The theoretical design is presented in Section 8.3. There, the amplification gain profiles are obtained for the different circuit parameter combinations, reproducing some features of the original KrTWPA. Following with this theoretical design, the physical design is then optimized to target the goals in Section 8.4. This section exposes all the simulations and design performed, with the final chosen design. Finally, in Section 8.5, the final remarks and the future work plans are commented.

This work was performed at NTT Basic Research Labs in Atsugi, Japan, with Dr. Imran Mahboob, in Dr. Shiro Saito's group, during my 2-month stay.

8.1 Quantum Amplification

A quantum-limited amplifier is one of the most important elements in a quantum computing experiment, as it was already introduced in Section 2.6.3. Quantum amplifiers excel at the noise figures, typically achieving noise levels close to the quantum limit of noise of $1/2$ photon. The noise temperature, as previously stated in Section 2.6.3, is defined as $T_N = N/(k_B)$, with N the noise power and k_B the Boltzmann constant.

An amplifier is usually characterized by its gain, G . Gain is defined as the increase in signal power, $A_{\text{out}} = \sqrt{G}A_{\text{in}}$, where A_{in} and A_{out} are the incoming

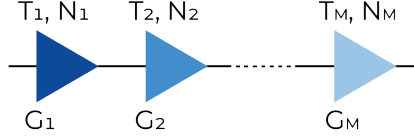


Figure 8.1: Schematic representation of an amplification chain with several amplifiers in series, each with its noise power, N_i , noise temperature, T_i , and gain, G_i .

and outgoing signal amplitudes.

In order to understand the importance of a quantum-limited amplifier, a typical amplification chain is shown in Fig. 8.1. The added noise from the first amplifier is N_1 and the effective noise temperature of the amplification is T_1 . However, the second amplifier noise, N_2 , will only affect the noise temperature minimally as $T_{\text{cas},2} = T_1 + \frac{T_2}{G_1}$, where $T_{\text{cas},2}$ is the cascaded noise temperature after the second amplifier. The cascaded noise temperature after M amplifiers is

$$T_{\text{cas},M} = \sum_{i=1}^M T_i + \frac{T_i}{\prod_{j=1}^{i-1} G_j}. \quad (8.1)$$

The first amplifier of the chain is thus the most important, since the noise from the subsequent amplifiers is reduced by the gain of the first one. In this scenario, a quantum-limited amplifier at the beginning of the chain allows for the best readout efficiency.

8.1.1 Benchmarking a quantum-limited amplifier

Real quantum-limited amplifiers do not reach the half a photon limit of noise, but stay slightly above due to imperfect design or uncontrolled noise mechanisms. The added noise over this $1/2$, N_{add} , is one of the most important benchmarks of these amplifiers.

However, the quantum-limited added noise is not the only important factor in the amplification. In the design of the quantum-limited amplifiers in the following section, these are the main goals:

- *Large gain.* Typically, 20 dB is the target gain of these amplifiers. The main purpose of this gain is to reduce the noise of the subsequent amplification stages, which usually provide a larger gain, usually around 40 dB for HEMT amplifiers.
- *Large bandwidth.* In quantum computing experiments, multiplexed readout is a common practice, which implies measuring several resonators simultaneously. Original quantum-limited amplifiers, such as Josephson Parametric Amplifiers (JPA)[Yam08; Cas08], rely on resonant amplification, where signal and pump interact in a non-linear resonator. How-

ever, these amplifiers, although some are frequency-tunable, have a limited bandwidth at their resonance frequency. Travelling-wave parametric amplifiers (TWPA) overcome this limitation by increasing the interaction time between the pump and signal while travelling through a non-linear medium. TWPAs can achieve much larger bandwidths thanks to avoiding the resonance bandwidth limitation.

- *Easy to fabricate.* Some TWPA devices require very precise tuning of junction parameters or the use of non-planar structures. By reducing fabrication complexity, devices are more reproducible and faster to manufacture. Moreover, some techniques may not be possible to implement in the available fabrication facilities.
- *Compact.* Some TWPAs require external coils, which make them more complicated to operate, and introduce a much larger amplification footprint. A compact device will make operation more reliable, and will make better use of the limited space in a refrigerator.

The reader is referred to [Esp21] for more amplification benchmarks, such as the 1 dB compression point, directionality, etc:

In the Kerr-reversed TWPA introduced in the following section, the first two target goals, large gain and large bandwidth, were already fulfilled by the design presented in [Ran21]. Thus, the main goal of this project is to modify the physical design so that the fabrication is considerably simpler and the TWPA magnetic flux is generated on-chip instead of with an external coil.

8.2 Kerr-reversed TWPA

TWPAs have inherent large bandwidth, so they outperform resonant quantum amplifiers for frequency multiplexing. However, TWPAs typically have to overcome two difficulties that do not usually play an important role in resonant amplification: phase and impedance mismatch.

In TWPAs, the signal travels through a non-linear medium simultaneously with the pump drive. The interaction time between both waves is increased by having a long non-linear medium. However, if the phases of the signals are not matched, the gain can be dramatically reduced.

The impedance mismatch, on the other hand, is not a feature by the TWPA itself, but depends on its relation with the environment. The microwave environment used in superconducting circuit experiments consist of equipment, components and cabling working typically at 50Ω impedance. Therefore, the amplifier needs to be impedance-matched to 50Ω , else it will reflect a considerable portion of the already weak incoming signal.

In this section, the mathematics behind TWPA amplification will be developed, and two strategies to overcome the phase mismatch will be explained, focusing on the Kerr reversal technique. Impedance matching will be assumed throughout this section. Section 8.3 will target the device theoretical design, while the physical configuration of the device will be presented in Section 8.4.

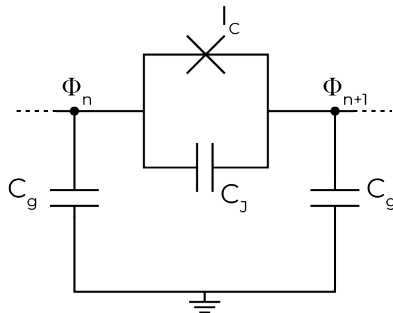


Figure 8.2: Example unit cell of a TWPA, consisting on a Josephson Junction in parallel to a capacitance to ground.

8.2.1 Mathematical Development of Amplification in TW-PAs

The non-linearity of the medium where the signals travel is indispensable so that an energy-transferring interaction occurs between both signal and pump waves. The strong pump alters the electromagnetic environment in the material, which then acts over the signal, increasing its power. The functional behavior of a TWPA is analogous to any parametric amplification process, such as a kid in a swing, where the energy deposited in changing the center mass results in larger *kid oscillations*.

Two main strategies are found in the literature to obtain the non-linear medium. One uses the non-linearity of large kinetic inductance materials, such as disordered superconductors[Eom12]. The other is based on Josephson Junctions[Mac15; Pla19; Ran21], the same nonlinear element of superconducting qubits. The Josephson junction-based TWPAs are composed of many individual cells repeated along the circuit. In each cell, a small part of the amplification takes place, and the sum of hundreds of cells provides a large gain.

An example of how to compute the gain of a single cell is shown for a cell consisting of a Josephson junction and a capacitance to ground in series with the rest of the cells, as seen in Fig. 8.2. Applying circuit quantization to this cell n , and relating to incoming (outgoing) flux from cell $n - 1$ ($n + 1$), the mathematical expression for current conservation is

$$C^g \frac{d^2 \Phi_n}{dt^2} = C \frac{d^2 (\Phi_{n+1} + \Phi_{n-1} - 2\Phi_n)}{dt^2} + \frac{1}{L_J} (\Phi_{n+1} + \Phi_{n-1} - 2\Phi_n) - \frac{1}{6I_0^2 L_J^3} \left((\Phi_{n+1} - \Phi_n)^3 - (\Phi_n - \Phi_{n-1})^3 \right), \quad (8.2)$$

where Φ_i is the flux at node i , C^g is the ground capacitance, C is the Josephson

capacitance, I_0 the critical current, and L_J the Josephson inductance.

This cell size is much shorter than the wavelength of the signals travelling through. Therefore, an approximation to the continuous can be made for the frequencies used in these experiments, $f > 1$ GHz, which leaves the expression as

$$C^g \frac{\partial^2 \Phi}{\partial t^2} - \frac{a^2}{L_J} \frac{\partial^2 \Phi}{\partial x^2} - Ca^2 \frac{\partial^2 \Phi}{\partial x^2 \partial t^2} = \frac{a^4}{2I_0^2 L_J^3} \frac{\partial^2 \Phi}{\partial x^2} \left(\frac{\partial \Phi}{\partial x} \right)^2 \quad (8.3)$$

where a is the unit cell length, with $a \ll \lambda$.

The solution to this type of equations is known from quantum and classical optics, and consist of three waves: a pump, an idler and a signal wave. The idler comes naturally from energy conservation. Four-wave mixing amplification is considered for this design, where a two-photon process occurs such that $2f_p = f_s + f_i$, where f_p , f_s , and f_i are the pump, signal, and idler frequency, respectively.

The expression of the total wave can be expressed using standard wave equation solutions

$$\Phi = \frac{1}{2} \sum_{j=\{p,s,i\}} \left[A_j(x) e^{i(k_j x - \omega_j t)} + \text{c.c.} \right], \quad (8.4)$$

where A_j is the slowly varying amplitude, and k_j and ω_j the wavevector and frequency of the wave j , respectively. The pump, signal and idler modes are defined as p, s, i respectively.

A few approximations are typically made to compute the wave evolution through the TWPA. As the pump power is much higher than the other waves, $A_p \gg A_i, A_s$, the pump wave is considered undepleted during the whole medium. Thus, A_p is constant. Moreover, both A_s and A_i are considered to vary very slowly, allowing to disregard spatial derivatives in Eq. (8.3).

After a few mathematical steps,

$$A_p(x) = A_{p0} e^{i\gamma_{pp}x}, \quad (8.5)$$

where A_{p0} is the initial pump amplitude and γ_{pp} is the self-Kerr modulation. The self-Kerr is the phase change on A_p caused by the same pump signal travelling through the medium and distorting the electromagnetic environment.

The other two amplitudes are

$$\begin{aligned} \frac{\partial a_s}{\partial x} &= i\gamma_{si} a_i^* e^{i\Delta k x}, \\ \frac{\partial a_i}{\partial x} &= i\gamma_{is} a_s^* e^{i\Delta k x}, \end{aligned} \quad (8.6)$$

where $a_{s,i}$ is a renormalized signal/idler amplitude. $\gamma_{si, is}$ is the signal-idler cross modulation, which is the phase change applied on the signal(idler) caused by the electromagnetic distortion of the idler(signal) travelling through the TWPA. Δk is the phase mismatch which is defined as

$$\Delta k = \Delta k_1 + \Delta k_{nl}, \quad (8.7)$$

which is the sum of the linear phase mismatch, Δk_l and the nonlinear phase mismatch, Δk_{nl} . The former is the difference in signal wavevectors,

$$\Delta k_l = 2k_p - k_s - k_i. \quad (8.8)$$

Δk_{nl} depends on the self-Kerr, γ_{pp} , and the cross-Kerr terms, γ_{ip} and γ_{sp} , which, again, are caused by the interactions between the signals mediated by the nonlinear medium. Δk_{nl} is defined as

$$\Delta k_{nl} = 2\gamma_{pp} - \gamma_{sp} - \gamma_{ip}. \quad (8.9)$$

The total gain can be obtained by comparing $a_s(x = 0)$ and $a_s(x = D)$, where D is the total length of the TWPA. Thus,

$$G_s = \left| \frac{a_s(x = D)}{a_s(0)} \right|^2 = \cosh^2(gD) + \left(\frac{\Delta k}{2g} \sinh(gD) \right)^2, \quad (8.10)$$

where g is the reduced gain, defined as

$$g = \sqrt{\gamma_{si}\gamma_{is}^* - \left(\frac{\Delta k}{2} \right)^2}. \quad (8.11)$$

As one can see, the total gain depends on Δk , and maximum gain is obtained at $\Delta k = 0$. Intuitively, parametric amplification must be based on proper phase matching of the pump and the signal. In a swing, the center of mass movements must be performed at specific positions for the oscillation amplitude to increase, thus phase-matching the pump and sign. Here something similar happens, if pump distortion of the medium is not aligned with the phase evolution of the signal, the gain is reduced.

The phase mismatch in Eq. (8.7) depends on two terms, Δk_l and Δk_{nl} , both with the same sign. Achieving a phase-matching is possible by modifying the sign of either of them. In the Kerr-reversed TWPA, the sign reversal is achieved by modifying the nonlinear term.

8.2.2 Kerr-reversed TWPA Basics

The nonlinear phase mismatch, Δk_{nl} , depends directly on the TWPA unit cell. Therefore, phase matching can be performed by achieving $\Delta k = 0$ at the single-cell level

In [Ran21], a new TWPA design is proposed, which consists of substituting the Josephson junction in the model described in Section 8.2.1 by a superconducting nonlinear asymmetric inductive element (SNAIL)[Fra17], as can be seen on Fig. 8.3. A SNAIL consists of a loop of three large junctions and a small junction. This system resembles the C-shunted flux qubit already described in Fig. 2.5, without the shunting capacitance. However, SNAILS are usually operated in a regime where the small Josephson junction is much smaller than the

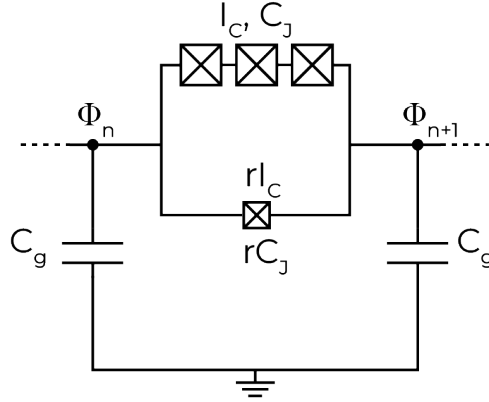


Figure 8.3: Kerr reversed TWPA Unit Cell. Each cell contains a SNAIL (three large junction in parallel to r times smaller junction), and a capacitance to ground, C_g .

big junction. This ratio*, r , is much lower than $1/3$, which then operates the circuit outside the double-well regime used in quantum annealing. Typically, r is around $0.05 - 0.1$.

There is an obvious benefit with this approach in that there is no engineered gap in the transmission, so there are no forbidden frequencies by design. By applying a different pump frequency, the operation point can be modified, thus allowing for gains at many different frequencies in the same device. Moreover, there are considerably less ripples than when engineering the dispersion relation, Δk_l , due to the better impedance matching.

However, the impedance matching in this device (as well as in the dispersively engineered TWPA) is achieved by adding a layer of metal on top of an alumina layer, which adds complexity into the fabrication process.

Furthermore, this device requires a global flux bias which is generated by an external coil. The necessity of an external coil is also detrimental for many reasons. First, the coil needs to be manufactured, which adds an extra level of complexity. Second, the size of a coil is typically comparable to that of the TWPA, thus increasing the TWPA footprint in the refrigerator, limiting its scalability if multiple TWPAs need to be added. The flux generated by the coil is uneven, biasing differently the individual cells, limiting the amplification efficiency. Finally, in flux qubit experiments, sources of flux such as the external coils can be detrimental and interfere with intended fluxes. Fluxes generated by on-chip lines, on the other hand, can be more easily shielded by superconducting sample boxes.

In Section 8.4 the physical design will be modified in order to improve fabrication and remove the necessity of the external coil while conserving its amplifying

*This ratio r is the same as α in the flux qubits. However, we keep the r notation for being consistent with the literature,

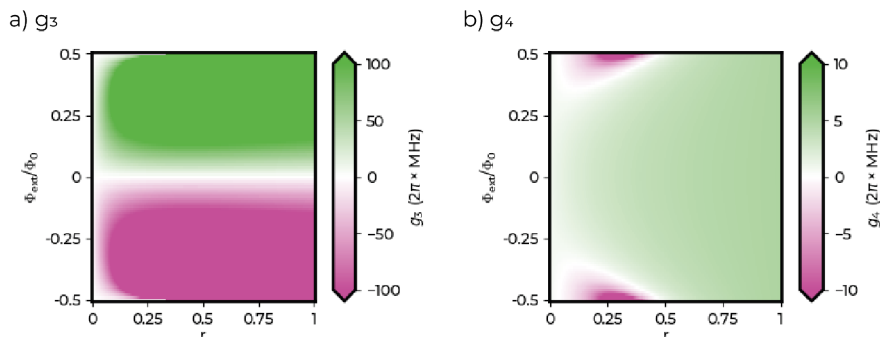


Figure 8.4: a) g_3 for different values of r and Φ_{ext} . b) g_4 for different values of r and Φ_{ext} .

features, which are calculated in the next section.

8.3 Theoretical Design

8.3.1 Gain and Phase matching in Kerr-reversed amplifier

The unit cell of the Kerr-reversed TWPA fulfills the following current-phase relation

$$I(\phi) = rI_0 \sin \phi + I_0 \sin \left(\frac{\phi - \phi_{\text{ext}}}{3} \right), \quad (8.12)$$

where ϕ_{ext} is the phase generated by the external coil. Note that here the one-mode approximation already introduced in Section 5.3.3 is performed, where only the main symmetric mode of the circuit is considered, assuming that the two difference modes are negligible. Although this cannot be applied directly to flux qubits, it is believed[Fra17] to hold for SNAILs that work in the low r regime.

Equation (8.12) can be expanded through Taylor and, up to leading order, is

$$\frac{I(\phi)}{I_0} \approx \frac{\Phi_0}{2\pi L} \phi - 3\Phi_0 \sqrt{\frac{R_Q}{\pi^3 Z^3}} g_3 \phi^2 - 4\Phi_0 \frac{R_Q}{\pi^2 Z^2} g_4 \phi^3 \quad (8.13)$$

where Φ_0 is the superconducting flux quantum, L is the total inductance, R_Q is the resistance quantum, Z is the device impedance, and g_3 and g_4 are the third and fourth order non-linearity parameters.

The non-linearity parameters g_3 and g_4 are the key elements of the TWPA design. In the KrTWPA design, the third order non-linearity is suppressed, $g_3 = 0$, to benefit a four-wave mixing process. For this TPWA $\Delta\kappa_{nl} \propto g_4 |A_P|^2$, which means that the sign of this non-linear phase-mismatch depends directly on the sign of g_4 , which can be tuned by the design parameters, thus effectively cancelling Δk_1 in Eq. (8.7).

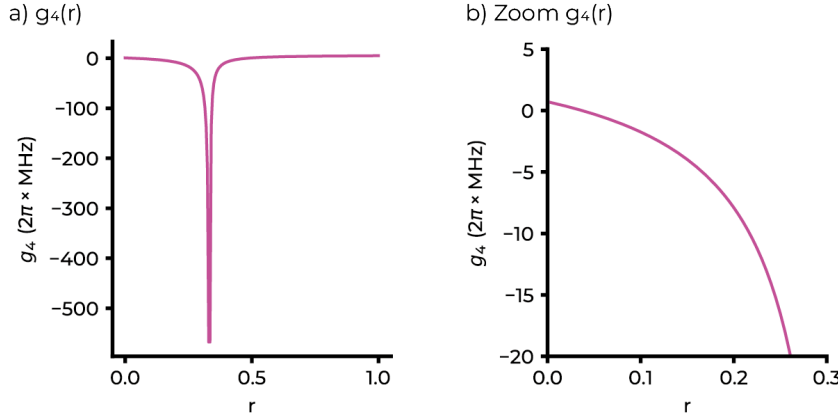


Figure 8.5: a) g_4 for different values of r for $\Phi_{\text{ext}} = 0.5$. b) Zoom on the lower r region g_4 for $\Phi_{\text{ext}} = 0.5$.

8.3.2 Design Parameters

Both g_3 and g_4 depend on several common circuit parameters. However, the capacitances of the circuit are not left as variables. The Josephson capacitances, C_J , are fixed because they are rather difficult to control in the fabrication, and they are usually determined by junction fabrication. Moreover, C_J is small compared to C_g , the capacitance to ground, reducing its effect on the circuit behaviour. C_g , on the other hand, is required to obtain the 50Ω impedance needed for impedance matching, so it needs to be adjusted when changing the other parameters. Finally I_0 has also been fixed for most of the parameter exploration, because of junction fabrication requirements.

Then, g_3 and g_4 depend only on r and ϕ_{ext} . In Fig. 8.4, the dependence of the two non-linear coefficients is shown against r and ϕ_{ext} . Two regions of the parameter space suppress g_3 , at $\phi_{\text{ext}} = 0.0$ and at $\phi_{\text{ext}} = 0.5$ for low values of r . These are the regions where 4-wave mixing dominates, as desired for this device. However, the Kerr-reversal only occurs for negative values of g_4 , which only occurs at the region around $\phi_{\text{ext}} = 0.5$.

In Fig. 8.5a), the behaviour of g_4 for $\phi_{\text{ext}} = 0.5$ is shown, where a clear divergence of g_4 is observed at $r = 1/3$ [†]. A zoom on the region lower than $r = 1/3$, where g_3 vanishes, is shown on Fig. 8.5b). There, it is seen that g_4 is only negative after $1/27$, a value that can be calculated from the Taylor expansion of Eq. (8.12).

Staying in the available range for $r \in (1/27, 1/3)$, and setting $\phi_{\text{ext}} = 0.5$, the gain simulations can be performed to decide the optimal set of parameters. The values used in the original work are $r = 0.07$, $\phi_{\text{ext}} = 0.5$, $I_0 = 2.19 \mu\text{A}$, $C_g = 250 \text{ fF}$, $C_J = 50 \text{ fF}$, and $N = 700$.

[†]Note that at $r = 1/3$ is where the double-well regime of flux qubits starts.

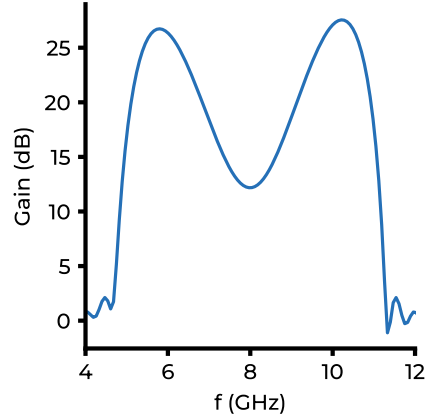


Figure 8.6: TWPA gain with default parameters and $A_p = 1.9 \sqrt{\text{rad}}$ pumping at 8 GHz.

In Fig. 8.6, the amplification for this set of parameters is calculated. This amplification is obtained for $f_p = 8$ GHz, as can be inferred from the dip in the transmission relation. The amplification is higher than 20 dB in a large frequency range. By modifying the input pump frequency all typical frequencies in the superconducting circuit experiments (4 – 8 GHz) are achieved.

An important aspect to comment for these simulations is that the initial power A_p is unknown and not specified in the original paper[‡]. This value has a strong effect in the simulation and, to the best of our knowledge, the simulations obtained for different f_p in the original work should correspond also to different A_p . In this sense, A_p is a value left to be optimized during the experiment, and the simulations performed here have to be repeated with real data.

Modifications on the initial parameters are seen in Fig. 8.7. Increasing the initial A_p clearly increases the gain profile. -75 dB correspond roughly to an amplitude of $1/\sqrt{\text{rad}}$. As the exact power is to be optimized in the experiment, this parameter is fixed to values that reproduce the original work [Ran21].

Higher r increases the gain because the non-linear $|g_4|$ is also larger. However, working at higher r largely increases L , which implies an equivalent increase in the required C_g for impedance matching. Keeping C_g low is desired if planar ground capacitance is to be used. Moreover, working at large r implies large gradients in the g_4 parameter, as seen in Fig. 8.5, which reduces TWPA reproducibility.

I_0 has an inverse dependence with gain because of its inverse relation to L_J and, thus, with L . As seen with r , larger L implies larger gain. The value of I_0 is to be changed from the original design due to the already know-how in the group on junction fabrication, which fixes $I_0 = 1.5 \mu\text{A}$, which is lower than

[‡]Input powers of ~ -75 dB are given, but the exact value used in the simulation is not given.

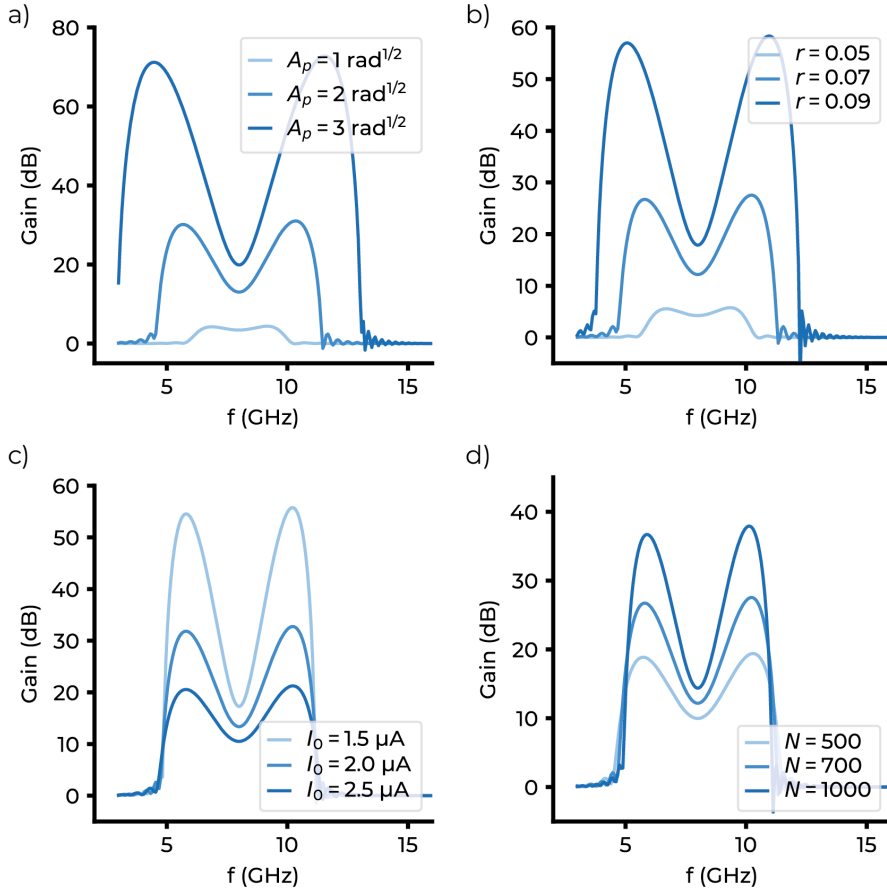


Figure 8.7: TWPA Gain profile when sweeping some parameters with respect to Fig. 8.6. The parameters swept are a) Pumping amplitude, A_p ; b) small junction ratio, r , c) Large junctions critical current, I_0 , d) Number of cells.

$I_0 = 2.19 \text{ } \mu\text{A}$. This gain reduction should be compensated with other parameter changes.

Adding more cells has also the obvious effect of increasing the gain, since the total gain is the sum of the individual unit cell gains. However, increasing N implies a larger TWPA size, thus the fabrication will set an upper limit.

The final parameters are still not fixed, as they will depend on the exact fabrication method, still to be determined. For the following section a lower $I_0 = 1.5 \text{ } \mu\text{A}$ is considered for the impedance matching, increasing the number of cells, N , for an equivalent result. However, it is likely that more parameters are also constrained by fabrication, thus implying further modifications.

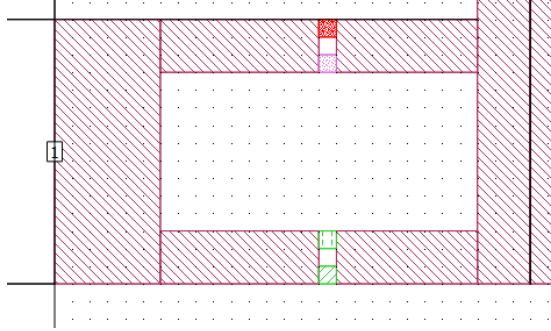


Figure 8.8: Sonnet modelling of the SNAIL unit cell. The two small squares on top are an ideal capacitance and an ideal inductance, that represent the three large Josephson junction. The two small squares on the bottom are the small Josephson modelled by an ideal inductance and capacitance in parallel.

8.4 Physical Design

The main design goal of this work is the reduction of fabrication complexity of Kerr-reversed TWPAs. The first goal to yield a planar structure has not been, as described in Section 8.4.1, since the capacitance obtained with purely planar structures is well below the requirements for impedance matching with the current design. However, a local flux line has been proposed to remove the necessity of the external coil.

8.4.1 Sonnet Simulations

In order to simulate the TWPA, Sonnet[§] software is used, a powerful finite-element solver widely used for measuring the rf response of microwave circuits, as already introduced in Section 6.1.2.

Sonnet is used to compute the transmission, S_{21} , and reflection, S_{11} , of the signal through a series of TWPA cells, which are the indicators of the impedance matching of the line. The benchmark of good impedance matching is $S_{11} < -20$ dB for the considered frequency range. Moreover, Sonnet provides the transmission line C_g and Z_0 independently to validate the results.

Quantum effects such as nonlinear L_J are not trivially implementable in Sonnet. To simulate Josephson junctions, an ideal inductance and capacitance were set in parallel, as seen in Fig. 8.8. The three big junctions of the SNAIL were approximated by a single one, where both their inductance and capacitance were added in series. Thus, the SNAIL was simulated as two of these parallel L and C , one for big junctions and another for the small junction, connected also in parallel.

However, the exact value L_J depends on the external flux applied. By setting $\phi_{\text{ext}} = 0.5\Phi_0$ on equation Eq. (8.12), one can compute the phase ϕ^* that

[§]<https://www.sonnetsoftware.com/>

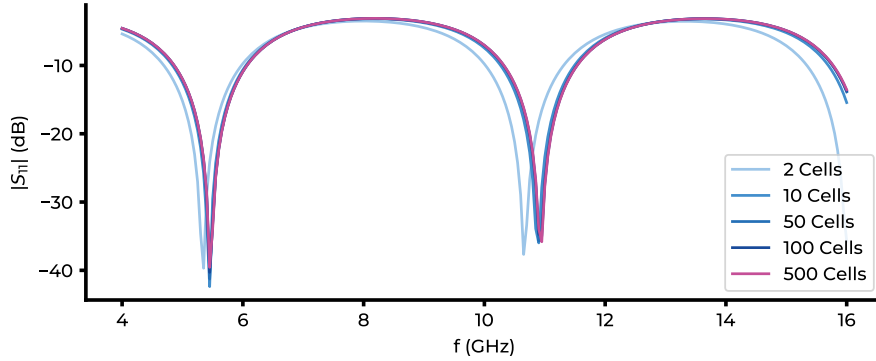


Figure 8.9: Sonnet simulations are performed with 2, 10, 50, 100 and 500 unit cells, and then they are cascaded up to 500 cells.

minimizes the energy, which is $\phi^* = \pi$ regardless of the value of r . Computing the inductance of both terms in the expression shows that the small junction should have negative inductance. Luckily, Sonnet allows for negative inductance values. Notice that a negative value for Josephson inductance increases the total L when connected in parallel for this range of parameters.

The total amount of cells that can be simulated with accuracy with Sonnet is limited unless one has several days (or weeks) to wait for the results of every simulation. To overcome that limitation, the python library *skrf* has been used to cascade lower cell results. *skrf* is an open-source library for RF/Microwave engineering.

To validate the *skrf* cascading method, a Sonnet simulation of a TWPA with 500 unit cells has been performed. Then, this simulation is compared with the result of smaller Sonnet TWPA simulations of 100, 50, 10, and 2 unit cells, and then cascading the result with *skrf*. The results in Fig. 8.9 show the agreement between all the different subdivisions, except for the smallest slicing of 2 cells. From now on, simulations are performed on 10 unit cells and cascaded to the final desired number of cells.

8.4.2 Planar Designs

The design shown in Fig. 8.10, consists of the junction loop with finger capacitances to ground. The device, in contrast to original KrTWPA, is a coplanar waveguide (CPW). Notice that the fingers to ground are only on one of the sides. The main reason for this is to leave the other side free to add a flux line in subsequent iterations. The resulting simulations show that the capacitance is far from the required for $Z = 50 \Omega$ by almost two orders of magnitude.

Several different iterations made it clear that the CPW approach could not provide the necessary C_g for impedance matching with the previous theoretical parameters. There are three alternative work arounds for this limitation. One

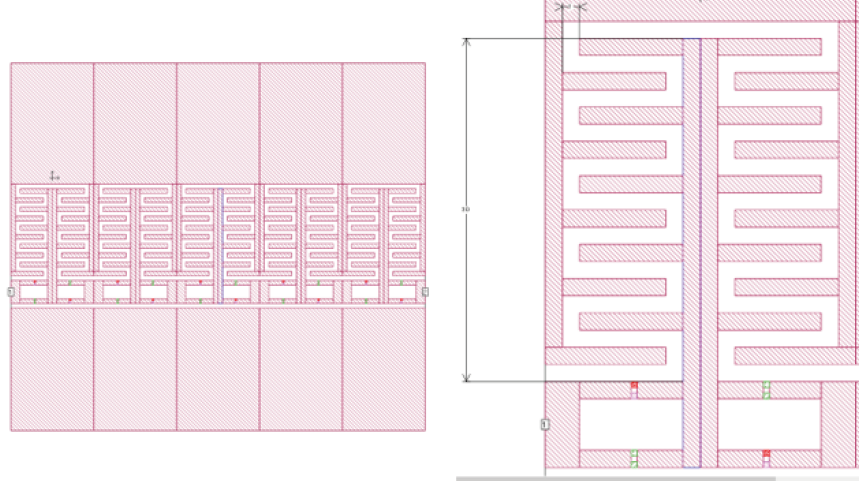


Figure 8.10: The global 10 unit cells of the first design test is shown on the left, with a zoom on two unit cells on the right. The SNAIL loop is modelled on the bottom and the finger capacitance to ground on the top.

would be to reduce the unit cell inductance by, at least, an order of magnitude. However, this would reduce the obtained gain, which would require either increasing the number of cells accordingly, making the TWPA impractically large, or changing the value of r , working in the regime with a large gradient, whose exact value is very difficult to control.

Another alternative would be to reduce the spacing between the ground plane and the feedline, which could have a huge impact on the capacitance. However, this would require an e-beam capable of working on the whole chip area, which was not available at that moment.

Finally, a multilayer structure with alumina in between metallic layers can be used, as performed in the original design. This is the approach taken in subsequent sections.

8.4.3 Multilayer designs

Simulations on the original KrTWPA are performed to validate the new method. It is important to note that, to our knowledge, simulations in the original design were performed considering an effective metamaterial with an inductance per length defined by L_J and disregarding C_J . The design is shown in Fig. 8.11, with the same central feedline with the junction loop (left) and a full metallic lid on top (right), with ~ 35 nm-thick alumina in between.

The results depicted in Fig. 8.12 show that the thickness, d , found for optimal impedance matching was comparable to the described in their work, around 35 nm. S_{11} shows low reflection along all the considered range, which is a good

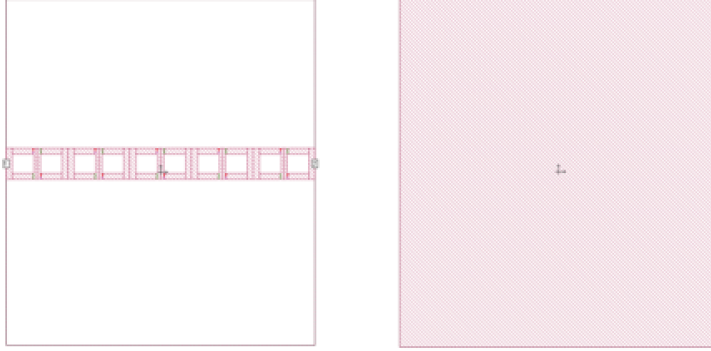


Figure 8.11: The microstrip geometry consists of the series of unit cells without ground plane (left) and a metallic layer on top (right) with alumina in between. This model consists of 10 unit cells.

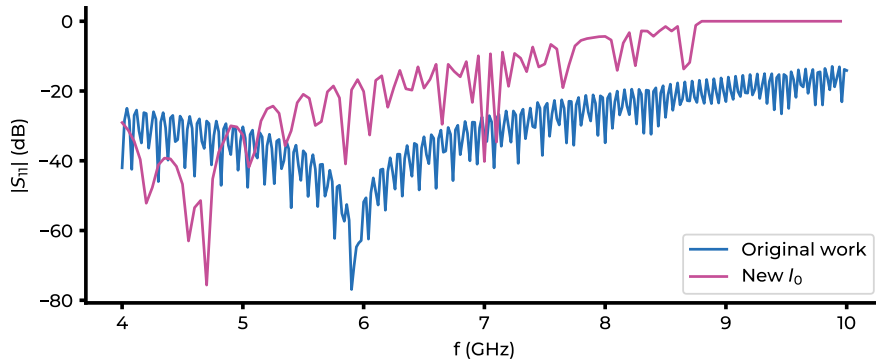


Figure 8.12: Comparison between the microstrip geometry with the original work parameters, and the simulation with the new value of $I_0 = 1.5 \mu\text{A}$

indicator of impedance matching. Apart from S_{11} , Sonnet also outputs Z_0 and C_g which validate the impedance matching, since $Z_0 \approx 50 \Omega$ and $C_g \approx 250 \text{ fF}$, as predicted by [Ran21].

Figure 8.12 also shows the simulations performed with the new values, which differ from the original values in the value of I_0 , now $1.5 \mu\text{A}$ for convenience for fabrication. A full reflection at high frequencies occurs because there is a stopband at $f = 1/\sqrt{LC_g} \approx 9.5 \text{ GHz}$, where L is the total loop inductance. Reducing I_0 causes an increase in L , and consequently also in C_g so that $Z = \sqrt{L/C} = 50 \Omega$. These two increments provokes a reduction in the TWPA stopband, that lowers until the useful cQED range.

Therefore, the circuit parameters decided on Section 8.3.2 have to be mod-

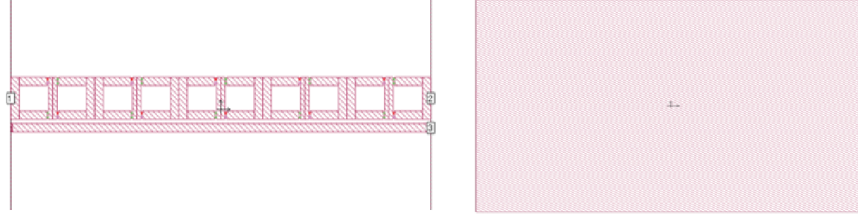


Figure 8.13: Microstrip as shown in Fig. 8.11 with the addition of a flux line close to the TWPA unit cells (left), with a metallic layer on top (right) with alumina in between.

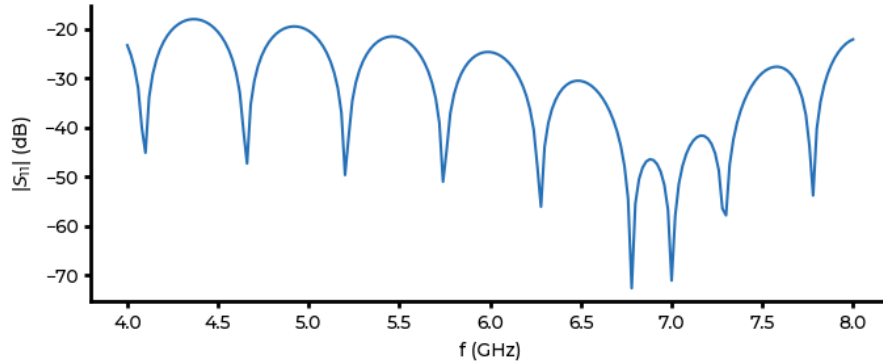


Figure 8.14: Reflection of the microstrip design with a flux line on the side from

ified so that the stopband is pushed higher in frequency. This implies either increasing I_0 , or reducing r . The former is chosen, and $I_0 = 2.19 \mu\text{A}$, so the original values are recovered. However, again, fabrication limitations will set the viable range of parameters.

The design shown in Fig. 8.13 is similar to the one shown in Fig. 8.12, with an extra line added close to the feedline. This line is intended to carry current, thus biasing the TWPA devices.

Placing such a close line could impact the transmission profile. However, the important element to consider is that the inductance of this flux line is much lower than the main feedline which, combined with the large capacitance, causes a huge impedance mismatch, thus not allowing the feedline signal to propagate through this line.

In Fig. 8.14, $|S_{11}|$ reflection of this TWPA design is shown. One can see that this extra line does not have a large effect on the results, mostly staying below -20 dB for the studied range.

However, the flux line can carry DC current, which is required for biasing the flux of the SNAILs, since zero-frequency signals can safely travel without impedance matching. Finally, an extra benefit of this flux line is that the biasing

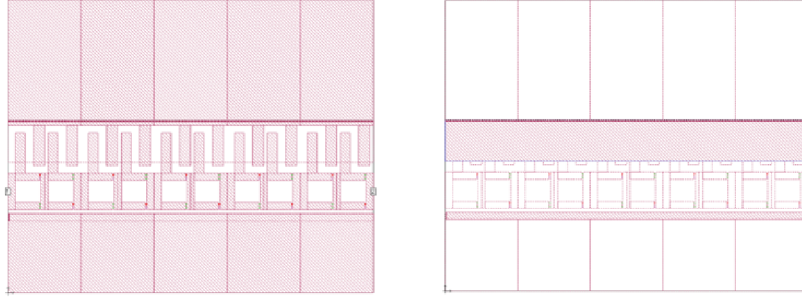


Figure 8.15: Design with CPW-like structure of the TWPA unit cell, in the left. The center part contains the unit cells, with ground on both sides of the CPW. On one side there are pads capacitively coupled to the top layer, on the right figure. The top layer has a big line that serves as extra capacitance for impedance matching, and the thinner one has current flowing through. Alumina fills the space between both layers.

of the unit cells is more uniform than with an external coil, which is expected to increase the amplification efficiency.

Similar results can be obtained with alternative designs. For example, the flux line could be placed on top if the top metallic layer can be patterned, as seen in Fig. 8.15. Another option would be the current to flow through the same top metallic layer that serves as the capacitor pad.

8.5 Conclusions & Future Work

An alternative design of Kerr-reversed TWPA has been proposed in which a flux line is directly placed on the chip and there is no need for an external coil. Leakage to this line is automatically reduced by impedance mismatching. Moreover, the parameter space has been narrowed, and it was shown that lower values of I_0 produced a stopband that limited the transmission at very low frequencies.

The final physical design and theoretical design parameters are not yet fixed and left for the fabrication limitations. The following steps are indeed to characterize the new possible junction values. Once these are obtained, the final design parameters have to be chosen with the tools presented in this work. Impedance matching with a layer of alumina on top should be easy to obtain by using the simulation templates developed in this work. With the final design, a TWPA should be fabricated and tested.

Finally, other options would be to explore different nonlinear unit cells. The SNAIL with three big junction was just reproduced from the original KrTWPA, but the number of junctions is still a parameter that can be modified. Moreover, different unit cells based on Josephson junction are to be explored. Together with the proposed strategies of reducing the capacitance demands, a planar structure could still be achieved.

Chapter 9

Conclusions and Perspectives

9.1 Conclusions

In this thesis, the development of building blocks to engineer coherent quantum annealers in the QCT lab at IFAE has been started. At the same time, these developments have represented the first coherent control of both a transmon qubit and a flux qubit in the QCT group, being the first-ever coherent control of superconducting qubits in Southern Europe.

Prior to flux qubit experiments, transmon qubit measurements were performed to properly validate the QCT lab setup, while developing all the software and hardware machinery for time-domain qubit control techniques. A Universal Approximant algorithm was implemented on the transmon qubit to demonstrate the approximation power of single-qubit quantum circuits, as proof of the group's capabilities of qubit coherent quantum control.

Flux qubits were designed so that they could perform coherent annealing schedules. The theoretical design was conceived with special focus on achieving low persistent currents, and thus long coherence times. A dispersive readout was designed to implement common coherence time benchmarking. A comparison with other types of flux qubits, along with a preliminary coupled prototype and a guide on how to perform annealing schedules, has been performed.

The flux qubit measured had decay times as high as $> 40 \mu\text{s}$, which are indicative of good quality for flux qubits. Moreover, the coherent control was realized at different flux locations to provide insights from noise mechanisms. However, no control at low frequencies close to the symmetry point was possible in these devices and more tests will be required. The decoherence times observed were very low, reaching a maximum value of 13 ns away from the optimal coherence conditions. This value is likely limited by flux noise, and is expected to be reduced closer to the qubit's symmetry point. All these results provide feedback on the Hamiltonian design performed in this thesis, and suggest possible routes to improve the qubit devices (see Section 9.2.2).

Moreover, a thorough analysis on the aluminum magnetic penetration depth,

λ , for thin superconducting films has been developed for varying thicknesses, reaching values of $\lambda = 163$ nm for 25 nm-thick films, and getting close to the bulk value, $\lambda_{\text{bulk}} = 50$ nm, for the thickest 200 nm films, with $\lambda = 54$ nm. This characterization, that was missing in the literature, provides a valuable resource for better superconducting circuit design. The dependence of the kinetic inductance on λ is known, so the calibration performed is particularly useful for flux-sensitive devices, such as flux qubits. New fitting and simulation techniques have been developed, while also pointing out the possibility that thin-film aluminum changes superconductivity type within the range studied (20 – 200 nm).

Finally, a new physical design of a Kerr-reversed TWPA has been developed, removing the need of an external coil, which improves its usability and reducing the amplifier footprint. This development is key for scaling up the qubit readout technology.

9.2 Perspectives

9.2.1 Universal Approximant

The natural continuation of the Universal Approximant algorithm would be to directly optimize the parameters in the superconducting device. An extra addition of a TWPA to the current setup would speed the measurement process, together with a more efficient software control. However, it is important that other training algorithms are explored. The gradient-based algorithms will have to face sampling noise even if single-shot with high fidelity is achieved. Genetic algorithms, on the other hand, take too many evaluations of the cost function to reach the final results. Therefore, other gradient-free algorithms would probably be required to train the qubit.

9.2.2 Flux Qubits

The devices measured in this thesis can still hold interesting experimental work. Driving through the local flux line the qubit may be operated in the sweet spot. If that is achieved, a full noise characterization could provide insights on the noise limitations. Moreover, single-qubit quantum annealing routines can be performed to understand the role of coherence in annealing.

The results in this thesis show that larger dispersive shifts would be beneficial for a more efficient readout during the whole flux range. The fabrication accuracy should be also improved in order to meet the target design values. For the upcoming device generation, it is necessary that they take place in house.

Furthermore, a natural step forward in the development of quantum annealers would be to measure coupled devices. An initial coupling mechanism has been proposed, which could serve as a benchmark of coupled devices. However, different couplers could be explored to provide a larger coupling without the need to increase the persistent current of the qubits or the mutual inductance.

The control of the qubit could also be improved by replacing the small junction with a DC-SQUID so that the qubit gap, Δ , is tunable, and its value can be increased to reduce thermal effects.

In order to move towards a many-qubit quantum annealer, current-based readout must be incorporated, which could consist in substituting the end path of a readout resonator with a flux-sensitive element. This would mainly imply an extra flux line, but the rest of the dispersive measurement should not be dramatically modified.

Regarding the flux qubit Hamiltonian analysis, the work in comparing different flux qubits points out that the single-variable approximation used in the literature is not valid for the low-junction number, and the role of extra the difference modes is not fully understood. In this direction, increasing simulation capabilities by using more powerful computational resources could allow identifying under which circumstances the single-mode approximation correctly predicts the qubit behavior.

Finally, the most optimal flux qubit circuit design for quantum annealing is still to be found. In this sense, a coherent quantum annealer prototype could provide very important information regarding the effect of decoherence in quantum annealing, which may lead to improved qubit designs.

9.2.3 Magnetic Penetration Depth of Thin Film Superconducting Aluminum

Although the magnetic penetration depth has been calibrated for thin film superconducting aluminum, a more systematic study could be performed on some of the thin film parameters. For example, a thorough analysis on the fabrication process could provide information about the effect of the aluminum quality in the penetration depth.

In order to properly determine the superconductivity type of aluminum two experiments have been conceived, both focusing on identifying the presence of vortices in the film. First, replicating an experiment of trapping single vortices on Nb [Nsa14] could be replicated on Al, focusing on varying the film thickness. Another alternative would be to use imaging techniques to identify the presence of vortices, as well as its distribution.

Another path would be to develop applications based on the results of this thesis study, such as generating superinductors based on thin-film aluminum. With thick enough films becoming type-I superconductors, an experiment could compare the results with the use of grounds with holes to remove the presence of vortices.

9.2.4 Kerr-reversed TWPA

The next step of the work in TWPA design will be to fabricate the devices. For that, new Josephson junction fabrication procedures must be performed to yield the required I_C for the amplifier. Then, a new iteration of the design values should be implemented.

In order to obtain coplanar waveguide amplifiers, increased ebeam capabilities are needed, or the circuit element should be changed. Indeed, SNAIL's could be replaced with another nonlinear superconducting circuit to explore whether the amplification can be achieved without such a high inductance. This could lead to lower capacitance requirements that may be fulfilled with planar capacitances.

Bibliography

- [Abr57] A A Abrikosov. “Magnetic properties of superconductors of the second group”. In: *Sov. Phys. - JETP (Engl. Transl.); (United States)* (1957).
- [Aha04] Dorit Aharonov et al. “Adiabatic quantum computation is equivalent to standard quantum computation”. In: *45th Annual IEEE Symposium on Foundations of Computer Science* (2004), pp. 42–51.
- [Alb15] Tameem Albash and Daniel A. Lidar. “Decoherence in adiabatic quantum computation”. In: *Physical Review A* 91 (2015), p. 062320.
- [Alb16] Tameem Albash and Daniel A. Lidar. “Adiabatic quantum computation”. In: *Reviews of Modern Physics* 90 (2016), p. 015002.
- [Alb17] Tameem Albash and Daniel A. Lidar. “Demonstration of a Scaling Advantage for a Quantum Annealer over Simulated Annealing”. In: *Physical Review X* (2017).
- [Alt19] Ehud Altman et al. “Quantum Simulators: Architectures and Opportunities”. In: *arXiv: Quantum Physics* (2019).
- [Apo89] Bruno Apolloni, C. Carvalho, and Diego de Falco. “Quantum stochastic optimization”. In: *Stochastic Processes and their Applications* 33 (1989), pp. 233–244.
- [Aum20] José Aumentado. “Superconducting Parametric Amplifiers: The State of the Art in Josephson Parametric Amplifiers”. In: *IEEE Microwave Magazine* 21 (2020), pp. 45–59.
- [Bar11] Rami Barends et al. “Minimizing quasiparticle generation from stray infrared light in superconducting quantum circuits”. In: *Applied Physics Letters* 99 (2011), p. 113507.
- [Bau20] Bela Bauer et al. “Quantum Algorithms for Quantum Chemistry and Quantum Materials Science.” In: *Chemical reviews* (2020).
- [Bha21] Kishor Bharti et al. “Noisy intermediate-scale quantum (NISQ) algorithms”. In: *ArXiv abs/2101.08448* (2021).
- [Bla04] Alexandre Blais et al. “Cavity quantum electrodynamics for superconducting electrical circuits: An architecture for quantum computation”. In: *Physical Review A* 69 (2004), p. 062320.

- [Bla21] Alexandre Blais et al. “Circuit quantum electrodynamics”. In: *Rev. Mod. Phys.* 93 (2 May 2021), p. 025005. DOI: 10.1103/RevModPhys.93.025005.
- [Boi16] Sergio Boixo et al. “Characterizing quantum supremacy in near-term devices”. In: *Nature Physics* 14 (2016), pp. 595–600.
- [Bor28] Max Born and V. Fock. “Beweis des Adiabatenatzes”. In: *Zeitschrift für Physik* 51 (1928), pp. 165–180.
- [Bou98] Vincent Bouchiat et al. “Quantum coherence with a single Cooper pair”. In: *Physica Scripta* 1998 (1998), pp. 165–170.
- [Bra71] B. L. Brandt, R. D. Parks, and R. D. Chaudhari. “Intermediate state of thin superconductors”. In: *Journal of Low Temperature Physics* 4.1 (1971), pp. 41–63. DOI: 10.1007/BF00628436.
- [Bro13] Peter Brooks, Alexei Y. Kitaev, and John Preskill. “Protected gates for superconducting qubits”. In: *Physical Review A* 87 (2013), p. 052306.
- [Bro23] Michael Brooks. “Quantum computers: what are they good for?” In: *Nature* 617.7962 (May 2023), S1–S3. DOI: 10.1038/d41586-023-01692-9.
- [Bru15] A. Bruno et al. “Reducing intrinsic loss in superconducting resonators by surface treatment and deep etching of silicon substrates”. In: *Applied Physics Letters* 106.18 (May 2015), p. 182601. ISSN: 0003-6951. DOI: 10.1063/1.4919761.
- [Bur23] Guido Burkard et al. “Semiconductor spin qubits”. In: *Rev. Mod. Phys.* 95 (2 June 2023), p. 025003. DOI: 10.1103/RevModPhys.95.025003.
- [Byl11] Jonas Bylander et al. “Noise spectroscopy through dynamical decoupling with a superconducting flux qubit”. In: *Nature Physics* 7 (2011), pp. 565–570.
- [Can21] V. Canivell et al. “Startup Qilimanjaro—towards a European full-stack coherent quantum annealer platform”. In: *EPJ Quantum Technology* 8 (2021), pp. 1–9.
- [Cas08] Manuel A. Castellanos-Beltran et al. “Amplification and squeezing of quantum noise with a tunable Josephson metamaterial”. In: *Nature Physics* 4 (2008), pp. 929–931.
- [Cha16] Nicholas Chancellor, Stefan Zohren, and Paul A Warburton. “Circuit design for multi-body interactions in superconducting quantum annealing systems with applications to a scalable architecture”. In: *npj Quantum Information* 3 (2016), pp. 1–7.
- [Chi03] Irinel Chiorescu et al. “Coherent Quantum Dynamics of a Superconducting Flux Qubit”. In: *Science* 299 (2003), pp. 1869–1871.
- [Chi08] Andrew M. Childs and Wim van Dam. “Quantum algorithms for algebraic problems”. In: *Reviews of Modern Physics* 82 (2008), pp. 1–52.

- [Cho11] Jerry M. Chow et al. “Simple all-microwave entangling gate for fixed-frequency superconducting qubits.” In: *Physical review letters* 107 8 (2011), p. 080502.
- [Cia20] Alessandro Ciani and Barbara Maria Terhal. “Stoquasticity in circuit QED”. In: *Physical Review A* (2020).
- [Cro20] Elizabeth Crosson and Daniel A. Lidar. “Prospects for quantum enhancement with diabatic quantum annealing”. In: *Nature Reviews Physics* 3 (2020), pp. 466–489.
- [Dai21] X. Dai et al. “Calibration of Flux Crosstalk in Large-Scale Flux-Tunable Superconducting Quantum Circuits”. In: *PRX Quantum* 2 (4 Oct. 2021), p. 040313. DOI: 10.1103/PRXQuantum.2.040313.
- [Dam01] Wim van Dam, Michele Mosca, and Umesh V. Vazirani. “How powerful is adiabatic quantum computation?” In: *Proceedings 2001 IEEE International Conference on Cluster Computing* (2001), pp. 279–287.
- [Dem03] Mustafa Demirplak and Stuart A. Rice. “Adiabatic Population Transfer with Control Fields”. In: *Journal of Physical Chemistry A* 107 (2003), pp. 9937–9945.
- [Dem20] Hans Dembinski and Piti Ongmongkolkul et al. “scikit-hep/iminuit”. In: (Dec. 2020). DOI: 10.5281/zenodo.3949207.
- [DiC10] Leonardo DiCarlo et al. “Preparation and measurement of three-qubit entanglement in a superconducting circuit”. In: *Nature* 467 (2010), pp. 574–578.
- [DiV00] David P. DiVincenzo and IBM. “The Physical Implementation of Quantum Computation”. In: *Protein Science* 48 (2000), pp. 771–783.
- [Dol77] G. J. Dolan. “Offset masks for lift-off photoprocessing”. In: *Applied Physics Letters* 31 (1977), pp. 337–339.
- [Dor89] Richard C. Dorf and James A Svovoda. *Introduction to Electric Circuits*. John Wiley and Sons, 1989.
- [Doy08] Simon Doyle et al. “Lumped Element Kinetic Inductance Detectors”. In: *Journal of Low Temperature Physics* 151 (2008), pp. 530–536.
- [Ear18] N. Earnest et al. “Realization of a Λ System with Metastable States of a Capacitively Shunted Fluxonium”. In: *Phys. Rev. Lett.* 120 (15 Apr. 2018), p. 150504. DOI: 10.1103/PhysRevLett.120.150504.
- [Eom12] Byeong Ho Eom et al. “A wideband, low-noise superconducting amplifier with high dynamic range”. In: *Nature Physics* 8 (2012), pp. 623–627.
- [Esp21] Martina Esposito et al. “Perspective on traveling wave microwave parametric amplifiers”. In: *Applied Physics Letters* (2021).

- [Fab55] T. E. Faber and A. B. Pippard. “The penetration depth and high-frequency resistance of superconducting aluminium”. In: *Proceedings of the Royal Society of London. Series A. Mathematical and Physical Sciences* 231.1186 (Sept. 1955), pp. 336–353. DOI: 10.1098/rspa.1955.0178.
- [Fal04] Giuseppe Falci et al. “Initial decoherence in solid state qubits.” In: *Physical review letters* 94 16 (2004), p. 167002.
- [Far00a] Edward Farhi et al. “Quantum Computation by Adiabatic Evolution”. In: *arXiv: Quantum Physics* (2000).
- [Far00b] Edward Farhi et al. “Quantum Computation by Adiabatic Evolution”. In: *arXiv: Quantum Physics* (2000).
- [For16] P. Forn-D’iaz et al. “Ultrastrong coupling of a single artificial atom to an electromagnetic continuum in the nonperturbative regime”. In: *Nature Physics* 13 (2016), pp. 39–43.
- [For18] P. Forn-D’iaz et al. “Ultrastrong coupling regimes of light-matter interaction”. In: *Reviews of Modern Physics* (2018).
- [Fra17] N. E. Frattini et al. “3-Wave Mixing Josephson Dipole Element”. In: *arXiv: Superconductivity* (2017).
- [Fuj16] Keisuke Fujii and Kohei Nakajima. “Harnessing disordered quantum dynamics for machine learning”. In: *arXiv: Quantum Physics* (2016).
- [Gam06] Jay M. Gambetta et al. “Qubit-photon interactions in a cavity: Measurement-induced dephasing and number splitting”. In: *Physical Review A* 74 (2006), p. 42318.
- [Gam07] Jay M. Gambetta et al. “Quantum trajectory approach to circuit QED: Quantum jumps and the Zeno effect”. In: *Physical Review A* 77 (2007), p. 012112.
- [Gao08] Jiansong Gao et al. “Experimental evidence for a surface distribution of two-level systems in superconducting lithographed microwave resonators”. In: *Applied Physics Letters* 92 (2008), p. 152505.
- [Gee12] K. Geerlings et al. “Demonstrating a driven reset protocol for a superconducting qubit.” In: *Physical review letters* 110 12 (2012), p. 120501.
- [Gen18] P. G. De Gennes. *Superconductivity of Metals and Alloys*. CRC Press, Mar. 2018. DOI: 10.1201/9780429497032.
- [Glo18] Fred W. Glover, Gary A. Kochenberger, and Yu Du. “Quantum Bridge Analytics I: a tutorial on formulating and using QUBO models”. In: *4OR* 17 (2018), pp. 335–371.
- [Gol12] D J Goldie and Stafford Withington. “Non-equilibrium superconductivity in quantum-sensing superconducting resonators”. In: *Superconductor Science and Technology* 26 (2012).

- [Göp08] M. Göppl et al. “Coplanar waveguide resonators for circuit quantum electrodynamics”. In: *Journal of Applied Physics* 104.11 (Dec. 2008), p. 113904. ISSN: 0021-8979. DOI: 10.1063/1.3010859.
- [Gro20] Jeffrey A. Grover et al. “Fast, Lifetime-Preserving Readout for High-Coherence Quantum Annealers”. In: *PRX Quantum* (2020).
- [Gub05] A. I. Gubin et al. “Dependence of magnetic penetration depth on the thickness of superconducting Nb thin films”. In: *Phys. Rev. B* 72 (6 Aug. 2005), p. 064503. DOI: 10.1103/PhysRevB.72.064503.
- [Gus16] Simon Gustavsson et al. “Suppressing relaxation in superconducting qubits by quasiparticle pumping”. In: *Science* 354 (2016), pp. 1573–1577.
- [Hah50] Erwin L. Hahn. “Spin Echoes”. In: (1950).
- [Hak67] R. R. Hake. “Paramagnetic Superconductivity in Extreme Type-II Superconductors”. In: *Phys. Rev.* 158 (2 June 1967), pp. 356–376. DOI: 10.1103/PhysRev.158.356.
- [Hal20] Tom Halverson et al. “Efficient simulation of so-called non-stoquastic superconducting flux circuits.” In: *arXiv: Quantum Physics* (2020).
- [Har09a] R. Harris et al. “Experimental demonstration of a robust and scalable flux qubit”. In: *Physical Review B* 81 (2009), p. 134510.
- [Har09b] Richard G. Harris et al. “Compound Josephson-junction coupler for flux qubits with minimal crosstalk”. In: *Physical Review B* 80 (2009), p. 052506.
- [Har18] R. Harris et al. “Phase transitions in a programmable quantum spin glass simulator”. In: *Science* 361 (2018), pp. 162–165.
- [Hau19] Philipp Hauke et al. “Perspectives of quantum annealing: methods and implementations”. In: *Reports on Progress in Physics* 83 (2019).
- [Her22] Dylan Herman et al. “A Survey of Quantum Computing for Finance”. In: 2022.
- [Hit21] María Hita-Pérez et al. “Ultrastrong Capacitive Coupling of Flux Qubits”. In: *Physical Review Applied* (2021).
- [Hou08] Andrew A. Houck et al. “Controlling the spontaneous emission of a superconducting transmon qubit.” In: *Physical review letters* 101 8 (2008), p. 080502.
- [Ino12] Kunihiro Inomata et al. “Large dispersive shift of cavity resonance induced by a superconducting flux qubit in the straddling regime”. In: *Physical Review B* 86 (2012), p. 140508.
- [Ith05] Grégoire Ithier. “Manipulation, readout and analysis of the decoherence of a superconducting quantum bit”. Theses. Université Pierre et Marie Curie - Paris VI, Dec. 2005.
- [Jak22] Dieter Jaksch et al. “Variational Quantum Algorithms for Computational Fluid Dynamics”. In: *AIAA Journal* (2022).

- [Jef14] Evan Jeffrey et al. “Fast accurate state measurement with superconducting qubits.” In: *Physical review letters* 112 19 (2014), p. 190504.
- [Jin14] Xiaoyue Jin et al. “Thermal and Residual Excited-State Population in a 3D Transmon Qubit.” In: *Physical review letters* 114 24 (2014), p. 240501.
- [Joh09] Mark W. Johnson et al. “A scalable control system for a superconducting adiabatic quantum optimization processor”. In: *Superconductor Science and Technology* 23 (2009), p. 065004.
- [Jos62] B.D. Josephson. “Possible new effects in superconductive tunnelling”. In: *Physics Letters* 1.7 (1962), pp. 251–253. ISSN: 0031-9163. DOI: [https://doi.org/10.1016/0031-9163\(62\)91369-0](https://doi.org/10.1016/0031-9163(62)91369-0).
- [Jur20] Petar Jurcevic et al. “Demonstration of quantum volume 64 on a superconducting quantum computing system”. In: *Quantum Science & Technology* 6 (2020).
- [Kad98] Tadashi Kadowaki and Hidetoshi Nishimori. “Quantum annealing in the transverse Ising model”. In: *Physical Review E* 58 (1998), pp. 5355–5363.
- [Kaf16] Dvir Kafri et al. “Tunable inductive coupling of superconducting qubits in the strongly nonlinear regime”. In: *Physical Review A* 95 (2016), p. 052333.
- [Kar19] Kenichi Karatsu et al. “Mitigation of cosmic ray effect on microwave kinetic inductance detector arrays”. In: *Applied Physics Letters* (2019).
- [Kat50] Tosio Kato. “On the Adiabatic Theorem of Quantum Mechanics”. In: *Journal of the Physical Society of Japan* 5 (1950), pp. 435–439.
- [Kau08] R. L. Kautz. “Picosecond pulses on superconducting striplines”. In: *Journal of Applied Physics* 49.1 (Aug. 2008), pp. 308–314. ISSN: 0021-8979. DOI: 10.1063/1.324387.
- [Khe20] Mostafa Khezri et al. “Anneal-path correction in flux qubits”. In: *npj Quantum Information* 7 (2020), pp. 1–8.
- [Kim23] Youngseok Kim et al. “Evidence for the utility of quantum computing before fault tolerance”. In: *Nature* 618 (June 2023), pp. 500–505. DOI: 10.1038/s41586-023-06096-3.
- [Kin21] Andrew D. King et al. “Scaling advantage over path-integral Monte Carlo in quantum simulation of geometrically frustrated magnets”. In: *Nature Communications* 12 (2021).
- [Kin22] Andrew D. King et al. “Coherent quantum annealing in a programmable 2,000 qubit Ising chain”. In: *Nature Physics* 18 (2022), pp. 1324–1328.
- [Kir83] Scott Kirkpatrick, Charles D. Gelatt, and Mario P. Vecchi. “Optimization by Simulated Annealing”. In: *Science* 220 (1983), pp. 671–680.

- [Kit20] Koki Kitai et al. “Designing metamaterials with quantum annealing and factorization machines”. In: *arXiv: Applied Physics* 2 (2020).
- [Kli18] Paul V. Klimov et al. “Fluctuations of Energy-Relaxation Times in Superconducting Qubits.” In: *Physical review letters* 121 9 (2018), p. 090502.
- [Kni07] Emanuel Knill et al. “Randomized Benchmarking of Quantum Gates”. In: *Physical Review A* 77 (2007), p. 012307.
- [Koc07] Jens Koch et al. “Charge-insensitive qubit design derived from the Cooper pair box”. In: *Physical Review A* 76 (2007), p. 042319.
- [Kra19] Philip Krantz et al. “A quantum engineer’s guide to superconducting qubits”. In: *Applied Physics Reviews* (2019).
- [Kru06] J. Krupka et al. “Measurements of Permittivity, Dielectric Loss Tangent, and Resistivity of Float-Zone Silicon at Microwave Frequencies”. In: *IEEE Transactions on Microwave Theory and Techniques* 54.11 (2006), pp. 3995–4001. DOI: 10.1109/TMTT.2006.883655.
- [Lad10] Thaddeus D. Ladd et al. “Quantum computers”. In: *Nature* 464 (2010), pp. 45–53.
- [Lec15] Wolfgang Lechner, Philipp Hauke, and Peter Zoller. “A quantum annealing architecture with all-to-all connectivity from local interactions”. In: *Science Advances* 1 (2015).
- [Li22] Kungang Li et al. “Long-lived transmons with different electrode layouts”. In: *MRS Advances* 7 (2022), pp. 273–277.
- [Lóp23] David López-Núñez et al. *Magnetic penetration depth of Aluminum thin films*. 2023.
- [Mac15] Chris Macklin et al. “A near-quantum-limited Josephson traveling-wave parametric amplifier”. In: *Science* 350 (2015), pp. 307–310.
- [Maj07] Johannes Majer et al. “Coupling superconducting qubits via a cavity bus”. In: *Nature* 449 (2007), pp. 443–447.
- [Mal18] Nataliya Maleeva et al. “Circuit quantum electrodynamics of granular aluminum resonators”. In: *Nature communications* 9.1 (2018), p. 3889.
- [Man09] Vladimir E. Manucharyan et al. “Fluxonium: Single Cooper-Pair Circuit Free of Charge Offsets”. In: *Science* 326 (2009), pp. 113–116.
- [Mar05] John M. Martinis et al. “Decoherence in Josephson qubits from dielectric loss.” In: *Physical review letters* 95 21 (2005), p. 210503.
- [Mat58] D. C. Mattis and J. Bardeen. “Theory of the Anomalous Skin Effect in Normal and Superconducting Metals”. In: *Phys. Rev.* 111 (2 July 1958), pp. 412–417. DOI: 10.1103/PhysRev.111.412.

- [McE21] Matthew J. McEwen et al. “Removing leakage-induced correlated errors in superconducting quantum error correction”. In: *Nature Communications* 12 (2021).
- [McK16a] David C. McKay et al. “Efficient Z gates for quantum computing”. In: *Physical Review A* 96 (2016), p. 022330.
- [McK16b] David C. McKay et al. “Universal Gate for Fixed-Frequency Qubits via a Tunable Bus”. In: *Physical review applied* 6 (2016), p. 064007.
- [McR20] C. R. H. McRae et al. “Materials loss measurements using superconducting microwave resonators.” In: *The Review of scientific instruments* 91 9 (2020), p. 091101.
- [Men19] Tim Menke et al. “Automated discovery of superconducting circuits and its application to 4-local coupler design”. In: *arXiv: Quantum Physics* (2019).
- [Mes61] A. M. L. Messiah. *Quantum Mechanics*. Dover Books, 1961.
- [Mes71] R. H. Meservey and Paul M. Tedrow. “Properties of Very Thin Aluminum Films”. In: *Journal of Applied Physics* 42 (1971), pp. 51–53.
- [Mon15] Ashley Montanaro. “Quantum algorithms: an overview”. In: *npj Quantum Information* 2 (2015).
- [Mot09] Felix Motzoi et al. “Simple pulses for elimination of leakage in weakly nonlinear qubits.” In: *Physical review letters* 103 11 (2009), p. 110501.
- [Neu17] Florian Neukart et al. “Traffic Flow Optimization Using a Quantum Annealer”. In: *ArXiv abs/1708.01625* (2017).
- [Nie11] Michael A. Nielsen and Isaac L. Chuang. *Quantum Computation and Quantum Information (10th Anniversary edition)*. Cambridge University Press, 2011.
- [Nov18] Sergey Novikov et al. “Exploring More-Coherent Quantum Annealing”. In: *2018 IEEE International Conference on Rebooting Computing (ICRC)* (2018), pp. 1–7.
- [Nsa14] Ibrahim Nsanzineza and Britton L. T. Plourde. “Trapping a single vortex in a superconducting microwave resonator”. In: *Bulletin of the American Physical Society* 2014 (2014).
- [OCo08] Aaron D. O’Connell et al. “Microwave dielectric loss at single photon energies and millikelvin temperatures”. In: *Applied Physics Letters* 92 (2008), p. 112903.
- [Oli13] William D. Oliver and Paul Welander. “Materials in superconducting quantum bits”. In: *MRS Bulletin* 38 (2013), pp. 816–825.
- [Orl91] Terry P. Orlando and Kevin A. Delin. *Foundations of Applied Superconductivity*. Adisson-Wesley, 1991.

- [Orl99] Terry P. Orlando et al. “Superconducting persistent-current qubit”. In: *Physical Review B* 60 (1999), pp. 15398–15413.
- [Ozf19] Isil Ozfidan et al. “Demonstration of a Nonstoquastic Hamiltonian in Coupled Superconducting Flux Qubits”. In: *Physical Review Applied* (2019).
- [Pai11] Hanhee Paik et al. “Observation of high coherence in Josephson junction qubits measured in a three-dimensional circuit QED architecture.” In: *Physical review letters* 107 24 (2011), p. 240501.
- [Pan22] Xianchuang Pan et al. “Engineering superconducting qubits to reduce quasiparticles and charge noise”. In: *Nature Communications* 13.1 (2022), p. 7196. DOI: 10.1038/s41467-022-34727-2.
- [Par17] Adrian Parra-Rodriguez et al. “Quantum networks in divergence-free circuit QED”. In: *Quantum Science and Technology* 3 (2017).
- [Pea64] J. Pearl. “Current distribution in superconducting films carrying quantized fluxoids”. In: *Applied Physics Letters* 5.4 (Aug. 1964), pp. 65–66. ISSN: 0003-6951. DOI: 10.1063/1.1754056.
- [Per08] Alejandro Perdomo-Ortiz, Salvador Elías Venegas-Andraca, and Alán Aspuru-Guzik. “A study of heuristic guesses for adiabatic quantum computation”. In: *Quantum Information Processing* 10 (2008), pp. 33–52.
- [Per21] Matilda Peruzzo et al. “Geometric Superinductance Qubits: Controlling Phase Delocalization across a Single Josephson Junction”. In: *PRX Quantum* (2021).
- [Pér21] Adrián Pérez-Salinas et al. “One qubit as a universal approximant”. In: *Phys. Rev. A* 104 (1 July 2021), p. 012405. DOI: 10.1103/PhysRevA.104.012405.
- [Phi87] W. A. Phillips. “Two-level states in glasses”. In: *Reports on Progress in Physics* 50 (1987), pp. 1657–1708.
- [Pip53] Alfred Brian Pippard and William Lawrence Bragg. “An experimental and theoretical study of the relation between magnetic field and current in a superconductor”. In: *Proceedings of the Royal Society of London. Series A. Mathematical and Physical Sciences* 216.1127 (1953), pp. 547–568. DOI: 10.1098/rspa.1953.0040.
- [Pla19] Luca Planat et al. “Photonic-Crystal Josephson Traveling-Wave Parametric Amplifier”. In: *Physical Review X* (2019).
- [Pog21] Ivan Pogorelov et al. “Compact Ion-Trap Quantum Computing Demonstrator”. In: *PRX Quantum* (2021).
- [Pol08] Stefano Poletto et al. “Coherent oscillations in a superconducting tunable flux qubit manipulated without microwaves”. In: *New Journal of Physics* 11 (2008), p. 013009.

- [Pop14] Ioan M. Pop et al. “Coherent suppression of electromagnetic dissipation due to superconducting quasiparticles”. In: *Nature* 508 (2014), pp. 369–372.
- [Pop24] Ioan Pop. “Granular Aluminum Flux qubit”. In: 2024. private communication.
- [Poz90] David M. Pozar. *Microwave Engineering*. John Wiley and Sons, 1990.
- [Pre18] John Preskill. “Quantum Computing in the NISQ era and beyond”. In: *Quantum* (2018).
- [Pro15] S. Probst et al. “Efficient and robust analysis of complex scattering data under noise in microwave resonators”. In: *Review of Scientific Instruments* 86.2 (Feb. 2015). DOI: 10.1063/1.4907935.
- [Pur16] Shruti Puri et al. “Quantum annealing with all-to-all connected nonlinear oscillators”. In: *Nature Communications* 8 (2016).
- [Ran21] Arpit Ranadive et al. “Kerr reversal in Josephson meta-material and traveling wave parametric amplification”. In: *Nature Communications* 13 (2021).
- [Rig10] Chad T. Rigetti and Michel H. Devoret. “Fully microwave-tunable universal gates in superconducting qubits with linear couplings and fixed transition frequencies”. In: *Physical Review B* 81 (2010), p. 134507.
- [Rip22] Juan José García Ripoll. *Quantum Information and Quantum Optics with Superconducting Circuits*. Spain: Cambridge University Press, 2022.
- [Rom82] J. Romijn et al. “Critical pair-breaking current in superconducting aluminum strips far below T_c ”. In: *Phys. Rev. B* 26 (7 Oct. 1982), pp. 3648–3655. DOI: 10.1103/PhysRevB.26.3648.
- [Rot16] H Rotzinger et al. “Aluminium-oxide wires for superconducting high kinetic inductance circuits”. In: *Superconductor Science and Technology* 30.2 (Nov. 2016), p. 025002. DOI: 10.1088/0953-2048/30/2/025002.
- [Roy21] Tanay Roy et al. “Tomography in the presence of stray inter-qubit coupling”. In: 2021.
- [Rug06] B. Ruggiero et al. “rf SQUID system as tunable flux qubit”. In: *Physics Letters A* 356.6 (2006), pp. 435–438. ISSN: 0375-9601. DOI: <https://doi.org/10.1016/j.physleta.2006.04.003>.
- [Sai69] D. Saint-James et al. *Type II superconductivity*. Pergamon, New York, 1969.
- [Sal16] A. Sala et al. “Shortcut to adiabaticity in spinor condensates”. In: *Physical Review A* 94 (2016).
- [San16] Daniel Thomas Sank et al. “Measurement-Induced State Transitions in a Superconducting Qubit: Beyond the Rotating Wave Approximation.” In: *Physical review letters* 117 19 (2016), p. 190503.

- [Sat22] C. D. Satrya et al. “Electromagnetic simulation and microwave circuit approach of heat transport in superconducting qubits”. In: *Journal of Physics Communications* 7 (2022).
- [Sen08] S. L. Sendelbach et al. “Magnetism in SQUIDs at millikelvin temperatures.” In: *Physical review letters* 100 22 (2008), p. 227006.
- [Set15] Eyob A. Sete, John M. Martinis, and Alexander N. Korotkov. “Quantum theory of a bandpass Purcell filter for qubit readout”. In: *Physical Review A* 92 (2015), p. 012325.
- [She17] Sarah Sheldon et al. “Characterization of hidden modes in networks of superconducting qubits”. In: *Applied Physics Letters* 111 (2017), p. 222601.
- [Sho04] Peter W. Shor. “Progress in Quantum Algorithms”. In: *Quantum Information Processing* 3 (2004), pp. 5–13.
- [Sho94] Peter W. Shor. “Algorithms for quantum computation: discrete logarithms and factoring”. In: *Proceedings 35th Annual Symposium on Foundations of Computer Science* (1994), pp. 124–134.
- [Sil67] Arnold H. Silver and James Edward Zimmerman. “QUANTUM STATES AND TRANSITIONS IN WEAKLY CONNECTED SUPERCONDUCTING RINGS.” In: *Physical Review* 157 (1967), pp. 317–341.
- [Sin09] Amit Singer and Mihai Cucuringu. “Uniqueness of Low-Rank Matrix Completion by Rigidity Theory”. In: *ArXiv* abs/0902.3846 (2009).
- [Sli12] Daniel H. Slichter et al. “Measurement-induced qubit state mixing in circuit QED from up-converted dephasing noise.” In: *Physical review letters* 109 15 (2012), p. 153601.
- [Slu19] Sergei Slussarenko and Geoff J. Pryde. “Photonic quantum information processing: A concise review”. In: *Applied Physics Reviews* 6.4 (Oct. 2019), p. 041303. ISSN: 1931-9401. DOI: 10.1063/1.5115814.
- [Smi19] Adam Smith et al. “Simulating quantum many-body dynamics on a current digital quantum computer”. In: *npj Quantum Information* 5 (2019).
- [Sta04] Gheorghe Stan, Stuart B. Field, and John M. Martinis. “Critical field for complete vortex expulsion from narrow superconducting strips.” In: *Physical review letters* 92 9 (2004), p. 097003.
- [Ste06] Karsten Sternickel and Alex I. Braginski. “Biomagnetism using SQUIDs: status and perspectives”. In: *Superconductor Science and Technology* 19 (2006), S160–S171.
- [Ste14] Michael Stern et al. “Flux qubits with long coherence times for hybrid quantum circuits.” In: *Physical review letters* 113 12 (2014), p. 123601.

- [Sus18] Yuki Susa et al. “Exponential Speedup of Quantum Annealing by Inhomogeneous Driving of the Transverse Field”. In: *Journal of the Physical Society of Japan* 87 (2018), pp. 023002–023002.
- [The20] A. Thevenot. *Test functions for optimization*. https://github.com/AxelThevenot/Python_Benchmark_Test_Optimization_Function_Single_Objective. 2020.
- [Tin04] M. Tinkham. *Introduction to Superconductivity*. Dover Books on Physics Series. Dover Publications, 2004. ISBN: 9780486134727.
- [Tur91] John P. Turneaure, Jürgen Halbritter, and Harry Alan Schwettman. “The surface impedance of superconductors and normal conductors: The Mattis-Bardeen theory”. In: *Journal of Superconductivity* 4 (1991), pp. 341–355.
- [Van03] C. H. Van Der Wal et al. “Engineering decoherence in Josephson persistent-current qubits”. In: *European Physical Journal B* 31.1 (2003), pp. 111–124. ISSN: 14346028. DOI: 10.1140/epjb/e2003-00015-9.
- [Vio98] Lorenza Viola and Seth Lloyd. “DYNAMICAL SUPPRESSION OF DECOHERENCE IN TWO-STATE QUANTUM SYSTEMS”. In: *Physical Review A* 58 (1998), pp. 2733–2744.
- [Voo16] Uri Vool and Michel H. Devoret. “Introduction to quantum electromagnetic circuits”. In: *International Journal of Circuit Theory and Applications* 45 (2016), pp. 897–934.
- [Wan14] C. Wang et al. “Measurement and control of quasiparticle dynamics in a superconducting qubit”. In: *Nature Communications* 5.1 (2014), p. 5836. DOI: 10.1038/ncomms6836.
- [Wat94] Koki Watanabe, Keiji Yoshida, and Takeshi Aoki Kohjiro. “Kinetic Inductance of Superconducting Coplanar Waveguides”. In: *Japanese Journal of Applied Physics* 33 (1994), p. 5708.
- [Web11] S. J. Weber et al. “Single crystal silicon capacitors with low microwave loss in the single photon regime”. In: *Applied Physics Letters* 98.17 (Apr. 2011), p. 172510. ISSN: 0003-6951. DOI: 10.1063/1.3583449.
- [Web17] Steven J. Weber et al. “Coherent Coupled Qubits for Quantum Annealing”. In: *Physical Review Letters* (2017).
- [Wu21] Xiaoling Wu et al. “A concise review of Rydberg atom based quantum computation and quantum simulation*”. In: *Chinese Physics B* 30.2 (Feb. 2021), p. 020305. DOI: 10.1088/1674-1056/abd76f.
- [Yam08] Tsuyoshi Yamamoto et al. “Flux-driven Josephson parametric amplifier”. In: *arXiv: Superconductivity* (2008).

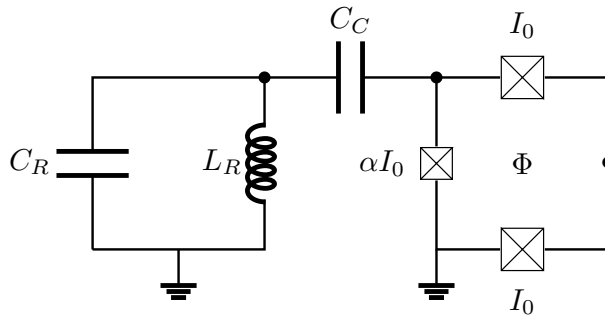
- [Yam22] T. Yamaji et al. “Spectroscopic observation of the crossover from a classical Duffing oscillator to a Kerr parametric oscillator”. In: *Phys. Rev. A* 105 (2 Feb. 2022), p. 023519. DOI: 10.1103/PhysRevA.105.023519.
- [Yan15] Fei Yan et al. “The flux qubit revisited to enhance coherence and reproducibility”. In: *Nature Communications* 7 (2015).
- [Yan20] Fei Yan et al. “Engineering Framework for Optimizing Superconducting Qubit Designs”. In: *arXiv: Quantum Physics* (2020).
- [Yos06] Fumiki Yoshihara et al. “Decoherence of flux qubits due to $1/f$ flux noise.” In: *Physical review letters* 97 16 (2006), p. 167001.
- [Yos14] Fumiki Yoshihara et al. “Flux qubit noise spectroscopy using Rabi oscillations under strong driving conditions”. In: *Physical Review B* 89 (2014), p. 020503.
- [Zha17] J. H. Zhang et al. “Observation of a many-body dynamical phase transition with a 53-qubit quantum simulator”. In: *Nature* 551 (2017), pp. 601–604.
- [Zhu12] Guanyu Zhu et al. “Circuit QED with fluxonium qubits: Theory of the dispersive regime”. In: *Physical Review B* 87 (2012), p. 024510.
- [Zhu21] Qingling Zhu et al. “Quantum computational advantage via 60-qubit 24-cycle random circuit sampling.” In: *Science bulletin* 67 3 (2021), pp. 240–245.
- [Zmu12] Jonas Zmuidzinas. “Superconducting Microresonators: Physics and Applications”. In: *Annual Review of Condensed Matter Physics* 3.1 (2012), pp. 169–214. DOI: 10.1146/annurev-conmatphys-020911-125022.

Appendix A

Circuit Quantization

A.1 Introduction

As an example we will use the following circuit



Note that in this circuit we have three kinds of elements: capacitors, inductors and Josephson Junctions (from now on, JJ).

The purpose is to write the Hamiltonian of these circuits. However, first the Lagrangian should be obtained. For that, we will use Kirchoff laws and an arbitrary description of the system.

A.2 Rules

A set of rules will be given so that following them, one arrives to the correct Hamiltonian. The idea is to obtain the movement equations for each node by using the Kirchoff relations for currents in a node

$$\sum I_{in} = \sum I_{out} \tag{A.1}$$

Once we have the equations of motion, the Lagrangian can be obtained knowing the relation

$$\frac{d}{dt} \left(\frac{\partial \mathcal{L}}{\partial \dot{x}_i} \right) = \frac{\partial \mathcal{L}}{\partial x_i} \quad (\text{A.2})$$

where q_i can be any coordinate. This last expression gives the movement equations for coordinate i .

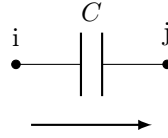
Our coordinates will always be the magnetic flux Φ_i . Hence, the first we should know is the intensity of every component in terms of the flux.

A.2.1 Basic components

We will deal with three basic components: capacitances, inductors and JJ. Every component has a different relation of the current, also depending on the current direction.

A.2.1.1 Capacitance

A capacitance is an element which stores charge and is characterized by its capacitance C .

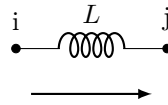


According to the direction of the intensity, the relation is

$$I = C(\ddot{\Phi}_j - \ddot{\Phi}_i) \quad (\text{A.3})$$

A.2.1.2 Inductance

An inductance is an element which develops a voltage when you change the current through it and is characterized by its inductance L .



According to the direction of the intensity, the relation is

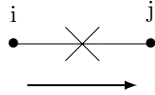
$$I = \frac{\Phi_j - \Phi_i}{L} \quad (\text{A.4})$$

A.2.1.3 Josephson Junction

A JJ is a circuit element made up of a tunnel junction between two superconductors. It is characterized by its capacitance C_J and its so-called Josephson energy E_J , assuming the resistive channel to be negligible. The relation between the current and the voltage through it is nonlinear and that makes it a key component for qubits. The JJ acts as an ideal JJ and a capacitance in parallel.



Then, each JJ has to be decomposed into its ideal JJ and its capacitance. The intensity flowing through a capacitance has already been written. Then, only the ideal JJ must be taken into account.



The intensity through an ideal JJ is, according to the current sign

$$I = I_o \sin \left(\frac{2\pi}{\Phi_0} (\Phi_j - \Phi_i) \right) \tag{A.5}$$

, where the following relation between the magnetic flux and the superconducting phase must be noted

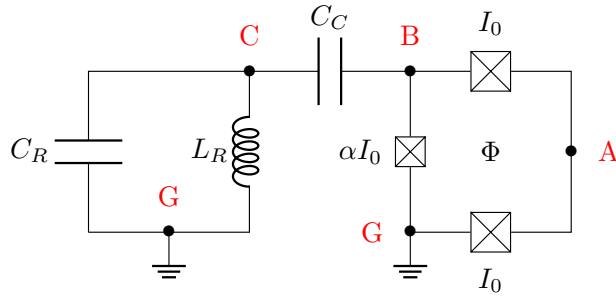
$$\varphi = \frac{2\pi}{\Phi_0} \Phi \tag{A.6}$$

being $\Phi_0 = \frac{2e}{h}$ the superconducting flux quantum.

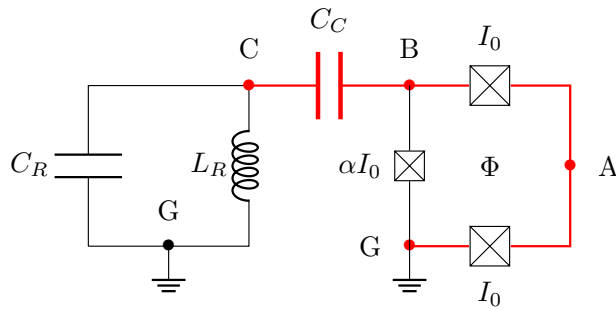
A.2.2 Spanning tree

1. First, all the nodes should be identified. Then, one of them should be put as ground. This is the same as choosing a zero in the energy or in a coordinate system.

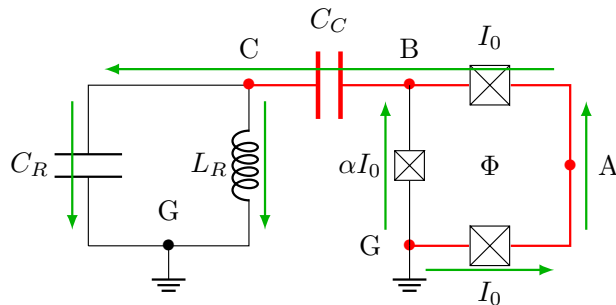
In our circuit the ground is already chosen, but could be any other. Note that there are two grounds because they are connected and, then, at the same voltage. All the remaining nodes are called active nodes. Let's put a letter on each of them.



2. Now, from the ground mode, all the nodes must be connected following only one path. That means, you choose branches in a way that you can go from the ground until every point following only one branch. The chosen branches will form the spanning tree. The remaining branches will be called closure branches and its flux will be given by the constraints of the circuit.

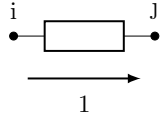


3. An arbitrary direction of the intensity in every branch has to be chosen. It has no importance, but it is necessary for being consistent.



4. Now the relation between the branch fluxes and the node fluxes depends

on which tree has been chosen. The following branch, 1, has a circuit element and is between the nodes i and j .



For the spanning branches, the relation is as follows

$$\Phi_1 = \Phi_j - \Phi_i \quad (\text{A.7})$$

However, for closure branches, it can hold a flux. If the closure branches are enclosing a closed loop surrounded by inductances or JJ, then a flux must be added to the relation. The sign of the flux is not clear, but one must be consistent. In our case, we decide the direction of the flux (if escaping from the page or going inwards), and then we sum it when the direction of the branch intensity coincides with that provoked by the flux, and negative if they go in opposite directions. Then, whenever there's a flux, the relation is

$$\Phi_1 = \Phi_j - \Phi_i \pm \Phi \quad (\text{A.8})$$

Now we have all the necessary to obtain the Hamiltonian of our circuit. The steps are:

- Movement Equations
- Lagrangian
- Conjugate moment
- Hamiltonian

A.3 Procedure

A.3.1 Movement equations

We must obtain three movement equations, for each of the three active nodes: A , B and C . We will use the Kirchhoff law $\sum I_{in} = \sum I_{out}$

- Node A

$$\begin{aligned} \sum I_{in} &= C_J (\ddot{\Phi}_A - \ddot{\Phi}_G) + I_0 \sin\left(\frac{2\pi}{\Phi_0} (\Phi_A - \Phi_G)\right) \\ &= C_J \ddot{\Phi}_A + I_0 \sin\left(\frac{2\pi}{\Phi_0} \Phi_A\right) \end{aligned} \quad (\text{A.9})$$

$$\sum I_{out} = C_J (\ddot{\Phi}_B - \ddot{\Phi}_A) + I_0 \sin\left(\frac{2\pi}{\Phi_0} (\Phi_B - \Phi_A)\right) \quad (\text{A.10})$$

Now, matching both equations, we reorganize the terms depending on the second time derivatives of the flux on the left side and the terms depending on the flux on the right-hand side, as it will be easier for later. Then, the movement equation for node A is

$$\boxed{C_J \left(2\ddot{\Phi}_A - \ddot{\Phi}_B \right) = I_0 \sin \left(\frac{2\pi}{\Phi_0} (\Phi_B - \Phi_A) \right) - I_0 \sin \left(\frac{2\pi}{\Phi_0} \Phi_A \right)} \quad (\text{A.11})$$

- Node B

$$\begin{aligned} \sum I_{in} &= I_0 \sin \left(\frac{2\pi}{\Phi_0} (\Phi_B - \Phi_A) \right) + C_J \left(\ddot{\Phi}_B - \ddot{\Phi}_A \right) \\ &\quad + \alpha I_0 \sin \left(\frac{2\pi}{\Phi_0} (\Phi_B - \Phi_G - \Phi) \right) + \alpha C_J \left(\ddot{\Phi}_B - \ddot{\Phi}_G \right) \\ &= I_0 \sin \left(\frac{2\pi}{\Phi_0} (\Phi_B - \Phi_A) \right) + \alpha I_0 \sin \left(\frac{2\pi}{\Phi_0} (\Phi_B - \Phi) \right) \\ &\quad + C_J \left(\ddot{\Phi}_B - \ddot{\Phi}_A \right) + \alpha C_J \ddot{\Phi}_B \end{aligned} \quad (\text{A.12})$$

$$\sum I_{out} = C_C \left(\ddot{\Phi}_C - \ddot{\Phi}_B \right) \quad (\text{A.13})$$

Combining both and reorganizing the terms we arrive to the movement equation for node B .

$$\boxed{C_J \left(\ddot{\Phi}_B - \ddot{\Phi}_A \right) + \alpha C_J \ddot{\Phi}_B + C_C \left(\ddot{\Phi}_B - \ddot{\Phi}_C \right) = -I_0 \sin \left(\frac{2\pi}{\Phi_0} (\Phi_B - \Phi_A) \right) - \alpha I_0 \sin \left(\frac{2\pi}{\Phi_0} (\Phi_B - \Phi) \right)} \quad (\text{A.14})$$

- Node C

$$\sum I_{in} = C_C \left(\ddot{\Phi}_C - \ddot{\Phi}_B \right) \quad (\text{A.15})$$

$$\begin{aligned} \sum I_{out} &= C_R \left(\ddot{\Phi}_G - \ddot{\Phi}_C \right) + \frac{\Phi_G - \Phi_C}{L_R} \\ &= -C_R \ddot{\Phi}_C - \frac{\Phi_C}{L_R} \end{aligned} \quad (\text{A.16})$$

Hence, the motion equations for node C are,

$$\boxed{C_C \left(\ddot{\Phi}_C - \ddot{\Phi}_B \right) + C_R \ddot{\Phi}_C = -\frac{\Phi_C}{L_R}} \quad (\text{A.17})$$

A.3.2 Lagrangian

The final step for finding the Lagrangian is to integrate all three movement equations, knowing that

$$\frac{d}{dt} \left(\frac{\partial \mathcal{L}}{\partial \dot{\Phi}_i} \right) = \frac{\partial \mathcal{L}}{\partial \Phi_i} \quad (\text{A.18})$$

Then we will obtain the dependence of the Lagrangian on each of the variables. Combining the three parts of the Lagrangian, avoiding the repetition of terms, one will obtain the final Lagrangian, except for constant terms.

- Node A

Integrating equation A.11 on both sides, we obtain

$$\begin{aligned} \mathcal{L} = & C_J \left(\dot{\Phi}_A^2 - \dot{\Phi}_A \dot{\Phi}_B \right) + E_J \cos \left(\frac{2\pi}{\Phi_0} (\Phi_B - \Phi_A) \right) \\ & + E_J \cos \left(\frac{2\pi}{\Phi_0} \Phi_A \right) + f_A \left(\Phi_B, \dot{\Phi}_B, \Phi_C, \dot{\Phi}_C \right) \end{aligned} \quad (\text{A.19})$$

- Node B

Using now equation A.14

$$\begin{aligned} \mathcal{L} = & C_J \left(\frac{\dot{\Phi}_B^2}{2} - \dot{\Phi}_A \dot{\Phi}_B \right) + \alpha C_J \frac{\dot{\Phi}_B^2}{2} + C_C \left(\frac{\dot{\Phi}_B^2}{2} - \dot{\Phi}_B \dot{\Phi}_C \right) \\ & + E_J \cos \left(\frac{2\pi}{\Phi_0} (\Phi_B - \Phi_A) \right) + \alpha E_J \cos \left(\frac{2\pi}{\Phi_0} (\Phi_B - \Phi) \right) \\ & + f_B \left(\Phi_A, \dot{\Phi}_A, \Phi_C, \dot{\Phi}_C \right) \end{aligned} \quad (\text{A.20})$$

- Node C

Finally, with A.17

$$\begin{aligned} \mathcal{L} = & C_C \left(\frac{\dot{\Phi}_C^2}{2} - \dot{\Phi}_B \dot{\Phi}_C \right) + C_R \frac{\dot{\Phi}_C^2}{2} + \frac{\Phi_C^2}{2L_R} \\ & + f_C \left(\Phi_A, \dot{\Phi}_A, \Phi_B, \dot{\Phi}_B \right) \end{aligned} \quad (\text{A.21})$$

Combining all the terms, except for constant terms, the total Lagrangian results in

$$\begin{aligned} \mathcal{L} = & C_J \left(\dot{\Phi}_A^2 - \dot{\Phi}_A \dot{\Phi}_B + \frac{\dot{\Phi}_B^2}{2} \right) + \alpha C_J \frac{\dot{\Phi}_B^2}{2} + C_C \left(\frac{\dot{\Phi}_B^2}{2} - \dot{\Phi}_B \dot{\Phi}_C + \frac{\dot{\Phi}_C^2}{2} \right) \\ & + C_R \frac{\dot{\Phi}_C^2}{2} + \frac{\Phi_C^2}{2L_R} + E_J \cos \left(\frac{2\pi}{\Phi_0} \Phi_A \right) + E_J \cos \left(\frac{2\pi}{\Phi_0} (\Phi_B - \Phi_A) \right) \\ & + \alpha E_J \cos \left(\frac{2\pi}{\Phi_0} (\Phi_B - \Phi) \right) \end{aligned} \quad (\text{A.22})$$

Reordering the terms one arrives the final expression

$$\mathcal{L} = \frac{C_J}{2} \dot{\Phi}_A^2 + \frac{C_J}{2} (\dot{\Phi}_A - \dot{\Phi}_B)^2 + \alpha \frac{C_J}{2} \dot{\Phi}_B^2 + \frac{C_c}{2} (\dot{\Phi}_B - \dot{\Phi}_C)^2 + \frac{C_R}{2} \dot{\Phi}_C^2 + \frac{\Phi_C^2}{2L_R} + E_J \cos\left(\frac{2\pi}{\Phi_0} \Phi_A\right) + E_J \cos\left(\frac{2\pi}{\Phi_0} (\Phi_B - \Phi_A)\right) + \alpha E_J \cos\left(\frac{2\pi}{\Phi_0} (\Phi_B - \Phi)\right) \quad (\text{A.23})$$

A.3.3 Conjugate Momentum and Hamiltonian

Once the Lagrangian has been obtained, the next steps are fairly simple and will not be written. The next step is to find the conjugate momenta, which will be the charge at each node.

$$q_i = \frac{\partial \mathcal{L}}{\partial \dot{\Phi}_i} \quad (\text{A.24})$$

And from here, one just has to follow the final expression for obtaining the Hamiltonian

$$H = \sum_i \dot{\Phi}_i q_i - \mathcal{L} \quad (\text{A.25})$$

To quantize the Hamiltonian one just has to promote the flux and the charge to quantum mechanical operators

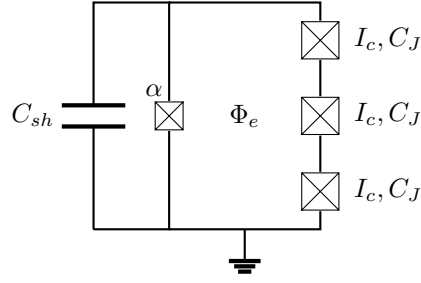
$$\begin{aligned} \Phi_i &\longrightarrow \hat{\Phi}_i \\ q_i &\longrightarrow \hat{q}_i \end{aligned} \quad (\text{A.26})$$

following the commutation relations

$$[\hat{\Phi}_i, \hat{q}_j] = \delta_{ij} i\hbar \quad (\text{A.27})$$

Appendix B

4-Josephson Junction Flux Qubit Hamiltonian



The Hamiltonian of the flux qubit above is

$$\mathcal{H} = \frac{(2e^2)}{2C_J} \frac{1}{3a+1} \times \left\{ (2a+1)(n_1^2 + n_2^2 + n_3^2) - 2a(n_1n_2 + n_1n_3 + n_2n_3) \right\} - E_J \left[\sum_{i=1}^3 \cos(\phi_i) + \alpha \cos\left(\sum_{i=1}^3 \phi_i + 2\pi f\right) \right], \quad (\text{B.1})$$

where E_J and C_J refer to the big junction, and $a \equiv \alpha + C_{sh}/C_J$.

Appendix C

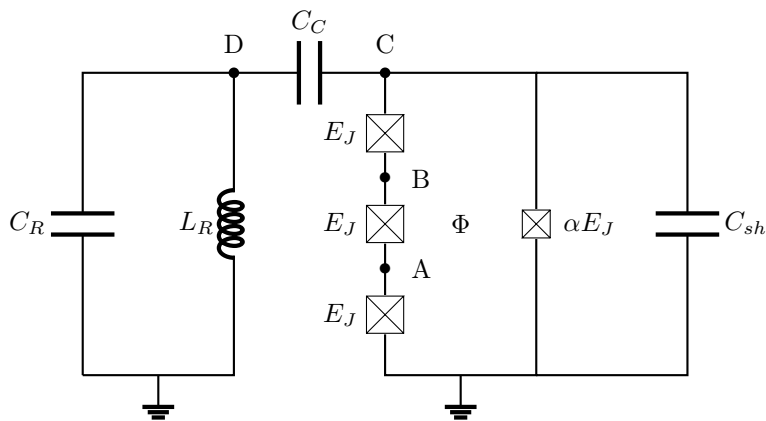
Qubit-Resonator Coupling

C.1 Introduction

We want to obtain the coupling strength and the dispersive shift and, in general, the interaction between a 4-Josephson junction flux qubit and a quarter-wave resonator. For that, the steps we will follow is: i) quantize the circuit; ii) follow the mathematical development for an easy simulation; iii) simulate it; iv) analyze the results. For the derivation we have closely followed [Ino12], where the difference is that their flux qubit consists only of three junctions and has no shunting capacitance.

C.2 Circuit Quantization

The circuit we want to quantize is the following.



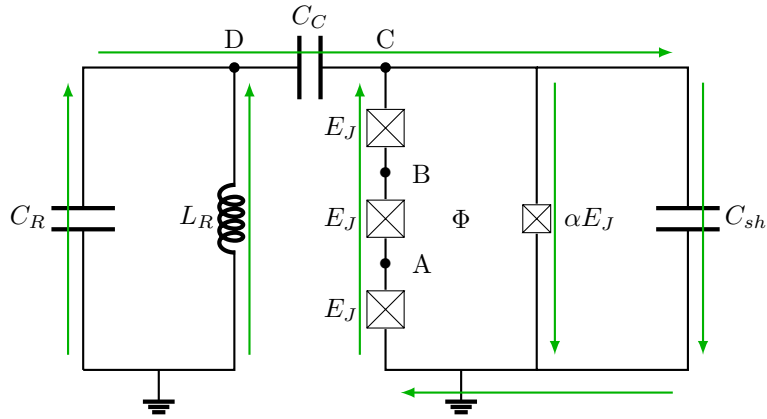
We should say a few things. As we see, on the right we have our 4-Josephson junction C-shunted flux qubit, with one junction α times smaller than the other

three. This qubit is coupled via a coupling capacitor, C_C to a resonator. This resonator is actually a quarter-wave resonator, but it can be modeled as an LC resonator. According to [Poz90], the equivalent circuit of a $\lambda/4$ resonator has the following values:

$$\begin{aligned} C &= \frac{\pi}{4\omega_0 Z_0}, \\ L &= \frac{1}{\omega_0^2 C}. \end{aligned} \tag{C.1}$$

C.2.1 Nodes, spanning tree and direction

For circuit quantization [Voo16], already explained in Appendix A, one has to decide the nodes and the spanning tree. The nodes have already been shown in the figure. The spanning tree chosen is easily seen if you go from the right ground until D, going gnd-A-B-C-D. Then one has to choose arbitrary directions which are a bit more difficult to explain, so here's the picture. Remember that these directions will not be important in the final Hamiltonian, but need to be chosen to be consistent throughout the procedure.



C.2.2 Movement equations

Once all the decisions have been made, it's time to find the movement equations for each node following the Kirchhoff's current law for the current incoming and

outgoing each node, $\sum I_{in} = \sum I_{out}$. The resulting equations for each node are

$$\begin{aligned}
\mathbf{A} : \quad & C_J \left(2\ddot{\phi}_A - \ddot{\phi}_B \right) = I_0 \sin \left(\frac{2\pi}{\Phi_0} (\phi_B - \phi_A) \right) - I_0 \sin \left(\frac{2\pi}{\Phi_0} \phi_A \right), \\
\mathbf{B} : \quad & C_J \left(2\ddot{\phi}_B - \ddot{\phi}_A - \ddot{\phi}_C \right) = I_0 \sin \left(\frac{2\pi}{\Phi_0} (\phi_C - \phi_B) \right) - I_0 \sin \left(\frac{2\pi}{\Phi_0} (\phi_B - \phi_A) \right), \\
\mathbf{C} : \quad & C_J \left(\ddot{\phi}_C - \ddot{\phi}_B \right) + C_C \left(\ddot{\phi}_C - \ddot{\phi}_D \right) + (C_{sh} + \alpha C_J) \ddot{\phi}_C = \\
& \alpha I_0 \sin \left(\frac{2\pi}{\Phi_0} (\Phi - \phi_c) \right) - I_0 \sin \left(\frac{2\pi}{\Phi_0} (\phi_C - \phi_B) \right), \\
\mathbf{D} : \quad & C_R \ddot{\phi}_D + C_R \left(\ddot{\phi}_D - \ddot{\phi}_C \right) = -\frac{\phi_D}{L_R}.
\end{aligned} \tag{C.2}$$

C.2.3 Lagrangian

Using the Euler-Lagrange equations, $\frac{d}{dt} \left(\frac{\partial \mathcal{L}}{\partial \dot{\Phi}_i} \right) = \frac{\partial \mathcal{L}}{\partial \Phi_i}$ to the previous equations, one obtains the following Lagrangian

$$\begin{aligned}
\mathcal{L} = & \frac{C_J}{2} \dot{\phi}_A^2 + \frac{C_J}{2} \left(\dot{\phi}_A - \dot{\phi}_B \right)^2 + \frac{C_J}{2} \left(\dot{\phi}_B - \dot{\phi}_C \right)^2 + \frac{C_C}{2} \left(\dot{\phi}_C - \dot{\phi}_D \right)^2 \\
& + \frac{C_{sh} + \alpha C_J}{2} \dot{\phi}_C^2 + \frac{C_R}{2} \dot{\phi}_D^2 + E_J \cos \left(\frac{2\pi}{\Phi_0} \phi_A \right) + E_J \cos \left(\frac{2\pi}{\Phi_0} (\phi_B - \phi_A) \right) \\
& + E_J \cos \left(\frac{2\pi}{\Phi_0} (\phi_C - \phi_B) \right) + \alpha E_J \cos \left(\frac{2\pi}{\Phi_0} (\Phi - \phi_C) \right) - \frac{\phi_D^2}{2L_R}.
\end{aligned} \tag{C.3}$$

It is more useful to write it in terms of branch variables, so that we have the flux at the junctions, the capacitance and the inductance instead of in the nodes. Then, looking at the circuit, one can easily find the following variable change

$$\begin{aligned}
\phi_1 &= \phi_A - \phi_{gnd} = \phi_A \\
\phi_2 &= \phi_B - \phi_A \\
\phi_3 &= \phi_C - \phi_B \\
\phi_R &\equiv \phi_D,
\end{aligned} \tag{C.4}$$

where 1, 2 and 3 are the big junctions and R refers to the resonator. Also, one can note that $\phi_1 + \phi_2 + \phi_3 = \phi_C$. Then, the Lagrangian looks like

$$\begin{aligned}
\mathcal{L} = & \frac{C_J}{2} \left(\dot{\phi}_1^2 \dot{\phi}_2^2 + \dot{\phi}_3^2 \right)^2 + \frac{C_{sh} + \alpha C_J}{2} \left(\dot{\phi}_1 + \dot{\phi}_2 + \dot{\phi}_3 \right)^2 \\
& + \frac{C_C}{2} \left(\dot{\phi}_1 + \dot{\phi}_2 + \dot{\phi}_3 - \dot{\phi}_R \right)^2 + \frac{C_R}{2} \dot{\phi}_R^2 - \frac{\phi_R}{2L_R} \\
& + E_J \left[\cos \left(\frac{2\pi}{\Phi_0} \phi_1 \right) + \cos \left(\frac{2\pi}{\Phi_0} \phi_2 \right) + \cos \left(\frac{2\pi}{\Phi_0} \phi_3 \right) \right. \\
& \left. + \alpha \cos \left(\frac{2\pi}{\Phi_0} (\phi_1 + \phi_2 + \phi_3 - \Phi) \right) \right]. \tag{C.5}
\end{aligned}$$

Another change is actually welcomed, as it is more convenient to deal with phase variable instead of flux variables, $\varphi_i = \frac{2\pi}{\Phi_0} \phi_i$, defining the new magnetic frustration parameter, $f \equiv \frac{\Phi}{\Phi_0}$. There's even another convenient *mass* definition:

$$\begin{aligned}
m'_1 & \equiv \left(\frac{\Phi_0}{2\pi} \right)^2 [(1 + \alpha)C_J + C_{sh} + C_C] \equiv m'_2 \equiv m'_3 \\
m'_4 & \equiv \left(\frac{\Phi_0}{2\pi} \right)^2 [\alpha C_J + C_{sh} + C_C] \\
m'_C & \equiv \left(\frac{\Phi_0}{2\pi} \right)^2 C_C \\
m'_R & \equiv \left(\frac{\Phi_0}{2\pi} \right)^2 (C_C + C_R). \tag{C.6}
\end{aligned}$$

With all these new definitions one arrives at the following expression of the Lagrangian

$$\begin{aligned}
\mathcal{L} = & \frac{1}{2} m'_1 \dot{\varphi}_1^2 + \frac{1}{2} m'_2 \dot{\varphi}_2^2 + \frac{1}{2} m'_3 \dot{\varphi}_3^2 + m'_4 (\dot{\varphi}_1 \dot{\varphi}_2 + \dot{\varphi}_1 \dot{\varphi}_3 + \dot{\varphi}_2 \dot{\varphi}_3) \\
& + E_J \cos \varphi_1 + E_J \cos \varphi_2 + E_J \cos \varphi_3 + \alpha E_J \cos (\varphi_1 + \varphi_2 + \varphi_3 - 2\pi f) \\
& - m'_C \dot{\varphi}_R (\dot{\varphi}_1 + \dot{\varphi}_2 + \dot{\varphi}_3) + \frac{1}{2} m'_R \dot{\varphi}_R^2 - \frac{1}{2L} \left(\frac{\Phi_0}{2\pi} \right) \varphi_R^2. \tag{C.7}
\end{aligned}$$

The generalized momenta, $p_i = \frac{\partial \mathcal{L}}{\partial \dot{\varphi}_i}$ is now easier to compute and one find the following matrix relation

$$\begin{pmatrix} p_1 \\ p_2 \\ p_3 \\ p_R \end{pmatrix} = \begin{pmatrix} m'_1 & m'_4 & m'_4 & -m'_C \\ m'_4 & m'_1 & m'_4 & -m'_C \\ m'_4 & m'_4 & m'_1 & -m'_C \\ -m'_C & m'_C & -m'_C & m'_R \end{pmatrix} \begin{pmatrix} \varphi_1 \\ \varphi_2 \\ \varphi_3 \\ \varphi_R \end{pmatrix} \tag{C.8}$$

C.2.4 Hamiltonian

Using the Legendre transformation, $\mathcal{H} = \sum_i p_i \dot{\varphi}_i - \mathcal{L}$ we arrive at the Hamiltonian, which can be written as

$$\mathcal{H} = \frac{1}{2} \vec{p}^T \mathbf{M}^{-1} \vec{p} + \mathcal{U}, \quad (\text{C.9})$$

where \mathbf{M}^{-1} is the inverse of the previous mass matrix and can be expressed as

$$\mathbf{M}^{-1} = \begin{pmatrix} m_1^{-1} & m_4^{-1} & m_4^{-1} & m_c^{-1} \\ m_4^{-1} & m_1^{-1} & m_4^{-1} & m_c^{-1} \\ m_4^{-1} & m_4^{-1} & m_1^{-1} & m_c^{-1} \\ m_c^{-1} & m_c^{-1} & m_c^{-1} & m_R^{-1} \end{pmatrix}, \quad (\text{C.10})$$

where these are new mass variables and, thanks to *mathematica* or python library *simpy*, one can get the exact expression of these variables,

$$\begin{aligned} m_1 &= \left(\frac{\Phi_0}{2\pi} \right)^2 C_J \left[1 + \frac{(\alpha + \beta)(\delta + \gamma) + \delta\gamma}{(2\alpha + 2\beta + 1)(\delta + \gamma) + 2\delta\gamma} \right], \\ \frac{1}{m_4} &= \frac{1}{m_1} - \left(\frac{2\pi}{\Phi_0} \right)^2 \frac{1}{C_J}, \\ m_C &= \left(\frac{\Phi_0}{2\pi} \right)^2 C_J \frac{F}{\gamma}, \\ m_R &= \left(\frac{\Phi_0}{2\pi} \right)^2 C_J \frac{F}{3\alpha + 3\beta + 3\gamma + 1}, \end{aligned} \quad (\text{C.11})$$

and we have defined a few more parameters

$$\begin{aligned} \beta &\equiv \frac{C_{sh}}{C_J}, \\ \gamma &\equiv \frac{C_C}{C_J}, \\ \delta &\equiv \frac{C_R}{C_J}, \\ F &= (3\alpha + 3\beta + 1)(\gamma + \delta) + 3\delta\gamma. \end{aligned} \quad (\text{C.12})$$

So, now, we have three Hamiltonians,

$$\mathcal{H} = \mathcal{H}_q + \mathcal{H}_R + \mathcal{H}_C, \quad (\text{C.13})$$

being the qubit, resonator and coupling Hamiltonian respectively. Using the relation $n_i = \frac{2\pi}{\Phi_0} \frac{p_i}{2e}$ and $E_C = \frac{e^2}{2C_J}$ we can define the qubit Hamiltonian

$$\begin{aligned} \mathcal{H}_q &= 4E_C \left\{ \left[1 + \frac{(\alpha + \beta)(\delta + \gamma) + \delta\gamma}{(2\alpha + 2\beta + 1)(\delta + \gamma) + 2\delta\gamma} \right]^{-1} (n_1^2 + n_2^2 + n_3^2) \right. \\ &\quad \left. + 2 \frac{(\alpha + \beta)(\delta + \gamma) - \delta\gamma}{(3\alpha + 3\beta + 1)(\delta + \gamma) + 3\delta\gamma} (n_1 n_2 + n_1 n_3 + n_2 n_3) \right\} \\ &\quad - E_J [\cos \varphi_1 + \cos \varphi_2 + \cos \varphi_3 + \alpha \cos(\varphi_1 + \varphi_2 + \varphi_3 - 2\pi f)]. \end{aligned} \quad (\text{C.14})$$

And this Hamiltonian is ready to be diagonalized. Next, let's look at the resonator Hamiltonian

$$\mathcal{H}_R = \frac{p_R^2}{m_R} + \frac{1}{2L_R} \left(\frac{\Phi_0}{2\pi} \right) \varphi_R^2, \quad (\text{C.15})$$

which can be redefined in the harmonic way

$$\mathcal{H}_R = \frac{p_R^2}{m_R} + \frac{1}{2} m_R \omega_R^2 \varphi_R^2, \quad (\text{C.16})$$

where we get the loaded resonant frequency

$$\omega_R = \frac{1}{\sqrt{L_R C_R}} \left(1 + \frac{(3\alpha + 3\beta + 1)\gamma}{(3\alpha + 3\beta + 3\gamma + 1)\delta} \right)^{1/2}. \quad (\text{C.17})$$

Now the Hamiltonian can be rewritten as usual

$$\mathcal{H}_R = \hbar\omega_R \left(a^\dagger a + \frac{1}{2} \right), \quad (\text{C.18})$$

with

$$\begin{aligned} \varphi_R &= \sqrt{\frac{\hbar}{2m_R\omega_R}} (a^\dagger + a) \\ p_R &= i\sqrt{\frac{\hbar m_R\omega_R}{2}} (a^\dagger - a) \end{aligned} \quad (\text{C.19})$$

In this situation we already know the eigenstates and eigenvalues of this Hamiltonian. Hence, we can move to the coupling Hamiltonian

$$\begin{aligned} \mathcal{H}_C &= 2e \left(\frac{\Phi_0}{2\pi} \right) \frac{n_1 + n_2 + n_3}{m_c} p_R = \\ &= 2i\gamma \sqrt{E_C E'_R} \sqrt{\frac{2}{F(3\alpha + 3\beta + 3\gamma + 1)}} (n_1 + n_2 + n_3) (a^\dagger - a), \end{aligned} \quad (\text{C.20})$$

where we have used the previous definition of F and $E'_R = \hbar\omega_R$

C.3 Numerical simulation

Once we have the Hamiltonians is now time to numerically find the values we want. Remember we are interested in the coupling strength between the qubit and the resonator and the qubit and, more specifically, the dispersive shift. The derivation has been done following the supplementary materials of [Yan15].

C.3.1 Qubit Hamiltonian

First, we will diagonalize our qubit Hamiltonian. Just to make it easier to handle, we will redefine it this way

$$\begin{aligned} \mathcal{H}_q = & 4E_C [\kappa_1 (n_1^2 + n_2^2 + n_3^2) + \kappa_2 (n_1 n_2 + n_1 n_3 + n_2 n_3)] \\ & - E_J [\cos \varphi_1 + \cos \varphi_2 + \cos \varphi_3 + \alpha \cos (\varphi_1 + \varphi_2 + \varphi_3 - 2\pi f)], \end{aligned} \quad (\text{C.21})$$

where the constants κ_1 and κ_2 have absorbed all the adimensional variables.

C.3.1.1 Define states

Now we have to choose a basis for performing the simulation. As no inductance is considered*, it is convenient to choose the charge basis as the basis in which we define our states. This is computationally and mathematical convenient because the resulting matrix representation of the Hamiltonian is a block diagonal matrix, with most of its elements equal to zero.

A general state is, then defined as

$$|\Psi\rangle = \sum_{i,j,k=-n_{max}}^{n_{max}} a_{i,j,k} |i, j, k\rangle, \quad (\text{C.22})$$

where each charge state $|i, j, k\rangle$ defines a state with i , j and k cooper pairs on junctions 1, 2 and 3 respectively. One has to check which is the maximum number of charges needed for the solution to converge. In our case, $n_{max} = 10$ is enough. Note that the number of states is $N = (2n_{max} + 1)^3$, and so the matrix is $N \times N$, so the computational costs scales quickly with increasing n_{max} . In this basis the capacitive part of the Hamiltonian is diagonal, making it easy to compute. However, one has to take care of constructing the correct matrix elements. Let's take a closer look.

First thing, one has to order the states in some way and be consistent with this decision. We will exemplify this process for $n_{max} = 10$ and it's easily

*Inductance is much smaller than Josephson one and, hence, considered negligible. If we would like to include it, the charge basis will not be convenient for its computational costs, and we should take a different approach.

followed for different n_{max} . This will be our ordering:

$$\begin{aligned}
|0\rangle &\equiv |-10, -10, -10\rangle \\
|1\rangle &\equiv |-10, -10, -9\rangle \\
&\dots \\
|20\rangle &\equiv |-10, -10, 10\rangle \\
|21\rangle &\equiv |-10, -9, -10\rangle \\
&\dots \\
|41\rangle &\equiv |-10, -9, 10\rangle \\
|42\rangle &\equiv |-10, -8, -10\rangle \\
&\dots \\
&\dots \\
|440\rangle &\equiv |-10, 10, 10\rangle \\
|441\rangle &\equiv |-9, -10, -10\rangle \\
&\dots \\
&\dots \\
&\dots \\
|9260\rangle &\equiv |10, 10, 10\rangle
\end{aligned} \tag{C.23}$$

It is easy to check how, for an ordered state, $|A\rangle$, how to find the representation in the charge basis,

$$|A\rangle \equiv |(A \operatorname{div} 21^2) - 10, (A \operatorname{div} 21) - 10, (A \operatorname{mod} 21) - 10\rangle, \tag{C.24}$$

where $a \operatorname{div} b$ is defined as the integer division between a and b (no remainder). Then, as an example,

$$\begin{aligned}
|440\rangle &\equiv |(440 \operatorname{div} 21^2) - 10, (440 \operatorname{div} 21) - 10, (440 \operatorname{mod} 21) - 10\rangle \\
&= |0 - 10, 20 - 10, 20 - 10\rangle = |-10, 10, 10\rangle.
\end{aligned} \tag{C.25}$$

C.3.1.2 Capacitive terms

With the basis defined, now it's time to check the matrix representations of the operators n_i^2 and $n_i n_j$. For convenience, we write it as a vector and then fill the diagonal thanks to the *scipy.sparse* library. It is a great idea to use the Kronecker product applied to vectors,

$$\vec{a} \otimes \vec{b} = \begin{pmatrix} a_1 \\ a_2 \\ \dots \\ a_n \end{pmatrix} \otimes \begin{pmatrix} b_1 \\ b_2 \\ \dots \\ b_M \end{pmatrix} = \begin{pmatrix} a_1 \vec{b} \\ a_2 \vec{b} \\ \dots \\ a_n \vec{b} \end{pmatrix} = \begin{pmatrix} a_1 b_1 \\ a_1 b_2 \\ \dots \\ a_1 b_m \\ a_2 b_1 \\ \dots \\ \dots \\ a_n b_m \end{pmatrix}. \tag{C.26}$$

With this product, one can define the n_i^2 and $n_i n_j$ terms. Note that, according to the ordering in (C.23), the n_3 diagonal vector will be

$$n_3 = \begin{pmatrix} -10 \\ -9 \\ \dots \\ 10 \\ -10 \\ \dots \\ 10 \\ \dots \\ \dots \\ \dots \\ 10 \end{pmatrix} = \vec{1} \otimes \vec{1} \otimes \begin{pmatrix} -10 \\ -9 \\ \dots \\ 9 \\ 10 \end{pmatrix} \equiv \vec{1} \otimes \vec{1} \otimes \vec{n}, \quad (\text{C.27})$$

where we have defined \vec{n} . With this in mind, the $n_i n_j$ diagonal vectors can be defined as

$$\begin{aligned} n_1 n_2 &\equiv \vec{n} \otimes \vec{n} \otimes \vec{1}, \\ n_1 n_3 &\equiv \vec{n} \otimes \vec{1} \otimes \vec{n}, \\ n_2 n_3 &\equiv \vec{1} \otimes \vec{n} \otimes \vec{n}. \end{aligned} \quad (\text{C.28})$$

Finally, defining

$$\vec{n}^2 = \begin{pmatrix} (-10)^2 \\ (-9)^2 \\ \dots \\ 9^2 \\ 10^2 \end{pmatrix} = \begin{pmatrix} 100 \\ 81 \\ \dots \\ 81 \\ 100 \end{pmatrix}, \quad (\text{C.29})$$

one can express

$$\begin{aligned} n_1^2 &\equiv \vec{n}^2 \otimes \vec{1} \otimes \vec{1}, \\ n_2^2 &\equiv \vec{1} \otimes \vec{n}^2 \otimes \vec{1}, \\ n_3^2 &\equiv \vec{1} \otimes \vec{1} \otimes \vec{n}^2. \end{aligned} \quad (\text{C.30})$$

Once we have the diagonal vectors of these operators, one just have to create a matrix with these vectors in the diagonal.

C.3.1.3 Josephson terms

For computing the Josephson terms of the Hamiltonian one has note that $\cos \varphi = (e^{i\varphi} + e^{-i\varphi})/2$. Then we can use the following useful relation

$$e^{\pm i\varphi} |n\rangle = |n \mp 1\rangle \quad (\text{C.31})$$

so the effect of a Josephson term is

$$\cos \varphi |n\rangle = \frac{1}{2} (|n+1\rangle + |n-1\rangle). \quad (\text{C.32})$$

Hence, the one-variable Josephson terms are easy to write down. For example

$$E_J \cos \varphi_1 |n_1, n_2, n_3\rangle = \frac{E_J}{2} (|n_1 + 1, n_2, n_3\rangle + |n_1 - 1, n_2, n_3\rangle). \quad (\text{C.33})$$

The fourth term is a bit trickier, but no so much

$$\begin{aligned} & \alpha E_J \cos(\varphi_1 + \varphi_2 + \varphi_3 + 2\pi f) |n_1, n_2, n_3\rangle \\ &= \frac{E_J}{2} (e^{-i2\pi f} |n_1 + 1, n_2 + 1, n_3 + 1\rangle + e^{i2\pi f} |n_1 - 1, n_2 - 1, n_3 - 1\rangle). \end{aligned} \quad (\text{C.34})$$

For writing the matrix representation, we can use again the kronecker product. First we'll do it for one variable basis, $|n\rangle$, and then for the three basis which is our case. Let's define this matrix

$$M_J = \begin{pmatrix} 0 & 1 & 0 & & \cdots & & & & & 0 \\ 1 & 0 & 1 & 0 & & & & & & \\ 0 & 1 & 0 & 1 & & & & & & \\ \vdots & & & & & & & & & \\ & & & & \ddots & & & & & \\ & & & & & & & & & \\ & & & & & & & & & \\ & & & & & & & & & \\ & & & & & & 1 & 0 & 1 & 0 \\ & & & & & & 0 & 1 & 0 & 1 \\ 0 & & & \cdots & & & 0 & 1 & 0 & \end{pmatrix} \equiv M_{JU} + M_{JL}, \quad (\text{C.35})$$

being an $N \times N$ matrix and the M_{JU} and M_{JL} being the upper and lower diagonal matrices respectively. This matrix has nonzero elements just in the upper and lower diagonals, which is computationally very efficient. With M_J you can find the matrix representation of a general $E_J \cos \varphi$ term

$$E_J \cos \varphi = \frac{1}{2} E_J M_J. \quad (\text{C.36})$$

Now, we can extend this result to our three variable system using the Kronecker product. Then,

$$\begin{aligned} \cos \varphi_1 &= \frac{1}{2} M_J \otimes \mathbf{I} \otimes \mathbf{I}, \\ \cos \varphi_2 &= \frac{1}{2} \mathbf{I} \otimes M_J \otimes \mathbf{I}, \\ \cos \varphi_3 &= \frac{1}{2} \mathbf{I} \otimes \mathbf{I} \otimes M_J. \end{aligned} \quad (\text{C.37})$$

The fourth junction matrix representation is, then,

$$\begin{aligned} & \cos(\varphi_1 + \varphi_2 + \varphi_3 + 2\pi f) = \\ & \frac{1}{2} (e^{-i2\pi f} M_{JL} \otimes M_{JL} \otimes M_{JL} + e^{i2\pi f} M_{JU} \otimes M_{JU} \otimes M_{JU}). \end{aligned} \quad (\text{C.38})$$

C.3.1.4 Eigenstates and eigenenergies

Once we know how to find all the matrix elements, we must write it in the code. We must know that, since the matrices can become quite large, there can be memory problems in the multiplications. For example, in the last case, one would have troubles making the kronecker product of three 21x21 matrices using the `numpy.kron` function. For that, we use the `scipy.sparse` library. We create the vector that we will later place in the correct diagonal, which is not the main one for the Josephson terms. For that one has to do the analysis on which diagonal will it be and, then, place the vector there. Once done we can sum all the matrices and then diagonalize with the `eigh` function. There we get the lowest eigenenergies and eigenvectors of our Hamiltonian. These states are then written in the charge basis. For example, our ground state will be

$$|\Psi_0\rangle = \sum_{i,j,k=-n_{max}}^{n_{max}} a_{0,(i,j,k)} |i, j, k\rangle, \quad (\text{C.39})$$

C.3.2 Resonator Hamiltonian

Nothing has to be done with the resonator Hamiltonian, except for writing it in the second quantization form, as we already did in (C.18). There we find that the appropriate basis is the number basis, $|k\rangle$, and we already know their eigenenergies, being $(l + \frac{1}{2})\hbar\omega_R$. We will usually work in Gigahertz, so that $\hbar = 1$, and one has to remember to multiply the ω per 2π to get the energy.

C.3.3 Coupling Hamiltonian

C.3.3.1 Define states

The coupling Hamiltonian involves the two systems, so one has to think not to end with too big matrices. For that, we will use the fact that we already know the eigenenergies and eigenstates of both the qubit and the resonator Hamiltonians alone. Then, as now we are going to simulate the whole system, it's a good idea to use these two basis as our computational basis. Then, expressing the qubit Hamiltonian eigenstates as $|\psi_q\rangle$ with energies ϵ_q and the resonator eigenstates $|k\rangle$ with energies $(l + \frac{1}{2})\hbar\omega_R$. Then, the basis we will use for our matrix representation is

$$|\Psi\rangle = |\psi_q\rangle \otimes |k\rangle. \quad (\text{C.40})$$

Then, the qubit and resonator Hamiltonian action over these states can be expressed as

$$\begin{aligned} \mathcal{H}_q |\Psi\rangle &= (\mathcal{H}_q \otimes \mathbf{I})(|\psi_q\rangle \otimes |k\rangle), \\ \mathcal{H}_R |\Psi\rangle &= (\mathbf{I} \otimes \mathcal{H}_R)(|\psi_q\rangle \otimes |k\rangle). \end{aligned} \quad (\text{C.41})$$

For the explanation, we will consider that we take the 10 lowest qubit energy eigenstates and the 5 lowest resonator eigenstates. So, the basis will have a total of 50 states. As we did in section (C.3.1.1), we will order our states:

$$\begin{aligned}
|0\rangle &\equiv |0, 0\rangle \\
|1\rangle &\equiv |0, 1\rangle \\
&\dots \\
|4\rangle &\equiv |0, 4\rangle \\
|5\rangle &\equiv |1, 0\rangle \\
&\dots \\
&\dots \\
|49\rangle &\equiv |9, 4\rangle
\end{aligned} \tag{C.42}$$

The way to find the relation between the ordered states and the qubit and resonator separate basis is the following

$$|A\rangle \equiv |A \operatorname{div} 5, A \operatorname{mod} 5\rangle . \tag{C.43}$$

Then, as an example,

$$|41\rangle \equiv |41 \operatorname{div} 5, 41 \operatorname{mod} 5\rangle = |8, 1\rangle . \tag{C.44}$$

C.3.3.2 Qubit and resonator terms

Using the equation (C.41) and the fact that we know our basis, we can easily construct our matrix representation of both Hamiltonians which will be two diagonal matrices. Then we just sum them both. Just to make it clear, these are the matrix representation of \mathcal{H}_q . The rest is trivial.

$$\mathcal{H}_q = \begin{pmatrix} \epsilon_0 & 0 & \dots & & 0 \\ 0 & \epsilon_1 & 0 & & \\ \vdots & & & & \\ & & & \ddots & \\ & & & & 0 & \epsilon_8 & 0 \\ 0 & & \dots & & 0 & 0 & \epsilon_9 \end{pmatrix} . \tag{C.45}$$

C.3.3.3 Coupling terms

Let's look again at the coupling Hamiltonian, but rewriting it in a simpler form

$$\mathcal{H}_C = \kappa_C (n_1 + n_2 + n_3)(a^\dagger - a) . \tag{C.46}$$

This Hamiltonian can be written as

$$\mathcal{H}_C = \kappa_C \mathcal{H}_{C,q} \otimes \mathcal{H}_{C,R} , \tag{C.47}$$

where $\mathcal{H}_{C,q} = n_1 + n_2 + n_3$ and $\mathcal{H}_{C,R} = a^\dagger - a$. We can see that neither the qubit nor the resonator operators are in diagonal in this basis.

We can start at looking at the qubit part, $\mathcal{H}_{C,q}$. It's not diagonal in our basis, but it is in the charge basis, and remember that we have our eigenstates expressed in this basis, as done for the ground in equation(C.39). Then, all we have to do is to compute all the matrix elements, 100 in total if only the 10 lowest are chosen. Mathematically, this is

$$\begin{aligned}
& \langle \psi_\alpha | \mathcal{H}_{C,q} | \psi_\beta \rangle = \\
& \left(\sum_{i,j,k=-n_{max}}^{n_{max}} a_{\alpha,(i,j,k)}^* \langle i,j,k | \right) (n_1 + n_2 + n_3) \cdot \left(\sum_{l,m,n=-n_{max}}^{n_{max}} a_{\beta,(l,m,n)} |l,m,n\rangle \right) = \\
& \sum_{i,j,k,l,m,n=-n_{max}}^{n_{max}} a_{\alpha,(i,j,k)}^* a_{\beta,(l,m,n)} (l+m+n) \langle i,j,k | l,m,n \rangle = \\
& \sum_{i,j,k,l,m,n=-n_{max}}^{n_{max}} a_{\alpha,(i,j,k)}^* a_{\beta,(l,m,n)} (l+m+n) \delta_{i,l} \delta_{j,m} \delta_{k,n} = \\
& \sum_{i,j,k=-n_{max}}^{n_{max}} a_{\alpha,(i,j,k)}^* a_{\beta,(i,j,k)} (i+j+k).
\end{aligned} \tag{C.48}$$

It is easy to see that this is not diagonal in the eigenbasis and the symmetric off-diagonal elements are conjugate of each other. It's, then a dense matrix where all the elements have to be computed in a long multiplication.

The resonator part of the coupling Hamiltonian is much easier, and it's easily analytically expressed

$$\begin{aligned}
\langle k | \mathcal{H}_{C,R} | l \rangle &= \langle k | (a^\dagger - a) | l \rangle = \langle k | \left(\sqrt{l+1} |l+1\rangle - \sqrt{l} |l-1\rangle \right) = \\
&= \sqrt{l+1} \delta_{k,l+1} - \sqrt{l} \delta_{k,l-1}.
\end{aligned} \tag{C.49}$$

In our 5x5 case, it's easy to write the whole matrix

$$\mathcal{H}_{C,R} = \begin{pmatrix} 0 & -1 & 0 & 0 & 0 \\ 1 & 0 & -\sqrt{2} & 0 & 0 \\ 0 & \sqrt{2} & 0 & -\sqrt{3} & 0 \\ 0 & 0 & \sqrt{3} & 0 & -2 \\ 0 & 0 & 0 & 2 & 0 \end{pmatrix}. \tag{C.50}$$

C.3.3.4 Eigenstates and eigenenergies

With the matrix representation of both $\mathcal{H}_{C,q}$ and $\mathcal{H}_{C,R}$, we can write the full coupling Hamiltonian matrix using (C.47) and summing to the previous qubit and resonator Hamiltonian, as in eq.C.13. We can now proceed to diagonalize it using the same procedure as it section (C.3.1.4). Then, we will have the

eigenstates and eigenenergies of the qubit-resonator system. If, as in our case, the qubit energy is lower than the resonator energy, we will see how the dressed states and see the shift of the qubit energy by the presence of the resonator.

C.4 Dispersive shift

The most important value of the qubit-resonator coupling is the dispersive shift, that is, the difference in the resonator frequency depending on the qubit states. This shift is the basis of our measurement procedure, so we need to make sure it's large enough so that we can distinguish between both states.

Let's take a look on the full Hamiltonian

$$\mathcal{H}/\hbar = \omega_r a^\dagger a + \sum_i \omega_i |i\rangle \langle i| + \kappa_C (n_1 + n_2 + n_3) (a^\dagger - a). \quad (\text{C.51})$$

Now, we can use the identity $\mathbf{I} = \sum_i |i\rangle \langle i|$ and rewrite it as ($\hbar \equiv 1$)

$$\mathcal{H} = \omega_r a^\dagger a + \sum_i \omega_i |i\rangle \langle i| + \sum_{ij} g_{ij} |i\rangle \langle j| (a^\dagger - a), \quad (\text{C.52})$$

where we have defined

$$g_{ij} \equiv \langle i| \kappa_C (n_1 + n_2 + n_3) |j\rangle. \quad (\text{C.53})$$

C.4.1 Schrieffer-Wolff perturbation theory

With equation (C.52) in mind we can perform some transformations so that we achieve a diagonal representation of this Hamiltonian. For that we will follow what's explained in the literature [Zhu12] [Bla21].

The Schrieffer-Wolff perturbation theory consists in finding a unitary transformation acting on the unperturbed Hamiltonian, \mathcal{H} , so that the resulting perturbed Hamiltonian, \mathcal{H}' , uncouples the desired subspaces, which in our case will be the product states of the qubit and resonator Hamiltonian. These define the projectors that will be used throughout the development,

$$P_{q,k} = |q, k\rangle \langle q, k| \quad (\text{C.54})$$

where $|q, k\rangle \equiv |\psi_q\rangle \otimes |k\rangle$ is the product basis we will consider.

For applying the Schrieffer-Wolff, one has to express the Hamiltonian in the following form

$$\mathcal{H} = \mathcal{H}_0 + V, \quad (\text{C.55})$$

where \mathcal{H}_0 is the free Hamiltonian already diagonal in our chosen basis[†] and V is a perturbation small enough so that we can treat it perturbationally.

[†]If what you want to uncouple is not all the states, but some subspaces, this free Hamiltonian must be block diagonal in your subspaces and not fully diagonal.

To this Hamiltonian, we are going to apply a unitary transformation

$$\mathcal{H}' = e^{iS}\mathcal{H}e^{-iS}, \quad (\text{C.56})$$

and apply the Baker-Campbell-Hausdorff (BCH) formula (Hadamard lema)

$$e^{iS}\mathcal{H}e^{-iS} = \mathcal{H} + [iS, \mathcal{H}] + \frac{1}{2!}[iS, [iS, \mathcal{H}]] + \dots = \sum_{n=0}^{\infty} \frac{1}{n!}[iS, \mathcal{H}]_n. \quad (\text{C.57})$$

It is useful to define a parameter λ , which later will be set to one, used for ordering the terms. This parameter corresponds to the order of perturbation of the terms.

$$\begin{aligned} \mathcal{H} &= \mathcal{H}^{(0)} + \lambda\mathcal{H}^{(1)} + \lambda^2\mathcal{H}^{(2)} + \dots, \\ S &= \lambda S^{(1)} + \lambda^2 S^{(2)} + \dots \end{aligned} \quad (\text{C.58})$$

where

$$\mathcal{H}^{(0)} = \mathcal{H}_0. \quad (\text{C.59})$$

Then one can explicitly compute eq.(C.57) and order it by these parameters λ .

$$\begin{aligned} \mathcal{H}' &= \mathcal{H} + [iS, \mathcal{H}] + \frac{1}{2!}[iS, [iS, \mathcal{H}]] + \mathcal{O}(\lambda^3) =, \\ &= \mathcal{H}_0 + \{ \lambda V + [i\lambda S_1, \mathcal{H}_0] \} + \{ [i\lambda^2 S_2, \mathcal{H}_0] \\ &\quad + [i\lambda S_1, \lambda V] + \frac{1}{2}[i\lambda S_1, [i\lambda S_1, \mathcal{H}_0]] \} + \mathcal{O}(\lambda^3). \end{aligned} \quad (\text{C.60})$$

Then, some conditions must be fulfilled. The first and most important, is that the resulting Hamiltonian doesn't couple different subspaces, that is

$$P_{q,k}\mathcal{H}'P_{p,l} = P_{q,k}e^{iS}\mathcal{H}e^{-iS}P_{p,l} = 0 \quad (\{q, k\} \neq \{p, l\}). \quad (\text{C.61})$$

This condition determines all the off-diagonal elements of \mathcal{H}' (to 0), but for the diagonal we will impose the following condition

$$P_{q,k}SP_{q,k} = 0, \quad (\text{C.62})$$

which means that the diagonal elements of generator S (that's how it's called) are zero. These two conditions uniquely determines \mathcal{H}' and S [Zhu12]. We will follow step by step all the development until we have our final desired dispersive Hamiltonian. If we look at equation (C.60) one should notice that the conditions (C.61) has to be fulfilled for every order of λ . Moreover, conditions (C.62) must also be satisfied for every order of λ in (C.58) for the generator S .

For the zeroth order, λ^0 , of (C.60) it's straightforward as \mathcal{H}_0 is already diagonal. Let's impose the first conditions on the order λ^1 .

$$P_{q,k}(V + [iS_1, \mathcal{H}_0])P_{p,l} = 0 \quad (\{q, k\} \neq \{p, l\}). \quad (\text{C.63})$$

This leads to

$$\begin{aligned}
\langle q, k | V | p, l \rangle &= -\langle q, k | [iS_1, \mathcal{H}_0] | p, l \rangle = \\
&= -i \langle q, k | \left[S_1 \left(\omega_R a^\dagger a + \sum_i \omega_i |i\rangle \langle i| \right) - \left(\omega_R a^\dagger a + \sum_i \omega_i |i\rangle \langle i| \right) S_1 \right] | p, l \rangle \\
&= -i (E_{p,l} - E_{q,k}) \langle q, k | S_1 | p, l \rangle,
\end{aligned} \tag{C.64}$$

where we have defined $E_{q,k} \equiv k\omega_R + \omega_q$. Then, the first order of the generator can be defined as

$$\langle q, k | S_1 | p, l \rangle = i \frac{\langle q, k | V | p, l \rangle}{E_{q,k} - E_{p,l}} \quad (\{q, k\} \neq \{p, l\}). \tag{C.65}$$

The diagonal terms are zero, since we have chosen the generator to be off-diagonal. Equation (C.63) is also zero for diagonal terms, since V has no terms in the diagonal and the commutator is zero ($E_{q,k} - E_{q,k} = 0$).

Now we should impose the same conditions to the second order. However, what this will give us is an expression for the second term of the generator, S_2 , so that $\mathcal{H}^{(2)}$ has no off-diagonal terms. This is something that we don't need, as we will only retain the first terms of the dispersive Hamiltonian. Hence, what we have to do, is to obtain the diagonal terms that appear in the second order of λ , and we will have found our dispersive Hamiltonian (up to second order). Then,

$$P_{i,n} \left([iS_2, \mathcal{H}_0] + [iS_1, V] + \frac{1}{2} [iS_1, [iS_1, \mathcal{H}_0]] \right) P_{i,n}. \tag{C.66}$$

The first term is zero ($E_{i,n} - E_{i,n} = 0$). The last term has the commutator $[iS_1, \mathcal{H}_0]$ which we have proved to be equal to $-V$ for the off-diagonal terms (C.64) and it's also equal for the diagonal terms as both are null. Then (C.66) is just

$$\frac{1}{2} P_{i,n} [iS_1, V] P_{i,n}. \tag{C.67}$$

Now come the hardest moment, the climax before the end. Be ready

$$\begin{aligned}
\frac{1}{2} P_{i,n} [iS_1, V] P_{i,n} &= \frac{i}{2} P_{i,n} S_1 V P_{i,n} - \frac{i}{2} P_{i,n} V S_1 P_{i,n} \\
&= \frac{i}{2} |i, n\rangle (\langle i, n | S_1 V | i, n\rangle - \langle i, n | V S_1 | i, n\rangle) \langle i, n|.
\end{aligned} \tag{C.68}$$

We can add the identity $\sum_{j,m} |j, m\rangle \langle j, m|$

$$\begin{aligned}
& \frac{i}{2} \sum_{j,m} |i, n\rangle \left(\langle i, n| S_1 |j, m\rangle \langle j, m| V |i, n\rangle - \right. \\
& \quad \left. \langle i, n| V |j, m\rangle \langle j, m| S_1 |i, n\rangle \right) \langle i, n| \\
&= \frac{i}{2} \sum_{j \neq i, m \neq n} |i, n\rangle \left(i \frac{\langle i, n| V |j, m\rangle}{E_{i,n} - E_{j,m}} \langle j, m| V |i, n\rangle - \right. \\
& \quad \left. i \langle i, n| V |j, m\rangle \frac{\langle j, m| V |i, n\rangle}{E_{j,m} - E_{i,n}} \right) \langle i, n| \\
&= -\frac{1}{2} \sum_{j \neq i, m \neq n} |i, n\rangle \langle i, n| \left(\frac{\langle i, n| V |j, m\rangle \langle j, m| V |i, n\rangle}{E_{i,n} - E_{j,m}} - \frac{\langle i, n| V |j, m\rangle \langle j, m| V |i, n\rangle}{E_{j,m} - E_{i,n}} \right). \tag{C.69}
\end{aligned}$$

One should note that both terms are actually the same, so, in the end

$$P_{i,n} \mathcal{H}^{(2)} P_{i,n} = |i, n\rangle \langle i, n| \sum_{j \neq i, m \neq n} \left(\frac{\langle i, n| V |j, m\rangle \langle j, m| V |i, n\rangle}{E_{j,m} - E_{i,n}} \right). \tag{C.70}$$

We must compute the term $\langle i, n| V |j, m\rangle$ and we will be almost ready.

$$\langle i, n| V |j, m\rangle = \langle i, n| \sum_{kl} g_{kl} |k\rangle \langle l| (a^\dagger - a) |j, m\rangle = g_{ij} \langle n| (a^\dagger - a) |m\rangle. \tag{C.71}$$

Then,

$$\langle i, n| V |j, m\rangle \langle j, m| V |i, n\rangle = g_{ij} \langle n| (a^\dagger - a) |m\rangle g_{ji} \langle m| (a^\dagger - a) |n\rangle. \tag{C.72}$$

With this equation I should note two things that I'm too tired to write it down. One is that $g_{i,j} = g_{j,i}^*$. For checking, one just applies the definition of $g_{i,j}$ in terms of the n_X operators and does the algebra. The other thing is

$$\begin{aligned}
& \langle n| (a^\dagger - a) |m\rangle \langle m| (a^\dagger - a) |n\rangle = \\
&= -\langle n| a^\dagger |m\rangle \langle m| a |n\rangle - \langle n| a |m\rangle \langle m| a^\dagger |n\rangle \\
&= -\langle n| a^\dagger a |n\rangle \delta_{m,n-1} - \langle n| a a^\dagger |n\rangle \delta_{m,n+1} \\
&= -\langle n| a^\dagger a |n\rangle (\delta_{m,n-1} + \delta_{m,n+1}) - \delta_{m,n+1}, \tag{C.73}
\end{aligned}$$

where we have used the commutation relation $[a, a^\dagger] = 1$. If one puts all these results into (C.70),

$$\begin{aligned}
& \langle i, n| \mathcal{H}^{(2)} |i, n\rangle = \sum_{j \neq i, m \neq n} \left(\frac{|g_{ij}|^2 a^\dagger a (\delta_{m,n-1} + \delta_{m,n+1}) + |g_{ij}|^2 \delta_{m,n+1}}{E_{i,n} - E_{j,m}} \right) = \\
&= \sum_{j \neq i} \frac{|g_{ij}|^2 a^\dagger a}{\omega_i + n\omega_R - (\omega_j + (n-1)\omega_R)} + \sum_{j \neq i} \frac{|g_{ij}|^2 a^\dagger a}{\omega_i + n\omega_R - (\omega_j + (n+1)\omega_R)} \\
&+ \sum_{j \neq i} \frac{|g_{ij}|^2}{\omega_i + n\omega_R - (\omega_j + (n+1)\omega_R)}. \tag{C.74}
\end{aligned}$$

Now, defining

$$\chi_{ij} = \frac{|g_{ij}|^2}{\omega_i - \omega_j - \omega_R} \equiv \frac{|g_{ij}|^2}{\omega_{ij} - \omega_R} \equiv \frac{|g_{ij}|^2}{\Delta_{ij}}, \quad (\text{C.75})$$

we arrive at

$$\begin{aligned} & \sum_{j \neq i} \frac{|g_{ij}|^2}{\omega_{ij} + \omega_R} a^\dagger a + \sum_{j \neq i} \frac{|g_{ij}|^2}{\omega_{ij} - \omega_R} a^\dagger a + \sum_{j \neq i} \frac{|g_{ji}|^2}{\omega_{ij} - \omega_R} \\ &= - \sum_{j \neq i} \frac{|g_{ji}|^2}{\omega_{ji} - \omega_R} a^\dagger a + \sum_{j \neq i} \frac{|g_{ij}|^2}{\omega_{ij} - \omega_R} a^\dagger a + \sum_{j \neq i} \frac{|g_{ji}|^2}{\omega_{ij} - \omega_R} \\ &= \sum_{j \neq i} [(\chi_{ij} - \chi_{ji}) a^\dagger a + \chi_{ij}] \end{aligned} \quad (\text{C.76})$$

The final and desired dispersive Hamiltonian is, then

$$\mathcal{H}' = \mathcal{H}_0 + \sum_{i, j \neq i} [(\chi_{ij} - \chi_{ji}) a^\dagger a + \chi_{ij}] |i\rangle \langle i|. \quad (\text{C.77})$$

We can define the following quantities

$$\begin{aligned} \Lambda_i &= \sum_{j \neq i} \chi_{ij}, \\ \chi_i &= \sum_{j \neq i} (\chi_{ij} - \chi_{ji}). \end{aligned} \quad (\text{C.78})$$

Then the final multilevel Hamiltonian is

$$\mathcal{H}' = \left(\omega_R + \sum_i \chi_i \right) a^\dagger a + \sum_i (\omega_i + \Lambda_i) |i\rangle \langle i|. \quad (\text{C.79})$$

Now it's easy to see the dispersive shift as a shift in the resonator frequency depending on the qubit state, and also a lamb shift in the qubit frequency, $\omega'_i \equiv \omega_i + \Lambda_i$.

Now if we stay just with the two lowest levels, and using $\sigma_Z = |0\rangle \langle 0| - |1\rangle \langle 1|$, and using the following identity:

$$a_0 |0\rangle \langle 0| + a_1 |1\rangle \langle 1| = \frac{a_0 + a_1}{2} \mathbf{I} - \frac{\delta_{01}}{2} \sigma_Z, \quad (\text{C.80})$$

where $\delta_{01} \equiv a_1 - a_0$. Then, the Hamiltonian can be read as

$$\begin{aligned} \mathcal{H}' &= \left(\omega_R + \frac{\chi_0 + \chi_1}{2} - \chi \sigma_Z \right) a^\dagger a - \frac{\omega'_{01}}{2} \sigma_Z + c \mathbf{I} \\ &= (\omega'_R - \chi \sigma_Z) a^\dagger a - \frac{\omega'_q}{2} \sigma_Z, \end{aligned} \quad (\text{C.81})$$

where we have dropped constant terms, redefined the resonator and qubit frequency and defined the dispersive shift as

$$\chi \equiv \frac{1}{2}(\chi_0 - \chi_1) = \frac{1}{2} \left(\sum_{j \neq 0} (\chi_{0j} - \chi_{j0}) - \sum_{j \neq 1} (\chi_{1j} - \chi_{j1}) \right). \quad (\text{C.82})$$

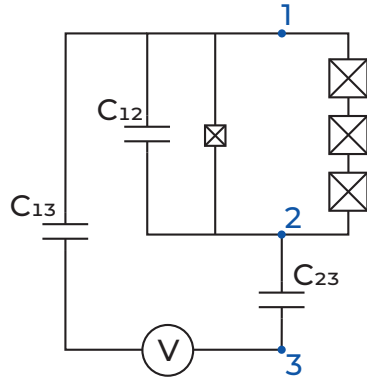
One can stop the sum at $j = 2$ it would be

$$\begin{aligned} \chi &= \frac{1}{2}(\chi_{01} - \chi_{10} + \chi_{02} - \chi_{20} - \chi_{10} + \chi_{01} - \chi_{12} + \chi_{21}) \\ \chi &= \chi_{01} - \chi_{10} + \frac{1}{2}(\chi_{02} - \chi_{20} - \chi_{12} + \chi_{21}). \end{aligned} \quad (\text{C.83})$$

And now, finally, we are ready to compute our dispersive shift up to second or the desired order.

Appendix D

Grounded Loop Capacitance Extraction



The grounded qubit loop has the circuit schematic shown above, which is considerably simpler than the floating qubit device.

The same process is followed, however. First, the voltage node is removed, and the Thevenin capacitance is obtained, which for this case is easy to compute analytically by finding effective capacitances in series and in parallel

$$C_{\text{th}} = C_{12} + \left(\frac{1}{C_{23}} + \frac{1}{C_{12}} \right)^{-1}. \quad (\text{D.1})$$

The $V_{\text{th}} = \beta V$ is obtained by the Kirchoff voltage laws, which as there is only one loop is straightforward,

$$\beta = \left(\frac{C_{13}}{C_{12}} + \frac{C_{12}}{C_{23}} + 1 \right)^{-1}. \quad (\text{D.2})$$

The final C_C and C_{sh} are then obtained through the same expressions as for the floating qubit

$$C_{th} = C_c + C_{sh}, \quad (D.3)$$

$$V_{th} = \frac{C_c}{C_c + C_{sh}} V. \quad (D.4)$$